Inkjet Printing of TiO_2

Thesis submitted in accordance with the
requirements of
The University of Liverpool
for the degree of
Doctor in Philosophy
By Josh Turner

September 30, 2019

Abstract

This thesis describes the formulation, optimisation, and development of inks for the deposition of TiO_2 using inkjet printing. TiO_2 is an industrially significant metal oxide (MO) with applications in photocatalysis, gas sensing, dye pigmentation, and self-cleaning materials, to name just a few. For applications that require a directly patterned thin film of TiO_2, inkjet printing is an attractive route to deposition. Inkjet printing of MOs, including TiO_2, is a process still in its infancy and requires further development. Most inks are based on colloidal suspensions of TiO_2, either purchased or synthesised using the sol-gel technique, that are typical in the spin and dip-coating processes. Our work aimed to instead base our inks on the solution precursors used in chemical vapour deposition (CVD), specifically titanium(IV) isopropoxide (TTIP). Due to the strong preference for the anatase TiO_2 polymorph in most applications, emphasis was placed on obtaining anatase and reducing the temperature at which this occurred. To this end, several ink formulations were developed including: a solution-based TTIP ink, a hybrid alkoxide/nanoparticle ink, titanium oxo-cluster inks, and niobium doped inks.

TTIP is moisture-sensitive, reacting with H_2O to ultimately form TiO_2 through a series of hydrolysis and polycondensation reactions. This property was exploited to produce a solution-based TTIP ink that reacts with ambient moisture to form TiO_2 post-deposition. The use of glycol ethers as stabilising agents was investigated, to inhibit the reactivity of the TTIP during ink storage and printing. 1,2-dimethoxy ethane was identified as the optimum stabiliser when using ^{i}PrOH as the carrier. Post-deposition phase analysis showed the films to be amorphous on a glass substrate. An annealing step of 450 °C for 40 minutes yielded anatase.

To reduce the annealing temperature required for anatase formation, the use of phase-pure anatase nanoparticles as seed sites for crystallisation was investigated. Addition of anatase nanoparticles to the solution-based TTIP ink was found to reduce the annealing temperature required for anatase formation to 200 °C for 160 minutes. This temperature is compatible with some flexible substrates, such as polyethylene terephthalate (PET), so printing and annealing was also demonstrated on PET. This hybrid alkoxide/nanoparticle ink is, to the best of our knowledge, the first example of a hybrid precursor/nanoparticle ink and the inclusion of crystal seed sites within an ink for inkjet printing.

Titanium oxo-clusters were investigated as a potential titanium source for inkjet inks. Several clusters were synthesised by the controlled hydrolysis of a reactive titanium precursor, such as TTIP, with H_2O. The $[Ti_{11}O_{13}(O^iPr)_{18}]$ cluster was identified as yielding the best ink when dissolved in a toluene carrier. An annealing temperature of 350 °C for 40 minutes was required to convert to amorphous TiO_2 to anatase, a reduction of 100 °C when compared to the solution-based TTIP ink. The printed oxo-cluster films were less continuous and less homogeneous than those produced with the TTIP and hybrid inks.

A niobium-doped $Ti(OEt)_4$ solution was provided by our industrial sponsors, EpiValence, with the intention of use as a potential ink to form a transparent conducting oxide (TCO) thin film. The solution was formulated into an ink and printed onto glass substrates, along with an analogous ink using the solution-based TTIP ink. Despite the inclusion of a niobium dopant, the TiO_2 films demonstrated a low transmittance and conductivity measurements could not be obtained. Further work would be required before the films produced by these niobium doped inks would be suitable for applications as TCOs.

Acknowledgements

First and foremost, I would like to thank my supervisors Professor Helen C. Aspinall and Dr Kate Black for their invaluable support, patience and guidance. Helen always provided me with an appropriate style of supervision, whether it be firm or relaxed. Her experience as a supervisor was evident from the start and I am extremely grateful for the numerous pieces of feedback she provided me with. I appreciated the up-front and direct comments that were tremendously beneficial in their honesty and openness. Kate always offered useful support and guidance, often with an alternate view to be explored. Through Kate's supervision, I was introduced to her expanding research group and the many wonderful individuals it contains. Both Kate and her research group provided the opportunity for friendly interaction in the additive manufacturing lab, the office, and the various meals out and conferences we attended. I wish I'd have taken more advantage of this growing community! It was an absolute pleasure and a privilege to work under the tutelage of both Helen and Kate. I wish you both the best of luck in all of your future endeavours.

Secondly, I would like to thank everyone at EpiValence, especially Simon Rushworth. His advice and candour were greatly appreciated. I always enjoyed travelling to the EpiValence site with him, and I valued every long car journey we did together. I am also grateful to all of my colleagues and friends at the University of Liverpool who helped me during my Ph.D, especially the technical training staff and the members of the 4th floor Chemistry laboratory. Special mentions to Josh and Alex whose MCHEM projects were with myself and Helen.

I would like to thank Alex and Sean for going through the Ph.D process alongside me, giving us all the understanding required to support one-another no matter the situation. Their continued friendship gave me the motivation to get out of bed when it was needed. I would also like to thank Mike, Steven, Patricia, Penelope, John, and Matthew for being great friends and keeping me social and sane.

Finally, the biggest thank you to my family. Hara and Simon, you gave me with life, a home that was far enough away from you to get some work done, and the financial support to continue eating during the last few months. Kris, you provided me with the camaraderie that only a brother could and I am grateful to have you back on the same continent as the rest of your family.

Nomenclature

acac - Acetyl acetone

AFM – Atomic force microscopy

ALD – Atomic layer deposition

CAD – Computer aided design

CIJ – Continuous inkjet

CMYK – Cyan, magenta, yellow, black

CVD – Chemical vapour deposition

DFT – Density functional theory

DLS – Dynamic light scattering

DME – 1,2-dimethoxyethane, $CH_3OCH_2CH_2OCH_3$

DMF – N,N-dimethylformamide, $HCON(CH_3)_2$

DOD – Drop-on-demand

DOS – Density of states

DSSC – Dye-sensitised solar cell

EDXS – Energy-dispersive X-ray spectroscopy

FTIR – Fourier-transform infrared spectroscopy

FTO – Fluorine doped tin oxide, SnO_2-SnF_2

FWHM – Full width at half maximum intensity

ITO – Indium tin oxide ($In_{2-x}Sn_xO_3$)

MO – Metal oxide

MOCVD – Metal organic chemical vapour deposition

NP – Nanoparticle

Oh – Ohnesorge number

PEN – Polyethylene naphthalate, $(C_{14}H_{10}O_4)_n$

PET – Polyethylene terephthalate, $(C_{10}H_8O_4)_n$

^{i}PPE – 2-isopropoxyethanol, $(CH_3)_2CHOCH_2CH_2OH$

PTFE – Polytetrafluoroethylene, $(C_2F_4)_n$

PZT – Lead zirconate titanate ($Pb[Zr_xTi_{1-x}]O_3$ for $0<x<1$)

Re – Reynolds number

RMC – Reactive molecular cluster

SEM – Scanning electron microscopy

SOS – Second order scattering

TCO – Transparent conducting oxide

TEM – Transmission electron microscopy

TLC – Thin-layer chromatography

TTIP – Titanium(IV) isopropoxide,$Ti(O^{i}Pr)_4$

We – Weber number

XANES – X-ray absorption near edge spectroscopy

XRD – X-ray diffraction

Contents

5 Nanoparticle and Hybrid Inks.. 101

Chapter 1

Introduction

1.1 Context of Research

The research in this thesis was funded by the EPSRC and specialty chemical manufacturer and supplier, EpiValence. At the start of the project in October 2015, the aim of the research was to further investigate the use of titanium(IV) isopropoxide (TTIP) in a solution-based ink towards the inkjet printing of TiO_2. Preliminary work had been performed, indicating that a solution of TTIP in propan-2-ol (^iPrOH) was not printable due to the reaction of TTIP with H_2O. A titanium oxo-cluster, $[Ti_{12}O_{16}(O^iPr)_{16}]$, had also been synthesised and so was of further interest. Finally, EpiValence provided niobium doped $Ti(OEt)_4$ solutions for formulation into printable inks for transparent conductive oxide (TCO) films.

The main objectives of the project were to:

- Formulate a solution-based TTIP ink that is compatible with inkjet technologies
- Optimise the TTIP ink for printing
- Minimise the thermal requirements for anatase TiO_2 formation
- Reproducibly synthesise titanium oxo-clusters
- Formulate titanium oxo-clusters into an optimised reactive molecular cluster (RMC) ink
- Formulate niobium doped titanium inks for inkjet printing
- Identify suitability of films for use as TCOs

1.2 Project Overview

The research described within this thesis covers the formulation and optimisation of inks for the inkjet printing of TiO_2 thin films. Inkjet printing is a relatively new technique for the deposition of functional metal oxides (MOs) and so relies on experience from well-established techniques such as dip or spin-coating. This has resulted in most inkjet deposited TiO_2 using colloidal, sol-gel derived inks. In the beginning of this thesis, an alternative approach was taken to formulate solution-based TiO_2 inks from a reactive TTIP precursor.

Most applications of TiO_2 favour the use of the anatase polymorph, which is typically obtained from amorphous TiO_2 after a thermal processing step. To reduce financial cost and increase the range of potential substrates, a reduced processing temperature is beneficial. As such, emphasis will be placed on the identification of the printed thin film crystallinity and the thermal processing requirements.

1.3 Thesis Structure

Chapter 2 reviews the relevant scientific literature, contextualising the experimental work contained in the thesis. To rationalise the choice of TiO_2 as our target material, its properties and applications are first discussed. A survey of TiO_2 deposition is then presented, identifying that there are three well-established techniques: dip-coating, spin-coating, and chemical vapour deposition (CVD). Inkjet printing is then introduced as a deposition technique, with a focus on the properties required for a good ink and the printing process itself. The contributions to inkjet printing of TiO_2 will then be discussed.

Chapter 3 describes the experimental procedures relevant to the thesis as a whole, including: chemical details and preparation, ink preparation, inkjet printing, and the characterisation of printed films. Experimental procedures specific to a chapter can be found at the end of their respective chapters.

In Chapter 4, the formulation and optimisation of solution-based TTIP inks deposited onto a glass substrate is reported. The work begins by building upon prior results obtained within the group, using TTIP as the reactive titanium precursor and ^{i}PrOH as a carrier solvent. Different glycol ether stabilisers are investigated as potential additives to the ink. After identifying the appropriate glycol ether, printed samples are characterised and discussed.

Chapter 5 reports on the addition of nanoparticles to the TTIP ink discussed in Chapter 4, resulting in the formulation of a novel hybrid alkoxide/nanoparticle ink. Following a brief introduction to nanoparticle inks, the synthesis of nanoparticles is presented. The synthesised nanoparticles are identified as insufficient for use in a hybrid ink. Addition of purchased anatase nanoparticles is then investigated. Seeding effects are observed in the printed hybrid inks, with anatase formation occurring at a reduced temperature when compared to the TTIP ink. Printing is also reported on PET.

Titanium oxo-clusters and their use as RMC inks is presented in Chapter 6. The previous findings of the group are first discussed, before presenting a brief survey of titanium oxo-cluster literature and the rationale behind RMC inks. The reported structures of each synthesised cluster are shown, along with two novel synthetic methods. Formulation and printing of RMC inks is presented and discussed.

In Chapter 7, doping is further explored as a topic of interest before the formulation and optimisation of doped inks is reported. After identifying a doped ink compatible with the inkjet printer using the provided EpiValence solution, a comparable ink was formulated by a small addition of $Nb(OEt)_5$ to the solution-based TTIP ink discussed in Chapter 4. Both inks displayed adhesion issues which led to poor characterisation data.

Finally, Chapter 8 provides a summary of the major outcomes of this thesis, along with the potential for further research. Some of the areas for further development include: optimisation of the hybrid alkoxide/nanoparticle ink formulation for printing on flexible substrates, further development of titanium oxo-cluster syntheses and subsequent formulation into RMC inks, instrumentation for effective conductivity measurements, and expansion towards other solution-based MO inks.

1.4 Publications and Conference Proceedings

One of the ink formulations discussed in Chapter 4 was published in the following scientific literature:

- Moisés de Araújo, Murilo F. Gromboni, Frank Marken, Stephen C. Parker, Laurence M. Peter, Josh Turner, Helen C. Aspinall, Kate Black, and Lucia H. Mascaro. Contrasting transient photocurrent characteristics for thin films of vacuum-doped "grey" TiO_2 and "grey" Nb_2O_5 *Applied Catalysis B: Environmental,* 2018, 237, 339-352.

Early work from Chapter 6 was presented according to the following conference proceeding:

- Josh Turner, Danielle Mehta, Helen C. Aspinall, Simon Rushworth, and Kate Black. Titanium oxo-alkoxide clusters as a new source material for high quality TiO_2 structures by inkjet printing. *International Conference on Digital Printing Technologies,* 2016, 64-67.

The key findings from Chapters 4 and 5 was published in the following scientific literature:

- Josh Turner, Helen C. Aspinall, Simon Rushworth, and Kate Black. A hybrid nanoparticle/alkoxide ink for inkjet printing of TiO2: a templating effect to form anatase at 200 °C. *RSC Advances,* 2019, **9**, 39143-39146

Chapter 2

Literature Review

The aim of this project was to build upon the use of inkjet printing as a technique for the deposition of functional thin films of metal oxides (MOs). Titanium dioxide (TiO_2) was used exclusively as the target MO demonstrator for this research. Contained in this literature review is the rationale behind the use of TiO_2 as an ideal demonstrator for inkjet printing of MOs. This is then followed by a brief look into the many applications of TiO_2 films and the various methods of TiO_2 deposition that have been documented in the literature. Inkjet printing will then be further analysed, as it is the chosen deposition technique for this project. The discussion includes a brief overview of inkjet printing and the formulation of inks, followed by an examination of the printing process itself. Finally, this chapter ends by examining the inkjet printing of TiO_2 that has been reported in the literature and contextualising the research presented within this thesis.

2.1 TiO_2

TiO_2 was chosen as the MO demonstrator for this project as it is an extremely useful material and has seen extensive research due to the wide range of potential applications it covers.[1, 2] Properties of TiO_2 include its behaviour as a large band gap semi-conductor, transparent thin film, high refractive index, and photocatalytic potential.[3] Furthermore, it is non-toxic, low cost, and displays high corrosion resistance.

2.1.1 Properties of TiO_2

TiO_2 crystallises naturally in three different polymorphs: rutile, anatase, and brookite.[4, 5] The occurrence of brookite is extremely rare compared to the anatase and rutile polymorphs. As such, brookite will not be discussed any further. Rutile is the thermodynamically favoured polymorph of TiO_2,[6] and is generally formed at higher temperatures when kinetic barriers are minimised. Anatase is a metastable phase and is commonly formed as the kinetic crystal polymorph at lower temperatures than those where rutile is obtained. The conversion of anatase to rutile is possible by thermal treatment,[7-10] although this process is irreversible as rutile is the thermodynamically favoured polymorph.

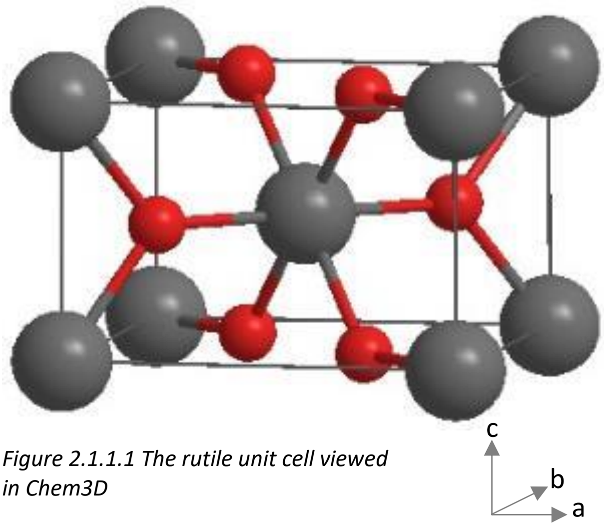

Figure 2.1.1.1 The rutile unit cell viewed in Chem3D

Rutile has a tetragonal unit cell that contains 2 titanium atoms and 4 oxygen atoms, with unit cell parameters of a = b = 4.594 Å, and c = 2.959 Å (See Figure 2.1.1.1). Each titanium atom is in an octahedral geometry, co-ordinated to 6 oxygen atoms, resulting in hexagonal closest packed O with Ti in half of the octahedral holes. The octahedral geometry is distorted, with four of the O-Ti-O bond angles being equal to 90°, two O-Ti-O bond angles being 98.8°, and the remaining two O-Ti-O bond angles being 81.2°. The Ti-O bonds that are located in the a-b axis plane exhibit a bond length of 1.980 Å, whereas the other Ti-O bonds display a shorter length of 1.949 Å. When viewed as polyhedra, rutile possesses layers of edge-sharing TiO_6 octahedra and edge-sharing OTi_3 trigonal slices, with vertex-sharing between layers. Rutile possesses a band gap of ca. 3.05 eV, a density of 4.23 g cm^{-3}, and a refractive index ca. 2.61.

Anatase differs from rutile in many ways, including an increased band gap of ca. 3.20 eV, a decreased density of 3.78 g cm^{-3}, and a refractive index ca. 2.561. Figure 2.1.1.2 shows the unit cell of anatase to also be tetragonal, with unit cell parameters of a = b = 3.776 Å, and c = 9.486 Å. The titanium atoms are 6 co-ordinate octahedral, with the unit cell containing 4 titanium atoms and 8 oxygen atoms. Unlike rutile, anatase exhibits distorted cubic closest packing of O with Ti filling half of the octahedral holes. As is the case with rutile TiO_2 the titanium octahedral geometry is distorted, albeit the distortion is to a greater extent as no ideal O–Ti–O bond angles of 90° are exhibited. Four of the O-Ti-O bond angles are 101.9°, with the remaining four O-Ti-O bond angles being equal to 78.1°. Along the vertically elongated c axis, the two Ti-O bond lengths are 1.973 Å, with the other four Ti-O bond lengths being 1.930 Å. When viewed as polyhedra, anatase possesses edge-sharing TiO_6 octahedra, with half vertex and half edge-sharing OTi_3 trigonal slices. The reduced density of anatase when compared to rutile is due to the less efficient packing of atoms within the unit cell, and so is less efficient throughout the extended crystal structure.

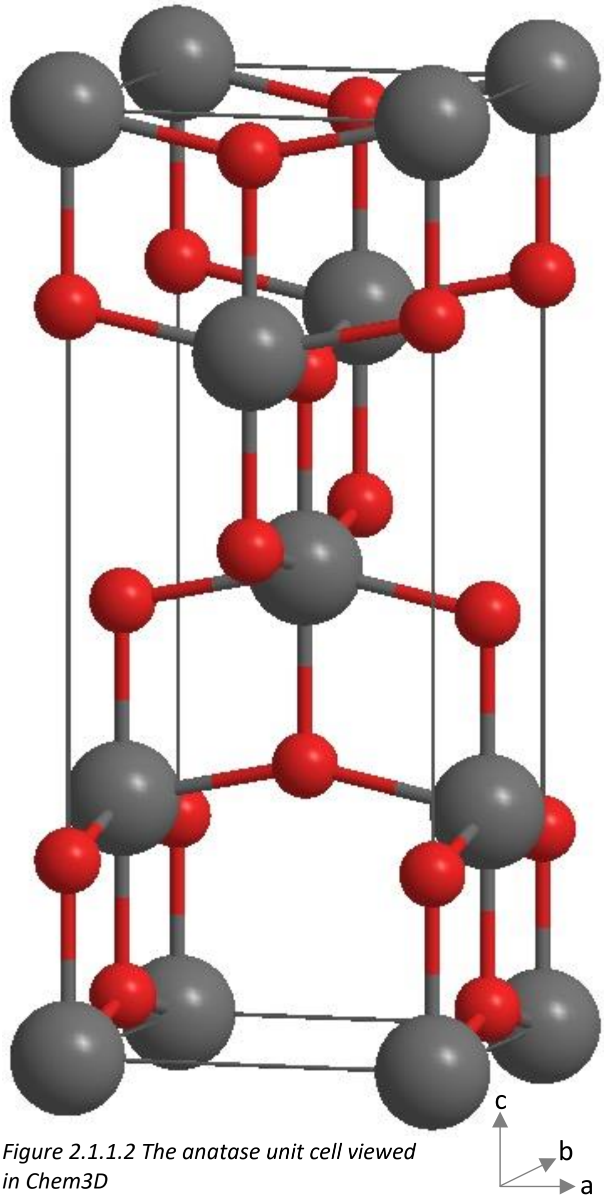

Figure 2.1.1.2 The anatase unit cell viewed in Chem3D

For many applications of TiO_2 the desired polymorph is anatase. Anatase generally exhibitss an increased photocatalytic activity when compared with rutile or amorphous TiO_2. This increased photocatalytic activity is a result of several factors. Recently, Zhang et al. performed an investigation into the differences in band structure, density of states, and effective mass of photogenerated charge carriers for anatase, rutile, and brookite, using density functional theory calculations.[11] It was modelled that anatase was an indirect band gap semiconductor, whereas rutile and brookite were direct band gap semiconductors. Anatase therefore exhibits longer lifetimes of photogenerated electrons and holes. The calculated effective mass of photogenerated charge carriers was also smaller in anatase, facilitating the migration of charge and thereby improving photocatalytic activity. Anatase also exhibits other advantages when compared to rutile, such as an increased surface area and increased stability for thin films and nanoscopic size ranges.[12, 13] Optical transmittance has been shown to decrease as the anatase phase is converted into rutile.

As alluded to previously, the anatase and rutile polymorphs are typically obtained through thermal processing routes of amorphous or partially crystalline TiO_2. However, the exact transition temperature or temperature range varies significantly from system to system and appears to be affected by many factors. It is also common to observe a mixture of both anatase and rutile around the transition temperature, with an increasing quantity of rutile appearing at higher temperatures and longer thermal treatment times.[7, 8, 14, 15] Anatase phase is typically obtained selectively through thermal processing steps at temperatures of between 400°C and 800°C. Most systems will begin to convert irreversibly to rutile phase at ca. 800°C.

2.1.2 Applications of TiO_2

TiO_2 has applications in almost every potential sector, and has been studied extensively as a result. Several reviews exist which list some of the many applications of TiO_2.[16-19] Diebold's report on the surface science of TiO_2 lists the following as some of the applications or uses of TiO_2: heterogeneous catalysis, photocatalysis, solar cells, gas sensing, white pigments, corrosion-protective coatings, optical coating, ceramics, varistors, earth sciences, bone implants, gate insulators, magnetic spin-valve systems, and Li-based batteries.[2]

TiO_2 sees extensive use as a white pigment and opacifier in applications such as paints, inks, and medicines due to its high brightness and extremely high refractive index. As an effective blocker for UVA and UVB, TiO_2 is also commonly found in sunscreens. Cements and tiles may also incorporate TiO_2 on their surface to provide sterilising, deodorising and anti-fouling properties. Thin film coatings of TiO_2 can be used to produce self-cleaning glass through the photocatalytic degradation of dirt and subsequent removal by rain. Some dye-sensitised solar cells (DSSCs) such as the Grätzel cell, incorporate a nano-structured layer of TiO_2 as an electron acceptor, transporter, and donor.

2.2 Deposition of TiO_2

The focus of this discussion is on the various techniques used to deposit TiO_2 thin films, the titanium source utilised, and the operating conditions required to form the desired end product. A note is also made of the substrate the TiO_2 film is deposited onto. TiO_2 can be deposited in its solid state, often as a colloidal suspension of nanoparticles, or as a solution-based precursor. In certain techniques, such as chemical vapour deposition (CVD), the use of solution-based precursors is essential to the deposition process. In CVD, deposition of the titanium containing precursor is followed by a post-deposition treatment to yield the desired layer of TiO_2.

2.2.1 Common Deposition Techniques

Table 2.2.1 summarises some of the TiO_2 deposition literature reviewed. It was found there were three prevalent and well-established deposition techniques used to produce films of TiO_2: CVD, dip-coating, and spin coating. Each deposition technique has specific precursor requirements with significant variations in the titanium sources used, along with associated advantages and disadvantages. A brief discussion of each technique is given, followed by a rationale behind the various titanium sources. There are several other deposition techniques that have been used for TiO_2, such as: ion beam assisted sputtering,[20] electrohydrodynamic atomisation,[21] spray coating,[22] atmospheric dielectric barrier discharge,[23] reactive magnetron sputtering,[24] plasma spray,[25] pulsed laser deposition,[26, 27] and ultrasonic spray pyrolysis[14, 28]. These will not be discussed.

CVD has seen extensive use as a deposition technique for MOs,[29-33] including TiO_2. In CVD, the precursor to be deposited is vaporised and directed to the substrate by an inert carrier gas. Deposition from the vapor phase by chemical decomposition on or near the substrate surface results in the formation of a solid thin film. A reactive source gas stream may also be directed to the substrate. Atomic layer deposition (ALD), a sub-set of CVD, is an extremely precise technique where conformal layers are grown on a substrate with atomic level control.

One advantage of CVD techniques is the high level of control offered by finely controlled experimental conditions, such as: substrate temperature, gas mixture composition, and gas pressure. Another advantage of CVD is the high film purity resulting from careful control of reaction conditions and removal of by-products through exhaust gases. Disadvantages of CVD include the high cost of both equipment and operating conditions, along with the requirements for high purity precursors that can be vaporised under conditions attainable within the CVD reactor. Direct patterning or selective deposition cannot be achieved without subtractive manufacturing. There are a multitude of other CVD processes that each see their own respective advantages and disadvantages, but this discussion is outside of the scope of this work. The book titled ‘Chemical Vapor Deposition’ is a useful resource.

Dip-coating is a conformal method of deposition where a substrate is slowly lowered into a feedstock of the coating material or precursor, left fully or partially submerged, and then removed at a controlled pace.[34] Many of the parameters can be varied to control the thickness of the resulting film. Advantages of dip-coating include low running costs, a homogeneous film, tuneable thickness, and a wide range of available feedstocks and substrate materials. Disadvantages include the requirements for finely controlled equipment, typically slow process times, and the inability to directly pattern. As a batch process, dip-coating is relatively low throughput compared to other continuous or roll-to-roll processes. Dip-coating requires the titanium precursor to be in the form of a solution that will adhere to the substrate.

Spin-coating also requires the titanium precursor to be in the form of a solution which will adhere to the substrate. The process of spin-coating uses centrifugal force to spread the coating solution uniformly over a substrate by spinning it at high speed.[35] Film thickness is controlled by several parameters including the spin speed, viscosity of the coating solution, and the concentration of the precursor material in the coating solution. The major advantages of spin-coating are the relative speed and simplicity of the process, with the high airflow inherent to fast spin speeds resulting in fast drying times. Spin-coating is a batch process and so suffers from low relative throughput. Material usage is also low for spin-coating, as a significant portion of the coating solution is flung from the substrate as it is spinning and resulting in high wastage.

Table 2.2.1 shows that the spin and dip-coating techniques often utilise the sol-gel process to produce a TiO_2 particle solution. In the sol-gel process, a colloidal solution (or sol) is formed by the reaction H_2O with a monomeric species such as a metal alkoxide. This sol undergoes further polycondensation reactions to form a diphasic system, containing both solid and liquid phases and exhibiting a gel-like behaviour. For some deposition methods, it is this sol-gel that is used as the TiO_2 precursor. In others, the solvent is removed from the sol-gel in a drying process and the resulting solid is dispersed into another medium for deposition. The sol-gel process offers an attractive route to formation of metal oxides, such as TiO_2, as it is a cheap and low-temperature technique. The disadvantage of sol-gel processing is that the polycondensation process is difficult to control and as such will suffer from batch-to-batch variation. The CVD technique utilises some form of titanium(IV) precursor, usually an alkoxide.

Table 2.2.1 Analysis of common deposition technique publications

Entry	Deposition Technique	Precursor	Substrate	Conditions	Comments	Reference
1	CVD	$Ti(O^iPr)_4$ (TTIP) or $Ti(O^iPr)_2(acac)_2$ where acac is acetyl acetone	Single crystal silicon (111)	450 – 700°C substrate temperature	Polycrystalline anatase above 550°C	[33]
2	CVD	$Ti(acac)_4$ or $Ti(O^iPr)_2(acac)_2$	Glass Silicon (100)	200 – 600°C substrate temperature	Polycrystalline anatase above 500°C	[36]
3	CVD (ALD)	$TiCl_4$	Silicon Silica	100 – 400°C substrate temperature	Anatase obtained at and above 150°C. Rutile present at 425°C	[37]
4	Dip-coating (sol-gel)	TTIP	Glass Quartz	100 – 1000°C heat treatments for 1 hour	Anatase at and above 500°C Rutile begins to appear at 750°C	[38]
5	Dip-coating (sol-gel)	TTIP or $Ti(OEt)_4$	Silicon wafers Soda-lime glass Pyrex glass	450°C for 15 hours as standard calcine temperature	Anatase after calcine Max peak at 350°C No rutile below 500°C	[39]
6	Spin-coating (sol-gel)	$Ti(O^nBu)_4$	Silicon (100)	Annealing up to 550°C	Anatase begins to form at 350°C	[1]

Table 2.2.1 (cont.) Analysis of common deposition technique publications

Entry	Deposition Technique	Precursor	Substrate	Conditions	Comments	Reference
7	Spin-coating (sol-gel)	TTIP	Silicon (100) Polycarbonate	Autoclaved between 100 – 200°C	Anatase phase identified	[40]
8	Spin-coating (sol-gel)	TTIP	Silicon (100) Polycarbonate	Post-deposition heat treatment up to 140°C	Anatase phase identified	[41]
9	Dip-coating (sol-gel)	$Ti(OBu)_4$	Glass Silica	100 – 900°C heat treatments for 1 hour	Anatase at and above 300°C Film loses adhesion after 700°C before rutile is formed	[42]
10	Dip-coating (sol-gel)	TTIP	SiO_2 coated glass	400°C for 3 hours as standard calcine temperature	Anatase after calcine Small presence of rutile also detected	[43]
11	Spin-coating (sol-gel)	TTIP	Fused silica	Dried at 20°C for 10 hours, desiccated at 20°C for 10 days	Precursor sol identified as anatase	[44]
12	Spin-coating	Titanium(IV) 2-ethylhexoxide (spin-coating)	Sapphire Quartz	Annealed to 900°C to obtain rutile phase	Anatase or anatase/rutile mixtures before annealing	[45]

Table 2.2.1 (cont.) Analysis of common deposition technique publications

Entry	Deposition Technique	Precursor	Substrate	Conditions	Comments	Reference
13	Dip-coating (sol-gel)	$Ti(OBu)_4$	Sapphire Silicon	Heat treatments from 400 - 1400°C for 2 hours	Anatase observed from 400 – 800°C 1000°C gives mixture 1200 – 1400°C rutile	[7]
14	Spin-coating (sol-gel)	TTIP	Quartz	Heat treatments from 600 - 1100°C for 4 hours	Pure anatase below 800°C Mixture between 800 – 1000°C. Pure rutile at 1100°C	[8]
15	CVD (ALD)	TTIP	SiO_2 coated Si	No post-deposition treatment that was characterised	As-deposited TiO_2 identified as amorphous	[15]
16	Spin-coating (sol-gel)	$Ti(OBu)_4$	Quartz	Calcination from 500 - 900°C for 2 hours	Anatase observed from 500 – 900°C	[46]
17	CVD (ALD)	TTIP	Si(100) Polycarbonate	80°C ALD temperature 120°C hydrothermal for 6 - 48 hours	Amorphous. Anatase after hydrothermal.	[46]

Table 2.2.1 (cont.) Analysis of common deposition technique publications

Entry	Deposition Technique	Precursor	Substrate	Conditions	Comments	Reference
18	Dip-coating (sol-gel)	TTIP	Indium tin oxide (ITO) glass	Calcined at 450°C for 4 hours	Anatase phase identified	[47]
19	Dip/spin coating (sol-gel)	$Ti(O^nBu)_4$	Glass discs	Calcination at 400 – 700°C for 1 hour	Anatase observed at and above 400°C	[48]
20	CVD	$Ti(OEt)_4$	Poly-methyl methacrylate optical fibres	Conditions < 160°C due to substrate not melting	Anatase phase observed	[49]
21	CVD	TTIP	p-type silicon	Annealing at 400, 600, and 800°C	400°C gave anatase 600°C gave mixture 800°C gave rutile	[50]

2.2.2 Titanium Alkoxides

As identified in Table 2.2.1, titanium(IV) alkoxides and titanium(IV) salts are commonly used as reactive titanium precursors. These molecules are Lewis acids that exhibit an extremely high reactivity with H_2O, leading rapidly to formation of TiO_2.[51] Most commonly used is the titanium(IV) isopropoxide (TTIP, $Ti(O^iPr)_4$) molecule due to its relatively low cost, high availability, and intermediate reactivity. The reaction scheme for the hydrolysis and condensation reactions of TTIP with H_2O is shown in Scheme 2.2.2.1. Peruzzo et al. describe several potential reactive pathways that metal alkoxides can undergo.[52]

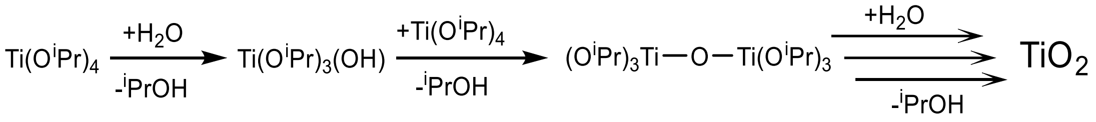

Scheme 2.2.2.1 Reaction pathway of TTIP and H_2O to form TiO_2

Titanium(IV) alkoxides have the general empirical formula of $Ti(OR)_4$, although their structures vary depending on the steric bulk of the alkoxide group. Titanium methoxide, for example, typically has a tetrameric structure with the formula $Ti_4(OMe)_{16}$. Titanium ethoxide also exhibits a tetrameric structure, which will often extend upon leaving the liquid to stand over time and results in a gelatinous solid. The gelatinous solid is easily returned to a colourless liquid form by gentle heating. With relatively bulkier ligands, TTIP exhibits a monomeric structure which does not form a gelatinous solid. Due to the high reactivity of the titanium(IV) alkoxides with H_2O, they will often gain a pale yellow colour during storage as a result of small H_2O exposure. This colouration can be reversed by refluxing the titanium(IV) alkoxide.

The hydrolytic rate of titanium alkoxides can be reduced through the use of chelating ligands or stabilisers. As the titanium alkoxides are Lewis acidic, the ligands used as stabilising agents are typically Lewis bases such as n,n-dimethylaminoethanol,[53] acetylacetone,[3] triethanolamine,[3] and n-methyldiethanolamine.[54] This stabilisation is the focus of the ink optimisation in Chapter 4. During the process of hydrolysis, titanium (IV) alkoxides form many intermediates before the final TiO_2 product is formed. One such class of intermediates are the titanium oxo-clusters. These are discussed and investigated further in Chapter 6.

2.2.3. TiO_2 Deposition Literature Review

Guilliard et al. investigate several different parameters in the sol-gel deposition of TiO_2 for applications in photocatalysis.[39] A total of six different films were produced, with variations in the precursor, solvent, and the use and identity of stabilising agents. Irrespective of the use of either a TTIP or $Ti(OEt)_4$ precursor, calcination at 450°C for 15 hours resulted in the presence of anatase phase as indicated by the X-ray diffraction (XRD) peak at $2\theta = 25.15°$. Film thickness did not appear to be affected by the use of either acetic acid or acetyl acetone stabilisers, although the film thickness was found to decrease when $Ti(OEt)_4$ in an EtOH solvent was used. The opacity and surface structure of the films was found to be strongly affected by the use of stabilisers, with the sample containing no stabilisers being opaque and consisting of aggregated cubic crystals with an approximate size of 300 nm. The various films produced by stabilised sols were transparent with either a blue, pink, orange or grey colouration, and consisted of aggregated particles of only 90 nm. It was deduced that the difference was caused by the accelerated and uncontrolled hydrolysis of the unstabilised alkoxide precursor, resulting in the formation of aggregated large TiO_2 islands.

A further investigation was performed on the sample consisting of TTIP in ${}^{i}PrOH$ with no stabilising agent. The thickness of a single layer was calculated to be ca. 220 nm, which was in good agreement with other comparable data. Prior to calcination, the as-deposited film was amorphous and it was deduced that no anatase phase was present below 200°C due to the absence of malic acid degradation upon irradiation. It was found that calcination between 400 – 500°C did not significantly affect crystallinity, but the film thickness was decreased. Furthermore, photocatalytic activity was decreased at calcination temperatures above 400°C due to the migration of Na ions from the glass substrate into the TiO_2 film and resulting in perturbation of the TiO_2 crystallinity.

Hanaor et al. report on the influence of introducing Cu(II) and Cu(III)/Fe(III) dopants to spin-coated TiO_2 films.[8] In the undoped film, XRD analysis shows the presence of only the anatase phase A(101) peak after annealing at 700°C. Between annealing temperatures of 800 – 1000°C, the undoped sample consists of a biphasic composition of anatase and rutile. At 1100°C, XRD analysis of the undoped sample shows only the rutile R(110) peak, indicating that the transformation from anatase to rutile is complete. Doping with Cu(II) was shown to promote the rutile transformation, with XRD analysis of the Cu(II) doped sample after an 800°C anneal showing a large predominance of the rutile phase. Doping with a Cu(III)/Fe(III) resulted in a similar albeit reduced promotion of rutile phase, with the complete transformation to rutile instead being observed at 1000°C.

Scanning electron microscopy (SEM) showed similar morphologies for both doped and undoped TiO_2 films, with anatase grain sizes of approximately 40 – 50 nm, and larger rutile grain sizes of 200 – 400 nm. UV-Vis transmittance measurements showed that the transmittance was decreased with the introduction of the Cu(II) and Cu(III)/Fe(III) dopants. A decreased overall transmittance was observed for biphasic anatase/rutile mixtures when compared to the pure anatase phase. Photocatalytic performance was noted to be poor, with only a minor reduction in dye degradation when compared to the uncoated substrate control experiment. Presence of dopants was found to have a negative effect on photocatalytic performance.

Wang et al. also discuss the influence of dopant introduction to spin-coated sol-gel TiO_2 thin film.[55] Nb was used as the metal dopant in this paper. For both the undoped and doped samples, calcination between 500 – 800°C resulted in the formation of anatase TiO_2 as shown by XRD. A 900°C calcination resulted in a mixed anatase/rutile phase for the undoped sample, whereas the Nb doped sample exhibited peaks associated with only the rutile phase. Optical transmittance was found to decrease slightly with the addition of a Nb dopant.

Through the use of hydrothermal treatment, Zhang et al. report on the amorphous to anatase transformation in ALD thin films of TiO_2 at 120°C.[46] TTIP and $TiCl_4$ precursors were both investigated. Silicon (100) n-type wafers were typically used as the substrate, although polycarbonate was also used. An additional substrate was also produced that consisted of a thin and discontinuous anatase layer, to demonstrate the importance of nucleation sites in the crystallisation process. X-ray absorption near edge structure (XANES) was used to investigate the crystallinity of the TiO_2 films. The film formed by ALD of the TTIP precursor onto a glass substrate was amorphous, but after hydrothermal treatment at 120°C for 12 hours the XANES spectra indicated anatase formation. It was noted that anatase crystallisation was likely complete at the “local level” after 12 hours, whilst increased hydrothermal treatment resulted in grain growth and longer-range order. The $TiCl_4$ derived thin film required a longer hydrothermal treatment of 24 hours for anatase formation. It was stated that films derived from TTIP formed anatase easier and of increased crystallinity, due to the already formed Ti-O bonds and the ordering effect of the bridging alkoxide groups. ALD of the TTIP precursor system was performed onto a polycarbonate substrate, with anatase phase being identified after 48 hours of hydrothermal treatment. The $TiCl_4$ precursor system deposited onto polycarbonate remained amorphous even after 48 hours of hydrothermal treatment.

To investigate the effect of preformed nucleation sites on the crystallisation process, islands of anatase crystallites with a mean thickness ca. 5 nm were deposited onto a silicon substrate. Using a $TiCl_4$ precursor, amorphous TiO_2 was grown onto the anatase seeded substrate using ALD. XANES shows that after just 6 hours of hydrothermal treatment, the deposited film was crystalline anatase. This is a significant reduction in hydrothermal time compared to the similar film obtained without the presence of anatase seeds. Finally, it was stated that the onset of crystallisation may be controlled by compressive stress in the amorphous TiO_2, and the presence of H_2O is crucial to the mechanism of anatase crystallisation in addition to high pressures.

M. Morozova et al. discuss the influence of various deposition techniques available for TiO_2 thin films, with an emphasis on the photoelectrochemical properties obtained.[47] Dip-coating, spray-coating and inkjet printing were all used to deposit sol-gel derived TiO_2 onto an ITO substrate. TTIP is used exclusively as the reactive titanium precursor, although all of the deposition techniques use a colloidal suspension of sol-gel derived TiO_2 particles. A non-polar cyclohexane solvent is used for both the dip and spray-coated samples, whereas the inkjet printed solution required the use of xylene due to the poor jetting performance of cyclohexane and interaction with the plastic ink tank. Calcination was performed for all samples at 450°C for 4 hours. XRD shows the films to all be of anatase phase. It was concluded that inkjet printing and dip-coating yielded a homogeneous thin film with a low number of bulk defects. Spray-coating was shown to give a higher relative number of bulk defects, although it is a quick technique for covering large areas with a cruder TiO_2 thin film. The ability of the inkjet printing technique to deposit regular and irregular patterns was noted.

2.2.4 Technique Comparison and Summary

Each technique discussed above offers several attractive benefits to the manufacture of thin films of TiO_2, whilst also exhibiting some process drawbacks. For both spin and dip-coating techniques, their nature as batch processes will always be a limiting factor for high-throughput processing of TiO_2 thin films. CVD is a costly deposition technique that requires a large upfront and continuous financial outlay in order to produce films of high quality. None of these techniques are capable of patterning without extensive pre-treatments or subtractive manufacturing, such as etching.

Inkjet printing has several advantages when compared to each of the above deposition techniques. Most prominent is the ability to directly pattern deposited material without the need for pre-treatment or subtractive manufacturing techniques. In addition to direct patterning, inkjet printing is also a highly versatile and tuneable process which is low-cost and low-waste. As such, inkjet printing was chosen as the deposition technique for this research and will now be discussed in more detail.

2.3 Fundamentals of Inkjet Printing

Inkjet printers see extensive use throughout the business and home markets. As with many other forms of printing, inkjet printing allows the direct patterning of digitised text or imagery onto a material substrate. Conventional use of inkjet printers is commercial printing onto a paper substrate using a traditional pigmented aqueous ink system with Cyan, Magenta, Yellow and Black colours (CMYK). However, as the process matures it is seeing increasing use as a deposition technique within the research sector. The range of functional materials that can be deposited by inkjet printing is continuously expanding. 'The Chemistry of Inkjet Inks' by Shlomo Magdassi is an invaluable resource for understanding the fundamentals of inkjet printing.[56]

2.3.1 Basics of Inkjet Printing

Inkjet printing is an additive manufacturing process, where one or more materials (in the form of an ink) is added, or deposited, onto another material (the substrate). Direct patterning is achieved by using computer aided design (CAD) software in combination with the native printer software. A 3-dimensional deposited material with a variable height can be obtained by subsequent layer-upon-layer depositions. There are multiple variants of inkjet printers, increasing the versatility of the deposition technique and facilitating a wide range of current and potential applications.

2.3.2 Types of Dispensing Devices

There are two main technologies utilised in inkjet printing; continuous inkjet (CIJ), and drop-on-demand (DOD) inkjet.[57] CIJ generates a continuous stream of variably charged droplets. As the dispensing device travels across the substrate, a deflection plate is used to direct the charged droplets either onto the substrate or into the ink collection gutter for future recirculation. The continuous jetting of ink is a major advantage of the CIJ technology as there is a constantly replenishing solvent front at the orifice of the dispensing device, although there are also several disadvantages associated with the process including the constant evaporation of solvent as it is being jetted.

DOD inkjet technology only generates droplets when required, rather than jetting them continuously. There are two leading subsets of DOD technologies, separated by their method of droplet formation and ejection; thermal, and piezoelectric (See Figure 2.3.2.1).[57] Thermal DOD utilises a heat resistor, or thin film heating element, to heat the nearby ink to its bubble nucleation temperature. This nucleation of bubbles causes an increased pressure within the dispensing device, followed by subsequent ejection of a droplet (See Figure 2.3.2.1). Due to the process requirements, there are many disadvantages associated with thermal DOD. The main disadvantage is that very few fluids can be used for thermal DOD as an acceptable bubble nucleation temperature is required, in addition to the ink being capable of withstanding the effects of highly localised temperature. Functional materials are difficult to formulate into a thermal DOD ink, as the thermal cycles tend to degrade the ink and affect the functional properties of the material. Lifetimes of thermal DOD dispensing devices are relatively short. An advantage of thermal DOD is the potential for very small drop sizes.

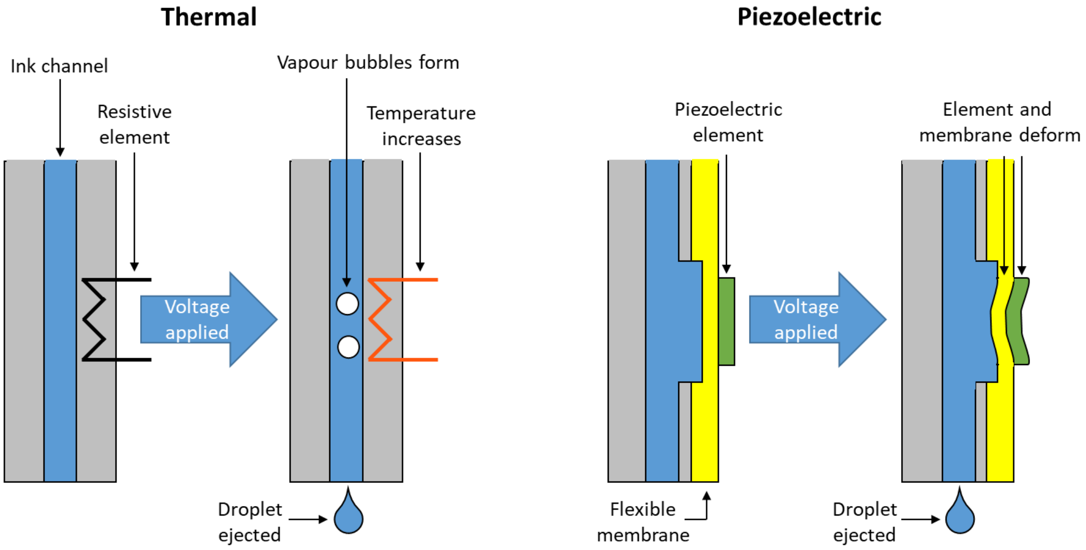

Figure 2.3.2.1 Thermal and Piezoelectric DOD ejection schematic

Piezoelectric DOD employs a piezoelectric element and a flexible membrane to achieve varying pressures within the dispensing device. A piezoelectric material exhibits the piezoelectric effect, whereby the application of a mechanical stress causes an accumulation of electric charge in a material. This phenomenon also occurs in reverse, with the application of electric charge to a piezoelectric material resulting in an internally generated mechanical strain. It is this reverse piezoelectric effect that is exploited in piezoelectric DOD inkjet technologies. A typical piezoelectric material is lead zirconate titanate (PZT, $Pb[Zr_xTi_{1-x}]O_3$ for $0<x<1$), a ceramic perovskite. To eject a droplet, an electrical impulse is sent from the printer to the piezoelectric element on the dispensing device. The electrical impulse causes a deformation of the piezoelectric element and flexible membrane. This deformation results in an increased ink pressure within the dispensing device, causing the ejection of an ink droplet (See Figure 2.3.2.1).

There are several advantages to piezoelectric DOD inkjet technologies, and that is why this was our chosen method of ink deposition. The advantages of piezoelectric DOD include: high levels of control over droplet size and frequency, droplet sizes in the picolitre range, long dispensing device lifetimes, and the ability to use a wide range of inks. The main disadvantage of piezoelectric DOD printing is the relatively high cost of the dispensing devices. There are also ideal viscosity and surface tension ranges for inks in a piezoelectric DOD system which will yield optimum droplet performance, although this varies among dispensing devices.

2.4 Properties of an Ideal Ink

The formulation of inks for an inkjet system is often very complex, due to the chemical, physical, and rheological property requirements for successful droplet formation and ejection.[56] First and foremost, the chemicals present in the ink should be compatible with every component they will contact, including: the ink vial, tubing, connective pipes/joints, the dispensing device internals, and the dispensing device externals and orifice. If the ink consists of a dispersion of particles, the particle size must be less than 1/100th of the diameter of the orifice in order to avoid blockages. Rheological properties of an ink are also important for dispensing devices to function optimally. Ideal ranges of viscosity and surface tension are quoted by the dispensing device manufacturer.

Ink formulation requirements necessitate the consideration of the effects each ink component will have on the overall properties of the ink. Often, ink formulation requires a compromise between two conflicting requirements in order to achieve optimum ink performance. Multifunctional ink components are often used to help reduce the total number of ink components and to alleviate the issue of compromised ink properties.

2.4.1 Ink Components

Although inks can vary greatly in complexity, most ink components can be summarised as either an active component, carrier, and additive or stabiliser. An active component is the material or precursor to be deposited, generally functional in nature. Active components can vary from nanoparticles, to reactive precursors, to coloured pigments and dyes. The bulk of the ink consists of the carrier, sometimes referred to as the vehicle, which is often water or an organic solvent. Most of the chemical and rheological properties of the ink are derived from the carrier component, resulting in the choice of carrier being an important and often overlooked decision. An ideal and simplistic ink would consist of solely the active component, or the active component and carrier. However, this is almost never the case. Most inks require the use of additional ink components in the form of additives.

Additives are used to overcome or minimise the issues associated with the active component, carrier, or the chosen inkjet dispensing device technology to be utilised. With respect to active components, additives are used to stabilise either chemically or physically. Chemical stabilisation is often used to prevent the reaction of active components with other ink components or the experimental conditions, inhibiting premature degradation or reaction. Additives can also physically stabilise a dispersion of particles, facilitating an even colloidal distribution and inhibiting the processes of aggregation, agglomeration, and sedimentation. Stabilisation of a particle dispersion is achieved primarily by increasing the zeta potential and thereby increasing the repulsive forces between the colloids, or by increasing the viscosity of the ink and reducing the influence of gravitational and inertial flow on the colloidal particles.

Through the use of co-solvents and humectants, issues associated with the carrier solvent can be minimised. Humectants are hygroscopic molecules that attract and retain H_2O molecules. When H_2O is the carrier solvent, as is often the case in commercial inkjet inks, humectants are used to prevent or deter the unfavourable ink compositional changes associated by the evaporation of H_2O at the dispensing device orifice. Co-solvents are often used to reduce the evaporation of the carrier. In addition, co-solvents can increase the solubility of the active component in the carrier and therefore increase ink loading. Another common use for additives is the modification of viscosity or surface tension of the ink. This increases the range of potential active components and carrier solvents that can be used within the optimal ranges of viscosity and surface tension for a given dispensing device.

Additives can also fulfil a number of roles that are only required for certain inks, and are often tailored to the specific ink formulation in question. An example of a niche additive is in the role of a fixative, in which the additive is used to improve adherence and stability of the active component onto the substrate. Fixatives are often used when printing onto fabrics or high-quality papers. Another role an additive can perform is that of a fungicide/biocide, whereby the additive prevents the growth of mould or fungus during the transport and shelf-life of the ink. Additives can also be used as buffering agents to control the pH of the ink solution, preventing ink degradation and improving overall stability of the individual ink components.

2.4.2 Rheological Properties

As alluded to previously, the rheological properties of an ink are extremely important for successful and satisfactory behaviour before, during, and after the jetting process. The properties of viscosity and surface tension are important for the behaviour of the ink. Ink density is a necessary value for theoretical calculations, and contact angle is a useful quantitative measure of wettability of a specific ink on a given substrate.

Viscosity is the measure of a fluid's resistance to deformation at a given rate, most easily visualised as a simple shear flow. In planar Couette flow, the model of which is shown in Figure 2.4.2.1, a fluid is trapped between one stationary plate and one plate moving at a constant speed.[58] Assuming laminar flow and no turbulence, the fluid particles move in sheets or layers parallel to the boundary plates. The speed of the fluid layers is greatest for the layer in contact with the moving plate, with the layer having a speed equal to that of the moving plate. The speed of each subsequent fluid layer is slower than the previous one, due to frictional forces resisting their motion. Speed reaches zero at the final fluid layer in contact with the stationary boundary plate. A resistive force is applied by the fluid to the moving plate in the opposing direction to the motion of the moving plate. An equal and opposite force is also applied to the stationary plate. Due to the resistive forces displayed by the fluid, an external force is required to maintain the constant speed of the moving plate. It is the relative strength of this external force that is a measure of the fluid's viscosity.

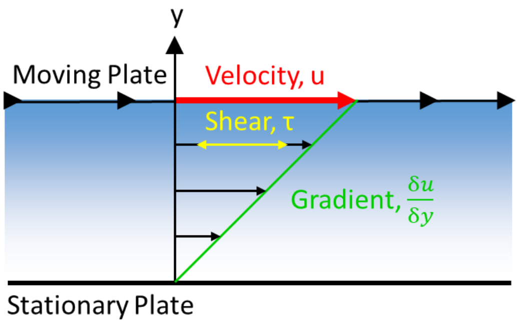

Figure 2.4.2.1 Schematic to show planar Couette flow

It is generally accepted that there are two different types of measured viscosity: dynamic and kinematic viscosity.[59] Dynamic viscosity (ν) is the measure of the resistive flow of a fluid when an external force is applied. A common instrument for measuring dynamic viscosity is a rotational viscometer, which is useful when measuring the viscosity of non-Newtonian fluids - fluids whose viscosity changes with the magnitude of the applied force. Kinematic viscosity (μ) is the measure of the resistive flow of a fluid under the weight of gravity, with no other external forces being applied. Ostwald viscometers, also known as glass capillary viscometers, are the common apparatus used to measure kinematic viscosity. This method is useful for Newtonian fluids – fluids that do not change viscosity with a change in applied force. Dynamic and kinematic viscosity are related by the fluid's density, and one can be converted to the other using equation (2.4.2.1). Density (ρ), or volumetric mass density, is the mass per unit volume of a given substance.

$$\nu . \rho = \mu \tag{2.4.2.1}$$

Surface tension is the measure of the attractive forces between molecules of a fluid, observed and measured at the fluid surface. The attraction of the molecules in the surface layer to the bulk fluid results in minimisation of the surface area. Figure 2.4.2.2 shows the attractive forces acting upon fluid molecules in the bulk and at the surface boundary. These attractive forces balance out on the molecules in the bulk, but the surface atoms experience a net pull into the fluid.

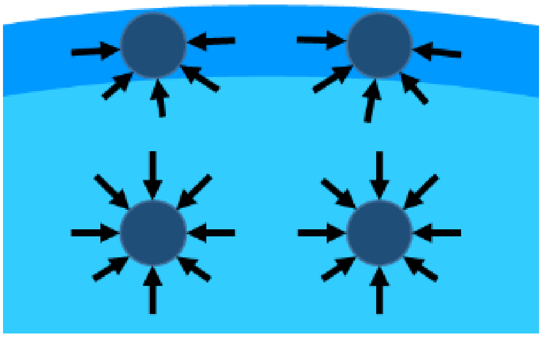

Figure 2.4.2.2 Schematic showing attractive forces acting on surface and bulk fluid atoms

However, the behaviour of a fluid droplet is complicated by the medium surrounding it. For a droplet deposited on a surface, as observed in inkjet printing, a liquid droplet is in contact with a solid substrate and surrounded by an ambient gas such as air. The attractive forces between the liquid atoms that gives rise to surface tension are called cohesive forces. Adhesive forces act upon the boundary atoms between the solid and liquid atoms at the solid-liquid interface, and the liquid and gas atoms at the liquid-gas interface. This results in the boundary atoms of the liquid experiencing a net pull from cohesive forces, and a net pull in the opposite direction from adhesive forces. The relative magnitudes of these two net forces determines the behaviour of the droplet on the substrate, with contact angle and degree of wetting being two useful parameters that result from this balancing of forces.

Both viscosity and surface tension can be adjusted using certain additives. Viscosity-modifiers are typically materials with a relatively high or low viscosity, and so their addition to an ink in small quantities has a large effect on the overall ink viscosity. A decrease in surface tension can be obtained using a class of additives known as surfactants, or surface-active agents. Surfactants reduce the interfacial tension between the liquid and neighbouring solid, liquid, and gas phases. In inkjet technologies, surfactants are primarily used to reduce the surface tension between the ink and the substrate, thereby reducing the solid-liquid contact angle and improving wettability.

Figure 2.4.2.3 illustrates the parameter of contact angle, which is defined as the angle of incidence (θ_C) between the solid-liquid (γ_{SL}) and liquid-gas (γ_{LG}) phases. Mathematically, each combination of solids, liquids, and gases has an equilibrium contact angle as given by the Young equation (2.4.2.2) where γ_{SL} is the interfacial energy between the solid and liquid, γ_{LG}

is the interfacial energy between the liquid and gas (ie the surface tension), γ_{SG} is the interfacial energy between the solid and gas, and θ_C is the equilibrium contact angle.[60] In reality, contact angle hysteresis is observed. There is a maximum angle known as the advancing angle (θ_A), and a minimum angle known as the receding angle (θ_R).[61] These two extremes of potential contact angles are generally observed when a substrate is tilted to the point at which the droplet begins to slide down the surface (See Figure 2.4.2.4).

$$\gamma_{SG} = \gamma_{SL} + \gamma_{LG} \cos \theta_C \tag{2.4.2.2}$$

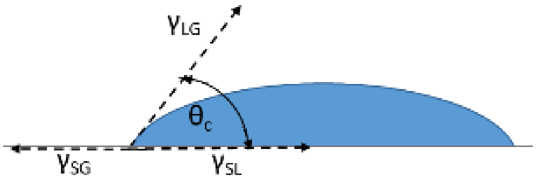

Figure 2.4.2.3 Schematic to illustrate contact angle and phase boundaries of a liquid deposited on a solid

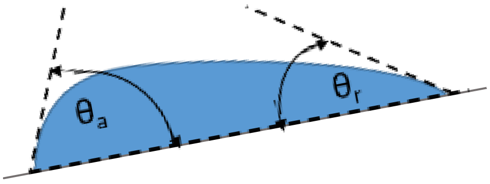

Figure 2.4.2.4 Schematic to illustrate advancing and receding contact angles on a tilted substrate

Closely related to both surface tension and contact angle is wettability. A simple view of wettability is to analyse the contact angle of the system. A low contact angle ($\theta < 90°$) is a high degree of wettability, indicating favourable interactions between the liquid and solid, causing the liquid to spread and cover a large surface area. A high contact angle ($\theta > 90°$) is a low degree of wettability, indicating the interactions between the liquid and solid to be less favourable than the interactions between the liquid itself, causing the liquid to minimise the surface area coverage of the solid. For systems in which the liquid is H_2O a surface exhibiting a low contact angle is called hydrophilic, whereas a surface exhibiting a high contact angle is called hydrophobic.

In reality, wettability is strongly influenced by the imperfections present on the solid surface. These imperfections are measured as surface roughness. When dealing with rough surfaces, there are two main models used to describe the wetting of a surface.[62] Systems that exhibit a high degree of wettability are described by the Wenzel model (See Figure 2.4.2.5), whereas systems exhibiting low wettability are described by the Cassie-Baxter model (See Figure 2.4.2.6). The Wenzel model assumes the solid surface maximises contact with the droplet, with the liquid penetrating into the troughs present on the surface. This is generally true when the solid-liquid interaction is energetically favourable. The Cassie-Baxter model minimises the contact between the solid surface and liquid droplet by assuming a trapped gas is present in the troughs of the surface. Gas will be trapped when the solid-gas interaction is more energetically favourable than the solid-liquid interaction, which involves increasing the surface area of the liquid and working in opposition to the surface tension.

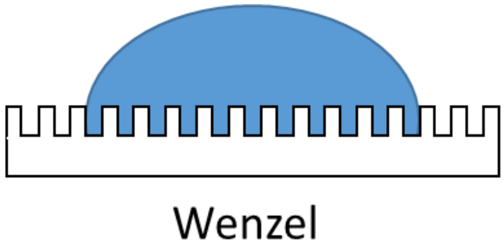

Figure 2.4.2.5 Schematic to illustrate the Wenzel model of surface wetting

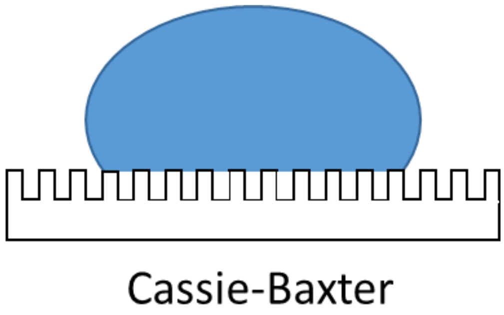

Figure 2.4.2.6 Schematic to illustrate the Cassie-Baxter model of surface wetting

2.4.3 Reynolds, Weber, and Ohnesorge Numbers

In the field of fluid dynamics, the physical properties of viscosity, surface tension, and density are often expressed as dimensionless numbers.[63-66] One such number is the Reynolds number, which gives the ratio of inertial to viscous forces within a fluid when a force is applied. The Reynolds number (Re) is given by equation (2.4.3.1), where ρ is the density of the fluid, υ is the velocity of the fluid, L is the characteristic length, μ is the dynamic viscosity of the fluid, and ν is the kinematic viscosity of the fluid. For inkjet systems, υ is the velocity of the fluid with respect to the substrate, and the characteristic length is the orifice diameter of the dispensing device. It is accepted that for systems resulting in a low Reynolds number, smooth and constant motion typical of laminar flow will be observed. Turbulent flow generally occurs at high Reynolds numbers, exhibiting unstable and chaotic flow.

$$Re = (\rho\, \upsilon\, \mathrm{L}) / \,\mu \;= (\upsilon\, \mathrm{L}) / \,\nu \tag{2.4.3.1}$$

Another dimensionless number used in fluid dynamics is the Weber number. For a droplet in flight, the Weber number relates the inertial forces of a droplet to its surface tension. The Weber number (We) is given by equation (2.4.3.2), where ρ is the density of the fluid, υ is the velocity of the fluid, l is the droplet diameter, and σ is the surface tension of the fluid. Inertial forces acting upon a droplet are deforming in nature, with the potential to atomise the droplet into a disperse spray. Surface tension is the cohesive force that opposes the deforming inertial forces acting upon the droplet during flight. It can then be deduced that a low Weber number is indicative of a system that yields a single spherical droplet, whereas a disperse spray of small droplets will be obtained with a high Weber number.

$$We = \;\rho\;\, (\upsilon)^2\, \mathrm{l} \,/\, \sigma \tag{2.4.3.2}$$

Both the Reynolds and Weber numbers can be mathematically related to obtain the Ohnesorge number. As a combination of both the Reynolds and Weber numbers, the Ohnesorge number relates the viscous, inertial, and surface tension forces acting upon a fluid and may be used to describe a droplet within an inkjet system. The Ohnesorge number (Oh) is given by equation (2.4.3.3), where μ is the dynamic viscosity of the fluid, ρ is the density of the fluid, σ is the surface tension of the fluid, L is the droplet diameter, Re is the Reynolds number, and We is the Weber number. For inkjet systems, it is often accepted that an ink with an Ohnesorge number $0.1 < Oh < 1$ will yield a steady stream of uniform droplets and thus is jettable. Z number, the reciprocal of the Ohnesorge number, is sometimes used when describing jettable inks. A satisfactory and jettable Z number is often given by $1 < Z < 10$.

$$Oh = \mu / \sqrt{(\rho \, \sigma \, \mathrm{L})} = \sqrt{We} \, / \, Re \qquad (2.4.3.3)$$

2.5 The Printing Process

Now that the fundamentals of a good ink have been introduced, the process of inkjet printing can be described in more detail. This research project utilised a DOD piezoelectric inkjet printer, and so this section will specifically be relevant to such systems. This section aims to describe the printing process chronologically, beginning with the topic of ink formulation. The generation of jetted droplets, behaviour on the substrate, and the subsequent formation and characterisation of the printed film is also covered. A short discussion of the advantages and disadvantages of inkjet printing will then conclude the section.

2.5.1 Ink Formulation

The first decision to be made when formulating an ink is to choose an appropriate active component. This may either be a reactive precursor to the target material, or already in the form of the desired deposit. A carrier solvent should also be chosen, which is suitable for use with the active component and has compatible physical properties with the inkjet system. At this junction, it is decided whether the ink requires any additive components. For a reactive precursor system, stabilising additives may be required. High molecular weight additives are often used to acquire an even dispersion of suspended particulates. A high surface tension can be reduced by adding surfactants to the ink formulation.

Once a satisfactory ink formulation has been created, the droplet diameter and therefore the resulting Ohnesorge number can be manipulated by using a dispensing device with a different orifice diameter. Long-term ink stability should also be monitored at this point to ensure that the ink remains stable during the required storage parameters. The long-term stability of the ink, or shelf-life, is often measured by observing the physical properties of the ink at several intervals and determining whether or not there is a significant change during ageing. The time after which the ink properties, such as viscosity, change drastically is the maximum time the ink remains stable.

2.5.2 Droplet Formation, Ejection and Flight

Printing with the desired ink formulation requires several jetting and print parameters to be optimised. For a DOD piezoelectric dispensing device, a pattern of electrical impulses is input into the printing software and sent to the printer. This pattern of electrical impulses is required to generate and eject a droplet, and is known as the waveform. It is this waveform that causes the reverse piezoelectric effect in the piezo element of the dispensing device, resulting in the droplet formation and ejection.

Table 2.5.2.1. Example Waveform

Parameter	Value
Rise Time 1 (µs)	a
Dwell Time (µs)	b
Fall Time (µs)	a
Echo Time (µs)	2b
Rise Time 2 (µs)	a
Idle Voltage (V)	0
Dwell Voltage (V)	x
Echo Voltage (V)	-x

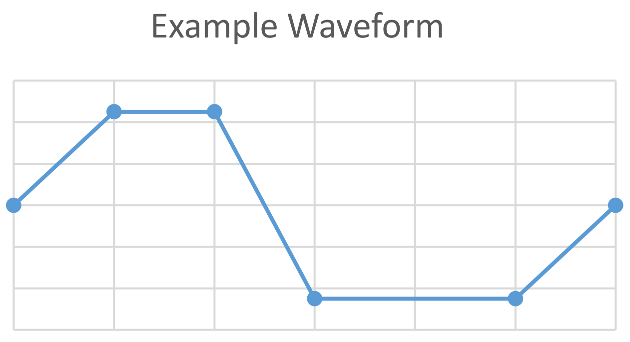

Figure 2.5.2.1 A graph to show the example waveform pattern

For the software used in this project, the waveform consisted of eight parameters. Each parameter was required to be set to an appropriate value as each parameter has a dramatic effect on the resulting meniscus perturbation and possible droplet ejection. The eight parameters were as follows: rise time 1, dwell time, fall time, echo time, rise time 2, idle voltage, dwell voltage, and echo voltage (See Table 2.5.2.1 for an example waveform). Idle voltage is the starting voltage and is typically set to 0 V. Dwell and echo voltage are the magnitudes of the voltages applied to the piezoelectric element that leads to the element and membrane distortion, perturbation of the ink and subsequent droplet production. Echo voltage is equal and opposite to the dwell voltage. Rise time is the length of time allowed for the voltage to reach the specified dwell voltage. Dwell time is the length of time the dwell voltage is applied for. Fall time is the time to go from the dwell voltage to the echo voltage and echo time is the length of time the echo voltage is applied for. Rise time 2 is the length of time to go from the echo voltage back to the idle voltage. Figure 2.5.2.1 shows a graphical representation of the example waveform.

Typically, a waveform is optimised for an inks' carrier solvent first as the carrier solvent will be less prone to reaction or blockage, and is significantly less expensive and more expendable than the formulated ink. Minor adjustments can be made, if necessary, to further optimise the waveform for the final ink formulation. To visualise the effects of changing the waveform and ascertain the suitability of a waveform for the jetting of an ink, the tip of the dispensing device can be imaged by a fixed camera and strobe. A live feed of the tip can be viewed in real time, giving instant feedback on the effects of waveform parameters. The strobe often has a tuneable delay, allowing the droplet formation and ejection to be visualised at several different timings during the jetting process. An ineffective waveform shows little to no perturbation of the ink meniscus at the tip of the dispensing device, whereas a well optimised waveform yields a controlled ejection of a single uniform, spherical droplet.

There are several intermediate phenomena observed during the optimisation of a waveform related to the ejection of droplets. As mentioned previously, a poor waveform will result in no change to the ink meniscus. A small change to the waveform may result in a small perturbation of the meniscus, with further alterations resulting in the initial formation of a droplet. However, without a sufficient magnitude of dwell voltage the force of ejection is incapable of overcoming the cohesive surface tension of the ink and the partially formed droplet will recede back into the dispensing device. Increasing the dwell voltage unnecessarily high will instead result in the ejection of several droplet fragments in rapid succession. In this situation, the magnitude of the driving force being applied to the potential droplet is so great that it overwhelms the cohesive forces of the liquid and forces several small droplets to be ejected during the course of one waveform pattern.

Other phenomena that are typically observed when optimising a waveform are the formation of liquid ligaments and satellite droplets. Liquid ligaments occur when the forming droplet is not cleanly ejected from the dispensing device orifice, instead forming a long liquid column. This liquid column then breaks into a leading droplet followed by a long liquid ligament. The liquid column itself will either return to the bulk of the ink within the nozzle after the droplet has separated, or the column itself can also separate from the bulk ink. A separated liquid ligament may either merge with the leading droplet or form satellite droplets, depending on the properties of the ink. A satellite droplet is a droplet that is formed in addition to the leading droplet, typically of a reduced volume. There may be one or several satellite droplets formed from a single liquid ligament.

After optimising a waveform to eject a single uniform and spherical droplet, the speed of the droplet can be measured by varying the delay of the illuminating strobe for the droplet imaging camera. The distance the droplets have travelled between two given strobe delays gives their speed. Droplet speed can be crudely controlled by altering the dwell and echo voltages. As there is minimal distance between the dispensing device and the substrate, in addition to the low mass of the droplets themselves, the effect of gravitational acceleration is generally ignored for such inkjet systems.

2.5.3 Droplet Impact, Spread, and Evaporation

Once a waveform has been obtained to generate a steady stream of uniform droplets, the physical printing parameters of print speed, U_T, and step size, p, must be optimised for the intended substrate. Print speed is the speed with which the dispensing device travels in relation to the substrate. This parameter is typically maximised in order to increase productivity, whilst ensuring an acceptable quality of print. Step size is the distance between two adjacent droplets, or pixel cells. A step size that is too large results in a discontinuous deposition of individual droplets, whereas a step size that is too small results in poor evaporation of volatiles and a build-up of ink on the substrate.

Derby et al. have proposed a mathematical method for identifying ideal physical print parameters.[67] In this article, upper and lower bounds are presented graphically along dimensionless axes. The mathematics involved is best presented in the article itself. An experimental study has also been published by Derby *et al.* adding a “phase diagram” for drop behaviour with emphasis on the thresholds for drop generation and formation of satellite drops.[68] The parallelogram indicates 4 boundaries; an upper and lower bound for both We_j (Weber number of the fluid jet), and the inverse Ohnesorge number, Z. It concludes that despite the large range of fluid properties over which stable drops can form, the region of practical ink design lies roughly in the $2 < Z < 20$ range.

Before discussing the physical processes displayed in a complex printing situation, a single droplet impact is first considered. Once a single droplet is produced and ejected by the print head, it will fall to the substrate and impact onto the substrate. There are several potential outcomes of a droplet impacting upon a substrate, ranging from total deposition to splashing or complete rebound.[69] For an idealised system, total deposition will occur. The process of droplet impact can be divided into three main stages. In the first stage, initial contact is made between the jetted droplet and the substrate. The second stage involves the formation of a thin, circular film as the droplet spreads across the substrate. Liquid travels radially outwards, causing an accumulation of mass at the boundary of the ring. Kinetic energy is partly dissipated due to viscous flow in the thin film. During the third stage, the film begins to recoil until the fluid settles into a brief equilibrium state with a defined droplet volume, height (h), diameter (d), and contact angle (θ_c), as shown in Figure 2.5.3.1.

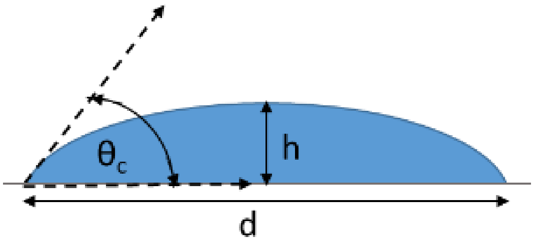

Figure 2.5.3.1 Schematic to show the droplet equilibrium state during the third stage of droplet

Following this brief, post-impact equilibrium, volatiles will begin to evaporate.[70] The process of evaporation is also described in three stages for a smooth substrate. In the first stage, the diameter remains constant while evaporation reduces the droplet height and decreasing contact angle until the receding angle (θ_r) is reached and the second stage begins. In the second stage, the contact angle remains constant at θ_r as the droplet diameter begins to decrease. Finally, in the third stage as evaporation continues, the droplet diameter and contact angle both diminish until all volatiles have evaporated. Any insoluble or non-volatile components are deposited onto the surface.

This regime is not always followed. Sometimes, the droplet edge becomes pinned by insolubles or surface imperfections. As the volatiles evaporate, the diameter cannot decrease as the solvent front is pinned and so the second stage of evaporation is not entered. Instead, replenishing flows of solution travel from the centre of the droplet to the pinned perimeter of the droplet, resulting in a flow of matter to the pinned contact line. This process continues until evaporation is complete, causing the majority of deposit to be located at the pinned contact line. This known as the coffee stain effect and is commonly observed for suspensions of insoluble particles such as coffee or red wine.

For a system involving multiple droplets printed in a line, the overall behaviour is similar to a single droplet. However, at sufficiently small spacings for the droplets to overlap, a body of liquid will be formed as the droplets coalesce. The desired effect is to obtain a straight and continuous line of deposit, but this is often not observed. Other than a uniform line, printed lines may exhibit: bulging, scalloping, discontinuity, and the stacked-coin effect (See Figure 2.5.3.2). The two process parameters that play an important role in the observed printed line behaviour are the inter-droplet distance, or step size, and a general parameter called delay. The understanding of inkjet printed pattern generation is described in great detail by Soltman in their thesis.[71]

Step size has a strong influence on coalescence of the droplets, with a strong deterministic effect on whether a uniform, scalloped, or discontinuous line is obtained.[72] At high droplet spacings, the drops will simply behave as individual sessile droplets and result in a discontinuous line of individual droplets. Reducing the step size such that the droplets now contact one-another, a scalloped line morphology will be observed. Necks form between the droplets at the point of contact, although the boundaries of the individual droplets can still be distinguished. Further reducing the inter-droplet distance reduces the prominence of scalloping until a uniform line is obtained. At this point, the overlap of the droplets is sufficient to form necks between the boundaries of the droplets and forming a straight edge to the coalesced body of liquid. It should be noted that the physical properties of an ink such as viscosity, surface tension, and contact angle are all factors which also effect the spreading process

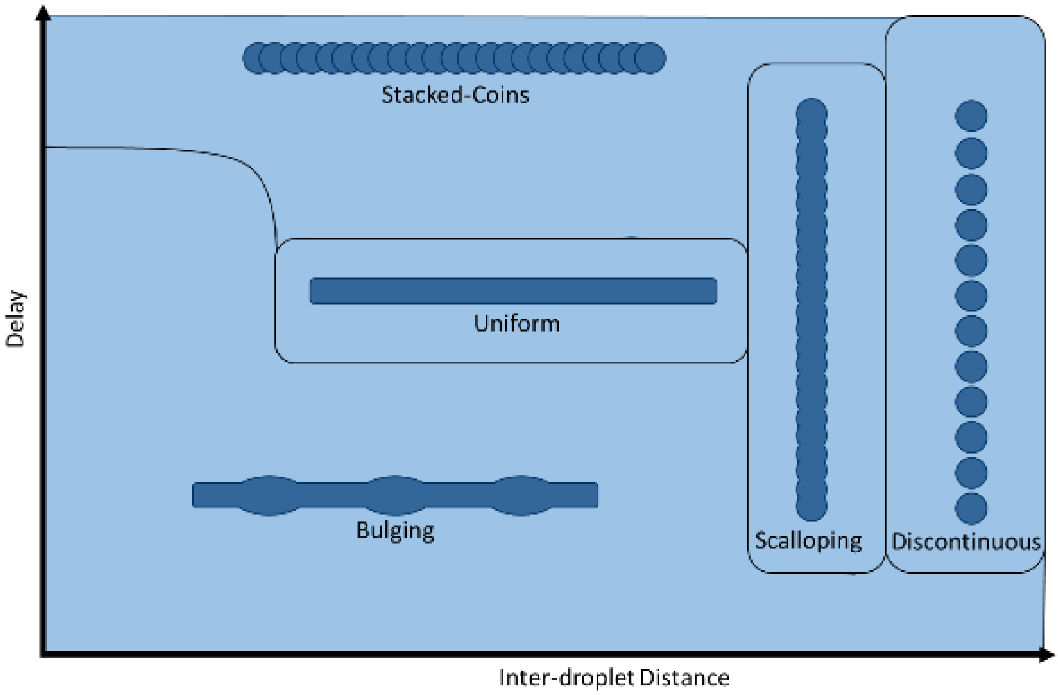

Figure 2.5.3.2 Schematic to show the effect of delay and inter-droplet distance on printed track

Delay, the other process parameter that plays an important role in printed line behaviour, is the relative rate of evaporation to print speed and is a complex combination of several factors. Some factors influencing delay are: the volatility of the chemical species present in the ink, the temperature of the substrate and surrounding medium, and frequency of droplet ejection. Simply put, as delay is increased the state of evaporation is more advanced for the previous droplet deposited in a line before the next droplet is deposited. Low delay leads to bulging lines, caused by an excessive build-up of liquid resulting in discreet regions of outflow. At a high enough delay, the stacked-coin effect is observed as each droplet has fully evaporated on the substrate before the neighbouring droplet is deposited.

2.5.4 The Printed Film

After discussing the optimisation of print parameters for the production of a uniform line of droplets, these parameters can then be used to print an image and yield a single pass of a printed film. An inkjet printer reads an image as a matrix of pixels, with each pixel resulting in a command. The Jetlab 4 printer used for this project operated in a binary fashion, where the two commands were either to eject a droplet or not. As such, the images used were all monochromatic with white pixels resulting in the command to eject a droplet of ink and black pixels resulting in no ejection. Some printers obey far more complex commands, such as desktop colour printers, where multiple inks and droplet sizes can be jetted to result in colour and tone gradients in the print.

During the printing process, the image matrix is read by the printer in a row by row fashion with each matrix element or pixel equating to a region of real space on the substrate. Step size determines the area of substrate each matrix element corresponds to. The dispensing device travels along the substrate at the defined print speed and jets a droplet at every white pixel. Neighbouring white pixels result in printed lines. After the dispensing device has travelled to and ejected a droplet at the location corresponding to the last white pixel on the row, it travels to the location at the start of the row immediately above and begins the process again. This repeats until the final droplet has been jetted.

For a binary inkjet system such as ours, extrapolation of the phenomena that occur for a one-dimensional line of printed droplets to a two-dimensional matrix of printed droplets is relatively simple. The additional dimension of droplet placement behaves the same as printed droplets in a line and similar phenomena are observed. The practical difference between neighbouring droplets ejected on the same row and neighbouring droplets ejected in the same column is delay, or more specifically time. This is due to the dispensing device travelling sideways along the rows of the matrix. As such, it is commonly observed that neighbouring printed lines can be distinguished from one-another in the same way individual droplets can be identified in printed lines that exhibit the stacked-coin effect.

Additional printed passes of the same image can be performed in succession, causing the prints to be layered on top of one-another. These multiple pass prints yield three-dimensional printed samples with a tuneable thickness, increasing in ca. multiples of the single pass thickness. Increasing the dimensions from two to three is more complex than increasing from one to two dimensions. This increased complexity is mainly due to the substrate effectively changing to the previously deposited print. There are several implications of printing onto the previously deposited print, including a change in contact angle and surface roughness. For extreme examples of relatively low delay, the previous deposit may still be liquid which results in a process known as wet-to-wet printing. Most systems exhibit sufficient delay that the previous printed layer has evaporated or solidified, yielding a wet-to-dry printed process.

2.5.5 Advantages and Disadvantages of Inkjet Printing

There are many advantages associated with inkjet technology. These include: the ability to accurately deposit precise amounts of materials, increased process economy and the reduction of manufacturing costs, high quality output, wide choice of substrate, implementation of just-in-time manufacturing, and direct patterning of the deposit. However, inkjet printing is a solution-based technology. It requires that the material to be deposited is obtainable as a solution, a solution-based precursor, or a colloidal suspension. Rheological properties of this solution must be compatible with inkjet technologies. Feature sizes are often a limiting factor with regard to inkjet printed functional materials which require very small, strict patterning of the material on the substrate, such as printed electronics. Productivity is also a challenge associated with inkjet printing, especially in industry. Drop placement accuracy is a variable which is difficult to control due to many external parameters, including jet-to-jet variations, nozzle and surface wetting, and sensitivity to nozzle straightness.

2.6 Processing and Analysis of the Printed Film

Once a printed sample has been generated, there are often several processing and analytical techniques performed post-deposition. Heat-treatments are typically performed to remove any residual ink volatiles from the film, also resulting in densification. Thermal or radiative sintering is also a common post-deposition treatment for inks containing particulates. Sintering is the process in which distinct particles are fused together, below the melting point of the bulk material. Certain ink components may be used that utilise a UV-curing step to fix the deposit and finish the drying process, negating the requirements for a thermal treatment step.

2.6.1 Film Thickness

After the deposited film has undergone all post-treatment steps, the sample is analysed to ensure the desired application demands have been met. Film thickness is one of the most significant physical properties of a functional thin film as it has a large overall effect on the structural, optical, electrical, and mechanical properties of the deposit. There are several methods to determine film thickness, varying in their simplicity and accuracy. The simplest method involves measuring the mass of the substrate before deposition and subtracting this from the mass of the sample measured after the post-deposition treatments. This difference is the mass of deposited material, and the thickness can be calculated from the density and area coverage of the material. Unfortunately, this method can only be used for relatively thick and heavy samples as thin films often weigh less than a balance can detect.

Film thickness can be calculated theoretically when the droplet diameter, active component content, total number of droplets, area covered, and density of deposited material are all known. This is discussed further in Chapter 3, section 3.4.2. Ellipsometry is an optical technique that can be used for characterising several properties of thin films, including film thickness.[73] The change in polarisation of light before and after interaction with the sample is measured and then compared to computational models. An output variable, such as thickness, is then given that best fits the computational model given the physical measurement. This technique requires several physical properties to be characterised before a useful output is given.

Stylus profilometry is a useful technique for measuring film thickness as it is a purely physical technique that does not require any computational models, theoretical calculations, or large assumptions.[74] However, stylus profilometry is a contact methodology and as such can be a destructive technique. A stylus profilometer measures the surface profile of a sample by moving the stylus tip into contact with the sample at a defined location, and then detecting the vertical stylus displacement as the tip is moved laterally across the sample. Film thickness can be obtained by measuring the step height between the substrate and the deposited film.

Atomic force microscopy (AFM) is a similar technique for measuring the profile of a sample.[74] Compared to stylus profilometry, AFM has higher resolution and is generally less destructive, although the technique is far more complex and the instrument is significantly more expensive. AFM uses an atomically fine tip located on a cantilever, with tip displacement being measured by the deflection of a beam incident to the top of the cantilever. There are three distinct imaging modes available to a typical AFM: contact mode where the tip is moved laterally across the sample at a constant height, tapping mode where the cantilever is oscillated up and down to result in transient contact with the surface as it ‘taps’ across the sample, and non-contact mode where the tip is kept at a constant height above the surface while experiencing attractive van der Walls forces from the sample.

2.6.2 Scanning Electron Microscopy

SEM is a non-contact technique that uses electrons to image the surface topography of a sample.[75] The standard topographical imaging mode uses the detection of secondary electrons to create an image of the sample surface. Secondary electrons are generated by inelastic scattering interactions of the beam electrons with conduction or valence electrons from the sample surface atoms. Compositional information can also be obtained with an SEM by detecting backscattered electrons. The atoms of the sample exhibit elastic scattering interactions with high energy electrons from the emitted beam, resulting in reflected or backscattered beam electrons. Elements of higher atomic number scatter more strongly than elements of lower atomic number. This difference in scattering between elements allows compositional information to be gathered.

Many SEMs are also equipped with energy-dispersive X-ray spectroscopy (EDXS) detectors, able to analyse the characteristic X-rays that are produced when the beam electrons interact with the atoms of the sample surface. The emitted X-rays generate an emission spectrum containing peaks that are characteristic of each element present within the sample. The relative intensities and characteristic peaks allow quantitative composition data to be obtained. Furthermore, the analysis area of the sample can be easily moved or varied in size to allow elemental composition to be quantified in targeted regions of interest.

2.6.3 Optical Spectroscopy

Optical spectroscopy is a common technique that can be used to determine the optical properties of transmittance, reflectance, and absorbance for thin films. An optical spectrometer emits a controlled beam of photons with specific wavelengths, ranging from ca. 100 – 1000 nm, encompassing the visible spectrum and some of the neighbouring ultraviolet and infrared spectra. A detector is positioned to measure the transmittance or reflectance of the incident photons and recorded as a percentage when compared to a reference sample. Measurement of the optical properties of a film generally require the film to be deposited onto a transparent substrate, such as glass. The transparent substrate is used as the reference sample so that the measured optical properties belong purely to the thin film. Absorbance is typically given as the remaining photons that were neither reflected nor transmitted, as shown in equation (2.6.3.1).

$$\%\,Absorbance = 100 - \%\,Reflectance - \%\,Transmittance \qquad (2.6.3.1)$$

2.6.4. X-Ray Diffraction

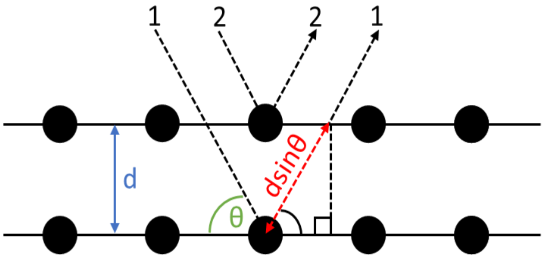

Figure 2.6.4.1 Schematic illustrating Bragg's Law parameters for a regular crystalline lattice

XRD is a useful technique for obtaining information about the structure of crystalline materials, such as the identification and relative abundance of different polymorphic compounds. In XRD, an emission source generates a beam of X-rays that is fired onto a sample. The electrons in the sample elastically scatter the X-rays, generating an interference pattern. Most of the interference is destructive in nature, resulting in the cancellation of the majority of the scattering pattern. At very specific locations, as given by Bragg's Law in equation (2.6.4.1),[76] constructive interference occurs that results in a reflecting spot in the interference pattern. Figure 2.6.4.1 shows Bragg's Law in effect, with the regular array of scattering bodies representing a symmetrically arranged crystalline material. In both Figure 2.6.4.1 and Bragg's Law equation (2.6.4.1.), d is the spacing between diffracting planes, θ is the incident angle of the X-rays, n is any integer, and λ is the wavelength of the X-rays.

$$2d\sin\theta = n\lambda \tag{2.6.4.1}$$

Figure 2.6.4.1 shows that the distance travelled by X-ray 1 is greater than the distance travelled by X-ray 2 by a total of 2dsinθ. For X-rays 1 and 2 to be in-phase and allow constructive interference to occur, the wavelength of the X-rays must be an integer multiple of this length. Typical crystal spacing is on the order of ca. 1-100 Å, which corresponds well to the wavelength of most X-rays (ca. 0.1 – 100 Å). As a wavelength similar in magnitude to the spacing of the diffracting planes is required for constructive interference, this compatibility of crystal spacing and wavelength explains why the electromagnetic radiation used is X-rays.

As there is a strong preference towards crystalline anatase TiO_2 for most applications, there is a need to distinguish between the various polymorphs of TiO_2. XRD is a common analytical technique that results in different spectra for anatase and rutile TiO_2, allowing a crystalline sample to be characterised as either anatase, rutile, or a mixture of the two. The XRD spectrum of the anatase polymorph contains a very large and distinctive peak at a 2 θ value ca. 25°, corresponding to the A(101) plane. Rutile TiO_2 also exhibits a very large peak at a 2 θ value ca. 27°, corresponding to the R(110) plane. These two large peaks, along with the other typically lower intensity peaks, allows the presence of either phase to be identified. Chan et al. calculate the percentage of rutile in their anatase / rutile mixtures according to equation (2.6.4.2), where x is the weight fraction of rutile in their powder, I_A and I_R are the X-ray intensities of the anatase (101) and rutile (110) peaks, respectively.[9]

$$x = (1 + 0.8\ I_A/I_R)^{-1} \tag{2.6.4.2}$$

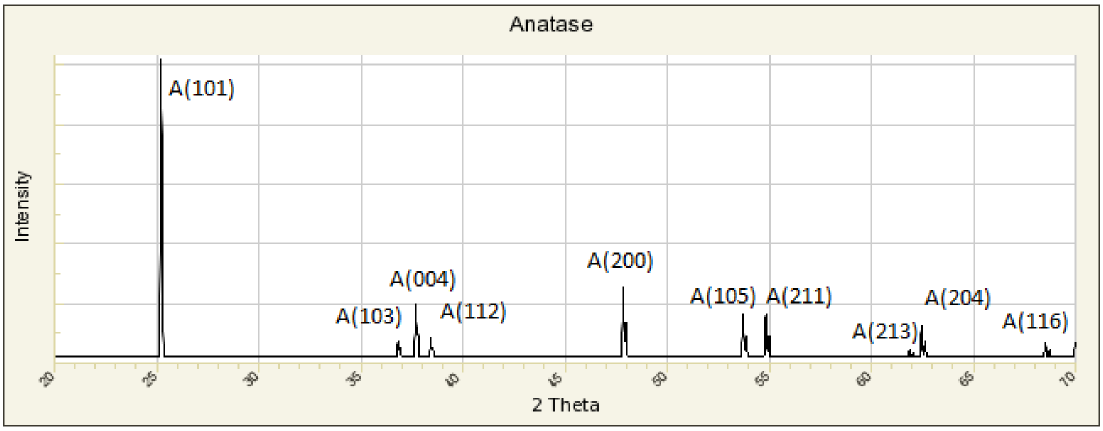

Figure 2.6.4.2 Computationally generated XRD spectrum of anatase TiO_2 from the RRUFF database

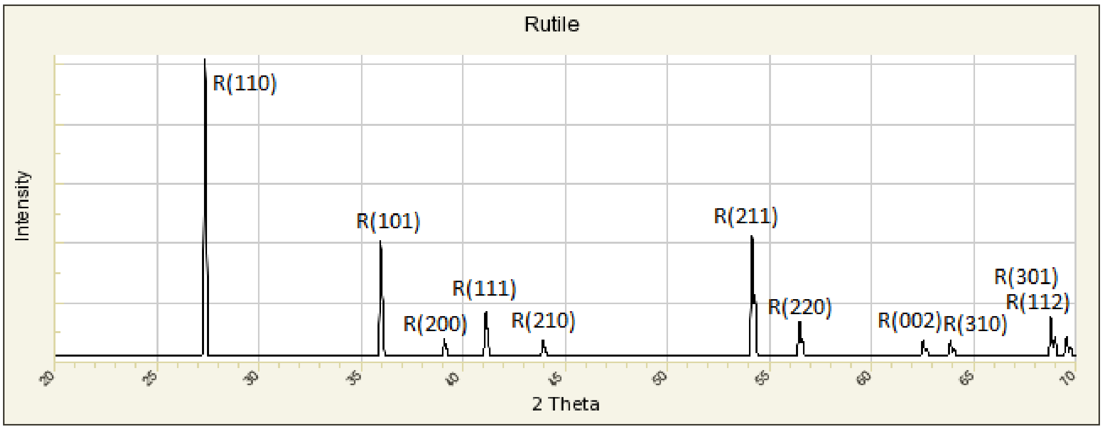

Figure 2.6.4.3 Computationally generated XRD spectrum of rutile TiO_2 from the RRUFF database

2.6.5 Raman Spectroscopy

Another technique which can be used to identify crystalline structure is Raman spectroscopy.[4] This technique is used to determine low-frequency molecular modes, such as vibrational and rotational modes, which behave as fingerprint identifiers for different molecules or crystal polymorphs. Raman spectroscopy utilises a laser beam to excite the system with inelastic scattering. The energy lost or gained by the inelastic interaction is

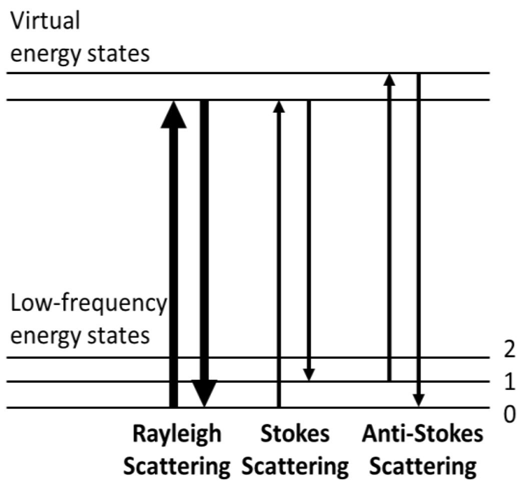

Figure 2.6.5.1 Schematic illustrating the types of scattering observed in Raman spectroscopy

detected, giving information about the low-frequency modes of the system. Raman scattering is divided into Stokes or Anti-Stokes scattering with Stokes scattering involving an energy gain for the molecular system and a reduction in energy of the laser, and Anti-Stokes scattering resulting in an energy loss for the molecular system and an increased laser energy (See Figure 2.6.5.1). The dominant process in Raman spectroscopy is Rayleigh scattering, an elastic interaction in which no energy is transferred and so no measurable changes occurs. As such, a detector filter is required to remove the Rayleigh scattering and improve sensitivity to the Raman scattering.

Raman spectroscopy can be used to differentiate between anatase and rutile phase TiO_2. Anatase has six Raman active modes: $1A_{1g}$, $2B_{1g}$, and $3E_g$. Rutile has four Raman active modes: B_{1g}, E_g, A_{1g} and B_{2g}. Frank et al. report their deconvolution of the A_{1g}/B_{1g} bands in the anatase and the second-order scattering (SOS) region in the rutile Raman spectra using isotopic substitution and measurements down to 5 K, alongside density functional theory (DFT) calculations.[77] In this paper, the Raman active atomic vibrations for both rutile and anatase are clearly depicted.

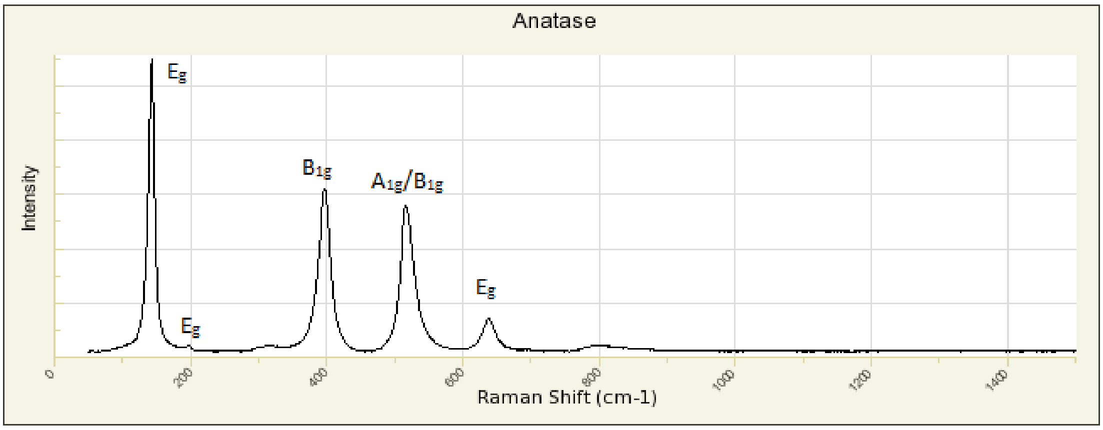

Figure 2.6.5.2 Computationally generated Raman spectrum of anatase TiO_2 from the RRUFF database

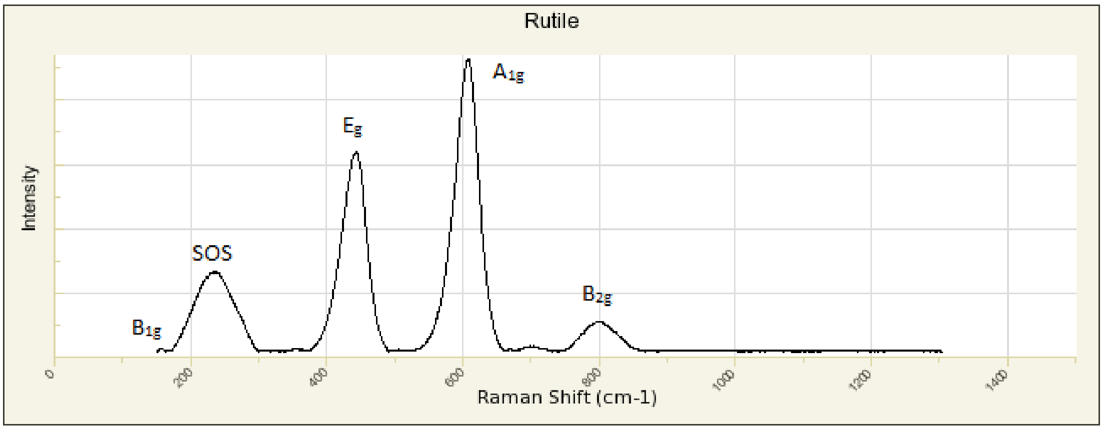

Figure 2.6.5.3 Computationally generated Raman spectrum of rutile TiO_2 from the RRUFF database

2.6.6 Sheet Resistance

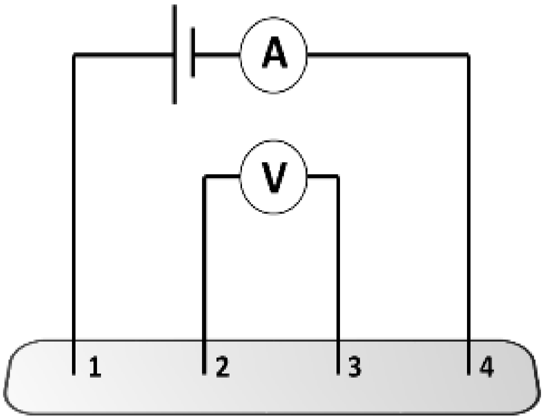

Figure 2.6.6 4-point probe for measuring sheet resistance

As a semiconductor with potential applications as a transparent conducting oxide, the conductivity of TiO_2 is an important property to be measured. For thin films, this property is typically reported in terms of sheet resistance. The standard instrument for measurement of thin film sheet resistance is a 4-point probe.[78] Figure 2.6.6.4 illustrates the standard set-up for a 4-point probe with connections 1 and 4 carrying current to and from the sample, and connections 2 and 3 sensing the voltage across the two inner probes to determine the sample resistivity.

2.7 Inkjet Printing of TiO_2

Inkjet printing has been used as a deposition method for many MO systems, with varied methodological approaches and a wide range of potential and realised applications. According to a review article by Liu et al. the first example of MO inkjet printing was reported in 1997.[79] In this seminal paper, Schultz et al. use an inkjet system to generate luminescent materials libraries comprised of phosphors with the general form $Gd_mAl_nO_x:Eu^{3+}_y$.[80] TiO_2 is one of the many target MOs for inkjet printing of thin film MOs.

Inkjet printing is a versatile deposition process, able to utilise colloidal or solution-based inks. Control of the thickness can be achieved by altering process parameters such as the number of printed passes. Furthermore, the deposit can be directly patterned onto the substrate without any pre-treatments or post-deposition etching. As a deposition technique, inkjet printing is cheap and low-waste, with no special processing requirements (such as elevated temperatures, inert gases etc). Inkjet printing does lack the finer control of processes such as CVD, and is limited to ink solutions that are compatible with the print system and dispensing device.

2.7.1 Types of TiO_2 Inks

TiO_2 inks typically consist of a colloidal suspension of either pre-purchased or sol-gel derived nanoparticles. This is likely an artefact from the standard and well-established spin coating and dip coating technique solutions. To form a stable ink that doesn't aggregate, agglomerate, or sediment, these colloidal suspensions typically use a high molecular weight stabiliser. These high molecular weight stabilisers often require a high temperature thermal processing step to remove. For applications such as electronics that require a continuous film, a sintering step is also required to fuse the nanoparticles together. These high temperature steps are incompatible with many substrates, including the flexible plastics many electronics are moving towards. There are also alkoxide or metal salt inks reported for the inkjet deposition of MOs such as TiO_2.

2.7.2 Inkjet Printed TiO_2 Literature Review

Inkjet printing of TiO_2, and indeed MOs as a whole,[79] is a field of research that is still relatively young yet of great interest. Table 2.7.2 summarises some of the key experimental information from published articles of inkjet printed TiO_2 films. It is immediately apparent that most inks consist of a colloidal suspension of nanoparticle TiO_2. However, precursor solutions based around the $Ti(O^iPr)_4$ molecule have been reported,[15, 21, 44, 47] although some examples of other Ti sources such as $Ti(O^nBu)_4$ can be found.[1] Stabilisers are generally used in these precursor systems. Arin et al. describe a system in which citric acid or triethanolamine may be used as stabilising agents for aqueous TiO_2 precursor solutions.[3] These stabilizing agents were chosen due to their mild and environmentally friendly behaviour, as shown by their use in the food and cosmetics industry. $Ti(O^nBu)_4$ is the titanium source, whilst ethanol is used as an effective metal alkoxide solvent and inhibitor of hydrolysis during the addition of H_2O.

TiO_2 colloidal ink is utilised by Lawrte et al. in their inkjet printed, UV-activated oxygen indicator composed of the colloidal TiO_2 photocatalyst, a redox dye and a sacrificial electron donor.[81] In this paper, it is stated that a solution of TTIP in ^iPrOH is added slowly to an excess of vigorously stirring water, leading to complete hydrolysis and formation of TiO_2 colloids which precipitate *in situ*. The resulting milky dispersion is then left at 120°C for 48 hours, then stirred overnight. Of note is the suggestion that the sacrificial electron donor, tartaric acid, as well as acting as a peptizing agent prevents the formation of rutile TiO_2 during the heat treatment.

Another example of colloidal ink, utilising stabilised nanocrystalline TiO_2 suspensions, is demonstrated by Cerná et al.[82] Unusually, $TiOCl_2$ was used as the precursor molecule, added dropwise to $KOH_{(aq)}$ until neutrality. After washing, HCl was then added to decrease the pH to 1. Hydrothermal treatment was then performed at 110 and 160°C for 6, 24 and 48 hours. The final ink was obtained by mixing the hydrothermally treated Ti dispersion with equal parts HCl, H_2O and an anionic surfactant (dodecylbenzene sulfonic acid) to prevent aggregation. Soda-lime glass plates were used as the substrate. Both one and two-layer samples were obtained, the second layer being printed using the 'wet-to-dry' method. Calcination was performed at 500°C for 30 min.

One example of an application of inkjet printed thin layer TiO_2 is as a component of a memristor device: a passive, nonlinear, two-terminal device that limits or regulates the flow of electrical current in a circuit and remembers the amount of charge that has previously flowed through it.[21] They are also non-volatile, which allows them to retain information without power. In this device, the TiO_2 layer is the active memristor, whilst the two terminals are Ag and Cu. Thus, the thin film of TiO_2 is printed directly onto the Cu substrate. Finally, the Ag layer is deposited onto the post-treated TiO_2 substrate. Post-treatment of the printed film involved annealing at 450°C for 3 hours, giving a 110 nm film of anatase phase TiO_2 as shown by XRD crystallite size calculations.

Table 2.7.2 Analysis of inkjet printed TiO_2 publications

Entry	Precursor	Ink Components	Substrate	Conditions	Comments	Ref.
1	TiO_2 nanopowder	H_2O carrier, Methacrylic acid / n-butyl acrylate copolymer dispersant, Ethylene glycol n-n-dimethylaminoethanol Methanol	HP 51636 transparent foil	400°C to burn out stabiliser	2.5 wt.% of TiO_2	53
2	Titanium(IV) bis(ammonium lactate) dihydroxide	H_2O carrier Graphene Oxide functional component	SiO_2/Si	1000°C anneal in vacuum	Nanocrystalline rutile identified	83
3	$Ti(OBu)_4$	H_2O carrier Carbowax viscosity modifier and binder	ITO glass	Calcined at 700°C for 2 hours	Anatase and rutile mixture, identified as 92.9 % anatase and 7.1 % rutile	84
4	$Ti(OBu)_4$	H_2O carrier, Ethanol co-solvent Citric acid, acetylacetone or triethanolamine as complexing agents	Glass	500 – 650°C sinter for 1 hour	Anatase at and above 500°C, small amount of rutile is identified at 650°C	3
5	TTIP	EtOH carrier, Polyethylene glycol anti-cracking agent, Acetylacetone sol stabiliser	Soda-lime glass	Thermally treated at 450°C for 4 hours	Anatase identified, with small presence of rutile	85

Table 2.7.2 (cont.) Analysis of inkjet printed TiO_2 publications

Entry	Precursor	Ink Components	Substrate	Conditions	Comments	Ref.
6	TiO_2 nanopowder	De-ionised H_2O carrier Dispersants $Na_4P_2O_7$	Glass slides Ceramic tiles	Ultrasonication prior to printing	P25 – identified 75 % anatase and 25 % rutile	[86]
7	TiO_2 nanopowder	H_2O carrier Dimethylformamide (DMF) drying agent (co-solvent)	Fluorine doped tin oxide (FTO) coated glass	Annealed from 150 - 450°C for 30 minutes	P25 – 80 % anatase and 20 % rutile	[87]
8	$TiOCl_2$ to create colloidal TiO_2	H_2O carrier HCl Dodecylbenzene sulfonic acid (anion surfactant)	Soda-lime glass plates	Hydrothermal treatment of the colloid at 110 and 160°C for 6, 24, and 48 hours. Films annealed at 500°C for 30 minutes	Sonicated prior to printing All samples were rutile due to pH = 1	[82]
9	TTIP to create a colloid	H_2O carrier Tartaric acid stabiliser Methylene blue (oxygen indicator)	Polyester sheets	Hydrothermal treatment of the colloid at 120°C for 48 hours	Colloidal TiO_2 identified as anatase	[81]
10	TiO_2 nanopowder	De-ionised H_2O carrier DMF (drying agent) Polyethylene glycol (humectant)	FTO glass	Printed films annealed at 150°C for 30 minutes then at 250°C for 30 minutes	Anatase phase identified	[88]

Table 2.7.2 (cont.) Analysis of inkjet printed TiO_2 publications

Entry	Precursor	Ink Components	Substrate	Conditions	Comments	Ref.
11	TiO_2 nanopowder	BuOH carrier EtOH dispersant Silica binder	Pyrex slides Soda-lime slides FTO glass	One sample set calcined at 450°C One sample set UV cured	-	[89]
12	TiO_2 nanopowder	H_2O carrier Dispersant Surfactant	FTO electrodes	No post-deposition treatment	Printed University logo No phase analysis	[90]
13	TiO_2 paste	Triton X-100 EtOH or H_2O carrier	ITO	450°C for 30 minutes	No phase analysis	[91]
14	TTIP	H_2O carrier EtOH co-solvent n-methyl-diethanolamine	Soda lime glass ITO Polycrystalline alumina	400°C for 1 hour	Anatase begins to appear at 350°C Rutile mixtures appear at 700°C	[54]
15	Rutile TiO_2 powder	H_2O, H_2O_2 Ethylene glycol, diethylene glycol, or glycerine as viscosity modifier	Polyethylene films	Chemical processing to convert rutile to anatase 120°C anneal after deposition	Formed a gelled peroxy-titanium complex before H_2O	[92]

Table 2.7.2 (cont.) Analysis of inkjet printed TiO_2 publications

Entry	Precursor	Ink Components	Substrate	Conditions	Comments	Ref.
16	TiO_2 nanopowder	DOWANOL PM carrier Organosilica binder EtOH ^{i}BuOH	ITO coated polyethylene terephthalate (PET)	Plasma treated ITO surface prior to printing Post-deposition plasma treatment of TiO_2	No phase analysis Increased photoactivity after plasma treatment	93
17	TiO_2 nanoparticle paste	EtOH carrier Ethylene glycol Terpineol	Polyethylene naphthalate (PEN)	150°C for 2 hours	No phase analysis	94
18	$TiCl_4$ to form nanoparticle TiO_2	Di(ethylene glycol) monoethyl ether carrier Nb dopant Tri(ethylene glycol) monoethyl ether $Ti(O^{i}Pr)_2(acac)_2$ dispersant	ITO	100°C anneal on a hot plate	Anatase phase identified for the nanoparticles	95
19	TiO_2 paste	Cyclohexanol carrier Polyethylene glycol DMF TWEEN-60 detergent	TiO_2 coated FTO	Baked at 500°C for 30 minutes	No phase analysis	96

Hybrid functional films are also prevalent in the literature. One such example is the solution processable TiO_2-graphene photoconducting matrix developed by Manga et al.[83] Titanium is sourced from a $Ti(O^nBu)_4$ precursor, whilst graphene oxide is the graphene source. As the graphene oxide is suitable for aqueous deposition, reaction of the Ti precursor with diethanolamine in ethanol yields the ionic salt Ti(IV) bis(ammonium lactate) dihydroxide which is water soluble and compatible for mixing with the graphene. The article demonstrates that this solution is suitable for both inkjet and spin-coating applications, yielding a graphene oxide-TiO_2 matrix that is photoconducting.

During the course of this research there have been many additions to the literature regarding the inkjet printing of TiO_2 thin films. Most contributions still utilise a colloidal solution of TiO_2 nanoparticles. Recently, Gadea et al. produced an ink based on a similar rationale to our own.[54] In their work, they use n-methyldiethanolamine as a nucleophilic ligand to inhibit the reaction of their TTIP precursor with H_2O. In order to reduce environmental impact, an H_2O carrier solvent is used. However, EtOH is used as a co-solvent at a 40 – 60 vol % ratio of EtOH to H_2O.

2.8 Project Context and Rationale

In this work, a DOD piezoelectric inkjet printer was used to print TiO_2 with an emphasis on obtaining anatase at a low temperature. To achieve this, initial work was performed to formulate and optimise a solution-based ink using TTIP as a reactive titanium source, ^{i}PrOH as a carrier, and a glycol ether stabilising agent. The use of a glycol ether and ^{i}PrOH system had not been reported, whilst the use of TTIP as a component, rather than as a precursor for a sol-gel, was uncommon in inks formulated for inkjet printing. It was proposed that a reduction in thermal budget could be achieved using a solution-based ink with low-molecular weight stabilisers. As a solution-based ink, issues associated with printer blockage and particle stability would be avoided, and a high temperature sintering step would not be required to form a continuous film.

2.9 References

1. Z. C. Wang, U. Helmersson and P. O. Kall, *Thin Solid Films*, 2002, **405**, 50-54.
2. U. Diebold, *Surface Science Reports*, 2003, **48**, 53-229.
3. M. Arin, P. Lommens, N. Avci, S. C. Hopkins, K. De Buysser, I. M. Arabatzis, I. Fasaki, D. Poelman and I. Van Driessche, *Journal of the European Ceramic Society*, 2011, **31**, 1067-1074.
4. U. Balachandran and N. G. Eror, *Journal of Solid State Chemistry*, 1982, **42**, 276-282.

5. M. Landmann, E. Rauls and W. G. Schmidt, *Journal of Physics Condensed Matter*, 2012, **24**.
6. M. Lazzeri, A. Vittadini and A. Selloni, *Physical Review B*, 2001, **63**, 155409.
7. R. Mechiakh, N. B. Sedrine, R. Chtourou and R. Bensaha, *Applied Surface Science*, 2010, **257**, 670-676.
8. D. A. H. Hanaor, G. Triani and C. C. Sorrell, *Surface and Coatings Technology*, 2011, **205**, 3658-3664.
9. C. K. Chan, J. F. Porter, Y.-G. Li, W. Guo and C.-M. Chan, *Journal of the American Ceramic Society*, 1999, **82**, 566-572.
10. J. G. Yu, H. G. Yu, B. Cheng, X. J. Zhao, J. C. Yu and W. K. Ho, *Journal of Physical Chemistry B*, 2003, **107**, 13871-13879.
11. J. Zhang, P. Zhou, J. Liu and J. Yu, *Physical Chemistry Chemical Physics*, 2014, **16**, 20382-20386.
12. D. Reyes-Coronado, G. Rodríguez-Gattorno, M. E. Espinosa-Pesqueira, C Cab, R. d. Coss and G. Oskam, *Nanotechnology*, 2008, **19**, 10.
13. H. Zhang and J. F. Banfield, *Chemical Reviews*, 2014, **114**, 9613-9644.
14. H. Y. Liu and G. J. Liu, *IEEE Transactions on Electron Devices*, 2017, **64**, 1108-1113.
15. W. S. Kwack, H. S. Moon, S. J. Jeong, Q. M. Wang and S. H. Kwon, *Transactions of Nonferrous Metals Society of China*, 2011, **21**, S88-S91.
16. N. Rahimi, R. A. Pax and E. M. Gray, *Progress in Solid State Chemistry*, 2016, **44**, 86-105.
17. J. Bai and B. Zhou, *Chemical Reviews*, 2014, **114**, 10131-10176.
18. Y. Bai, I. Mora-Seró, F. De Angelis, J. Bisquert and P. Wang, *Chemical Reviews*, 2014, **114**, 10095-10130.
19. Y. Ma, X. Wang, Y. Jia, X. Chen, H. Han and C. Li, *Chemical Reviews*, 2014, **114**, 9987-10043.
20. J. Pan, C. Leygraf, D. Thierry and A. M. Ektessabi, *Journal of Biomedical Materials Research*, 1997, **35**, 309-318.
21. N. Duraisamy, N. M. Muhammad, H. C. Kim, J. D. Jo and K. H. Choi, *Thin Solid Films*, 2012, **520**, 5070-5074.
22. Q. Song, Y. Zhu, H. Zheng, F. Zhang and M. Wu, *Materials & Design*, 2016, **98**, 108-112.
23. Q. Chen, Q. Liu, J. Hubert, W. Huang, K. Baert, G. Wallaert, H. Terryn, M.-P. Delplancke-Ogletree and F. Reniers, *Surface and Coatings Technology*, 2017, **310**, 173-179.
24. M. Dominik, A. Leśniewski, M. Janczuk, J. Niedziółka-Jönsson, M. Hołdyński, Ł. Wachnicki, M. Godlewski, W. J. Bock and M. Śmietana, *Biosensors and Bioelectronics*, 2017, **93**, 102-109.
25. K. Wen, M. Liu, X. Liu, C. Deng and K. Zhou, *Coatings*, 2017, **7**, 169.
26. S. Agarwal, M. S. Haseman, K. D. Leedy, D. J. Winarski, P. Saadatkia, E. Doyle, L. Zhang, T. Dang, V. S. Vasilyev and F. A. Selim, *Journal of Electronic Materials*, 2018, **47**, 2271-2276.
27. K. Krupski, A. M. Sanchez, A. Krupski and C. F. McConville, *Applied Surface Science*, 2016, **388**, 684-690.
28. H. Y. Liu and R. C. Huang, *IEEE Transactions on Electron Devices*, 2018, **65**, 2517-2524.
29. K. Black, H. C. Aspinall, A. C. Jones, K. Przybylak, J. Bacsa, P. R. Chalker, S. Taylor, C. Z. Zhao, S. D. Elliott, A. Zydor and P. N. Heys, *Journal of Materials Chemistry*, 2008, **18**, 4561-4571.
30. J. S. Wrench, K. Black, H. C. Aspinall, A. C. Jones, J. Bacsa, P. R. Chalker, P. J. King, M. Werner, H. O. Davies and P. N. Heys, *Chemical Vapor Deposition*, 2009, **15**, 259-+.

31. J. M. Gaskell, S. Przybylak, A. C. Jones, H. C. Aspinall, P. R. Chalker, K. Black, R. J. Potter, P. Taechakumput and S. Taylor, *Chemistry of Materials*, 2007, **19**, 4796-4803.
32. J. M. Gaskell, A. C. Jones, H. C. Aspinall, S. Przybylak, P. R. Chalker, K. Black, H. O. Davies, P. Taechakumput, S. Taylor and G. W. Critchlow, *Journal of Materials Chemistry*, 2006, **16**, 3854-3860.
33. M. Balog, M. Schieber, S. Patai and M. Michman, *Journal of Crystal Growth*, 1972, **17**, 298-301.
34. A. Gans, E. Dressaire, B. Colnet, G. Saingier, M. Z. Bazant and A. Sauret, *Journal*, 2019, DOI: 10.1039/C8SM01785A.
35. A. G. Emslie, F. T. Bonner and L. G. Peck, *Journal of Applied Physics*, 1958, **29**, 858-862.
36. T. Maruyama and S. Arai, *Solar Energy Materials and Solar Cells*, 1992, **26**, 323-329.
37. J. Aarik, A. Aidla, H. Mändar and T. Uustare, *Applied Surface Science*, 2001, **172**, 148-158.
38. Y. Djaoued, S. Badilescu, P. V. Ashrit, D. Bersani, P. P. Lottici and J. Robichaud, *Journal of Sol-Gel Science and Technology*, 2002, **24**, 255-264.
39. C. Guillard, B. Beaugiraud, C. Dutriez, J.-M. Herrmann, H. Jaffrezic, N. Jaffrezic-Renault and M. Lacroix, *Applied Catalysis B: Environmental*, 2002, **39**, 331-342.
40. M. Langlet, A. Kim, M. Audier, C. Guillard and J. M. Herrmann, *Journal of Materials Science*, 2003, **38**, 3945-3953.
41. M. Langlet, A. Kim, M. Audier, C. Guillard and J. M. Herrmann, *Thin Solid Films*, 2003, **429**, 13-21.
42. K. K. Saini, S. D. Sharma, Chanderkant, M. Kar, D. Singh and C. P. Sharma, *Journal of Non-Crystalline Solids*, 2007, **353**, 2469-2473.
43. M. Addamo, V. Augugliaro, A. Di Paola, E. García-López, V. Loddo, G. Marcì and L. Palmisano, *Thin Solid Films*, 2008, **516**, 3802-3807.
44. Y. G. Sheng, L. P. Liang, Y. Xu, D. Wu and Y. H. Sun, *Optical Materials*, 2008, **30**, 1310-1315.
45. C. Sudakar, P. Kharel, R. Suryanarayanan, J. S. Thakur, V. M. Naik, R. Naik and G. Lawes, *JOURNAL OF MAGNETISM AND MAGNETIC MATERIALS*, 2008, **320**, L31-L36.
46. Z. Zhang, G. Triani and L.-J. Fan, *Journal of Materials Research*, 2011, **23**, 2472-2479.
47. M. Morozova, P. Kluson, P. Dzik, M. Vesely, M. Baudys, J. Krysa and O. Solcova, *Journal of Sol-Gel Science and Technology*, 2013, **65**, 452-458.
48. H. Lin, Y. Huang, S. Li, C. Luan, W. Huang, X. Wang and X. Feng, *Journal of Semiconductors*, 2017, **38**, 113004.
49. M. Quesada-Gonzalez, K. Baba, C. Sotelo-Vazquez, P. Choquet, C. J. Carmalt, I. P. Parkin and N. D. Boscher, *Journal of Materials Chemistry A*, 2017, **5**, 10836-10842.
50. H. Y. Liu, Y. L. Hsu, H. Y. Su, R. C. Huang, F. Y. Hou, G. C. Tu and W. H. Liu, *IEEE Sensors Journal*, 2018, **18**, 4022-4029.
51. F. Biechel, J. Dubuc and M. Henry, *New Journal of Chemistry*, 2004, **28**, 764-769.
52. V. Peruzzo, M. A. Chiurato, M. Favaro and P. Tomasin, *Mass Spectrometry Reviews*, 2018, **37**, 22-42.
53. S. J. Kim and D. E. McKean, *Journal of Materials Science Letters*, 1997, **17**, 141-144.
54. C. Gadea, D. Marani and V. Esposito, *Journal of Physics and Chemistry of Solids*, 2017, **101**, 10-17.
55. G. Q. Wang, W. Lan, G. J. Han, Y. Wang, Q. Su and X. Q. Liu, *Journal of Alloys and Compounds*, 2011, **509**, 4150-4153.
56. S. Magdassi, *The Chemistry of Inkjet Inks*, World Scientific, Singapore, 2009.
57. H. P. Le, *Journal of Imaging Science and Technology*, 1998, **42**, 49-62.
58. C. K. K. Lun, S. B. Savage, D. J. Jeffrey and N. Chepurniy, *Journal of Fluid Mechanics*, 1984, **140**, 223-256.

59. J. Kestin, H. E. Khalifa and R. J. Correia, *Journal of Physical and Chemical Reference Data*, 1981, **10**, 71-88.
60. T. S. Chow, *Journal of Physics: Condensed Matter*, 1998, **10**, L445-L451.
61. Š. Šikalo, H. D. Wilhelm, I. V. Roisman, S. Jakirlić and C. Tropea, *Physics of Fluids*, 2005, **17**, 062103.
62. A. Marmur, *Langmuir*, 2003, **19**, 8343-8348.
63. B. Derby, *Journal of the European Ceramic Society*, 2011, **31**, 2543-2550.
64. G. D. Martin, S. D. Hoath and I. M. Hutchings, *Journal of Physics: Conference Series*, 2008, **105**, 012001.
65. B. Derby, *Annual Review of Materials Research*, 2010, **40**, 395-414.
66. J. E. Fromm, *IBM Journal of Research and Development*, 1984, **28**, 322-333.
67. J. Stringer and B. Derby, *Langmuir*, 2010, **26**, 10365-10372.
68. Y. Liu and B. Derby, *Physics of Fluids*, 2019, **31**.
69. D. B. van Dam and C. Le Clerc, *Physics of Fluids*, 2004, **16**, 3403-3414.
70. C. Bourges-Monnier and M. E. R. Shanahan, *Langmuir*, 1995, **11**, 2820-2829.
71. D. B. Soltman, PhD Thesis, University of California, Berkeley, 2011.
72. Z. Du, R. Xing, X. Cao, X. Yu and Y. Han, *Polymer*, 2017, **115**, 45-51.
73. A. Rothen, *Review of Scientific Instruments*, 1945, **16**, 26-30.
74. M. Conroy and J. Armstrong, *Journal of Physics: Conference Series*, 2005, **13**, 458-465.
75. K. C. A. Smith and C. W. Oatley, *British Journal of Applied Physics*, 1955, **6**, 391-399.
76. W. H. Bragg and W. L. Bragg, *Proceedings of the Royal Society of London. Series A, Containing Papers of a Mathematical and Physical Character*, 1913, **88**, 428-438.
77. O. Frank, M. Zukalova, B. Laskova, J. Kürti, J. Koltai and L. Kavan, *Physical Chemistry Chemical Physics*, 2012, **14**, 14567-14572.
78. F. M. Smits, *The Bell System Technical Journal*, 1958, **37**, 711-718.
79. X. Liu, T.-J. Tarn, F. Huang and J. Fan, *Particuology*, 2015, **19**, 1-13.
80. X.-D. Sun, K.-A. Wang, Y. Yoo, W. G. Wallace-Freedman, C. Gao, X.-D. Xiang and P. G. Schultz, *Advanced Materials*, 1997, **9**, 1046-1049.
81. K. Lawrie, A. Mills and D. Hazafy, *Sensors and Actuators B-Chemical*, 2013, **176**, 1154-1159.
82. M. Cerna, M. Vesely, P. Dzik, C. Guillard, E. Puzenat and M. Lepicova, *Applied Catalysis B-Environmental*, 2013, **138**, 84-94.
83. K. K. Manga, S. Wang, M. Jaiswal, Q. L. Bao and K. P. Loh, *Advanced Materials*, 2010, **22**, 5265-5270.
84. M. Yang, L. H. Li, S. Q. Zhang, G. Y. Li and H. J. Zhao, *Sensors and Actuators B-Chemical*, 2010, **147**, 622-628.
85. M. Cerna, M. Vesely and P. Dzik, *Catalysis Today*, 2011, **161**, 97-104.
86. I. Fasaki, K. Siamos, I. Arabatzis, M. Arin, P. Lommens, I. Van Driessche, S. C. Hopkins and B. A. Glowacki, *Applied Catalysis A: General*, 2012, **411-412**, 60-69.
87. Y. Oh, J. Kim, H. G. Yoon, S. N. Lee and H. K. Kim, *Journal of the Electrochemical Society*, 2012, **159**, B34-B38.
88. R. Cherrington, D. J. Hughes, S. Senthilarasu and V. Goodship, *Energy Technology*, 2015, **3**, 866-870.
89. M. Králová, P. Dzik, V. Kašpárek, M. Veselý and J. Cihlář, *Molecules*, 2015, **20**, 16582.
90. Y. Kunugi, Y. Kato, H. Uematsu and Y. Shimoyama, *Journal of Photopolymer Science and Technology*, 2015, **28**, 403-406.
91. I. Bernacka-Wojcik, P. J. Wojcik, H. Aguas, E. Fortunato and R. Martins, *Journal of Colloid And Interface Science*, 2016, **465**, 208-214.

92. N. S. Shabanov, A. S. Asvarov, A. Chiolerio, K. S. Rabadanov, A. B. Isaev, F. F. Orudzhev and S. S. Makhmudov, *Journal of Colloid and Interface Science*, 2017, **498**, 306-312.
93. H. Tomáš, S. Masoud, D. Petr, K. Richard, Ď. Zuzana, V. Michal and Č. Mirko, *Flexible and Printed Electronics*, 2017, **2**, 035010.
94. M. Cesarini, F. Vasile and D. Natali, *Semiconductor Science and Technology*, 2019, **34**, 024005.
95. I. M. Hossain, D. Hudry, F. Mathies, T. Abzieher, S. Moghadamzadeh, D. Rueda-Delgado, F. Schackmar, M. Bruns, R. Andriessen, T. Aernouts, F. Di Giacomo, U. Lemmer, B. S. Richards, U. W. Paetzold and A. Hadipour, *ACS Applied Energy Materials*, 2019, **2**, 47-58.
96. A. J. Huckaba, Y. Lee, R. Xia, S. Paek, V. C. Bassetto, E. Oveisi, A. Lesch, S. Kinge, P. J. Dyson, H. Girault and M. K. Nazeeruddin, *Energy Technology*, 2019, **7**, 317-324.

Chapter 3

Experimental Procedures

3.1 Chemical Details and Preparation

Purified propan-2-ol (^{i}PrOH) was obtained from an MBraun MB-SPS 5-Solvent Purification System and stored over 3 Å "Molsiv" Molecular sieves (Type 3A, 1/16th inch pellets) in a clean, oven dried Schlenk flask (500 cm^3). Karl Fisher titration using a C30 Coulometric KF Titrator gave the H_2O content as 99.9 ppm (~0.01 %). Ethanol (double rectified absolute alcohol, ≥ 99.9 %) was obtained from Brenntag and stored over 3 Å "Molsiv" Molecular sieves (Type 3A, 1/16th inch pellets) in a clean, oven dried Schlenk flask (100 cm^3). Distilled H_2O was obtained from a Fistreem Cyclon Ultrapure Water Still and used without further purification.

The following chemicals were purchased from Sigma-Aldrich and used without further purification: titanium(IV) isopropoxide [TTIP] (≥ 97.0 %), tetraethylene glycol dimethyl ether (≥ 99 %), diethylene glycol dimethyl ether (Reagent Plus®, 99 %), 1,2-dimethoxyethane (anhydrous, 99.5 %, inhibitor-free), titanium(IV) oxide (anatase nanopowder, <25 nm particle size, 99.7 % trace metals basis), titanium(IV) ethoxide (≥ 97.0 %), niobium(V) ethoxide (99.5 % trace metals basis), 2-isopropoxyethanol (99 %), tetrahydrofuran (anhydrous, ≥ 99.9 %, inhibitor-free), toluene (anhydrous, 99.8 %), and 1-Butanol (≥ 99 %).

Acetonitrile (HPLC Gradient grade), hydrochloric acid (analytical reagent grade, 37 %), and glacial acetic acid (99.5 %) were purchased from Fisher Scientific and used without further purification.

Triethylene glycol dimethyl ether (99 %, extra pure, stabilised) was purchased from Acros Organics and used without further purification.

Niobium doped titanium inks were supplied by EpiValence and used without further purification.

3.2 Ink Preparation

3.2.1 Glassware

All inks were prepared using standard Schlenk techniques, under an inert N_2 atmosphere. Prior to use the glassware was immersed into KOH solution (1.1 M, in ^{i}PrOH) for 15 minutes, rinsed with H_2O, immersed into HCl solution (6.0 M, in H_2O) for 15 minutes, rinsed with H_2O and stored in an oven set to 150°C. The Schlenk flask, tap, and stopper were removed from the oven before use and assembled using Dow Corning high vacuum grease on all ground glass joints. Three purge cycles of vacuum evacuation and N_2 filling were performed, after which the stopper was replaced with a septum under positive N_2 pressure.

3.2.2 Ink Formulation

To a clean, oven dried Schlenk flask (100 cm^3) was added dry ^{i}PrOH, glycol ether, then TTIP, via syringes purged in triplicate with N_2. The resulting solution was stirred for 5 minutes to ensure homogeneity. All inks were prepared to a total volume of 40 mL. An example ink formulation for the 0.15 M TTIP ink stabilised with 10 molar equivalents of DME, discussed in 4.3.2, is given below.

A clean, oven dried Schlenk flask (100 cm^3) containing a magnetic stirrer bar was charged with dry ^{i}PrOH (32.0 mL) and 1,2-dimethoxyethane (DME) (6.24 mL, 0.06 mol). To the resulting solution was then added TTIP (1.76 mL, 0.006 mol) under constant stirring. After 5 minutes of stirring, the clear and colourless ink solution was ready for analysis and printing.

3.2.3 Density Measurement

Volumetric flasks (25.0 cm^3) were calibrated by weighing the flasks before and after making up to the mark with distilled H_2O (25 mL) in a temperature-controlled laboratory set to 20°C. Using a value of 0.9982 g cm^{-3} for the density of H_2O at 20°C, the calibrated volume of each flask was then calculated. To measure ink density a clean, previously calibrated volumetric flask (25.0 cm^3) was weighed on an analytical balance at 20°C. To this flask was added ink solution (25 mL) and made up to the volumetric mark. The flask was then stoppered and immediately re-weighed on the analytical balance. Density was obtained by calculating the difference between the two masses and dividing by the calibrated flask volume. The process was performed in triplicate, and an average value calculated for ink density, along with a percentage spread.

3.2.4 Surface Tension Measurement

Surface tension was measured using the capillary rise method with a DWK Life Sciences (Kimble) 14818 Tensiometer, Capillary Surface Tension Apparatus (See Figure 3.2.4.1). The surface tension was obtained immediately after the density measurements, using the same sample of ink. Positive pressure was applied to the vessel with a 3-way valve pipette filler, causing the ink to rise to the top of the capillary. After the ink had returned to its rest position, the height of the ink was measured both inside and outside of the capillary. Negative pressure was then applied using the pipette filler, causing the ink to evacuate the capillary. Once the negative pressure was removed, the ink returned to its rest position and the height of the ink was again measured both inside and outside of the capillary. The above process was then repeated with both positive and negative pressures, to give a total of four different pairs of measurements.

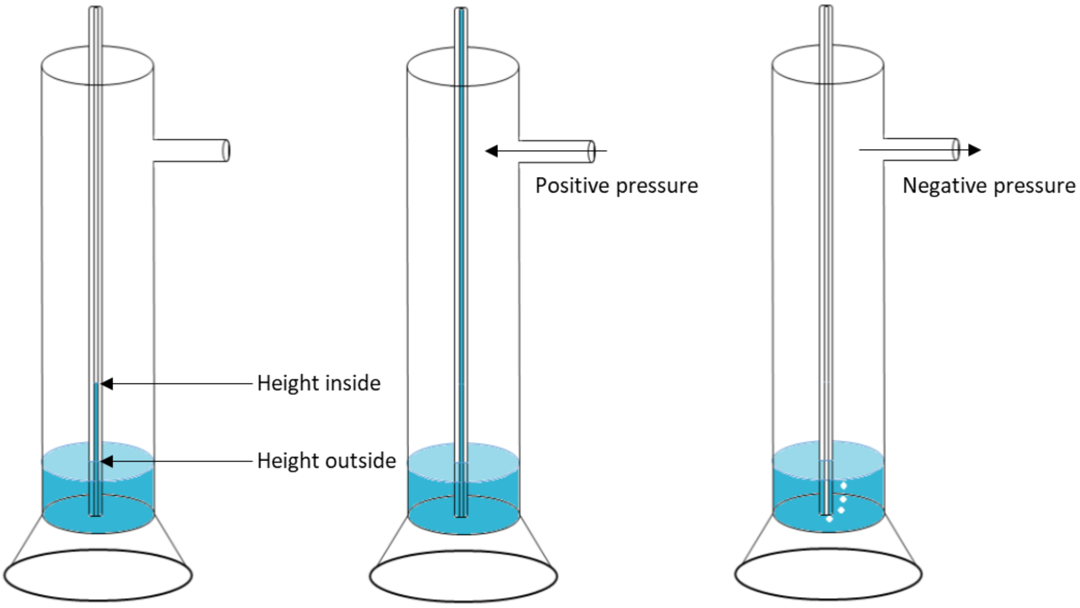

Figure 3.2.4.1 A diagram to show the surface tension apparatus

Data was processed by subtracting the height of the ink outside of the capillary from the height of the ink inside of the capillary, giving the capillary rise as a value with centimetre units. Surface tension was then calculated using equation (3.2.4.1), where γ is surface tension in dyne cm^{-1}, Δh is the capillary rise in cm, r is the capillary radius of 0.025 cm, δ is the ink density in cm^{-3} at 20°C, and g is the acceleration due to gravity of 980.7 cm s^{-2}. After calculating the four surface tension values for each pair of measurements, an average value and percentage spread were calculated.

$$\gamma = \frac{1}{2}\, \Delta h \; r \; \delta \; g \tag{3.2.4.1}$$

3.2.5 Viscosity measurement

A Rheosense *micro*VISC viscometer was used to measure ink viscosity in a temperature-controlled laboratory set to 20°C. ^{i}PrOH was first loaded into the viscometer and flushed through the system, using the 400 µL µVISC portable viscometer pipettors supplied with the viscometer. For inks that consisted of a bulk carrier other than ^{i}PrOH, the viscometer was then flushed with the bulk carrier of the ink to be analysed. Ink solution (400 µL) was then loaded into the viscometer and analysed. Three measurements were obtained, with an average value and percentage spread calculated. After analysing all of the samples, ^{i}PrOH was loaded into the viscometer and flushed through the system to ensure no ink remained.

3.3 Inkjet Printing

3.3.1 Printer Cleaning and Preparation

Printing was performed using a MicroFab JetLAB 4 Tabletop Printing Platform, fitted with a MicroFab MJ-ATP-01-080 drop-on-demand single jet dispensing device with an 80 µm orifice diameter. Quoted requirements for this dispensing device are a viscosity of < 20 mPa s and a surface tension range of 20 -70 mN m^{-1}. Cleaning of the dispensing device was performed before, after, and as necessary during the printing process. To clean the dispensing device, a Luer lock syringe was fitted and the glass tip immersed in Cole-Parmer Micro-90 cleaning solution (5 % in H_2O) which was heated to 70°C. The cleaning solution (~2 mL) was drawn through the device, after which the device was removed and the solution ejected from the syringe to ensure any dislodged material wasn't passed back into the dispensing device. The above process was performed a further two times. After the third cycle, fresh cleaning solution (~2 mL) was drawn into the syringe before reattaching the dispensing device. The device was then attached and the cleaning solution from the syringe forced to pass through the device. A uniform jet of cleaning solution being ejected from the dispensing device indicated a successful cleaning process. In the cases where the above cleaning process using Micro-90 solution did not unblock the dispensing device, the glass tip was immersed in H_2O and sonicated for 5 minutes using a VWR USC 300 TH Ultrasonic Cleaner at full power. After sonication, the Micro-90 cleaning solution process described above was then repeated in its entirety.

Prior to printing, ^{i}PrOH was passed through the tubing from the ink reservoir and into the dispensing device under positive overpressure. The cleanliness of the dispensing device was then confirmed by the presence of a stable stream of ^{i}PrOH. If the stream of ^{i}PrOH showed any instability, the dispensing device was cleaned again. For inks consisting of a carrier other than ^{i}PrOH, the same process of passing the carrier through the tubing was then repeated with the ink carrier to ensure no residual ^{i}PrOH remained within the printing system.

3.3.2 Waveform Generation

To jet a steady stream of uniform droplets, a suitable waveform must be generated within the JetLAB software. The waveform dictates the pattern of electrical impulses sent to the piezoelectric element within the dispensing device, causing a perturbation at the ink meniscus. A suitable waveform results in generating a perturbation of sufficient magnitude to eject a single droplet, without ejecting satellite droplets or ligaments, and allowing the meniscus to return to a stable state before the next piezoelectric pressure pulse.

Table 3.3.2.1 Example Waveform

Parameter	**Value**
Rise Time 1 (μs)	a
Dwell Time (μs)	b
Fall Time (μs)	a
Echo Time (μs)	2b
Rise Time 2 (μs)	a
Idle Voltage (V)	0
Dwell Voltage (V)	x
Echo Voltage (V)	-x

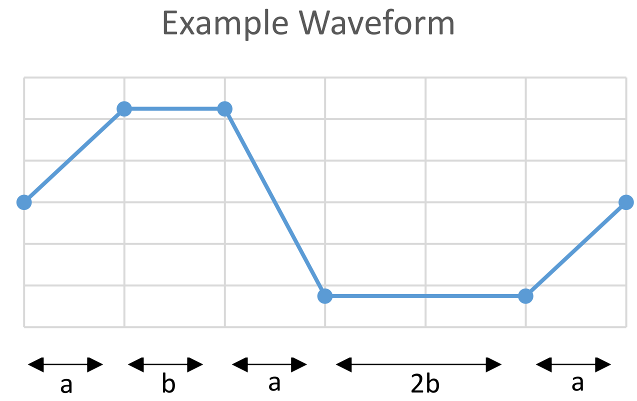

Figure 3.3.2.1 A graph to show the example waveform pattern

When investigating the ideal waveform parameters, it was advised to set rise time 1, fall time and rise time 2 to the same values as each other. Echo time was always set to double the value of dwell time. Idle voltage was always set to 0 V. Dwell voltage was set to a positive value, with the echo voltage always being set to be of equal magnitude but negative to dwell voltage. Table 3.3.2.1 shows the advised form for an example waveform. Figure 3.3.2.1 shows a graphical representation of the example waveform. A waveform was first generated for the neat carrier solvent before attempting to optimise for a given ink. When generating and optimising waveforms, parameters were changed incrementally and the effect on the meniscus perturbation or ejected droplet was noted as either beneficial or detrimental to the overall jetting performance. A waveform was considered optimised when adjusting any parameter lead to a detrimental effect on the jetted stream of droplets. Waveforms were optimised using a strobe delay set to 200 μs and a jetting frequency of 500 Hz.

3.3.3 Droplet Size Analysis

After optimisation of the jetting waveform, 50 consecutive images were captured of the ejected ink droplets with a strobe delay set to 200 µs and a jetting frequency of 500 Hz. The droplet images were then analysed in the ImageJ software package by importing them as an image sequence. A clean, new dispensing device with an 80 µm diameter orifice was used to calibrate the scale, with 80 µm equal to 14 pixels. To increase the contrast between the droplet and the rest of the image, the threshold was adjusted and the colour converted from greyscale to black and white. The droplet perimeter was calculated using the 'analyse particle' function within the ImageJ software. Droplet diameter was then calculated by assuming a perfect spherical shape and dividing the perimeter by pi.

Statistical analyses were performed on the calculated droplet diameters using the Minitab 18 software. After entering the droplet diameters, an average and moving range was generated using an individuals moving range analysis.

3.3.4 Glass Substrate Preparation

Unless stated otherwise, all printing was performed with a 30°C stage temperature onto cleaned glass slides (Thermo Scientific, Menzel-Gläser, 76 x 26 mm, 1.0 – 1.2 mm thickness). The glass slides were manually cleaned in warm soapy water, rinsed with absolute EtOH, individually mounted into a slide box, and left to dry under ambient conditions.

3.3.5 Track Optimisation

Jetting a continuous stream of uniform droplets is not the end of the optimisation process for inkjet printing. Further parameters must be identified and optimised to obtain a satisfactory print. One such parameter is the speed of the dispensing device relative to the substrate, also called print speed. Another parameter is droplet spacing, or step width, which is the distance in millimetres between droplets while printing and is equivalent to the distance between the centres of two pixels in a printed image. Optimisation of the print speed and step width is a complex process as each parameter can have a dramatic effect on the printed tracks. The identity of the substrate and substrate temperature also affects the optimum conditions, necessitating a track optimisation process for every combination of ink, substrate, and temperature.

For a controlled substrate and temperature, the optimisation process involved screening several parameter combinations of print speed and step width using pre-written scripts within the printing software. Print speeds of 6, 8, 10, and 12 mm s^{-1} were investigated. Four tracks were printed at each speed, with step widths of 0.05, 0.1, 0.15, and 0.2 mm, leading to a total of 16 individual tracks. The 16 tracks were then observed under an optical microscope, and the optimum print parameters were determined by the printed track with the neatest edges, and the straightest continuous line. The step size parameter dictated the scale factor required to scale the print from the digital information to the final produced print, as each pixel is a binary command whether to eject a droplet onto the substrate or not.

3.3.6 Printing of Samples

Printing of samples was performed by running custom written scripts. There were two different types of scripts written for printing the samples within this project; a script commanding the printing of a square array, or a script commanding the printing of a monochrome bitmap image. Both types of script specify the print speed and step size to be utilised. The second type of script requires a monochrome bitmap image, with the individual pixels corresponding to square grid co-ordinates spaced by the defined step size. Each white pixel gives the command to eject a droplet. Black pixels command the system to move over their resulting grid co-ordinate without jetting, or to finish printing along that row if there are no further white pixels along the row.

For an example square array print with a step width of 0.1 mm, executing the command to print a 100 by 100 square array translates into printing a square sample of 10 mm by 10 mm dimensions, or 1 cm^2. Executing the command once yields a single printed pass. If the substrate is not moved, subsequent executions will print additional layers which build upon the previous deposit. However, it was important to ensure the ink was still being jetted from the dispensing device and no partial or full blockages had occurred between consecutive printed passes. As such, the dispensing device was returned to the maintenance position and ensured to be jetting a uniform stream of ink droplets between each printed pass. The manual confirmation of jetting also provides sufficient time to ensure any subsequent print passes were performed on a dry surface; this is known as wet-to-dry printing. If subsequent print passes were performed immediately after one another, there may not have been enough time for all of the ink volatiles to evaporate; this could lead to wet-to-wet printing. Wet-to-wet printing suffers from several drawbacks, including reduced print resolution, bleeding, and inhomogeneous material deposition.

3.4 Characterisation of Printed Films

3.4.1 Optical Micrographs

A Leitz Instruments metalloplan metallurgical microscope, fitted with a Nikon CF Plan 2.5x objective lens and bright-field reflection illumination was used to view the printed samples. Images were captured by means of an Infinity 2-3C CCD digital camera (3 MB, frame size 2080 pixels x 1536 pixels) using Infinity Capture (version 6.5.6) software.

3.4.2 Theoretical Film Thickness Calculations

Theoretical film thickness for the printed square array samples were calculated using the measured ink droplet diameter, formulated ink concentration, number of droplets, area covered, and standard densities of MO_x. The calculation assumes all droplets are uniform and spherical, ink concentration is homogeneous, all droplets are successfully jetted, a perfect 1 cm^2 is printed, complete conversion of $M(OR)_x$ to MO_x uniform density of MO_x, and complete evaporation of all organics. The calculation for theoretical film thickness (*T*, in µm per pass) is shown in equation (3.4.2.1), where *d* is the droplet diameter in µm, $[M(OR)_x]$ is the ink's metal alkoxide concentration in mol dm^{-3}, *a* and *b* are the length and width of the array (equating to the total number of printed droplets), Mr_{MOx} is the molar mass of the metal oxide in g mol^{-1}, ρ is the density of the metal oxide in g cm^{-3}, and *A* is the printed area in cm^2.

$$T = \frac{\left\{\frac{4}{3}.\pi.\left(\frac{d}{2}\right)^3\right\} x10^{-15}.[M(OR)_x].a.b.Mr_{MO_x}}{\rho.A} x10^4 \qquad (3.4.2.1)$$

The $\frac{4}{3}.\pi.\left(\frac{d}{2}\right)^3$ term converts the droplet diameter into a droplet volume, with the $x10^{-15}$ converting the units from $µm^3$ to dm^3. Multiplication of the droplet volume by the molar concentration of the metal alkoxide gave the number of moles per droplet, with $a.b$ giving the total number of droplets per print command. Using the molar mass of the corresponding metal oxide, the total mass of deposited metal was calculated. Dividing the total mass by the previously multiplied metal oxide density and area of the print gives the theoretical film thickness in units of cm^3. A final multiplication by $1x10^4$ converts the units into µm. A percentage spread was also calculated, using the average droplet diameter ± the moving range.

3.4.3 Profilometry

2-dimensional profiles of the printed samples were obtained using an Ambios XP-Plus 200 Advanced Stylus Profiling System, with the following settings; 10 µm range, step up/down profile, 0.10 mm s^{-1} speed, 12 mm sample length, forward direction, 16-point average, and 2 mg force. Prior to use, the profilometer was calibrated using a reference sample with a known step height of 10857 Å. Four total measurements were taken for each sample, two in parallel with the direction of printing and two perpendicular to them. Figure 3.4.3.1 shows the four different measurements with left and right being perpendicular to the printed tracks, and the bottom and top measurements being parallel to the printed tracks.

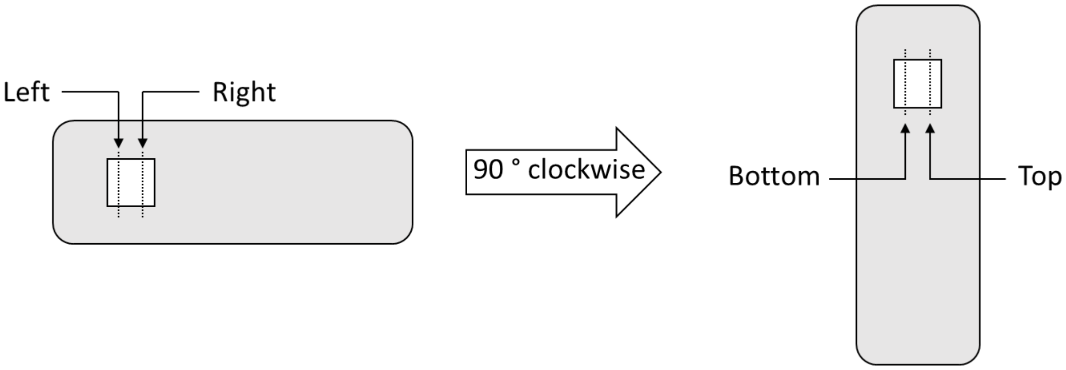

Figure 3.4.3.1 Schematic showing the four different profilometry measurements performed for each sample

3.4.4 Drop-tested Sample Generation

For analytical techniques where the inkjet printed samples were insufficient, thicker drop-tested samples were generated. Ink solution (20 µL) was pipetted onto a cleaned glass slide heated to 30°C. The sample was left to evaporate for 5 minutes.

3.4.5 Annealing Process

Annealing was performed using a Carbolite MTF 12/38/250 horizontal tube furnace. Unless stated otherwise, the furnace was pre-heated to the desired annealing temperature. Samples were loaded into the centre of the tube to ensure they were exposed to an accurately measured annealing temperature. After the samples had been annealed for the desired length of time, they were immediately removed from the furnace and allowed to cool to room temperature under ambient conditions.

3.4.6 Raman Spectroscopy

Raman spectra were obtained using a Renishaw inVia Reflex Qontor Confocal Raman Microscope with a 532 nm laser, 2400 l mm^{-1} grating, Renishaw Centrus 5134M5 detector, set to a single acquisition at a laser power of 1 % and an exposure time of 10.0 seconds. Baseline correction of the obtained spectra was performed within the software.

3.4.7 X-Ray Diffraction

A Rigaku Miniflex fitted with a Cu Kα emission source was used to carry out XRD measurements. Results were obtained within the 2θ range of 20 – 70°, with a sampling of 0.01° and a scan speed of 0.05. Where necessary, baseline corrections were performed in Origin 2016 software.

3.4.8 Scanning Electron Microscopy

Samples were prepared for SEM analysis by securing them onto a stub with carbon tape. A Cr coating was necessary as the samples were not conductive enough and would charge and distort the image. 60 seconds of Cr sputtering was performed using Quorum Q150T ES sputter coater, resulting in a coating of ~15 nm Cr. The samples were then imaged using a JEOL JSM 7001F FEGSEM, fitted with an in-lens Schottky field emissions source, and an Oxford Instruments INCA X-act EDX detector.

3.4.9 Transmission Electron Microscopy

Transmission electron microscopy (TEM) was performed on a JEM ARM200F, fitted with a Cs Image corrector and an Orius SC200 camera. Samples of ink were drop-tested onto ultra-smooth carbon foil (5.0 nm, S116-3, Agar Scientific) with a lacey carbon film Cu mesh 200 J50-10 TEM grid. We are grateful to Dr. Leonardo Lari from the University of York and Dr. K. Yoshida for performing the TEM measurements at the Oarai JAEA-Tohoku site.

3.4.10 4-point Probe Sheet Resistance

Sheet resistance was measured using a CMT-SR2000N Automatic Mapping Four Point Probe. The printed samples were placed under the probe and 4 measurements were taken.

3.4.11 Elemental CHN Analysis

Elemental composition for carbon, hydrogen and nitrogen content were obtained with a Thermo Flash EA 112 Series instrument.

3.4.12 Wettability of Printed Films

A Kruss DSA 100 was used to measure the contact angles of H_2O on 5 pass printed 1 cm^2 samples. All samples were measured at a laboratory temperature of 23.0°C, using the sessile drop method. Prior to any contact angle measurements, the dispensing needle width was measured using a Vernier calliper and used to calibrate the image scale. A dispensing volume of 0.5 mL was used. The ellipse ($tangent^{-1}$) method was used for the contact angle calculations within the Kruss Advanced software. A droplet was then ejected onto a corner of the substrate and the measured contact angle recorded. This process was repeated for each of the four corners for a total of four measurements. A mean and standard deviation was calculated for the four measurements.

3.4.13 Transmittance Spectroscopy

Transmittance spectra were obtained using a Shimadzu Solidspec-3700 spectrophotometer between wavenumbers of 250 and 900 cm^{1}.

Chapter 4

Solution-based TTIP Ink Optimisation

4.1 Introduction

This work began by building upon the experience and results obtained previously within the group, both practically and philosophically. The rationale behind this project involves taking experience from metal oxide deposition within the metal organic chemical vapor deposition (MOCVD) and ALD techniques, specifically the reactive precursors, and applying it to the additive manufacturing deposition method of inkjet printing. Titanium dioxide (TiO_2) is used as the target metal oxide for the demonstrative use of reactive alkoxide precursor ink formulations. TiO_2 is the ideal candidate demonstrator as it has several industrially important uses, is extremely well characterised and documented within the literature, and is environmentally and physiologically benign.[1-5] Titanium (IV) tetraisopropoxide ($Ti(O^iPr)_4$, TTIP) was the primary alkoxide investigated due to its intermediate reactivity,[6, 7] low cost and commercial availability.

Before discussing my contribution to this project, the foundational work performed by a previous member of the group is presented in section 4.1.1. Section 4.1.2 covers the preparatory work that was undertaken prior to result acquisition, such as the physicochemical characterisation of the constituent chemical compounds within the ink formulations. Different glycol ethers are used as stabilising agents for TTIP inks in section 4.2. The resulting prints are compared and assessed, with the most suitable glycol ether being identified for future ink formulations. Further optimisation of the ink formulation is investigated in section 4.3. After identifying a suitable ink formulation, section 4.4 presents the phase analysis before and after annealing the samples, along with the characterisation of the printed films. Section 4.5 concludes the chapter by summarising the results and discussing their implications, particularly with respect to the future chapters.

4.1.1 Previous Work

Previous work within the group showed that an ink formulation consisting of 0.1 M TTIP in propan-2-ol (^iPrOH) could be drop-tested to yield an amorphous film of TiO_2, which could be annealed at 450°C to yield small anatase peaks within the XRD spectrum. However, it was established that attempting to print this ink formulation would result in partial hydrolysis of the ink both before and during the printing process. Formation of TiO_2 prior to droplet ejection and evaporation lead to consistent blocking of the dispensing device orifice. Furthermore, it was established that the H_2O content of off the shelf ^iPrOH was innately too high, so the solvent would first need to be dried.

To further inhibit hydrolysis of the TTIP and subsequent formation of solid TiO_2, the use of a low molecular weight additive that could stabilise the TTIP to hydrolysis was investigated. Glycol ethers had seen a similar use as a stabiliser in previous precursor work conducted by the group. A short study was conducted using an ink that consisted of 0.05 M TTIP stabilised with 5 molar equivalents (with respect to TTIP) of tetraglyme and a carrier solvent of ^iPrOH. Jetting of the ink could be achieved when the ink was stabilised with tetraglyme. Triglyme containing inks were also formulated, but were never loaded into the inkjet printer.

4.1.2 Preparatory Work

My contribution to this work began by further investigating the use of glycol ethers as stabilisers to TTIP ink formulations. A total of four glycol ethers were considered: tetraglyme, triglyme, diglyme, and 1,2-dimethoxyethane (DME). The structures of the glycol ethers are presented in Figure 4.1.2.1. Prior to formulating and printing any inks, ^iPrOH was dried over 3 Å molecular sieves using standard Schlenk techniques. After drying, the rheological properties of density, surface tension, and viscosity were obtained experimentally, along with the other chemicals to be used within the ink formulations (See Table 4.1.2.1).

The values of both viscosity and density for ^iPrOH were comparable to those found in literature, with Ku et al. reporting values of 2.4143 mPa s for viscosity (a 4.54 % difference) and 0.7853 g cm^{-3} for density (a 0.22 % difference).[8] Surface tension of ^iPrOH was found to have a 12.82 % difference to that reported by Vasquez et al.[9] The rheological properties of DME were also found to have good agreement to the literature values, with Zheng et al. reporting a viscosity of 0.4341 mPa s (a 2.45 % difference) and a density of 0.8665 g cm^{-3} (a 0.41 % difference).[10] Conesa et al. report on the density and kinematic viscosity of DME, diglyme, triglyme, and tetraglyme.[11] Good agreement was found with all densities, with the largest difference being 0.54 % for DME. As kinematic viscosity was measured by Conesa et al. to compare their data to the dynamic viscosity data in Table 4.1.2.1 their kinematic viscosity was multiplied by their reported densities to yield dynamic viscosities. Here, the largest difference was found to be 8.34 % for the viscosity of triglyme. Density and surface tension were not determined experimentally for TTIP due to its sensitivity to moisture, which it would be exposed to when using either apparatus.

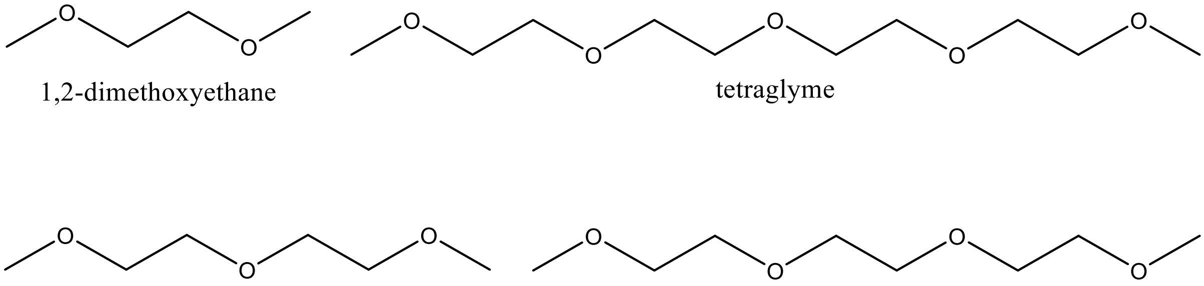

1,2-dimethoxyethane

tetraglyme

diglyme

triglyme

Figure 4.1.2.1 Structures of 1,2-dimethoxyethane (DME), diglyme, triglyme, and tetraglyme

Table 4.1.2.1 Rheological properties of ink components at 20°C

Chemical	**Viscosity mPa s**	**Density g cm^{-3}**	**Surface Tension mN m^{-1}**	**Chemical Formula**
^{i}PrOH	2.529	0.7870	19.27	$CH_3CHOHCH_3$
Tetraglyme	3.998	1.0073	32.16	$CH_3[OCH_2CH_2]_4OCH_3$
Triglyme	2.354	0.9864	30.22	$CH_3[OCH_2CH_2]_3OCH_3$
Diglyme	1.045	0.9435	27.57	$CH_3[OCH_2CH_2]_2OCH_3$
DME	0.445	0.8630	23.41	$CH_3OCH_2CH_2OCH_3$
TTIP	3.469	-	-	$Ti[OCH(CH_3)_2]_4$

Table 4.1.2.2 ^{i}PrOH Waveform

Parameter	**Value**
Rise Time 1 (µs)	20
Dwell Time (µs)	20
Fall Time (µs)	20
Echo Time (µs)	40
Rise Time 2 (µs)	20
Idle Voltage (V)	0
Dwell Voltage (V)	45
Echo Voltage (V)	-45

A sample of dry ^{i}PrOH was transferred to an inkjet printer vial and loaded onto the printer. After flushing the line through with ^{i}PrOH, a waveform was created which generated a steady stream of uniform droplets (See Table 4.1.2.2). To analyse this, 50 images were captured of the generated droplets with a strobe delay of 200 ms. For each image, the droplet diameter was calculated. Statistical analysis of the droplet diameters was used to yield an average droplet diameter of 64.96 µm and a moving range of 1.60 µm.

4.2 0.05 M TTIP Inks

The work contained within this section aims to determine the identity and molar equivalents of glycol ether stabiliser most suitable for use in TTIP ink formulations. To do this, a total of eight inks were formulated. Every ink consisted of a 0.05 M final concentration of TTIP, in a solvent carrier of ^{i}PrOH. Each ink was stabilised by one of the four glycol ethers: tetraglyme, triglyme, diglyme, and DME. Although the previous work utilised 5 molar equivalents of glycol ether stabiliser, 2.5 molar equivalents were also examined. If less stabiliser was also found to be effective at inhibiting hydrolysis of the TTIP, there would be fewer organic impurities present within the printed film and the elemental purity of the prints would improve. Table 4.2.0.1 shows the rheological properties measured for each of these ink formulations, along with their designated name with which they will be referred. Table 4.2.0.2 summarises the printed properties of each ink.

Table 4.2.0.1 Rheological properties of 0.05 M inks at 20°C

Ink Composition	**Ink Designation**	**Viscosity mPa s**	**Density g cm^{-3}**	**Surface Tension mN m^{-1}**
^{i}PrOH	^{i}PrOH	2.529	0.7870	19.27
0.05 M TTIP, 2.5 eq tetraglyme	4.2.1.a	2.972	0.7902	20.34
0.05 M TTIP, 5 eq tetraglyme	4.2.1.b	2.916	0.7952	20.47
0.05 M TTIP, 2.5 eq triglyme	4.2.2.a	2.941	0.7870	20.74
0.05 M TTIP, 5 eq triglyme	4.2.2.b	2.968	0.7930	20.41
0.05 M TTIP, 2.5 eq diglyme	4.2.3.a	3.077	0.7870	20.26
0.05 M TTIP, 5 eq diglyme	4.2.3.b	2.979	0.7883	20.29
0.05 M TTIP, 2.5 eq DME	4.2.4.a	3.073	0.7844	20.19
0.05 M TTIP, 5 eq DME	4.2.4.b	2.893	0.7859	20.23

Table 4.2.0.2 Printed properties of 0.05 M inks

Ink Designation	Average Droplet Diameter ± Moving Range µm	Print Speed mm s^{-1}	Step Size mm	Average Track Width µm
^{i}PrOH	65.0 ± 1.6	-	-	-
4.2.1.a	70.1 ± 2.7	6	0.1	64.3
4.2.1.b	72.5 ± 2.4	10	0.1	125.8
4.2.2.a	69.3 ± 2.2	10	0.1	394.3
4.2.2.b	74.2 ± 2.9	10	0.1	324.4
4.2.3.a	74.9 ± 2.1	6	0.1	298.8
4.2.3.b	69.2 ± 4.0	6	0.1	238.3
4.2.4.a	65.0 ± 2.2	10	0.1	320.6
4.2.4.b	63.2 ± 2.0	10	0.1	247.8

4.2.1 Tetraglyme Stabilised Inks

Tetraglyme was the first glycol ether stabiliser to be investigated. Inks were prepared to a final concentration of 0.05 M with respect to TTIP, one containing 2.5 molar equivalents and one with 5 molar equivalents of tetraglyme. Rheological properties of both inks and pure tetraglyme were obtained experimentally (See Table 4.2.0.1). The ink containing 2.5 molar equivalents of tetraglyme was then loaded into the printer and jetted using the same waveform as ^{i}PrOH. Good jetting was achieved with this waveform; no modifications were required. Images of 50 droplets were then captured and analysed to yield an average droplet diameter of 70.13 µm and a moving range of 2.68 µm.

Optimum parameters of print speed and step width were then investigated by screening printed tracks at print speeds of 6, 8, 10, and 12 mm s^{-1} and step widths of 0.05, 0.1, 0.15, and 0.2 mm. Figure 4.2.1.1 shows the straightest and most uniform track, with an average width of 64.3 µm, obtained with a print speed of 6 mm s^{-1} and a step width of 0.1 mm. The track is difficult to see, implying that the quantity of the TiO_2 deposit is low.

Figure 4.2.1.1 Printed track using ink 4.2.1.a at 6 mm s^{-1} print speed and 0.1 mm step size on a glass substrate

After identifying optimum print parameters, a square array was printed. With an optimum step size of 0.1 mm, a printed array of 100 by 100 droplets produced a 10 mm by 10 mm square, or 1 cm^2. Figure 4.2.1.2.a shows an optical micrograph of the printed 1 cm^2 using Ink 4.2.1.a. Individual printed tracks can be seen within the print, although the tracks appear to fluctuate in width by bulging in and out. The top and left edge are both relatively neat.

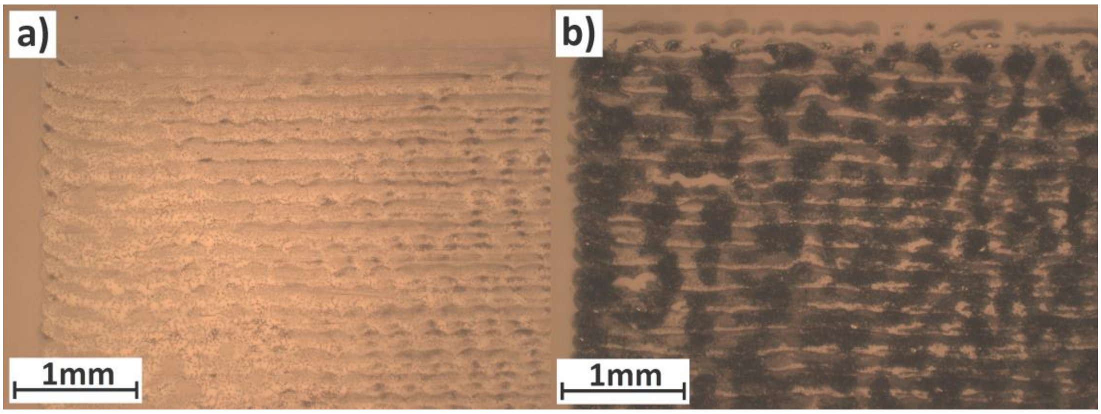

Figure 4.2.1.2 Printed 1 cm^2 using ink 4.2.1.a at optimised print conditions on a glass substrate. Image a) is 1 pass and b) is 5 passes. Image brightness has been increased by 20 % for clarity.

Another 1 cm^2 was printed, this time repeating the print command a total of five times, yielding a printed sample of 5 printed passes. An optical micrograph of the printed 5 pass 1 cm^2 using ink 4.2.1.a is shown in figure 4.2.1.2.b. In comparison with the single pass sample, this print is darker due to the increased quantity of material deposited. Furthermore, the edges are less well defined because of imperfect droplet placements, which could be caused by turbulence or a small partial blockage of the nozzle. Material deposition does not appear to be uniform due to the varying size of dark patches.

The printing process was then repeated using the 0.05 M TTIP ink stabilised with 5 molar equivalents of tetraglyme, ink 4.2.1.b, after thoroughly flushing the printer through with ^iPrOH. Again, good jetting was obtained with the waveform used for pure ^iPrOH with no further optimisation required. 50 droplets were imaged and analysed, resulting in an average droplet diameter of 72.52 µm and a moving range of 2.36 µm. Optimum print parameters were found to be a print speed of 6 mm s^{-1} and a step size of 0.1 mm, yielding a track width of 125.8 µm. The track shown in Figure 4.2.1.3 is easier to distinguish than the track obtained with the previous ink. It contains unusual spots or regions of darker deposit, indicating an inhomogeneous deposit. Figures 4.2.1.4.a and b show the resulting 1 and 5 pass prints of 1 cm^2 obtained when using ink 4.2.1.b. The single pass sample shows the same unusual spots and regions of darker deposit as the printed track, dispersed over what appears to be a thin printed film. However, the 5 pass sample shows very discrete regions of deposit without any thin film-like regions in the general shape of the desired print.

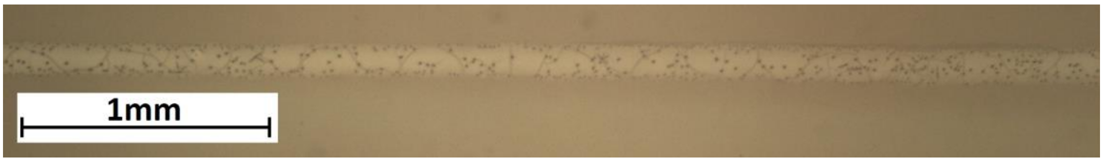

Figure 4.2.1.3 Printed track using ink 4.2.1.b at 6 mm s^{-1} print speed and 0.1 mm step size on a glass substrate

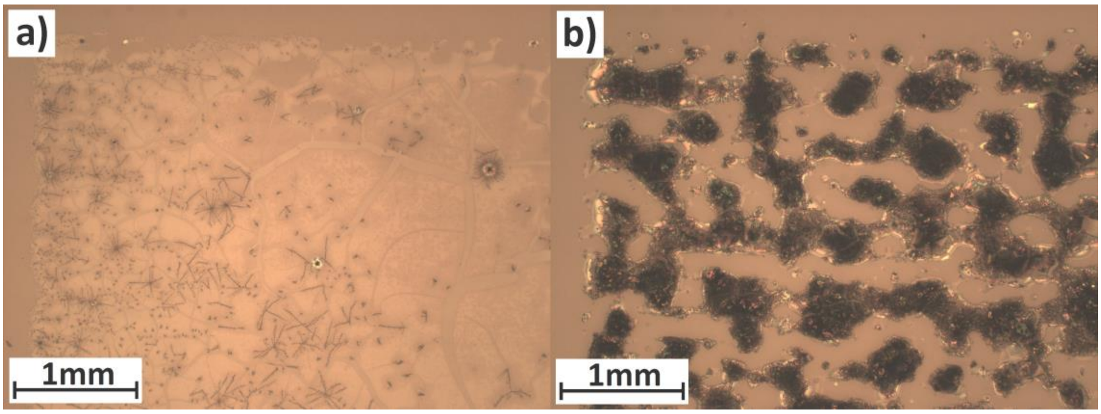

Figure 4.2.1.4 Printed 1 cm^2 using ink 4.2.1.b at optimised print conditions on a glass substrate. Image a) is 1 pass and b) is 5 passes. Image brightness has been increased by 20 % for clarity.

4.2.2 Triglyme Stabilised Inks

Following the successful screening of tetraglyme as a potential stabiliser for a TTIP based ink formulation, triglyme was then investigated. Inks 4.2.2.a and b were then investigated in a similar fashion to the tetraglyme stabilised inks 4.2.1.a and b above, using the ^{i}PrOH waveform. Using ink 4.2.2.a, a printed track was generated using the identified optimum parameters. The boundaries of the track appear as small white particulates, with the internal region of the track appearing almost identical to the rest of the substrate; this implies that there is either a very thin printed film, or that the track consists of two coffee-stain edges. Figures 4.2.2.2.a and b show the resulting 1 and 5 pass prints of 1 cm^2 using ink 4.2.2.a. The single pass sample resembles the single pass obtained when using ink 4.2.1.b; unusual spots and regions of darker deposit, dispersed over what appears to be a thin printed film in the desired shape of the print. The 5 pass print is similar, with a higher prevalence of darker or thicker regions.

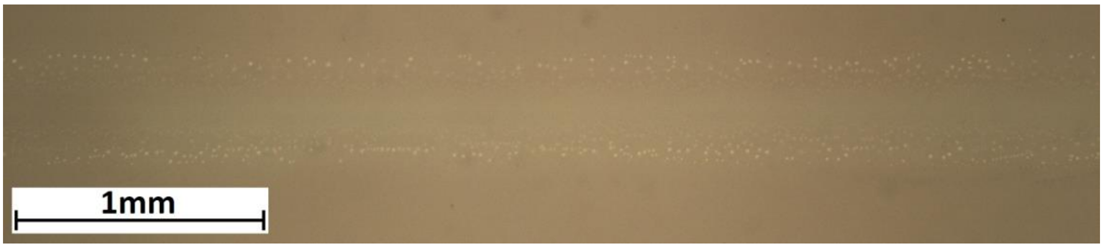

Figure 4.2.2.1 Printed track using ink 4.2.2.a at 10 mm s^{-1} print speed and 0.1 mm step size on a glass substrate

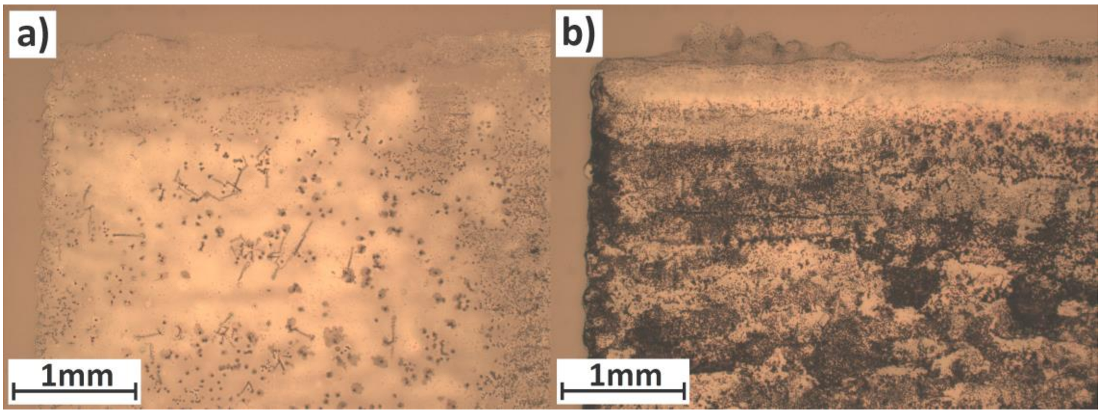

Figure 4.2.2.2 Printed 1 cm^2 using ink 4.2.2.a at optimised print conditions on a glass substrate. Image a) is 1 pass and b) is 5 passes. Image brightness has been increased by 20 % for clarity.

Using ink 4.2.2.b, Figure 4.2.2.3.a shows the straightest, most uniform track. However, it is extremely difficult to make out any of the printed track in the image; this suggests the printed deposit is very thin. Figure 4.2.2.3.b shows the same image with an increased contrast. 1 and 5 pass prints of 1 cm^2 are shown in Figures 4.2.2.4.a and b. Both prints appear to contain grainy solids. The single pass print appears to consist of a thin film of deposited material with regions of thicker and grainy deposit. The 5 pass sample consists entirely of grainy material of variable thickness, with well-defined print edges.

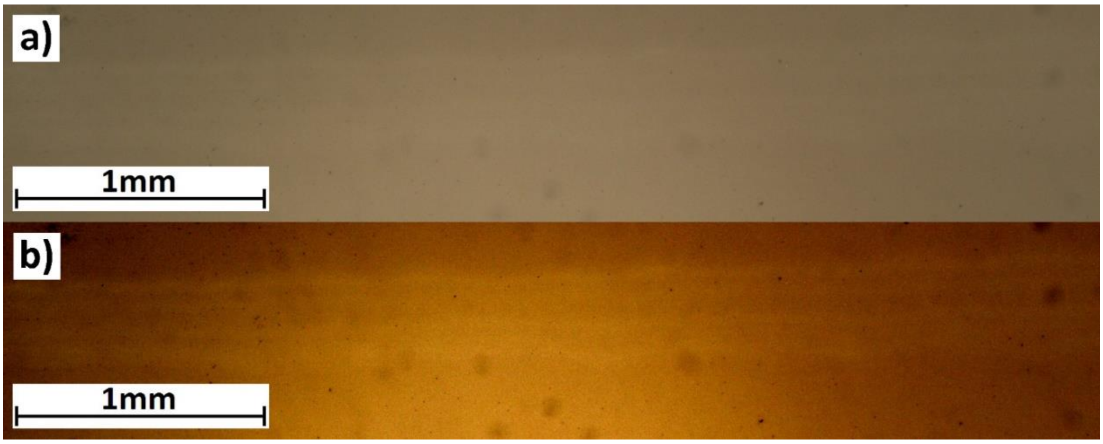

Figure 4.2.2.3 Printed track using ink 4.2.2.b at 10 mm s^{-1} print speed and 0.1 mm step size on a glass substrate. Image a) is the original image and b) is the same image after digital contrast enhancement for visual clarity

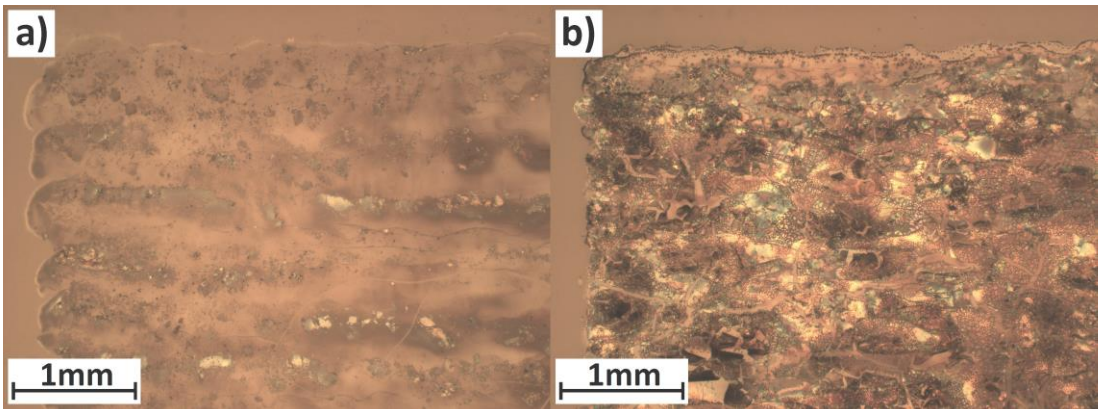

Figure 4.2.2.4 Printed 1 cm² using ink 4.2.2.b at optimised print conditions on a glass substrate. Image a) is 1 pass and b) is 5 passes. Image brightness has been increased by 20 % for clarity.

4.2.3 Diglyme Stabilised Inks

Previous work within the group involved the use of tetraglyme, along with a brief view at triglyme. Whilst both of these glycol ethers displayed stabilising effects to the reactive TTIP, they also have a high boiling point and low volatility in comparison to the lighter glycol ether species. Diglyme, along with DME, has a lower boiling point and as such could be removed far easier with little or no heating. However, as these lighter glycol ethers contain less oxygen atoms per molecule, it was possible they may not exhibit comparable stabilising effects to the reactive TTIP as the heavier glycol ethers. In order to assess this, inks 4.2.3.a and b were formulated and assessed in the same manner as inks 4.2.2.a and b, and 4.2.1.a and b.

Having similar physicochemical properties to ^{i}PrOH, it was found that the waveform used for jetting ^{i}PrOH as also suitable for jetting both of the diglyme inks. Figure 4.2.3.1 shows the optimised printed track obtained when using ink 4.2.3.a. The track has well defined edges, with an internal deposit which is barely visible; this suggests the presence of a thin printed film. Track width fluctuates to a small degree. The almost dashed appearance of the track edge suggests that some coffee staining effects are being observed, but the distribution of material is not homogeneous along the edge.

Figure 4.2.3.2.a shows the resulting single pass 1 cm^2 print when using ink 4.2.3.a. The left edge of the print consists of well-defined individual tracks. Approximately 1 mm in from the left edge, the individual tracks begin to flow and merge with one-another; this suggests that as we move from edge to bulk there is insufficient time for solvent evaporation. Figure 4.2.3.2.b shows that the 5 pass printed 1 cm^2 is similar to the single pass sample, with a well-defined edge that loses individually defined tracks as you approach the bulk of the sample. The darker regions of the print are where the tracks appear to have merged together,

indicating that the deposited material may be being transported before adhering to the substrate.

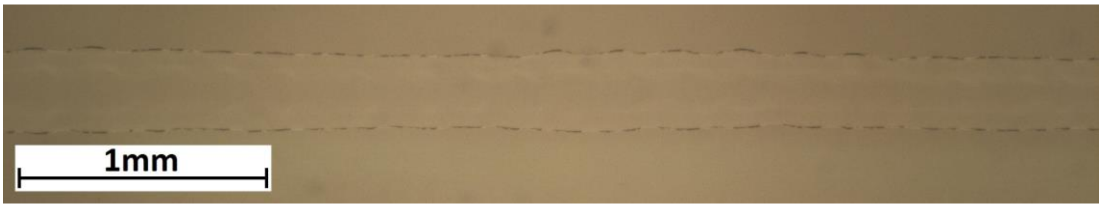

Figure 4.2.3.1 Printed track using ink 4.2.3.a at 6 mm s^{-1} print speed and 0.1 mm step size on a glass substrate

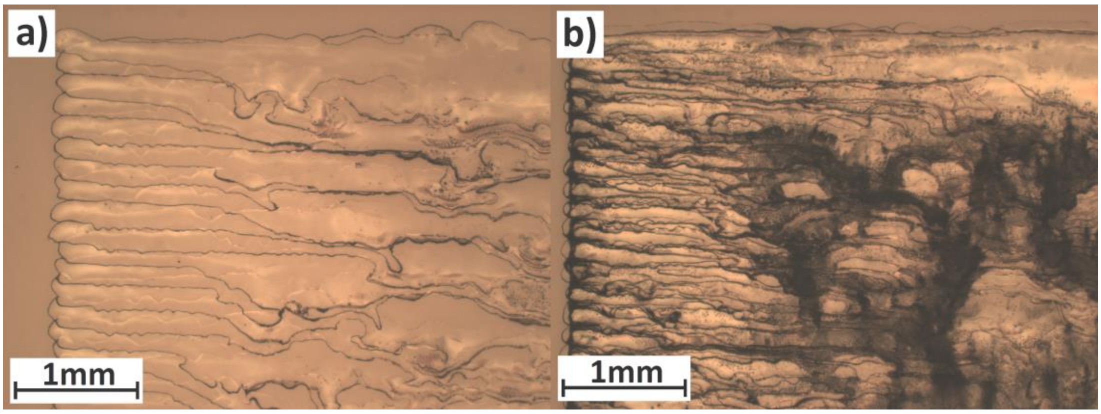

Figure 4.2.3.2 Printed 1 cm^2 using ink 4.2.3.a at optimised print conditions on a glass substrate. Image a) is 1 pass and b) is 5 passes. Image brightness has been increased by 20 % for clarity.

Figures 4.2.3.3 and 4.2.3.4.a and b show that the prints using ink 4.2.3.b are comparable to the same prints obtained when using ink 4.2.3.a. However, the printed track does not have the dashed track edge, indicating that material deposition is more uniform at the boundary. The left edges of both the 1 and 5 pass printed 1 cm^2 are also less neat when using ink 4.2.3.b.

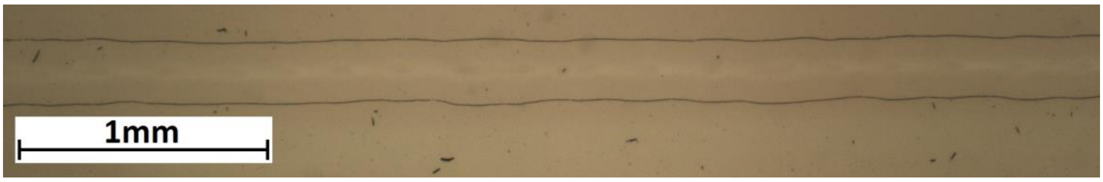

Figure 4.2.3.3 Printed track using ink 4.2.3.b at 6 mm s^{-1} print speed and 0.1 mm step size on a glass substrate

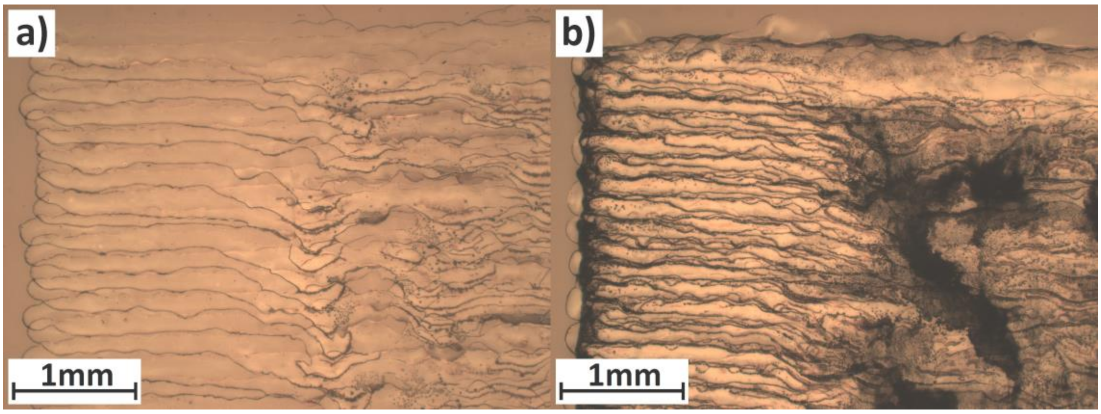

Figure 4.2.3.4 Printed 1 cm^2 using ink 4.2.3.b at optimised print conditions on a glass substrate. Image a) is 1 pass and b) is 5 passes. Image brightness has been increased by 20 % for clarity.

4.2.4 DME Stabilised Inks

After the successful jetting of diglyme stabilised inks, two DME inks were formulated and investigated; inks 4.2.4.a and b. Once again, the waveform generated for jetting pure ^{i}PrOH was suitable for jetting a steady and uniform stream of droplets for both inks so no modification to the waveform was required. Figure 4.2.4.1 shows the optimised track obtained when printing with ink 4.2.4.a. The top and bottom boundaries of the track have a different appearance, with the bottom boundary exhibiting a straighter and more uniform edge whilst the top boundary varies a little more in uniformity. The 1 and 5 pass prints of 1 cm^2 using ink 4.2.4.a are shown in Figures 4.2.4.a and b. Both prints display clearly defined individual print tracks with well-defined edges. Around 3 mm into the prints, the tracks become less defined and material deposition begins to be affected by the flow of unevaporated ink.

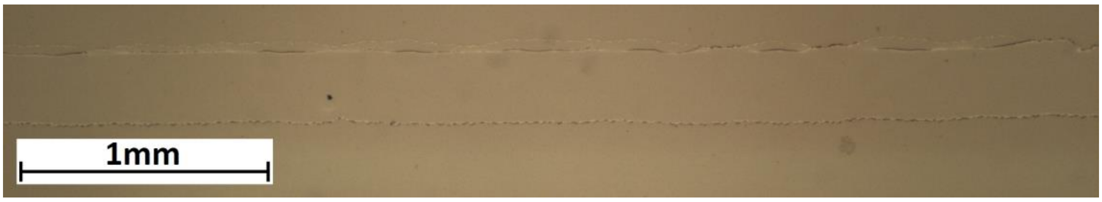

Figure 4.2.4.1 Printed track using ink 4.2.4.a at 10 mm s^{-1} print speed and 0.1 mm step size on a glass substrate

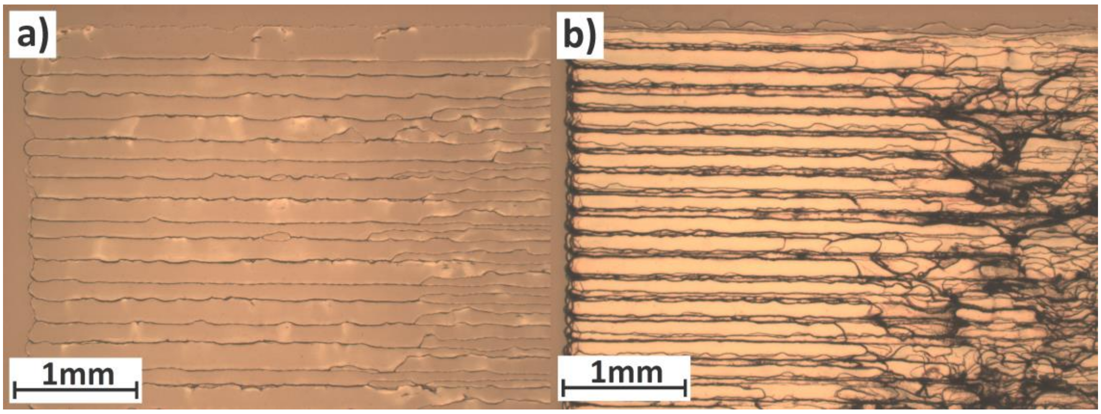

Figure 4.2.4.2 Printed 1 cm^2 using ink 4.2.4.a at optimised print conditions on a glass substrate. Image a) is 1 pass and b) is 5 passes. Image brightness has been increased by 20 % for clarity.

When using ink 4.2.4.b, the printed track has well defined edges that are somewhat jagged in appearance. Figures 4.2.4.4.a and b show that the printed 1 cm^2 obtained when using ink 4.2.4.b are similar to those when using ink 4.2.4.a. For the left edge of the 5 pass print shown in Figure 4.2.4.4.b, it appears that each printed pass has a minor offset from prior passes. This minor offset could indicate that a partial blockage may have occurred. Despite this apparent minor offset, the boundaries of the printed tracks can still be seen clearly in the print. Material deposition appears to be influenced by the flow of ink away from the edges of the print.

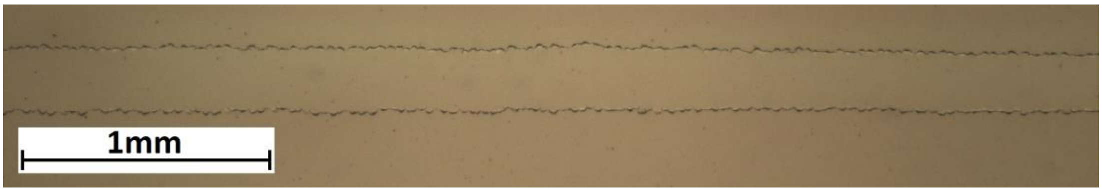

Figure 4.2.4.3 Printed track using ink 4.2.4.b at 10 mm s^{-1} print speed and 0.1 mm step size on a glass substrate

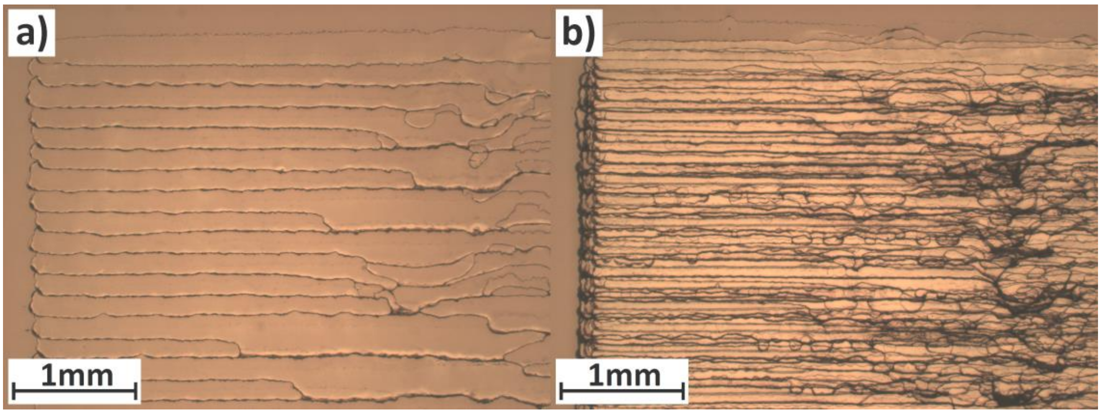

Figure 4.2.4.4 Printed 1 cm^2 using ink 4.2.4.b at optimised print conditions on a glass substrate. Image a) is 1 pass and b) is 5 passes. Image brightness has been increased by 20 % for clarity.

4.2.5 Discussion of Glycol Ether Stabilised Prints

Following the printing of the 0.05 M TTIP inks with each of the four glycol ether stabilisers, it was apparent that when using DME the printed samples were the neatest and most controlled. Therefore, DME was identified as the glycol ether to be used for stabilisation of the TTIP inks. When printing with the diglyme stabilised inks, and to a lesser extent the DME stabilised inks, some fluidic flows are observed away from the edges of the print and towards the bulk. Furthermore, the DME and diglyme containing prints did not display the granular deposits as found with the heavier triglyme and tetraglyme stabilised inks. The granular deposits are more prevalent in the multiple pass prints and may be attributed to the low volatility of the glycol ether species being utilised as the stabiliser.

With increasing Mw, the boiling points of the glycol ether series increases. DME has a boiling point of 85°C, diglyme has a boiling point of 162°C, triglyme has a boiling point of 216°C, and tetragyme has a boiling point of 275°C. As the heterogeneous granular deposits are only observed when the heavier triglyme and tetraglyme are used, it can be deduced that their rate of evaporation is low enough to allow the TTIP and any hydrolysis products to still move via the liquid glycol ether stabiliser. Figure 4.2.1.4.b shows that when using ink 4.2.1.b, the higher molar equivalents of tetraglyme cause the print to be discontinuous, forming discrete deposits of TiO_2. These deposits suggest the volatility of tetraglyme is so low and that the quantity of tetraglyme is sufficiently high that the TTIP and any intermediate hydrolysis products are still within a mobile phase throughout the entire printing process, with the first printed pass still being mobile after the final pass.

Diglyme stabilised inks, and to a lesser extent the DME stabilised inks, exhibit fluidic patterns of material flow as you move away from the edge of the prints and towards the bulk. This suggests that at the edges of the prints, the stabiliser evaporates sufficiently quickly such that no material is enabled to flow. However, as we move from the edges of the print to the bulk the stabiliser evaporates on a timescale that allows a brief flow of TTIP or intermediate hydrolysis products; but evaporates fast enough to be removed before any significant aggregation or orientation can occur in the deposit, as demonstrated by the granular deposits observed in the tetraglyme and triglyme prints. The difference in evaporation rates between the edge of the print and the bulk could be explained by a building partial pressure of the evaporating species in the bulk of the sample, but a low and constantly diminishing partial pressure at the edge due to diffusion into the atmosphere.

4.3 0.1 M and 0.15 M TTIP Inks

After ascertaining that the TTIP inks containing DME as the stabiliser demonstrated the most favourable print qualities, it was decided that the quantity of TiO_2 deposit was too low. To increase the loading of TTIP further, the concentration of TTIP was doubled from 0.05 to 0.1 M. With DME identified as the favoured stabiliser additive for the TTIP, all further work was performed using only DME. With an increased concentration of TTIP, both 2.5 and 5 molar equivalents of DME were again investigated. Rheological properties of viscosity, density, and surface tension were obtained for the 0.1 M TTIP inks stabilised with 2.5 and 5 molar equivalents of DME. The results are shown in Table 4.3.0.1, along with the final ink formulation of 0.15 M TTIP stabilised with 10 molar equivalents of DME. Table 4.3.0.2 summarises the printed properties for these DME stabilised inks.

Table 4.3.0.1 Rheological properties of TTIP inks stabilised with DME at 20°C

Ink Composition	**Ink Designation**	**Viscosity mPa s**	**Density g cm^{-3}**	**Surface Tension mN m^{-1}**
^{i}PrOH	^{i}PrOH	2.529	0.7870	19.27
DME	DME	0.445	0.8630	23.41
0.1 M TTIP, 2.5 eq DME	4.3.1.a	2.893	0.7885	20.78
0.1 M TTIP, 5 eq DME	4.3.1.b	2.733	0.7893	20.80
0.15 M TTIP, 10 eq DME	4.3.2.	1.892	0.7992	20.57

Table 4.3.0.2 Printed properties of TTIP inks stabilised with DME

Ink Designation	**Average Droplet Diameter ± Moving Range µm**	**Print Speed mm s^{-1}**	**Step Size mm**	**Average Track Width µm**
^{i}PrOH	65.0 ± 1.6	6	0.1	-
4.3.1.a	68.6 ± 1.4	10	0.1	229.8
4.3.1.b	83.7 ± 2.6	6	0.1	157.9
4.3.2	65.9 ± 1.6	10	0.1	143.7

4.3.1 0.1 M TTIP Ink

Ink 4.3.1.a was loaded into the inkjet printer and found to generate a steady stream of uniform ink droplets when jetted with the ^{i}PrOH waveform. Figure 4.3.1.1. shows the track obtained when printing at the optimised print parameters. The track is uniform, consisting of two straight and parallel edges connected by what appears to be a thin film of uniform TiO_2 deposit. There is minimal to no coffee-stain effect at the edges. Optical micrographs of the 1 and 5 pass printed 1 cm^2 samples using ink 4.3.1.a are shown in Figures 4.3.1.2.a and b. The single pass print displays neat edges at the left and top boundaries. However, ~1 mm into the sample, the well-defined tracks begin to flow into one-another. This was also observed for the previous DME stabilised inks, although the phenomenon appears to be exacerbated for ink 4.3.1.a. This may be caused by the doubled concentration of TTIP within the ink; the volume of DME can be ruled out as this ink contains the same volume of DME as ink 4.2.4.b. Figure 4.3.1.2.b shows that, aside from what appears to be a single pass of a few misplaced tracks along the left of the image, the 5 pass sample has somewhat well-defined print edges. Material deposition looks more uniform than the other prints discussed so far, as evidenced by the less distinguished deviations in the darkness of the image.

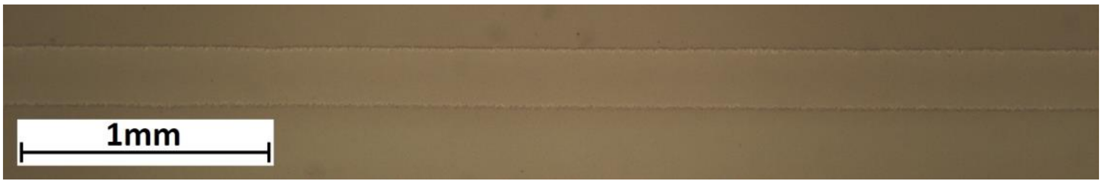

Figure 4.3.1.1 Printed track using ink 4.3.1.a at 10 mm s^{-1} print speed and 0.1 mm step size on a glass substrate

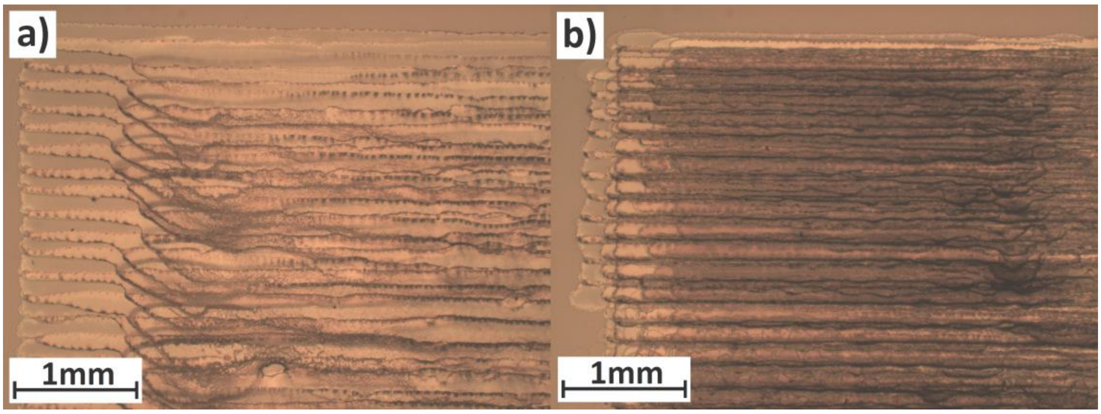

Figure 4.3.1.2 Printed 1 cm^2 using ink 4.3.1.a at optimised print conditions on a glass substrate. Image a) is 1 pass and b) is 5 passes. Image brightness has been increased by 20 % for clarity.

For ink 4.3.1.b, the waveform generated for jetting pure ^{i}PrOH was again found suitable for jetting a steady, uniform stream of droplets. A neat track was obtained when using the optimised print parameters, as shown in Figure 4.3.1.3. The bulk of the track seems to be homogeneous in nature, although a significant quantity of the deposited material appears to be located at the edges of the track. This apparent coffee stain effect may be caused by the increased quantity of DME within the ink as although it is the same 5 molar equivalents as the inks discussed in section 4.2, the doubling in the concentration of TTIP also results in doubling the concentration of the stabiliser.

The 1 and 5 pass printed 1 cm^2 samples, shown in Figures 4.3.1.4.a and b, again show that the print consists of neat tracks with minimal divergence from the desired print pattern. Unlike when using ink 4.3.1.a, the 1 cm^2 prints obtained when using ink 4.3.1.b do not appear to exhibit the phenomena whereby the tracks flow into one-another. However, the constituent tracks do not look as neat in the 1 cm^2 print as the single track does. There is some unwanted deposit obtained in the 5 pass sample, shown at the top right of Figure 4.3.1.4.b; this may have been caused by a partial blockage of the dispensing device. Due to the darker print obtained for the 5 pass sample compared to the previous 5 pass sample when using ink 4.3.1.a, it can be assumed that more material has been deposited. This makes sense when you compare the 83.66 µm average droplet diameter when using ink 4.3.1.b with the 68.55 µm average droplet diameter when using ink 4.3.1.a; an ~22 % increase in droplet size leads to an ~82 % increase in droplet volume, resulting in a far greater total quantity of jetted TTIP, and therefore TiO_2 deposit.

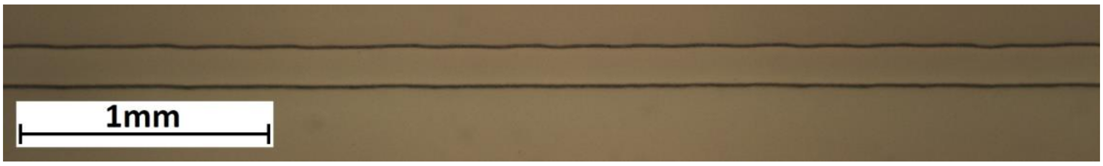

Figure 4.3.1.3 Printed track using ink 4.3.1.b at 10 mm s^{-1} print speed and 0.1 mm step size on a glass substrate

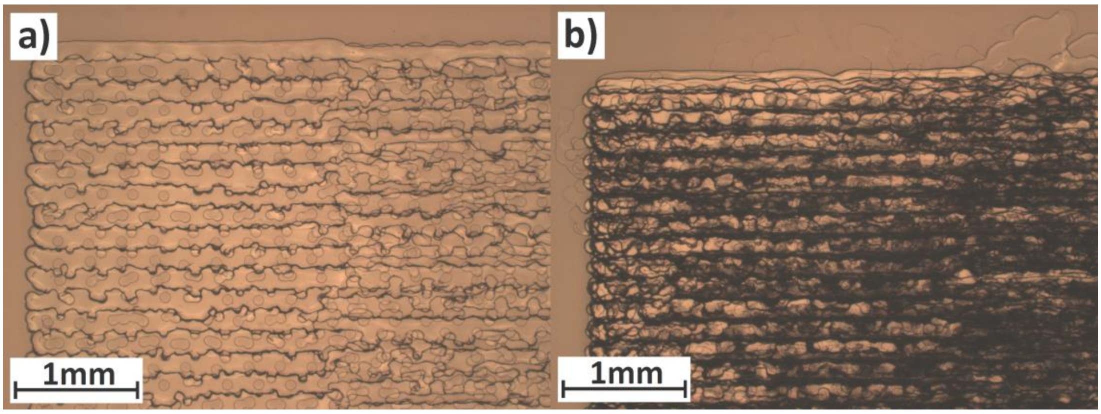

Figure 4.3.1.4 Printed 1 cm^2 using ink 4.3.1.b at optimised print conditions on a glass substrate. Image a) is 1 pass and b) is 5 passes. Image brightness has been increased by 20 % for clarity.

4.3.2 0.15 M TTIP Ink

Following the success of the increased concentration to 0.1 M TTIP, the concentration was then further increased to 0.15 M with respect to TTIP. Both 2.5 and 5 molar equivalents of DME were found to be insufficient to stabilise the TTIP to hydrolysis during the printing process, with the dispensing device blocking often. To overcome the increased rate of blockage, 10 molar equivalents of DME were used to stabilise the 0.15 M TTIP ink and found to inhibit blockage. After formulating the ink, its rheological properties at 20°C were obtained, shown in Table 4.3.0.1, designated as ink 4.3.2.

A steady stream of droplets was obtained for ink 4.3.2 when using the waveform for neat ^{i}PrOH. The printed track obtained with the optimised print conditions is shown in Figure 4.3.2.1. Distribution of the deposited TiO_2 is biased to the edges of the print, indicating some degree of coffee-staining. However, it can also be seen that the distribution of material is also uneven within the bulk of the track. The bottom edge is straighter than the top edge, which exhibits a high degree of undulation. Optical micrographs of 1 and 5 pass 1 cm^2 printed samples using ink 4.3.2 are shown in Figures 4.3.2.2.a and b. In the single pass print, the constituent tracks are visible. There are a few stray droplets at the top left of the image, although the resulting deposit appears less dense than the rest of the printed sample; this suggests the deposits are a result of small satellite droplets which began to form during the end of the print. Both the left and top edges of the print are relatively ill-defined compared to the previous two DME containing inks. A small amount of flow is also observed in the single pass print, which begins at roughly 1.5 mm in from the left edge. The 5 pass print exhibits similarities to the single pass print, with relatively ill-defined edges and stray droplets.

Figure 4.3.2.1 Printed track using ink 4.3.2 at 10 mm s^{-1} print speed and 0.1 mm step size on a glass substrate

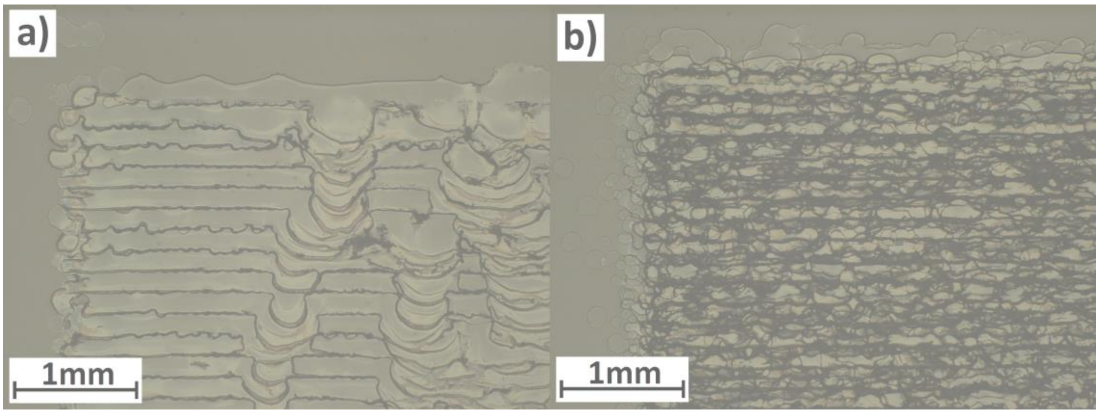

Figure 4.3.2.2 Printed 1 cm² using ink 4.3.2 at optimised print conditions on a glass substrate. Image a) is 1 pass and b) is 5 passes. Image brightness has been increased by 40 % for clarity.

4.3.3 0.15 M TTIP Ink Ageing Study

To assess the stability of ink 4.3.2, an ageing study was performed. This involved measuring the viscosity of a freshly made ink sample and then repeating this measurement at regular time intervals. Density and surface tension were not measured as the experimental procedure involved large volumes of the ink to be exposed to atmosphere, which would be unrealistic for a storage process. After the first t = 0 measurement, ageing times of 1, 3, 5, and 7 days were given between viscosity measurements to determine the initial degradation of the ink. Ageing times of 14, 21, and 28 days were then used to ascertain the longer-term stability of the ink. Figure 4.3.3.1 shows that there is a slight increase in viscosity as the ink ages. This increase is likely caused by a small quantity of H_2O reacting with the TTIP in the ink and undergoing sol-gel reactions. However, the increase over the entire 28 day ageing time is only 0.025 mPa s, a 1.34 % increase to the initial viscosity measurement.

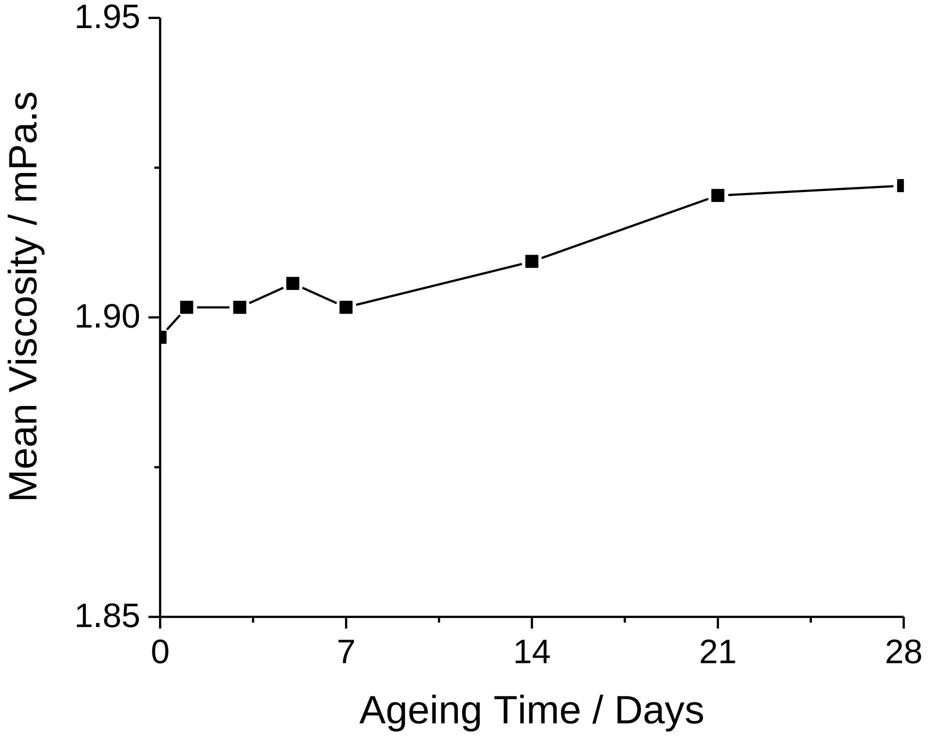

Figure 4.3.3.1 Ageing data for ink 4.3.2 over a 28 day maturation time

4.3.4 Discussion of 0.1 M and 0.15 M TTIP Prints

Use of DME facilitated the stabilisation of increased TTIP concentration. With increasing volumes of DME the ink viscosity decreases; this is exemplified by the viscosity of ink 4.3.2 being in-between that of neat ^{i}PrOH and DME. Such a drastic change in viscosity was expected to necessitate an alteration to the ^{i}PrOH waveform. This was not the case, with all DME inks being suitable for jetting with the ^{i}PrOH waveform.

All three inks in section 4.3. (4.3.1a and b, and 4.3.2) displayed satisfactory printed tracks with straight, parallel edges and continuous deposition. Figure 4.3.1.2.a shows that for a printed 1 cm^{2}, the 0.1M TTIP ink stabilised with 2.5 equivalents of DME consists of tracks which vary in width, appearing to flow downwards. This is not observed for the same ink stabilised instead with 5 molar equivalents of DME, as shown in Figure 4.3.1.4.a, although the constituent tracks that make up the printed sample are less ideal than those obtained individually. As the concentration is increased to 0.15 M TTIP, the tracks within the printed 1 cm^{2} again exhibit a small downwards flow along sections of their length (See Figure 4.3.2.2.a). The downwards flow may be a result of the stage not being perfectly flat, in combination with a build-up of vapour from the evaporating volatiles causing a transient increase in the lifetime of the fluid and enabling the deposit to flow.

Multiple pass prints showed minimal deviation from the previous and subsequent layers, although some stray material is observed on the top left of Figure 4.3.1.2.b, the top right of Figure 4.3.1.4.b, and top of Figure 4.3.2.2.b. The left edge of the print in Figure 4.3.1.4.b is an example of a neat edge with overlapping print passes.

4.4 Characterisation of Printed Films

4.4.1 Annealing, XRD and Raman Investigation

XRD was used to identify the crystallinity of the printed samples. However, even after annealing at temperatures known to produce anatase phase there were no discernible peaks within the spectra; it was determined this was due to the thin and likely non-uniform topography of the prints. Therefore, it was determined that XRD analyses would be performed on thicker drop-tested samples. Whilst there is a significant difference in the deposition and evaporation regimes between a single pipetted 20 µL droplet and 10,000 inkjet printed droplets of ~0.000268 µL volume (assuming droplet diameters of 80 µm), it is assumed that the drop-tested TiO_2 deposit will behave similarly under thermal treatment and be representative of the inkjet printed deposit.

Figure 4.4.1.1 shows the XRD trace obtained for the drop-tested sample using ink 4.3.2 without any heat treatment. There are no peaks present above the baseline noise, indicating that the sample lacks crystallinity or long-range order, so is amorphous in nature. This is not surprising as the literature indicates most TiO_2 deposited from precursors is amorphous and requires heat treatment.

Drop-tested samples were then annealed at increments of 50°C, with a residence time of 40 minutes. The A(101) peak is the most prominent peak in the anatase XRD spectrum, present at 2 θ of ca. 25°; this peak was first observed when a drop-tested sample of ink 4.3.2 was annealed at 400°C for 40 minutes (See Figure 4.4.1.2). The observed A(101) peak is barely visible over the noisy baseline, with no other peaks being distinguishable. It was therefore decided that a higher annealing temperature was still required.

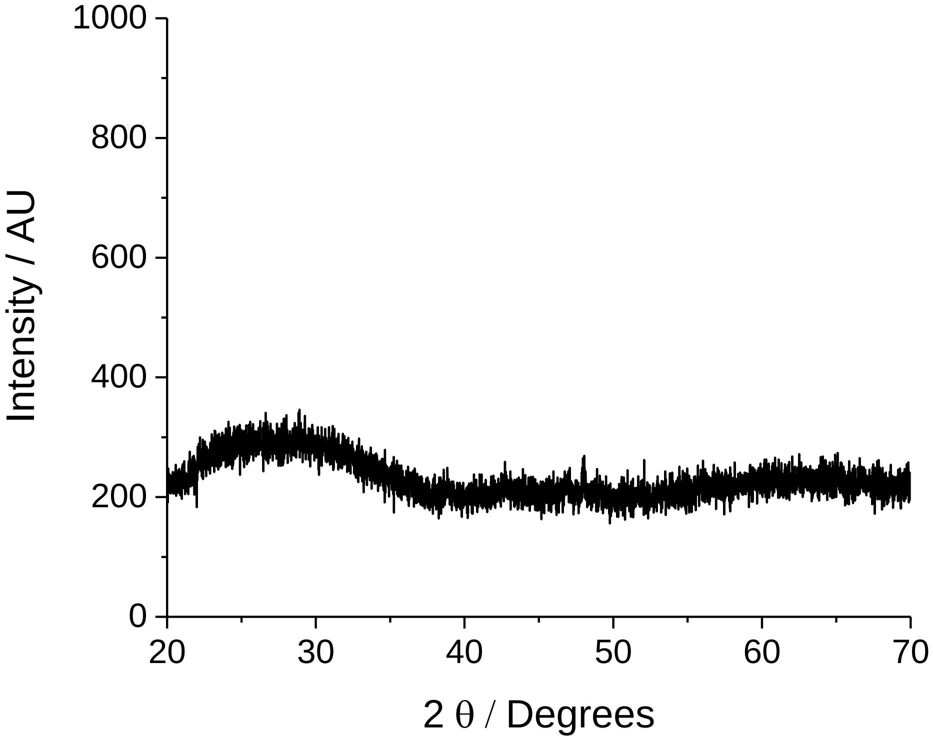

Figure 4.4.1.1 XRD spectrum of drop-tested sample using ink 4.3.2 on a glass substrate before annealing

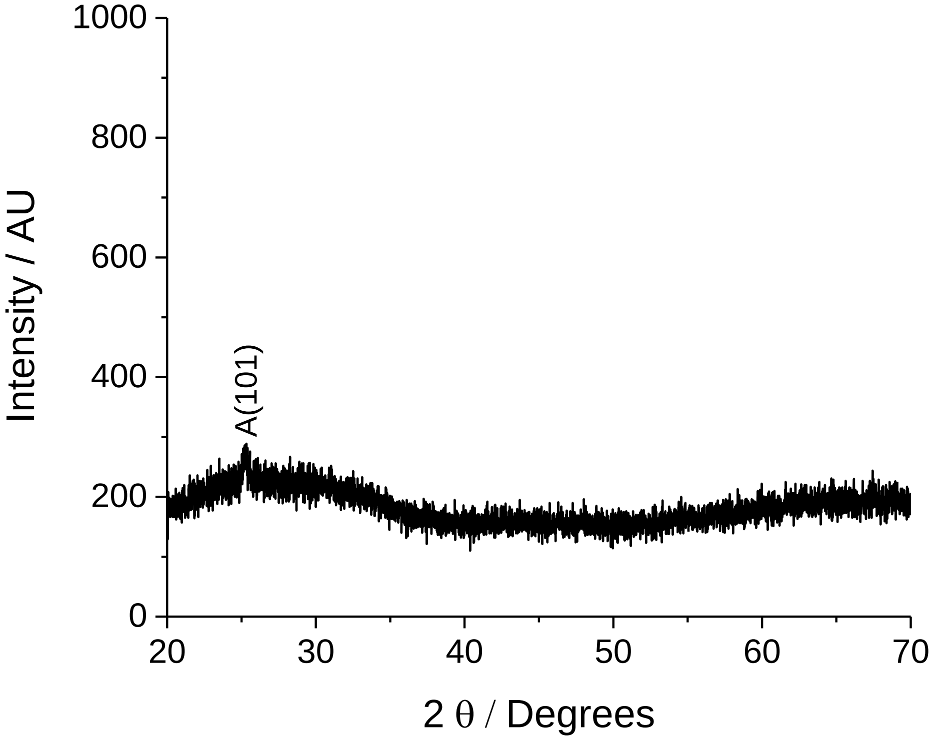

Figure 4.4.1.2 XRD spectrum of drop-tested sample using ink 4.3.2 on a glass substrate after annealing at 400°C for 40 minutes

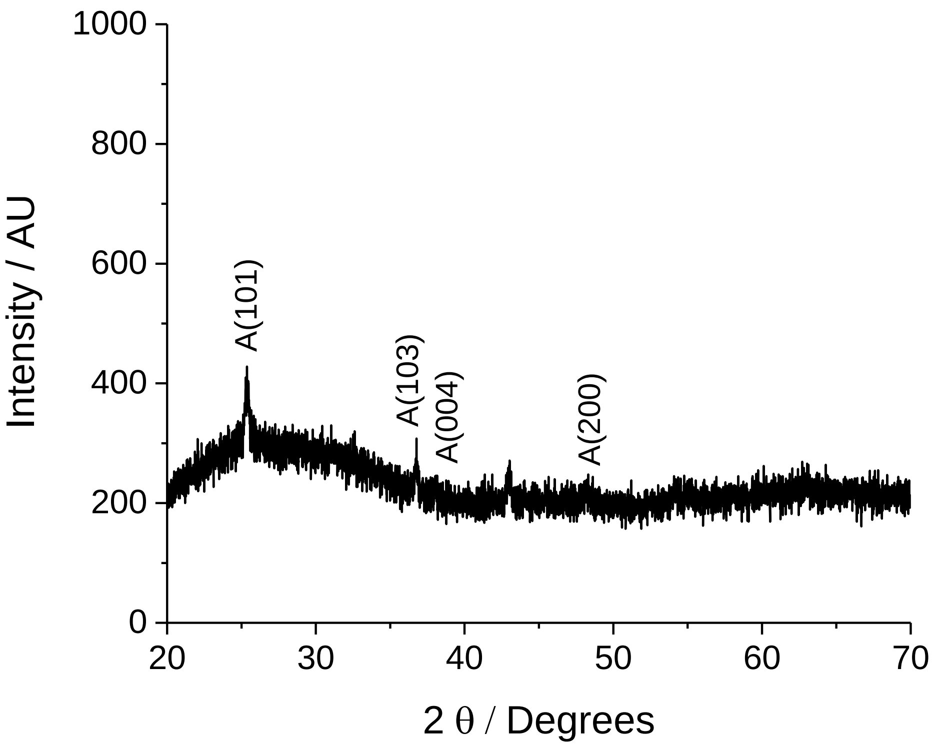

Figure 4.4.1.3 XRD spectrum of drop-tested sample using ink 4.3.2 on a glass substrate after annealing at 450°C for 40 minutes

An annealing temperature of 450°C was determined to be a suitable temperature for obtaining anatase phase TiO_2 for drop-tested samples of ink 4.3.2. The A(101) peak is well defined, with other peaks also beginning to become visible (See Figure 4.4.1.3). It is shown in Figure 4.4.1.4 that increasing the residence time from 40 to 80 minutes, whilst still at an annealing temperature of 450°C, results in an increased intensity of the A(103) peak. However, the baseline noise was still high enough to obscure the presence of any other low-intensity peaks that were expected to be present.

A drop-tested sample of ink 4.3.2 was annealed at 650°C for 40 minutes, the resulting XRD trace is shown in Figure 4.4.1.5. 650°C is a high temperature for anatase formation, with the possibility of promoting the more thermodynamically stable rutile phase TiO_2.[12-14] This is shown to be true by the presence of the R(211) and R(310) peaks. The intensity of the anatase peaks is increased in comparison with the 450°C annealed samples.

Raman spectroscopy was used to analyse the phase of the deposited TiO_2 further. Figure 4.4.1.6 shows the overlaid Raman spectra for an inkjet printed 5 pass 1 cm^2 sample using ink 4.3.2. As with the XRD, it was found that the printed samples were too thin and/or irregular to analyse. A drop-tested sample using ink 4.3.2 was then analysed with Raman spectroscopy, after which it was annealed at 450°C for 40 minutes and re-analysed (See Figure 4.4.1.7). The high intensity E_g mode is present, along with the lower intensity A_{1g}, B_{1g}, and second E_g modes; this shows that anatase phase is indeed formed under the annealing conditions used. However, it is only shown for drop-tested samples of ink 4.3.2. It is assumed that this is also true for the inkjet printed samples.

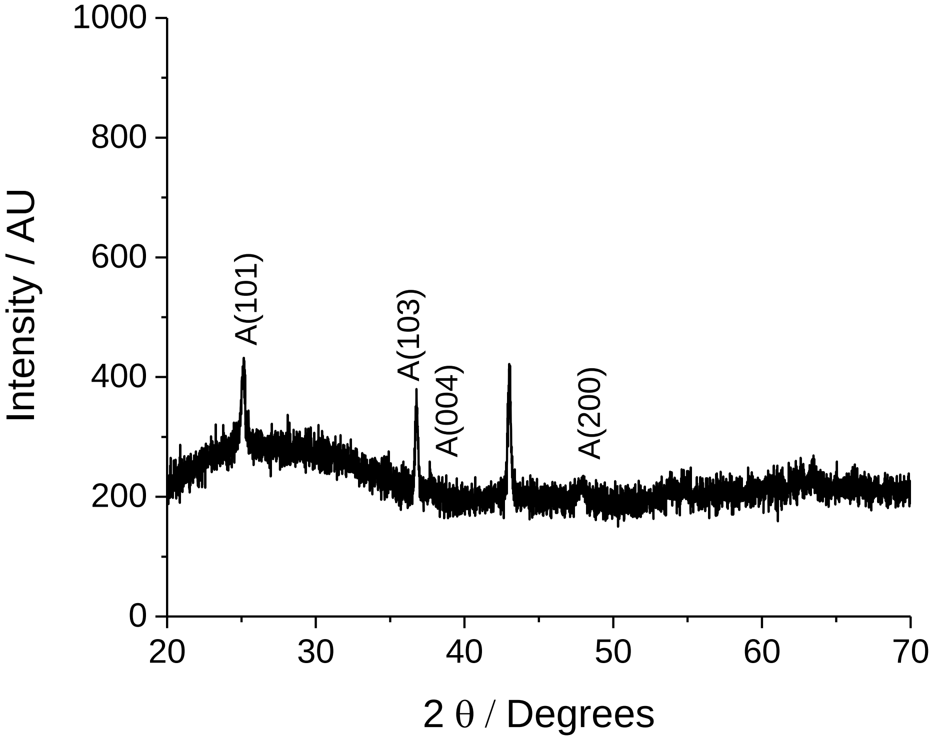

Figure 4.4.1.4 XRD spectrum of drop-tested sample using ink 4.3.2 on a glass substrate after annealing at 450°C for 80 minutes

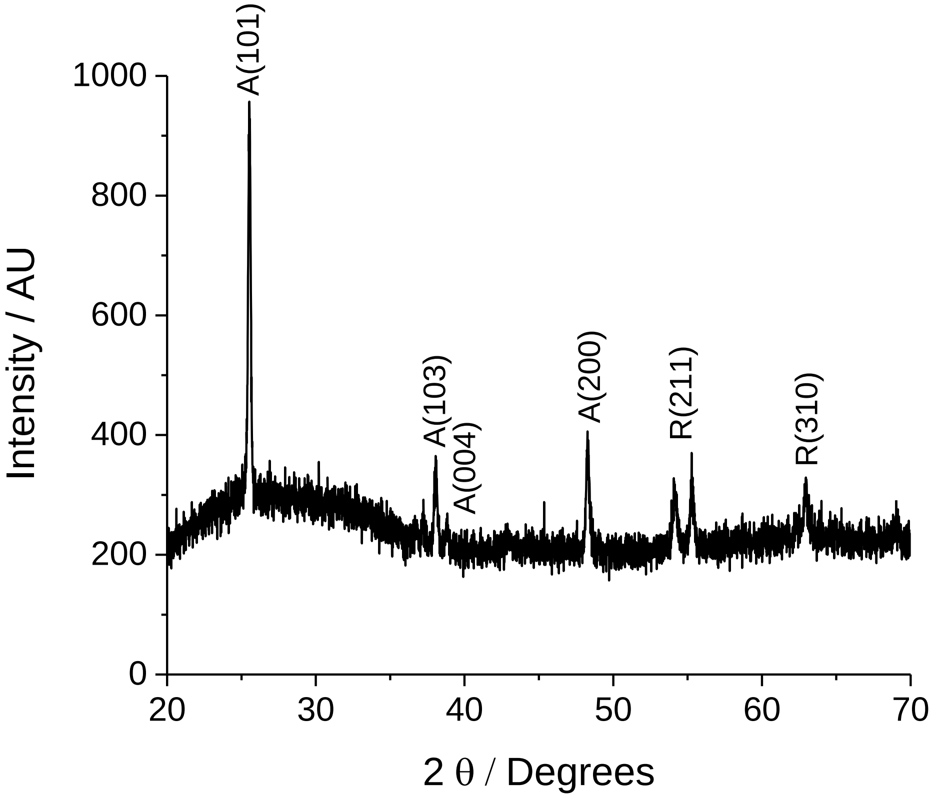

Figure 4.4.1.5 XRD spectrum of drop-tested sample ink 4.3.2 on a glass substrate after annealing at 650°C for 40 minutes

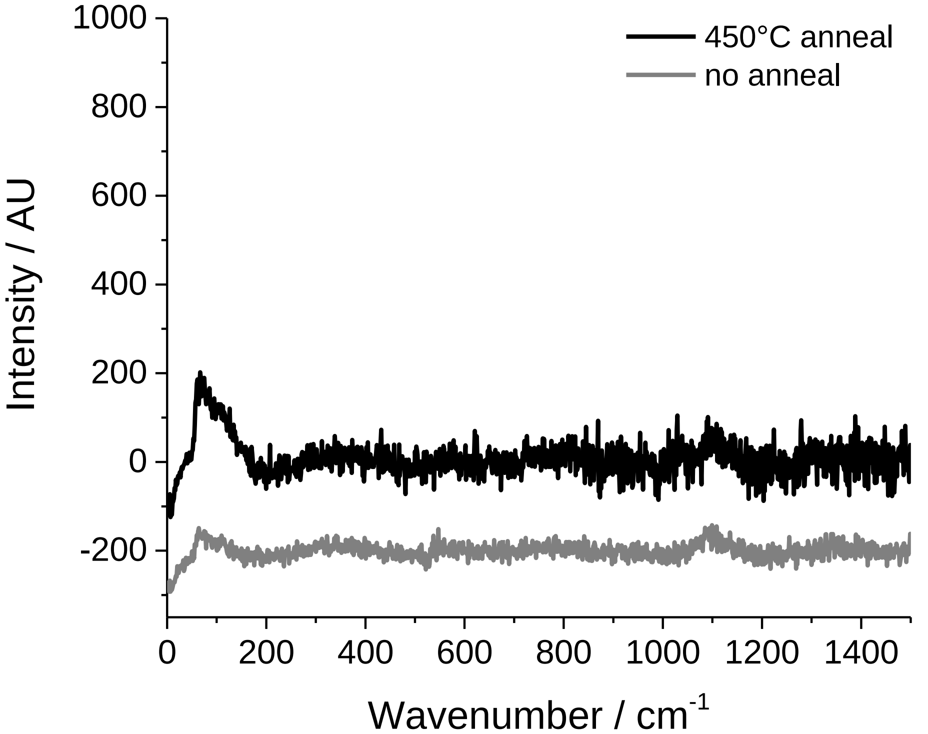

Figure 4.4.1.6 Raman spectra of printed 1 cm^2 samples using ink 4.3.2 on a glass substrate before and after annealing at 450°C for 40 minutes

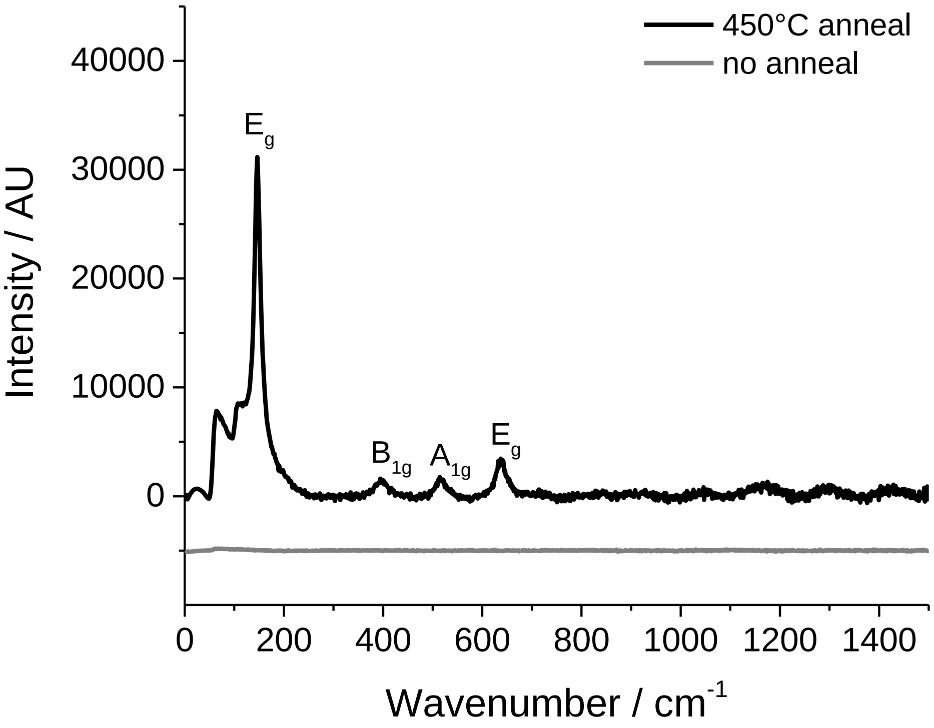

Figure 4.4.1.7 Raman spectra of drop-tested samples using ink 4.3.2 on a glass substrate before and after annealing at 450°C for 40 minutes

4.4.2 Profilometry, Optical Transmittance, and Wettability

A theoretical film thickness was calculated for ink 4.3.2 using the equation and assumptions stated in section 3.4.2 of the Experimental Chapter. For a single printed pass of a 100 x 100 droplet square array using the average droplet diameter of 65.94 µm, the theoretical film thickness was calculated as 46.11 nm. Multiplying the theoretical film thickness of 46.11 nm for a single printed pass by 5 yields a theoretical film thickness of 230.55 nm for a 5 pass 1 cm^2 sample. Such a low thickness may explain the apparent difficulty of analytical techniques being sensitive enough to obtain meaningful data from even the thicker printed samples. Several assumptions were made when using the calculation for theoretical film thickness, which detracts from the overall significance and credibility of the obtained values. An experimentally obtained value for film thickness is far more credible, reducing the uncertainty in the reported thickness.

Profilometry was used to further investigate the thickness of the printed films. The profiles are denoted as left, right, top, or bottom, as illustrated in Figure 4.4.2.1. Figures 4.4.2.2, A.4.4.2.2, 4.4.2.3, and A.4.4.2.3 show the profiles obtained for printed 5 pass 1 cm^2 samples using ink 4.3.2. All four Figures show that the sample is approximately the correct size, with a discernible profile of ~10,000 µm width. Large and sharp peaks are present, interconnected by troughs at or very near to the baseline; this suggests that the profile consists of thicker areas of deposit and regions of thin or no deposit. As the prints consist of 100 parallel tracks it is proposed that the thicker areas of deposit correlate to the coffee-stain boundaries of the individual tracks, whilst the regions of thin deposit correspond to the internal printed track which contains less deposit (See Figure 4.3.2.1 for the printed track using ink 4.3.2). As the profile is of a 5 pass 1 cm^2 print, rather than a single pass, it is likely that the height discrepancy between the boundaries and internal deposit of the tracks is increased due to the overlapping prints.

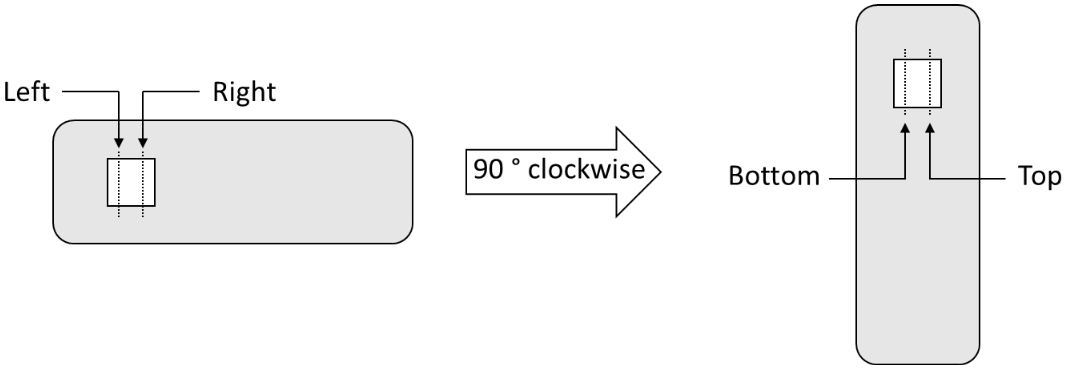

Figure 4.4.2.1 Schematic showing the four different profilometry measurements performed for each sample

The left and right profiles shown in Figures 4.4.2.2 and A.4.4.2.2 display an unfortunate curvature in their baselines, rendering the average thickness data obtained from them useless; an average thickness of -38 nm is given by the left profile. This baseline curvature could be caused by interactions between the stylus tip and the printed deposit, perhaps sufficient to have scraped some deposit from the substrate and subsequently slowing the stylus down and resulting in a slight transient bend in the stylus. It is unlikely that the substrate itself is the cause of the curvature, due to the absence of the curvature in other measured profiles on similar substrates. Furthermore, the minimum of the curvature is observed near the centre of the sample which implies it is a sample related phenomenon.

Figures 4.4.2.3 and A.4.4.2.3 have a flat baseline, allowing the average thickness data to be used with more confidence than the previous profiles. However, the top and bottom profiles are taken in parallel with the printed tracks rather than perpendicular to them as is the case with the left and right profiles. Parallel measurements to the tracks may cause inaccuracies due to primarily measuring either a track boundary or the internal deposit. The top profile gives a thickness of 466 nm, whilst the bottom profile gives a thickness of 776 nm; these two values give a mean thickness of 621 nm for the 5 pass 1 cm^2 printed sample using ink 4.3.2. With a theoretically calculated film thickness of 230.60 nm, the mean experimentally obtained thickness of 621 nm is 169 %, or 2.69 times larger. Although a significant increase in thickness was found experimentally, this was unsurprising when considering the number of assumptions made in the theoretical film thickness calculation. The largest assumptions likely to contribute to this difference are the droplet size consistency, complete evaporation of all volatiles, and the density of the TiO_2 deposit. The evaporation of volatiles can be facilitated through the annealing process, as well as a probable increase in density through thermally-assisted densification.

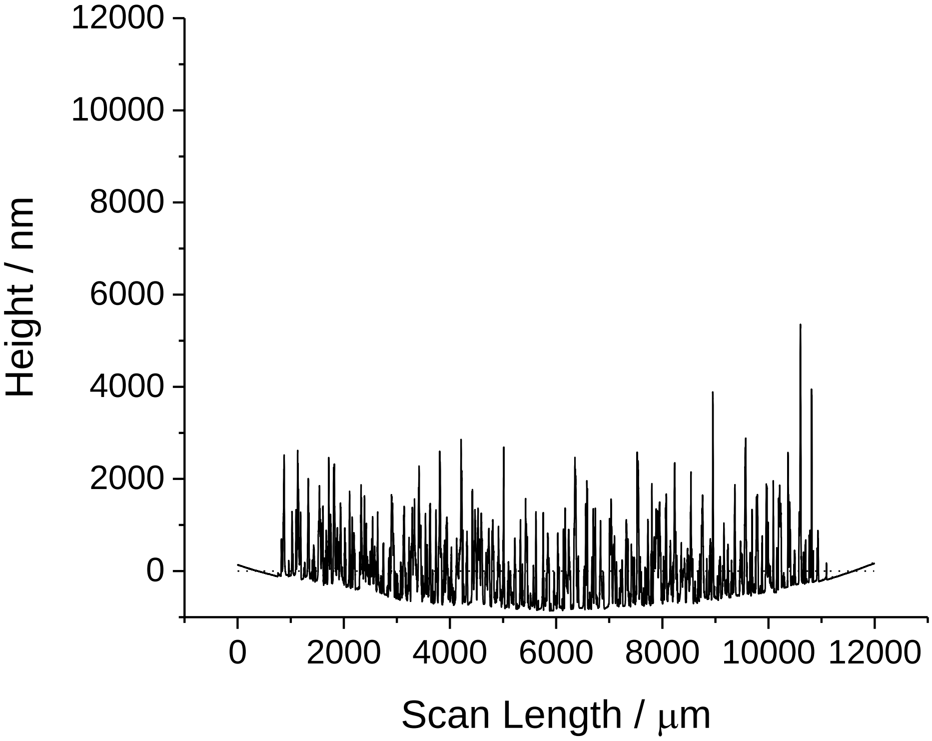

Figure 4.4.2.2 Left profile of 5 pass 1 cm² print using ink 4.3.2 on a glass substrate without annealing (average height of -38 nm)

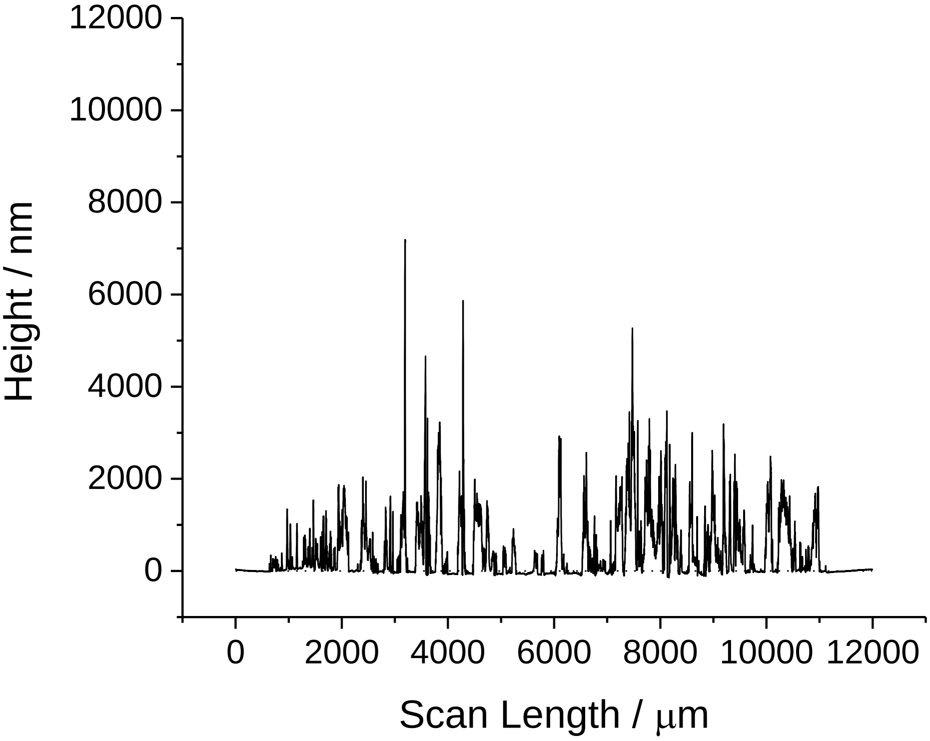

Figure 4.4.2.3 Top profile of 5 pass 1 cm² print using ink 4.3.2 on a glass substrate without annealing (average height of 466 nm)

Profilometry was also performed on an inkjet printed 5 pass 1 cm^2 sample using ink 4.3.2 after annealing the sample at 450°C for 40 minutes. Figures 4.4.2.4 and 4.4.2.5 show the measured left and top profiles. A4.4.2.4 and A4.4.2.5 show the measured right and bottom profiles. In all four figures the large and sharp peaks appear within a range of roughly 10,000 µm; this suggests that the print is the desired size of 1 cm^2. However, there are some peaks present just outside of this range, suggesting a small amount of material is present outside of the desired print area. This undesired material may be due to a partial blockage of the dispensing device, or turbulence during droplet flight at the edges of the print.

Unlike the previously analysed sample, Figures 4.4.2.4 and A.4.4.2.4 show the left and right profiles do exhibit a flat baseline. Both profiles consist of extreme, regular changes in height. The height never reaches the baseline within the confines of the print (scan lengths of ~1000 to 11000 µm) which suggests that although the thickness of the deposit fluctuates, there is a continuous TiO_2 film. There are several peaks present within the two profiles that exceed 5000 nm in height, showing how extreme the measured thickness varies. With an average measured height of 666 nm, the left profile is similar to the 697 nm average measured height of the right profile. The mean of the two profiles is 682 nm.

Figures 4.4.2.5 and A.4.4.2.5 show the measured top and bottom profiles for the annealed sample. It is immediately apparent that whilst the two profiles do exhibit extreme changes in height, it is not as prevalent in the top and bottom profiles as it is in the left and right profiles. This is due to the left and right profiles measuring perpendicular to the direction of the printed tracks, capturing every track boundary. The average measured heights for the top and bottom profiles have a larger spread than for the left and right profiles, with the top profile giving 731 nm and the bottom profile giving 619 nm as an average measured height. The mean of these two measurements is 675 nm, similar to the 682 nm mean of the left and right profiles. A mean of 678 nm was calculated for all four annealed sample profiles.

It was predicted that annealing would decrease the mean height of the film due to the complete removal of the organic ink components, along with the densification of the TiO_2 deposit. The mean value of 678 nm for the annealed sample is 9.18 % larger than the mean measured thickness of 621 nm for the sample without annealing. An increased thickness after thermal treatment, although unexpected, may be explained by; sample variation between prints, a less reliable mean thickness value for the sample without annealing due to the omitted left and right profiles, or expansion of the film as internally trapped organic ink components are removed.

Profilometry was also performed on two printed 5 pass 1 cm^2 samples using ink 4.3.1.b, one was analysed without any thermal treatment and the other was analysed after annealing at 450°C for 40 minutes. None of the profiles exhibited a curved baseline, and so all four measurements were used to calculate the mean sample thicknesses of each of the two samples. Without annealing, the mean value was 2100 nm. A mean value of 1060 nm was obtained for the annealed sample. These two samples exhibit the predicted change in mean height after annealing, with a 49.52 % decrease. However, these are two different samples and this does not consider sample variation. Furthermore, both mean thickness values are significantly larger than those obtained for the profiles of the samples using ink 4.3.2. A higher thickness was also predicted for the printed ink 4.3.1.b sample using the theoretical film thickness calculations, giving a value of 62.8 nm per pass, which is 36.2 % higher than the 46.1 nm per pass calculated for the ink 4.3.2 sample. Despite the increased TTIP concentration from 0.1 to 0.15 M, the lower concentration ink 4.3.1.b exhibited larger droplets than the higher concentration ink 4.3.2; the 26.87 % increased droplet size outweighed the contribution of the increased concentration to yield a thicker theoretical film thickness. This agrees with and explains the experimental findings.

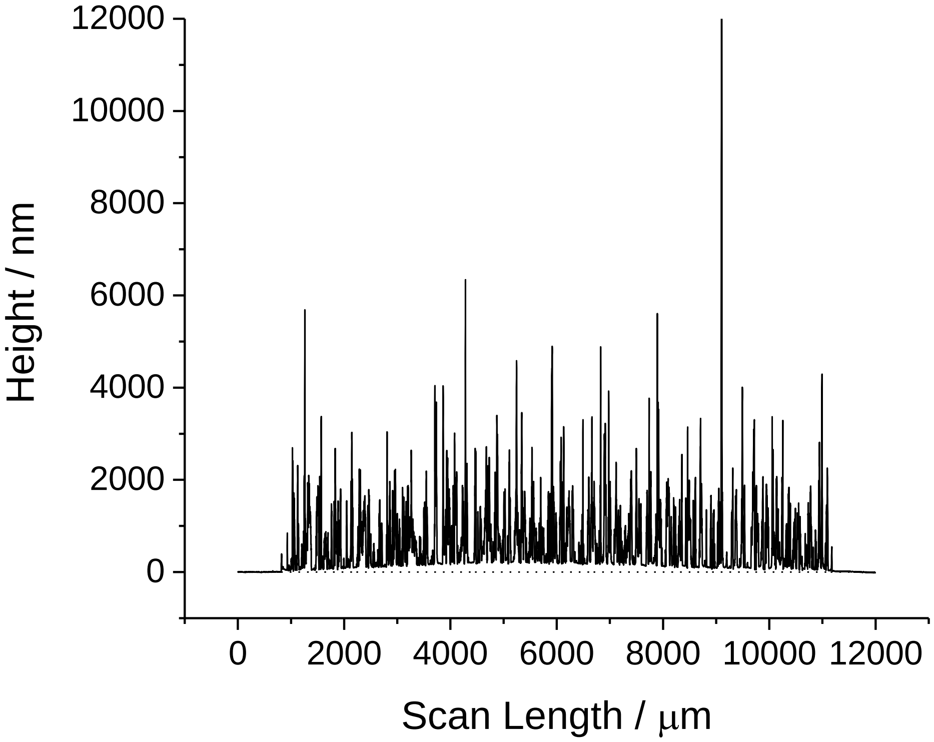

Figure 4.4.2.4 Left profile of 5 pass 1 cm² print using ink 4.3.2 on a glass substrate after 450°C for 40 minutes (average height of 666 nm)

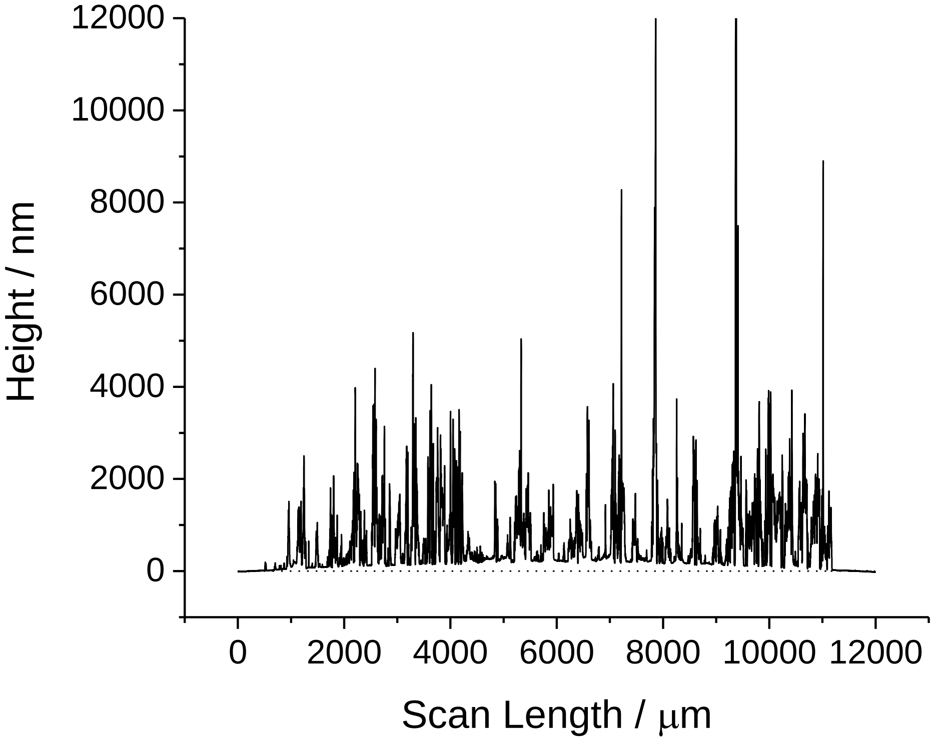

Figure 4.4.2.5 Top profile of 5 pass 1 cm² print using ink 4.3.2 on a glass substrate after 450°C for 40 minutes (average height of 731 nm)

Optical transmittance of printed 5 pass 1 cm^2 samples using ink 4.3.2 were analysed using spectrophotometric analysis. One sample was not heat treated, the other was annealed at 450°C for 40 minutes. A range between 250 nm and 900 nm was used as this encompasses the visible spectrum (approximately 380 nm to 740 nm). Transmittance is a measure of the quantity of emitted light photons that travel through the sample and into the in-line detector, opposite the photo-emission source. Units of percentage are used for transmittance as the detected photon intensity measured after passing through the sample is given as a percentage of those measured when passing through a reference material, cleaned glass slides in this instance. By reporting the sample transmittance as a percentage of the transmittance of clean glass slides, the glass slide substrate the sample was printed on is subtracted from the transmittance measurement and only the transmittance of the printed sample is given.

As the printed samples are varying shades of white, it was expected that there would be some degree of reflectance at all visible wavelengths, causing the detected transmittance to be below 100 % at all times. Figure 4.4.2.6 shows this to be true, with a detected transmittance of approximately 48 % for most of the visible range. There is a slight decrease in transmittance with decreasing wavelength, and a marked decrease at ~350 nm. This large decrease in transmittance is greater for the sample without any annealing.

The 250 to 400 nm range consists of the UV wavelengths, specifically the UVA (315 - 400 nm), UVB (280 – 315 nm), and UVC (100 – 280 nm). The band gap of TiO_2 is typically reported as within the UVA band,[15, 16] with the wavenumbers of UVA converted to energies of 3.94 to 3.10 eV. It is proposed the decrease in transmittance is due to absorbance, rather than reflection, in the UV region of the spectra. The decrease is larger in the sample without annealing, possibly caused by an increased absorbance.

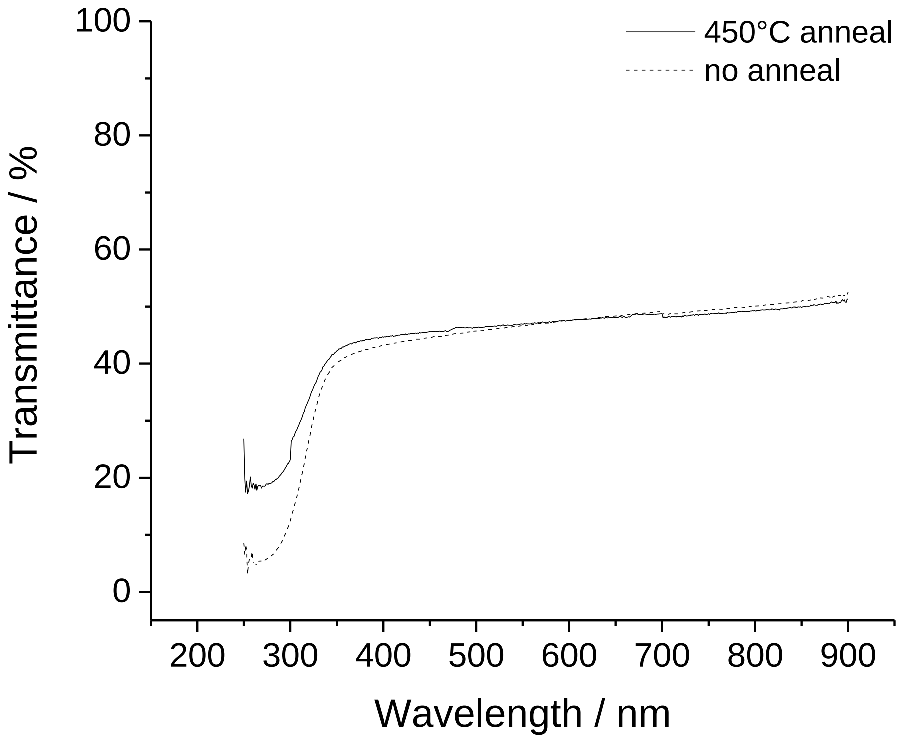

Figure 4.4.2.6 Optical transmittance of printed 5 pass 1 cm^2 using ink 4.3.2 on a glass substrate with and without annealing

The contact angle of distilled H_2O on inkjet printed TiO_2 samples was investigated, to ascertain any potential applications of the inks as hydrophobic or hydrophilic additive manufacturing treatments (See Figure 4.4.2.7). A mean contact angle of 83° was found for the printed 5 pass 1 cm^2 using ink 4.3.2 without any annealing. A mean contact angle of 35° was found for the sample that had been annealed at 450°C for 40 minutes, which is a reduction of 59.2 % compared to the sample that was not annealed. The contact angle of the annealed sample was comparable to other reported contact angles for H_2O on anatase. Contact angle during or immediately after irradiation with UV was not tested. TiO_2 is reported to behave as a hydrophilic surface upon UV irradiation.[17, 18 19-22]

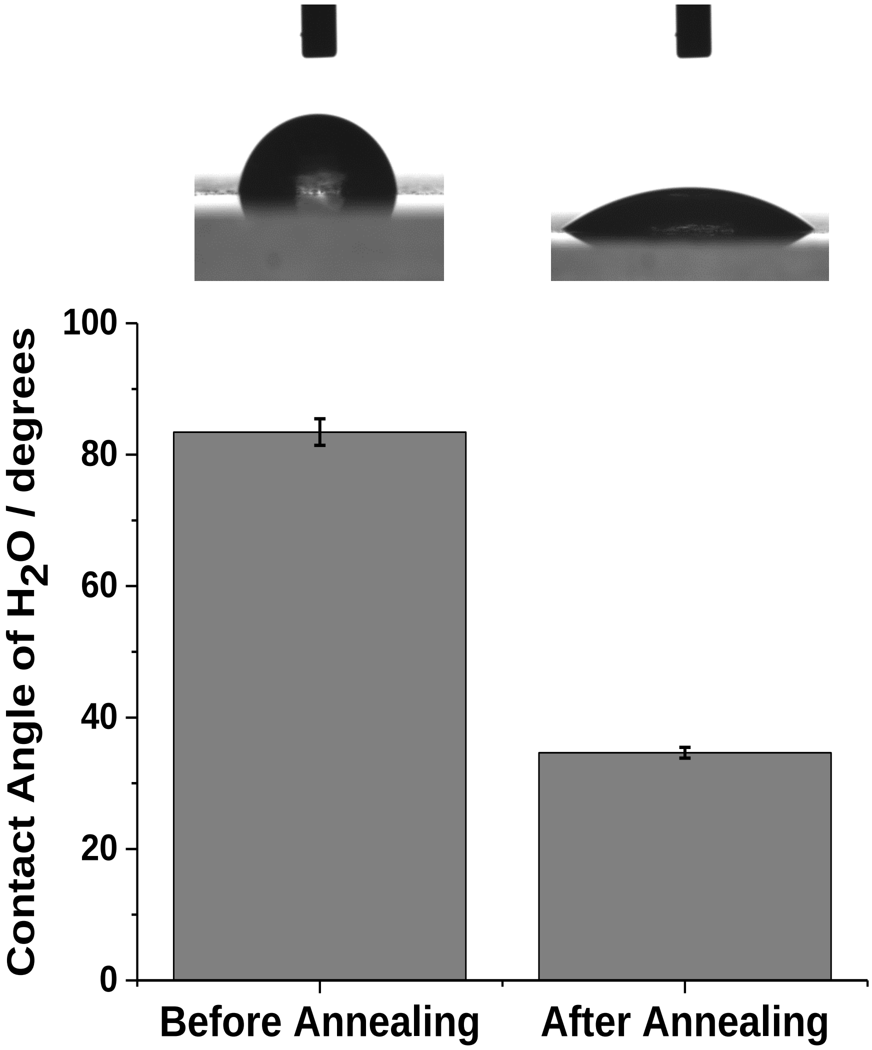

Figure 4.4.2.7 Contact angles of distilled H_2O on 5 pass 1 cm^2 prints using ink 4.3.2 on a glass substrate with and without annealing at 450°C for 40 minutes. Error bars show standard contact angle deviation. Inset images show one of the imaged sessile H_2O droplets

4-point probe sheet resistance measurements were performed on printed samples of inks 4.3.1 and 4.3.2 before and after annealing. The only sample which gave a reading was a 5 pass printed sample of ink 4.3.1 without any annealing, with results of 24.89, 22.00, 28.63 mΩ $\square^{-1}$. This indicates a high sheet resistance, and therefore a low conductivity. Unfortunately, these were the only measurements that did not yield an error on the instrument and so no further sheet resistance measurements can be used as a comparison. The inability to obtain 4-point probe sheet resistance measurements may be explained by the relative softness of the deposited TiO_2 films when compared with the probe tips and substrate, causing the probe tips to simply penetrate through the films and fail to measure the high sheet resistance of the glass slide substrates.

4.4.3 SEM and TEM

SEM was used to investigate the surface topography of the printed films. Figure 4.4.3.1 shows SEM images obtained for an as-deposited inkjet printed 5 pass sample of ink 4.3.2. At low magnification, it is evident that the films are inhomogeneous. The results match well with the profilometry profiles. As magnification is increased, it appears that the deposits consist of cracked films. The cracking is likely formed as trapped solvent escapes from inside the forming film. Higher magnifications indicate the regions of un-cracked film to be homogeneous and smooth.

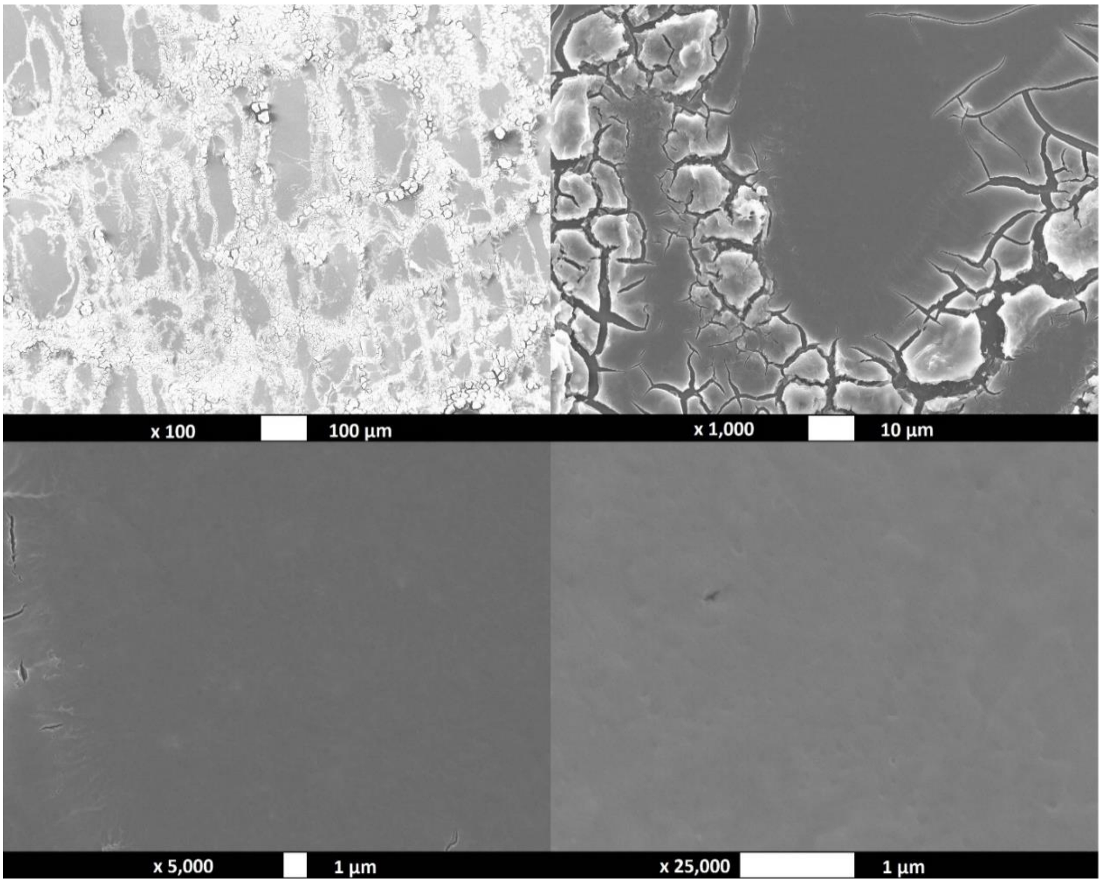

Figure 4.4.3.1 SEM of inkjet printed 5 pass ink 4.3.2 on a glass substrate without thermal treatment

SEM analysis was also performed on an inkjet printed 5 pass sample of ink 4.3.2 after annealing the sample at 450°C for 40 minutes (See Figure 4.4.3.2). Annealing does not appear to significantly affect the surface topology of the prints. At higher magnifications, there does appear to be an increase in stress-induced fractures of the film. However, this may not have been caused by the thermal anneal and instead may simply be due to the image being of a different sample. Figure 4.4.3.3 shows the same annealed sample when imaged at a different location. These images instead illustrate the cracks of the film, showing there is a large material build-up or shift at the very edges. Again, the apparent difference in height or thickness of the film agrees with the profilometry measurements.

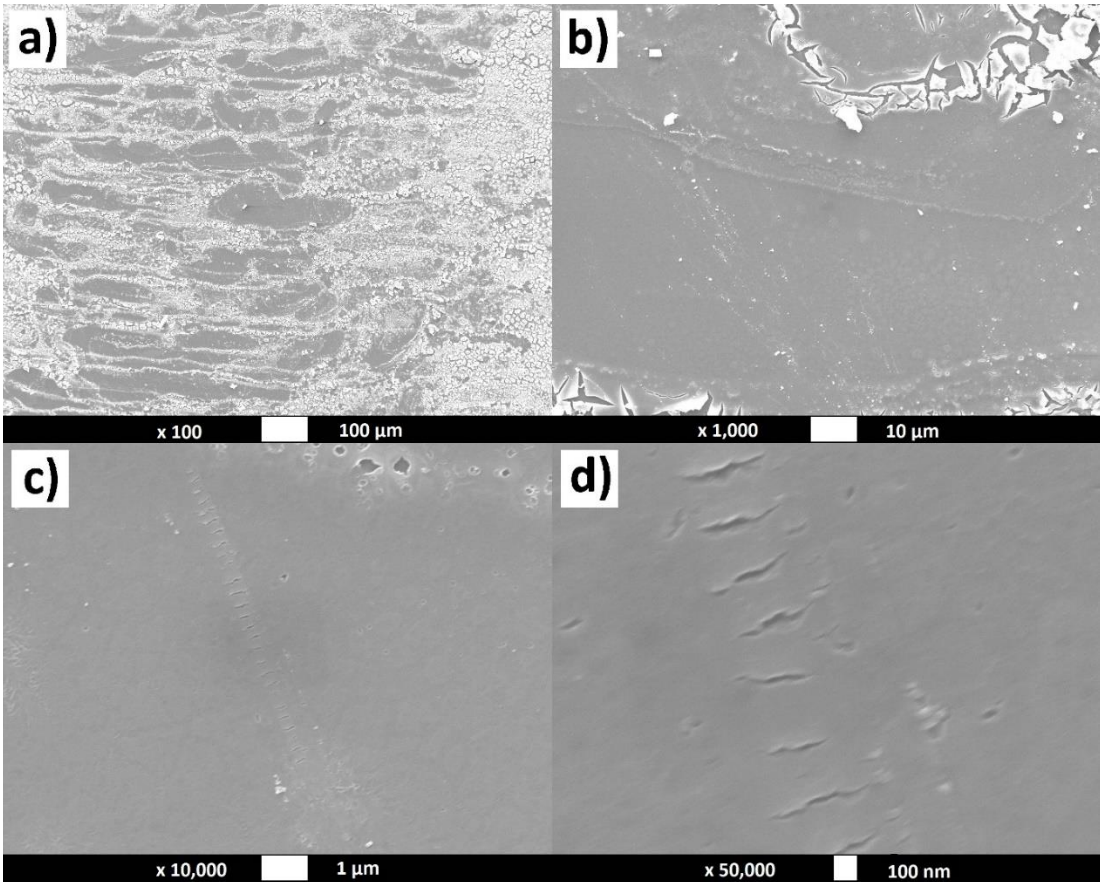

Figure 4.4.3.2 SEM of inkjet printed 5 pass ink 4.3.2 on a glass substrate after annealing at 450°C for 40 minutes

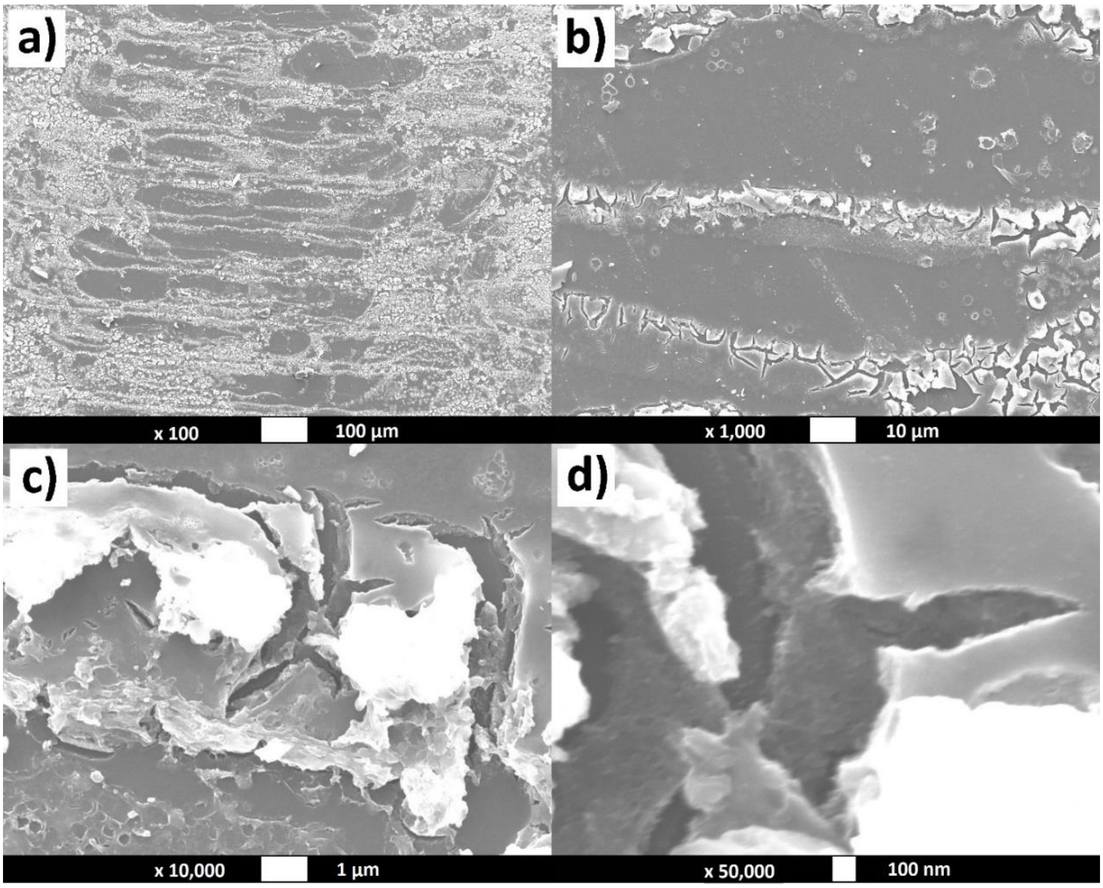

Figure 4.4.3.3 Alternate SEM of printed 5 pass ink 4.3.2 on a glass substrate after a 450°C anneal for 40 minutes

TEM was performed to obtain high resolution images of the sample surface, with emphasis on the temperature induced crystallisation of the TiO_2 thin films. Figure 4.4.3.4 shows TEM images of ink 4.3.2 after drying under ambient conditions. Image 4.4.3.4.a) shows that there is good cover of the TEM grid. Image 4.4.3.4.b) shows that the material is amorphous, due to the highly disordered and chaotic nature of the material. After annealing at 450°C for 40 minutes, Figures 4.4.3.5.a) and b) show that nanoparticles have formed and the material is now polycrystalline, indicating a high level of order that Raman and XRD analysis confirm is anatase formation. Higher magnification images indicate that there is still some amorphous TiO_2 present in the sample, suggesting for total conversion to anatase either a longer residence time or a higher annealing temperature is required.

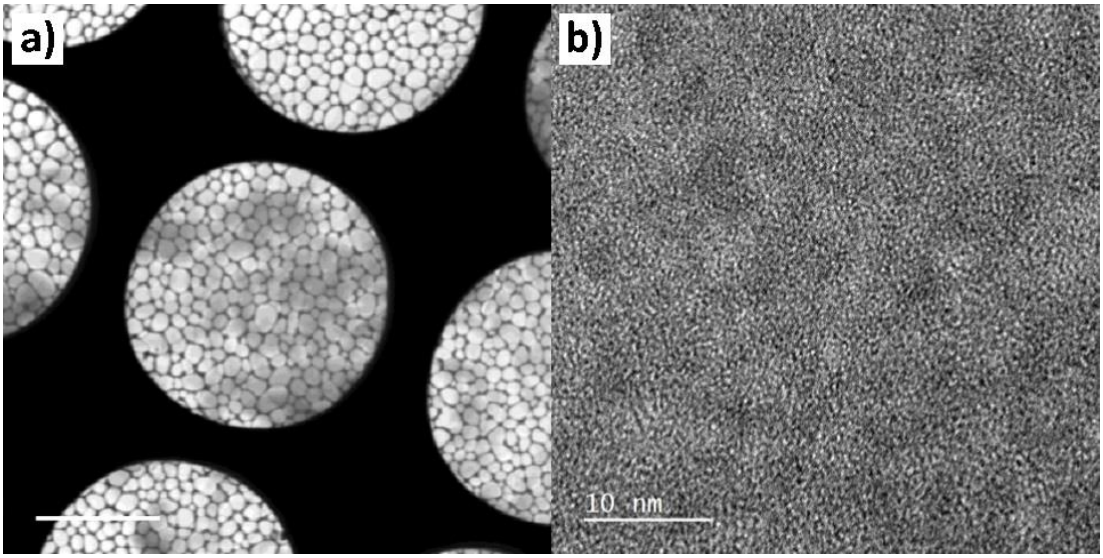

Figure 4.4.3.4 TEM images of drop-tested ink 4.3.2 dried under ambient conditions. Image a) is deposited on TEM grid, image b) is on ultra-smooth carbon foil

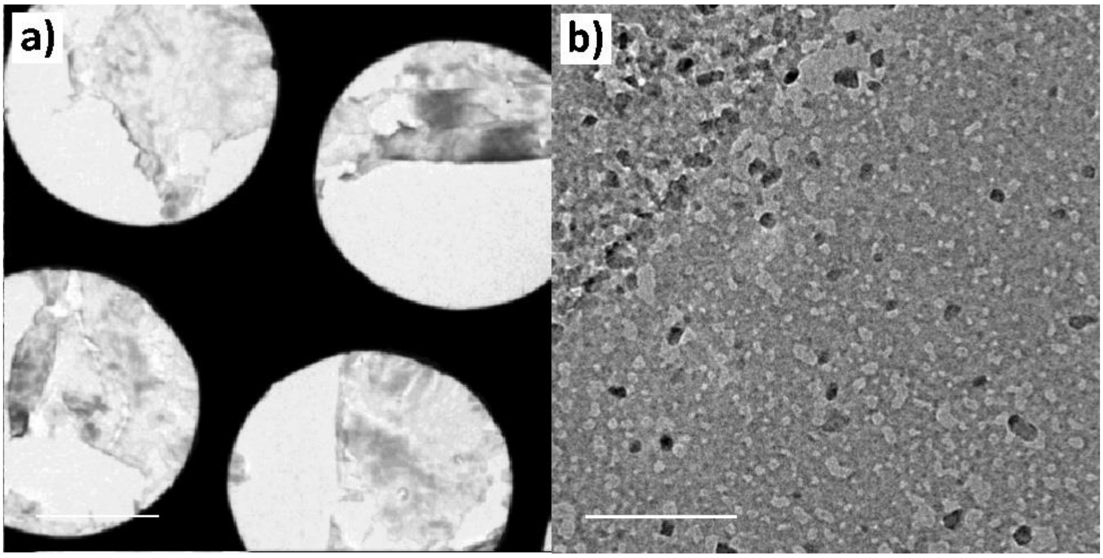

Figure 4.4.3.5 TEM images of drop-tested ink 4.3.2 after annealing at 450°C for 40 minutes. Image a) is deposited on TEM grid, image b) is on ultra-smooth carbon foil

4.5 Solution-based TTIP Ink Discussion & Conclusion

Previous research within the group suggested that tetraglyme and triglyme were potential candidates for use as stabilising agents with respect to the hydrolysis of TTIP into TiO_2. Due to time restraints, diglyme and DME had yet to be assessed. This work began by formulating multiple inks to investigate which of the four glycol ethers above would be best suited for use as a stabiliser to TTIP in inkjet printed inks. DME was identified as the best candidate due to the neat and stable tracks produced when printing with DME stabilised inks. It is suggested that having a similar boiling point to the ^{i}PrOH carrier solvent, the DME stabiliser is able to evaporate at a comparable rate and eliminate any Marangoni flows associated with surface tension gradients due to the changing chemical composition of the evaporating ink.

Using DME, the loading of the ink was increased up to a maximum of 0.15 M with respect to TTIP. Stability of the ink over a 28 day maturation period was shown by only a small increase in viscosity. Printed samples using ink 4.3.2 proved difficult to characterise due to the small quantity of TiO_2 deposited, necessitating the use of thicker drop-tested samples. Raman and XRD spectra show the as deposited drop-tested ink to be amorphous. Annealing temperatures of 450°C were shown to yield peaks related to anatase phase in both the XRD and Raman spectra.

Profilometry and SEM imagining indicated that the deposited films were not homogeneous in nature, with the films displaying a variable thickness caused by cracking. However, the profilometry results exhibit extreme fluctuations in sample height that are in disagreement with the smoother SEM images. It is proposed that the profilometry data suffers from unfavourable stylus-sample interactions, resulting in the stylus bouncing or dragging through the sample, yielding unreliable data. The unreliability of the profilometry data is exacerbated by the distorted baselines observed in many of the profiles. TEM showed that whilst crystallisation had begun to occur under the annealing conditions used, there was still a small presence of amorphous TiO_2.

Overall, the TTIP ink was optimised for inkjet printing and characterised. However, further increasing the loading of titanium in the ink would be advantageous as less printed passes would be required for the same quantity of TiO_2 deposit. Furthermore, a reduction in the thermal budget required for the formation of anatase would reduce the associated costs with producing thin film inkjet printed anatase. A significant reduction in the annealing temperatures required would also allow flexible plastic substrates to be used, increasing the applications of the films greatly.

4.6 References

1. N. Rahimi, R. A. Pax and E. M. Gray, *Progress in Solid State Chemistry*, 2016, **44**, 86-105.
2. U. Diebold, *Surface Science Reports*, 2003, **48**, 53-229.
3. J. Qiu, S. Zhang and H. Zhao, *Sensors and Actuators B: Chemical*, 2011, **160**, 875-890.
4. K. Nakata and A. Fujishima, *Journal of Photochemistry and Photobiology C: Photochemistry Reviews*, 2012, **13**, 169-189.
5. H. Ijadpanah-saravi, M. Safari, A. Khodadadi-Darban and A. Rezaei, *Analytical Letters*, 2014, **47**, 1772-1782.
6. M. E. Simonsen and E. G. Søgaard, *Journal of Sol-Gel Science and Technology*, 2010, **53**, 485-497.
7. F. Biechel, J. Dubuc and M. Henry, *New Journal of Chemistry*, 2004, **28**, 764-769.
8. H. C. Ku and C. H. Tu, *Journal of Chemical and Engineering Data*, 1998, **43**, 465-468.
9. G. Vazquez, E. Alvarez and J. M. Navaza, *Journal of Chemical & Engineering Data*, 1995, **40**, 611-614.
10. P. J. Zheng, X. Y. Meng, J. T. Wu and Z. G. Liu, *INTERNATIONAL JOURNAL OF THERMOPHYSICS*, 2008, **29**, 1244-1256.
11. A. Conesa, S. Shen and A. Coronas, *International Journal of Thermophysics*, 1998, **19**, 1343-1358.
12. A. W. Czanderna, C. N. R. Rao and J. M. Honig, *Transactions of the Faraday Society*, 1958, **54**, 1069-1073.
13. Z. Zhang, G. Triani and L.-J. Fan, *Journal of Materials Research*, 2011, **23**, 2472-2479.
14. A. S. Bakri, M. Z. Sahdan, F. Adriyanto, N. A. Raship, N. D. M. Said, S. A. Abdullah and M. S. Rahim, *AIP Conference Proceedings*, 2017, **1788**, 1-8.
15. S. G. Kumar and L. G. Devi, *Journal of Physical Chemistry A*, 2011, **115**, 13211-13241.
16. J.-M. Herrmann, *Catalysis Today*, 1999, **53**, 115-129.
17. R. Wang, K. Hashimoto, A. Fujishima, M. Chikuni, E. Kojima, A. Kitamura, M. Shimohigoshi and T. Watanabe, *Nature*, 1997, **388**, 431-432.
18. J. P. W. Treacy, H. Hussain, X. Torrelles, G. Cabailh, O. Bikondoa, C. Nicklin, G. Thornton and R. Lindsay, *The Journal of Physical Chemistry C*, 2019, **123**, 8463-8468.

19. M. Takeuchi, K. Sakamoto, G. Martra, S. Coluccia and M. Anpo, *The Journal of Physical Chemistry B*, 2005, **109**, 15422-15428.
20. K. Midtdal and B. P. Jelle, *Solar Energy Materials and Solar Cells*, 2013, **109**, 126-141.
21. R. J. Isaifan, A. Samara, W. Suwaileh, D. Johnson, W. Yiming, A. A. Abdallah and B. Aïssa, *Scientific Reports*, 2017, **7**, 9466.
22. T. Adachi, S. S. Latthe, S. W. Gosavi, N. Roy, N. Suzuki, H. Ikari, K. Kato, K.-i. Katsumata, K. Nakata, M. Furudate, T. Inoue, T. Kondo, M. Yuasa, A. Fujishima and C. Terashima, *Applied Surface Science*, 2018, **458**, 917-923.

Chapter 5

Nanoparticle and Hybrid Inks

5.1 Background and Introduction

After optimising the alkoxide ink formulation in Chapter 4, it was decided that further work was required in order to increase the loading of titanium within the inks. Increasing the concentration of TTIP within the ink above 0.15 M resulted in regular blocking of the dispensing device, necessitating the use of an additional titanium source. As discussed in Chapter 2, a commonly used titanium source for inkjet inks are TiO_2 nanoparticles.[1, 2] Nanoparticle containing inks offer several advantages, most notable of which is the ability to deposit the desired material in the correct phase as the ink itself contains the chosen material. Within the scope of this project, this advantage translates to direct deposition of TiO_2 in the anatase phase.

Unfortunately, nanoparticle containing inks also present several challenges: evenly dispersing the nanoparticles into solution, stabilising the nanoparticles with respect to aggregation, agglomeration, and sedimentation, jetting the nanoparticle ink, and sintering the nanoparticles together post-deposition to form a continuous film.[3, 4] It was proposed that by adding nanoparticles to the alkoxide ink formulated in Chapter 4 not only would titanium loading be increased; the challenge of post-deposition sintering could also be alleviated by

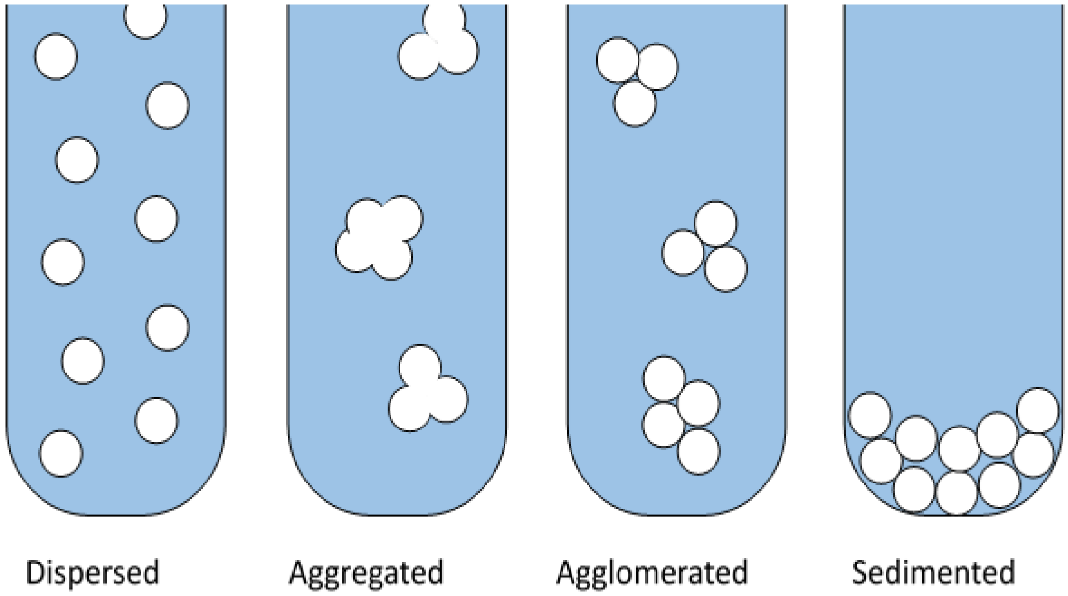

Figure 5.1.1 Illustrations of the aggregation, agglomeration, and sedimentation phenomena

the TTIP. The TTIP was predicted to hydrolyse and form TiO_2 between the anatase nanoparticles, creating a connective matrix for the nanoparticles. Furthermore, addition of phase-pure anatase within the printed deposit would potentially reduce the thermal budget required for the transition of amorphous TiO_2 into anatase; the anatase nanoparticles behaving as seeds or templates for the amorphous TTIP-sourced TiO_2, reducing the energetic barrier of anatase crystallisation. This hybrid ink strategy is, to the best of our knowledge, the first example of hybrid alkoxide / nanoparticle ink formulation.

Section 5.2 begins by discussing the in-house synthesis of anatase nanopowders, including their characterisation and ink formulations. Unfortunately, when passing the synthesised nanoparticle inks through the inkjet dispensing device the prevalence of blockages was too high. At this point it was decided that anatase nanoparticles would be purchased from Sigma-Aldrich. Section 5.3 describes the characterisation of these purchased nanoparticles, formulating them into a hybrid ink, and the subsequent analysis of the printed samples generated when using this hybrid ink. Annealing studies were performed to deduce the minimum temperature at which the amorphous TiO_2 derived from the TTIP component of the hybrid ink was changing into anatase phase. After showing this occurring at just 200°C by Raman and XRD, the hybrid ink was also printed onto a flexible plastic substrate which was thermally robust enough to handle the heat treatment. Concluding remarks and potential implications are given in Section 5.4, with Section 5.5 containing the experimental procedures specific to this Chapter.

5.2 Nanoparticle Synthesis

There are several synthetic procedures present within the literature for the formation of anatase nanoparticles.[5-14] Not all of these syntheses are suitable for use within a hybrid inkjet ink formulation though.[3] Criteria that must be met include: high phase purity of anatase, fast synthetic procedure, minimal particle size, and a monodisperse particle size. As a consequence of the required size and dispersity control, all synthetic methods utilising a sol-gel route were deemed insufficient. In-house synthesis of anatase TiO_2 nanoparticles was performed using hydrothermal and reflux syntheses.

5.2.1 Hydrothermal Synthesis

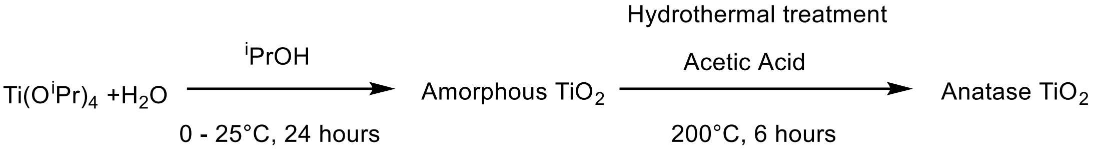

Scheme 5.2.1.1 Reaction scheme for the hydrothermal synthesis of anatase TiO_2 nanoparticles

The first nanoparticle synthesis performed was via a hydrothermal route, reported by Reyes-Coronado et al.[15] In the paper, it is shown that the anatase nanoparticles synthesised by this method had a radius of between 3 and 6 nm, increasing by hydrothermal treatment time at 200°C. Note that it is the nanoparticle radius that is reported rather than the size or diameter, which is between 6 and 12 nm. Performing the synthesis according to the literature yielded a pale white powder, confirmed to be crystalline anatase by Raman. Elemental CHN and IR analyses both indicated the presence of incorporated acetic acid.

XRD analysis of the hydrothermally synthesised nanoparticles was performed; the resulting spectrum is shown in Figure 5.2.1.1. All of the expected anatase peaks are present, including the large A(101) peak at a 2 θ of 25°. Lattice imperfections and grain boundaries reduce long-range order, therefore reducing crystallinity and XRD peak intensity.[16] Due to the small peak intensities present it was concluded that the particles were indeed nanosized, as smaller crystallites decrease long-range order. The Scherrer equation was used to calculate the crystallite size, as shown in equation (5.2.1.1); with τ being the mean size of the ordered domains (in this instance, the nanoparticle size), K being the dimensionless shape factor, λ being the X-ray wavelength, β being the full width at half maximum intensity (FWHM) in radians, and θ equal to the Bragg angle.[17] A FWHM intensity was measured for the A(101) peak (~25°) of the XRD, giving a value of 0.01274 radians. Using Kλ=1.38654 Å, the crystallite size was calculated to be 11.15 nm. The crystallite size is equivalent to the nanoparticle diameter, giving a nanoparticle radius of 5.58 nm. This size is in agreement with the reported radius of 3.3-6.3 nm by Reyes-Coronado et al.[15] However, the in-house synthesis involved a solvothermal treatment time of just 6 hours. This is a short solvothermal treatment time relative to the large particle size obtained; in the literature it was reported that a solvothermal time greater than 20 hours was required to yield particles above a 5 nm radius.

$$\tau = \frac{K.\lambda}{\beta.cos\theta} \tag{5.2.1.1}$$

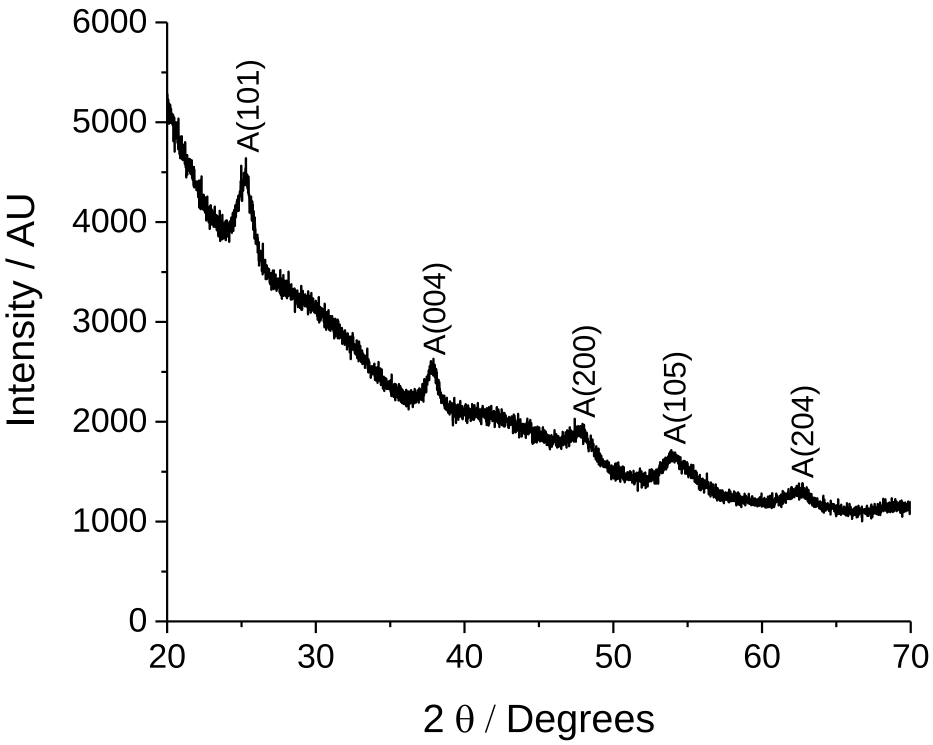

Figure 5.2.1.1 XRD pattern of hydrothermally synthesised nanopowder

5.2.2 Reflux Synthesis

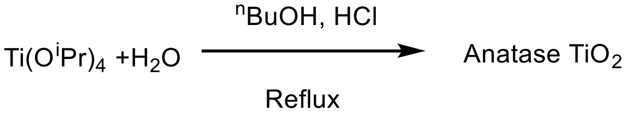

$$Ti(O^iPr)_4 + H_2O \xrightarrow[\text{Reflux}]{^n\text{BuOH, HCl}} \text{Anatase } TiO_2$$

Scheme 5.2.2.1 Reaction scheme for the reflux synthesis of anatase TiO_2 nanoparticles

A reflux synthesis reported by Burunkaya et al. was also identified as a promising route to anatase nanoparticles.[18] The anatase nanoparticles produced when refluxing $Ti(OEt)_4$ in ^{n}BuOH with HCl were stated to have an average particle size of ~3.5 nm. Substituting TTIP in place of the $Ti(OEt)_4$, the synthesis was repeated to yield a fine white powder which was analysed by Raman and XRD techniques. Both techniques obtained poor characterisation data, which indicated a minimal presence of anatase. The A(101) peak in the XRD was too ill-defined for the application of the Scherrer equation crystallite size analysis. Elemental CHN and IR spectroscopy suggested that the nanopowder contained a small amount of hydrocarbon impurity.

5.2.3 Printing with Synthesised Nanoparticles

Inks were formulated that contained the synthesised nanoparticles, using ^{i}PrOH as a carrier solvent. An ^{i}PrOH carrier solvent was chosen as it has been shown to be a suitable carrier for jetting the previous inks discussed in Chapter 4. Furthermore, when formulating a hybrid TTIP

/ nanoparticle ink, it is likely that ^{i}PrOH will be used as it is the parent alcohol of the isopropoxide ligand. Sonication was used to evenly disperse the nanoparticles into the ^{i}PrOH. Both the hydrothermal and reflux synthesised nanoparticle inks were found to block the dispensing device within very short timescales, before 50 consecutive droplet images could be captured. At this time, it was decided that previously prepared nanoparticles would be purchased and investigated for use in the formulation of a hybrid alkoxide / nanoparticle ink.

5.3 Nanoparticle and Hybrid Alkoxide / Nanoparticle Inks

5.3.1 Purchased Nanoparticle Analysis

Anatase phase TiO_2 nanopowder was purchased from Sigma-Aldrich and used to investigate the viability of a hybrid alkoxide / nanoparticle ink formulation for inkjet printing. The nanopowder had a quoted particle size of <25 nm. Provided the particles did not undergo significant aggregation or agglomeration, they would be small enough to pass through the 80 µm orifice of the dispensing device without increasing the likelihood of partial or complete blockage. Prior to any ink formulation, the purchased nanoparticles were characterised by Raman spectroscopy (See Figure 5.3.1.1). A clear and clean spectrum was obtained, containing sharp peaks assigned to the E_g, B_{1g}, and A_{1g} modes. There was no significant peak shift or broadening observed.

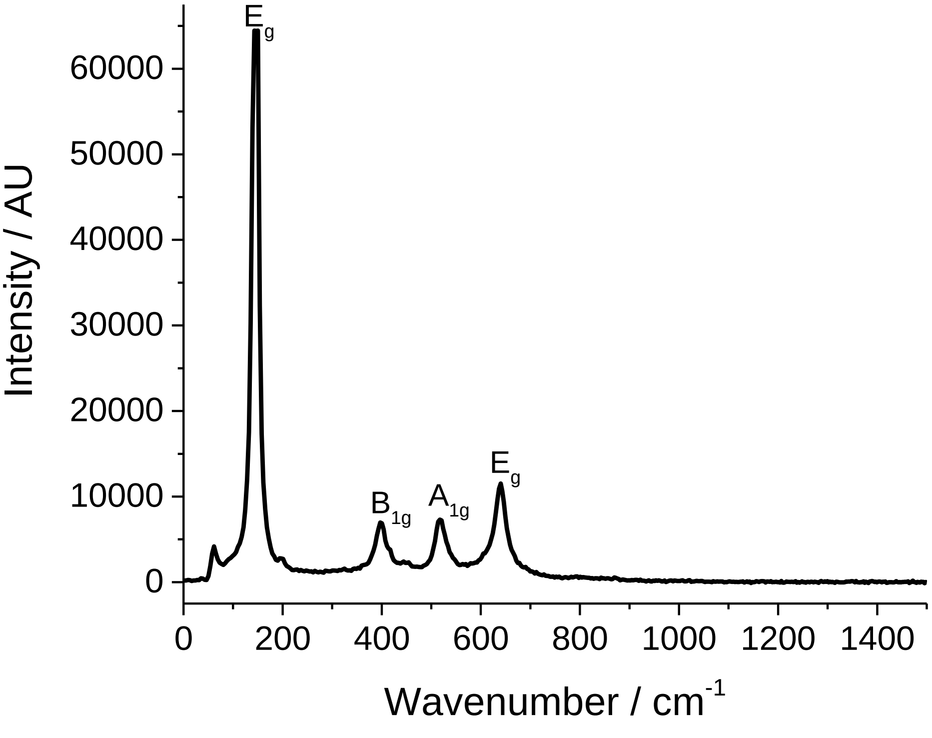

Figure 5.3.1.1 Raman spectrum of the purchased anatase nanopowder

Further characterisation of the purchased nanoparticles was obtained using XRD (See Figure 5.3.1.2). The expected A(101), A(004), A(200), A(105), and A(204) peaks are all present. The FWHM intensity was measured for the A(101) peak (25°) in the XRD pattern as 8.339 x 10^{-3} radians. Using this value in the Scherrer equation, the crystallite size was calculated as 17.04 nm; this agrees well with the <25 nm size quoted by the nanoparticle supplier, Sigma-Aldrich. The crystallite sizes calculated by the Scherrer equation indicate that the hydrothermally synthesised nanoparticles from 5.2.1. are smaller than those purchased from Sigma-Aldrich (11.15 and 17.04 nm, respectively). As the synthesised nanoparticles are identified as smaller crystallites yet result in blockage this indicates that either the synthesised nanoparticles are larger than the Scherrer equation calculates and consist of aggregates of ca. 11.15 nm crystallites, or the synthesised nanoparticles undergo significant aggregation or agglomeration when in solution or during the sonication process.

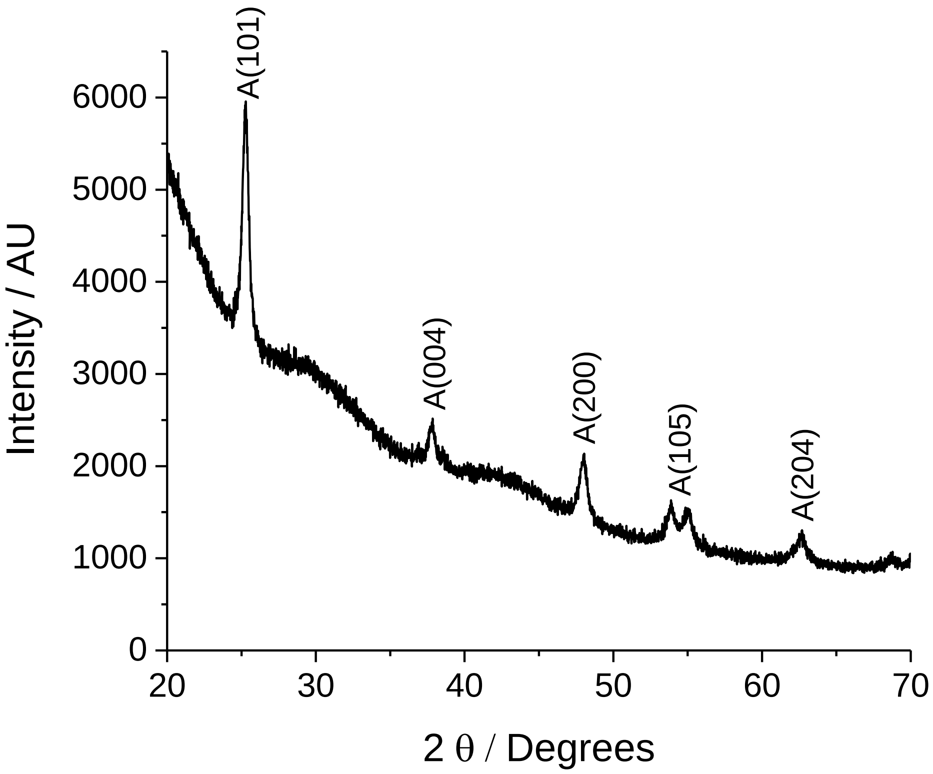

Figure 5.3.1.2 XRD pattern of the purchased anatase nanopowder

5.3.2 Nanoparticle Ink Formulation and Printing

After characterising the purchased nanoparticles, two inks were formulated which were similar to the alkoxide inks discussed in Chapter 4 to allow comparisons to be drawn. One ink consisted of a 0.1 M final concentration of Ti from nanoparticles, with a 1.5 M concentration of DME, in ^{i}PrOH; this ink will be designated ink 5.3.1. The other ink consisted of a final concentration of 0.1 M Ti from nanoparticles, 0.15 M TTIP, 1.5 M DME, in ^{i}PrOH. This is equivalent to the same 0.15 M TTIP ink discussed in Chapter 4, ink 4.3.2, with the addition of a 0.1 M concentration of Ti in the form of nanoparticles; this ink will be designated ink 5.3.2. Prior to printing, the nanoparticles were dispersed into the ink by sonication.

Sonicating a sample with the intention of homogeneous dispersion of nanoparticles is a complex process. There exists a time under sonication where the particles are at their smallest and most disperse. Prior to this time, the acoustic cavitation energy is agitating the particles such that their aggregates (strong, chemically bonded particles) are being fragmented. After this time, the excess sound energy causes the particle size to increase as agglomerates (weak, physically bonded particles) begin to form. Thus, the minimum in an average particle size versus sonication time graph is the ideal time for sonication to be performed. Dynamic light scattering (DLS) studies showed the presence of minima after a 120 minute sonication time. However, the hydrodynamic radius was only slightly larger after 60 minutes of sonication. It was decided a 60 minute sonication time was appropriate for all further nanoparticle inks in order to reduce preparation time and reduce the time required to wait for the ink to cool after sonication.

The rheological properties of the two nanoparticle inks were measured after 60 minutes of sonication and subsequent cooling to 20°C, the results of which are shown in Table 5.3.2. Addition of nanoparticles did not significantly affect the viscosity, density, or surface tension when compared to the base ink 4.3.2.

Table 5.3.2.1 Rheological properties of nanoparticle inks at 20°C

Ink Composition	**Ink Designation**	**Viscosity mPa s**	**Density g cm^{-3}**	**Surface Tension mN m^{-1}**
^{i}PrOH	^{i}PrOH	2.529	0.7870	19.27
DME	DME	0.445	0.8630	23.41
0.15 M TTIP, 1.5 M DME	4.3.2	1.892	0.7992	20.57
0.1 M NP, 1.5 M DME	5.3.1	1.953	0.7942	20.44
0.1 M NP, 0.15 M TTIP, 1.5 M DME	5.3.2	1.900	0.8040	20.70

The nanoparticle inks were then loaded into the inkjet printer and screened for appropriate printing parameters. Both inks jetted a steady stream of uniform droplets using the waveform generated for ^{i}PrOH, which was expected given their similar rheological properties to ink 4.3.2. Table 5.3.2.2 summarises the optimised properties of each ink as it was printed.

Figure 5.3.2.1 shows that the printed track when using ink 5.3.1 does not display straight edges, or an even deposition of material. The single and multiple pass printed square arrays, shown in Figures 5.3.2.2.a and b show that material deposition remains uneven for larger prints. There are also several stray droplets placed outside of the print boundaries.

Table 5.3.2.2 Measured and optimum print properties of nanoparticle inks

Ink Designation	Droplet Diameter µm	Print Speed mm s^{-1}	Step Size mm	Track Width µm
5.3.1	63.1 ± 1.3	10	0.1	211.8
5.3.2	77.3 ± 1.2	10	0.1	208.0

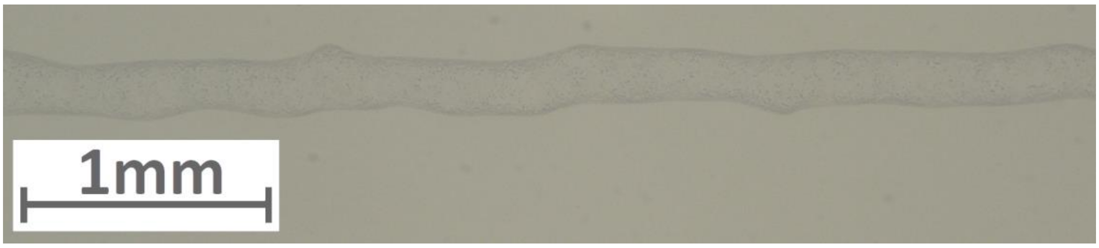

Figure 5.3.2.1 Printed track using ink 5.3.1 at 10 mm s^{-1} print speed and 0.1 mm step size on a glass substrate. Image brightness has been increased by 40 % for clarity.

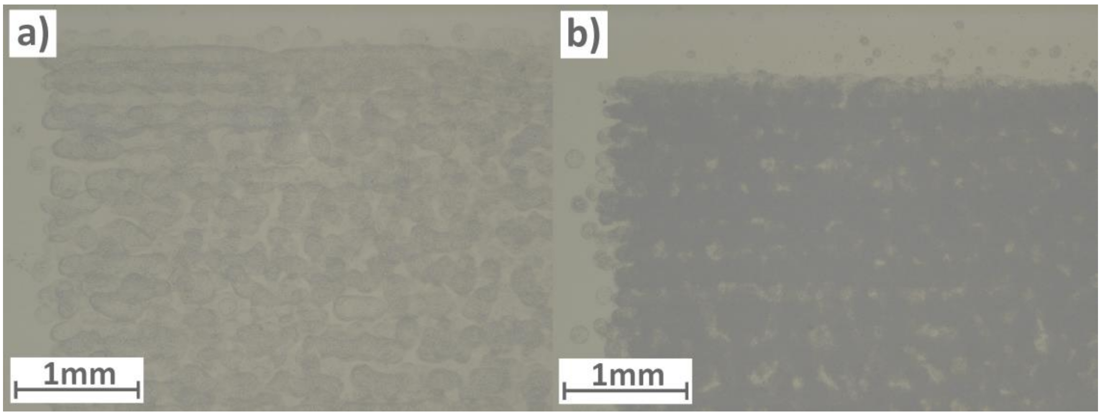

Figure 5.3.2.2 Printed 1 cm^2 using ink 5.3.1 at optimised print conditions on a glass substrate. Image a) is 1 pass and b) is 5 passes. Image brightness has been increased by 40 % for clarity.

When printing with the TTIP containing ink 5.3.2 (See Figure 5.3.2.3), the printed track displays straighter edges and a more even material deposition when compared to the track using ink 5.3.1 (See Figure 5.3.2.1); although the edge is still neither straight nor homogeneous in material deposition. Figure 5.3.2.4. a) also shows an uneven deposition of TiO_2 for the single pass print, however Figure 5.3.2.4. b) demonstrates a thicker and more uniform deposition of material for the bulk of the multiple pass print. The top edge is straight and well defined. The left edge appears to consist of less material than the rest of the print; this could be due to the left edge being the starting position for jetting along each row and consequently exhibiting the first droplet phenomena.

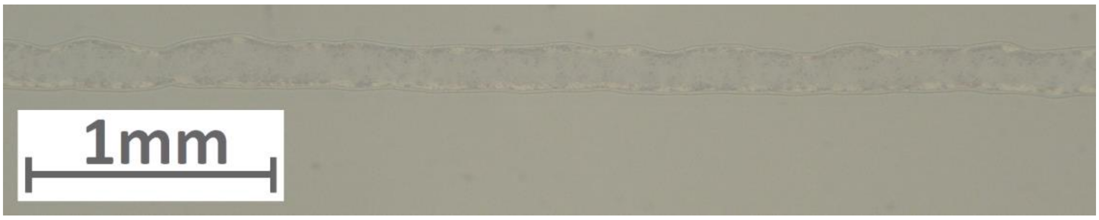

Figure 5.3.2.3 Printed track using ink 5.3.2 at 10 mm s^{-1} print speed and 0.1 mm step size on a glass substrate. Image brightness has been increased by 40 % for clarity.

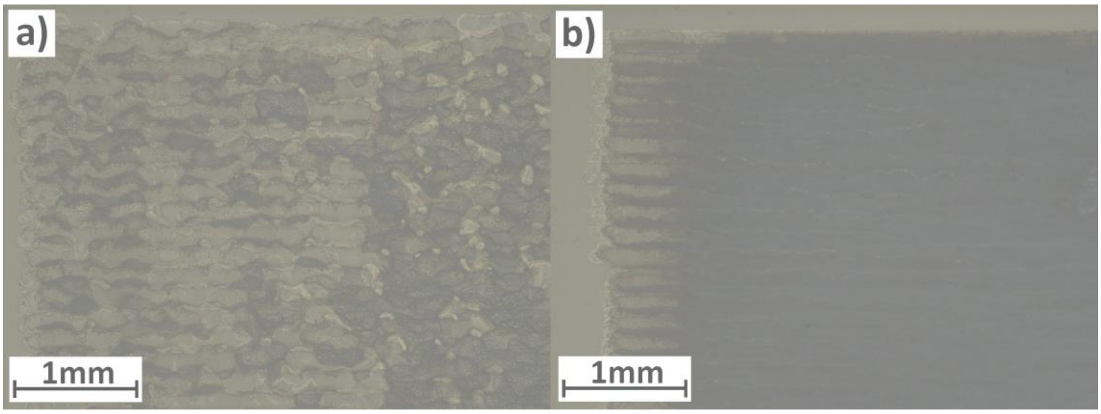

Figure 5.3.2.4 Printed 1 cm^2 using ink 5.3.2 at optimised print conditions on a glass substrate. Image a) is 1 pass and b) is 5 passes. Image brightness has been increased by 40 % for clarity.

5.3.3 Hybrid Ink Ageing Study

An ageing study was performed for the hybrid ink 5.3.2. The ink was sonicated for 60 minutes and then left to cool prior to each viscosity measurement. Sonication was required to evenly redisperse the nanoparticles into the ink. It was important to allow the ink to cool prior to measurement as viscosity is highly temperature dependent. Figure 5.3.3.1 shows the results of the ageing study. As was the case with ink 4.3.2, there is a slight increase in viscosity as the ink ages. Again, this is likely caused by the reaction of H_2O with the TTIP present in the ink. An increase in mean viscosity from 1.9013 to 1.9307 mPa s was observed, resulting in a 1.55 % increase. The decrease in viscosity when t = 1 day is likely to result from the ink solution not having cooled to 20°C prior to the measurement being taken.

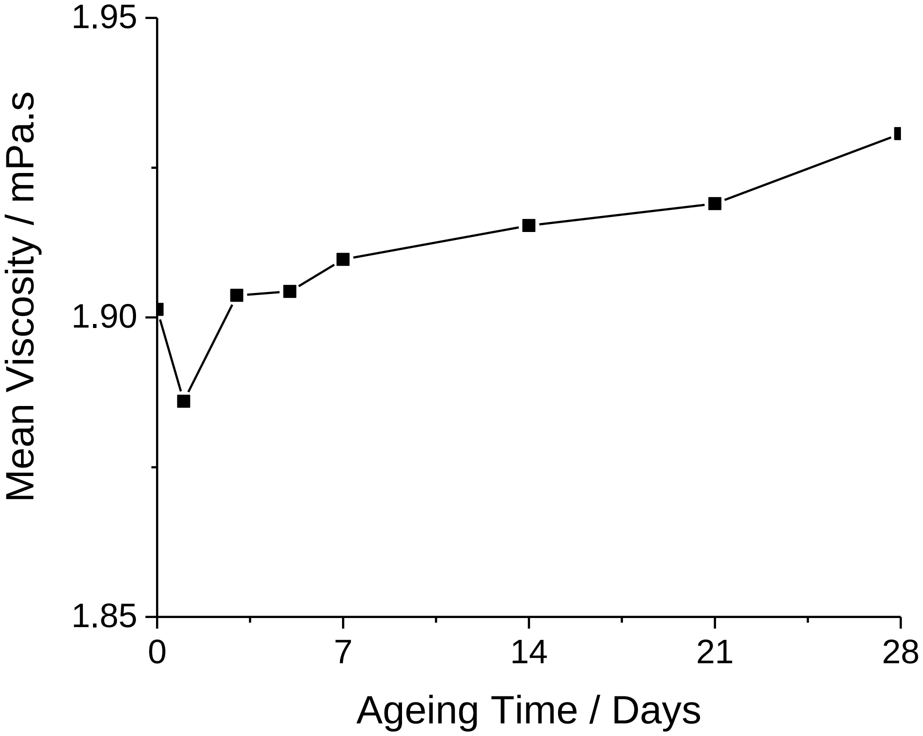

Figure 5.3.3.1 Ageing data for ink 5.3.2 over a 28 day maturation time

5.3.4 Annealing, XRD, and Raman Investigation

Drop-tested samples of ink 5.3.2 were analysed using XRD prior to annealing. Anatase peaks were observed at small intensities due to the presence of phase pure anatase nanoparticles within the ink formulation. Annealing studies were then performed to investigate the temperature at which the anatase peaks increase in intensity, indicating that the TTIP derived TiO_2 was converting from an amorphous state to anatase phase. Initial annealing at 400°C caused an increase in the intensity of the A(101) peak within the XRD spectra (See Figure 5.3.4.1). Lower annealing temperatures were investigated, with temperatures as low as 200°C causing an increase in the A(101) peak intensity (See Figure 5.3.4.2). For this investigation, the same samples were used for each pair of measurements; a measurement was taken prior to annealing, and another was taken of the same sample after annealing. It was important to compare the same sample before and after annealing as it was the change in A(101) peak intensity after annealing that was being examined.

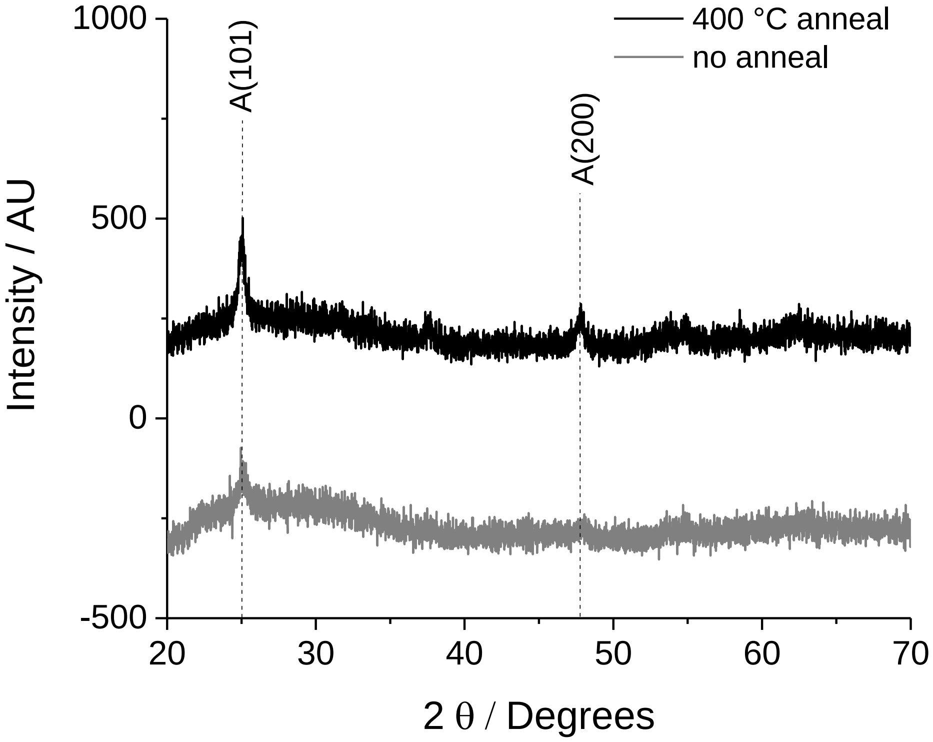

Figure 5.3.4.1 XRD spectra of drop-tested ink 5.3.2 on a glass substrate before and after annealing at 400°C for 40 minutes

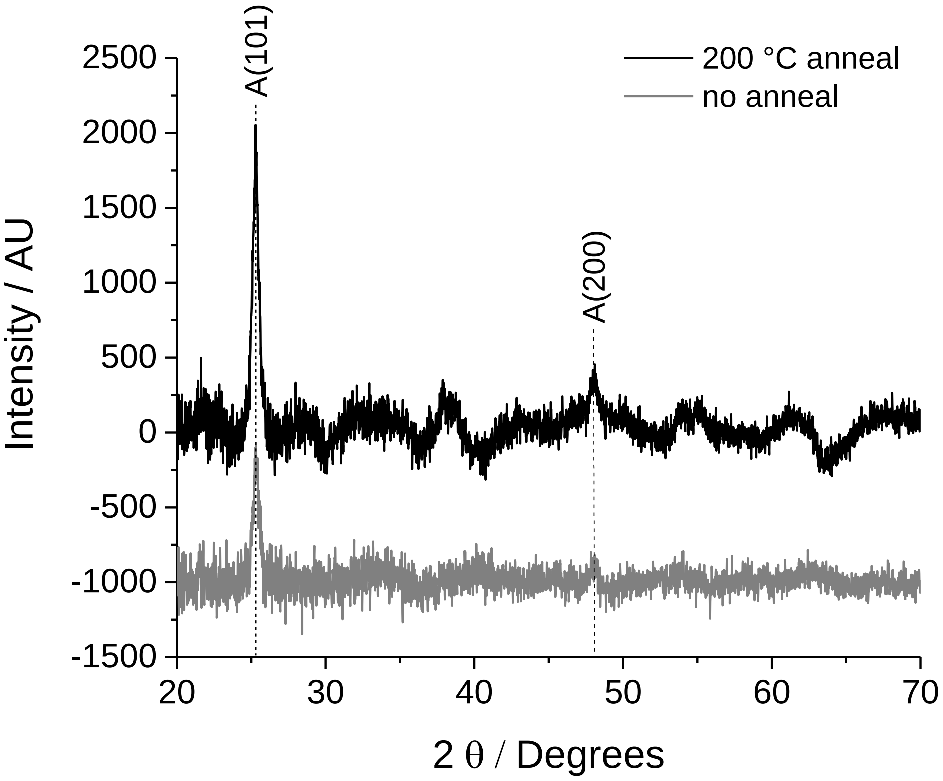

Figure 5.3.4.2 XRD spectra of drop-tested ink 5.3.2 on a glass substrate before and after annealing at 200°C for 160 minutes

Following a successful identification of the minimum temperature required to form anatase by XRD analysis, Raman spectroscopy was used to support the XRD results. A drop-tested sample of ink 5.3.2 was placed into the Raman spectrometer. The beam was focussed onto the sample, with the exact location of the sample being saved. After obtaining the sample spectrum prior to annealing, the sample was carefully removed and annealed at 200°C for 160 minutes. The sample was then placed into the Raman spectrometer and moved to the same location as it was analysed previously. Another sample spectrum was then obtained of the same sample spot after annealing; the results of these two spectra are shown in Figure 5.3.4.3.

Prior to annealing the higher intensity E_g stretch of anatase is visible, showing the presence of the anatase nanoparticles in the deposit. The lower intensity B_{1g}, A_{1g}, and E_g stretches can also be identified just above the baseline. After annealing the intensity of all anatase peaks is increased greatly, with the large E_g peak intensity being increased by a factor of 12.3 after the heat treatment. This suggests that the anatase crystallinity has increased after annealing, supporting the findings from the XRD data. As lower temperatures are required for the crystallisation of anatase from amorphous TiO_2 in the presence of phase pure anatase nanoparticles, this indicates that the anatase nanoparticles are acting as nucleation sites or seeds for the crystallisation of the amorphous precursor material.

An annealing temperature of 200°C is 250°C lower than that required for ink 4.3.2. This reduced annealing temperature is sufficiently low enough to facilitate printing on some of the more thermally robust flexible plastic substrates, such as polyethylene terephthalate (PET). Although lower temperatures have been reported elsewhere, there are often inherent drawbacks associated with the processing. The apparent seeding effect displayed by the nanoparticles in ink 5.3.2 is, to the best of our knowledge, the first example of the inclusion of seeds in an inkjet ink formulation.

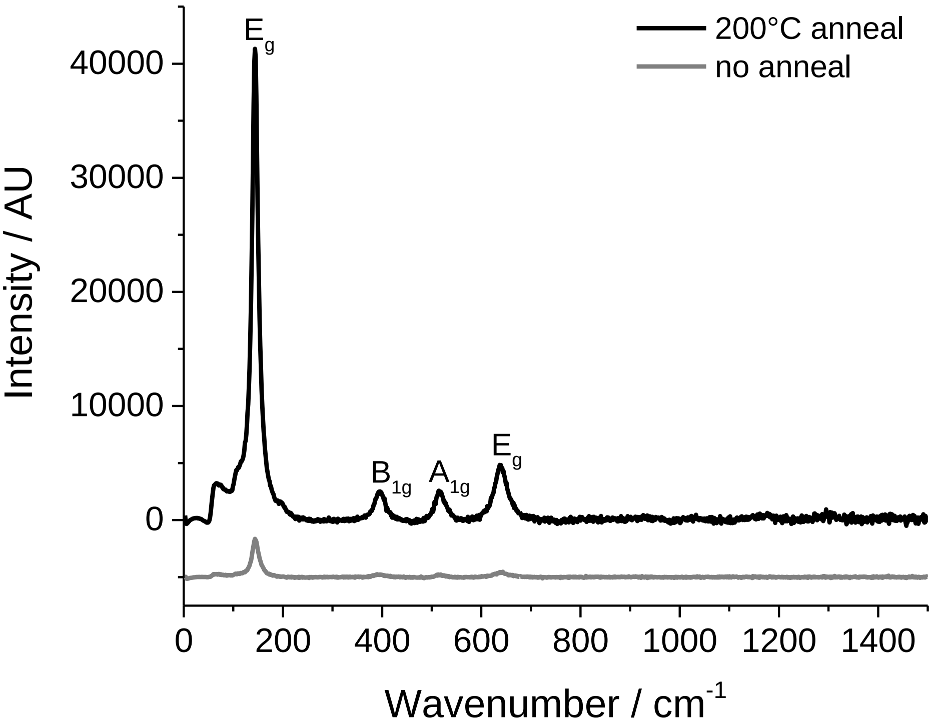

Figure 5.3.4.3 Overlaid Raman spectra of drop-tested ink 5.3.2 on a glass substrate before and after annealing at 200°C for 160 minutes

5.3.5 Profilometry, Optical Transmittance, and Wettability

Profilometry was performed on 5 pass 1 cm^2 printed samples using both inks 5.3.1 and 5.3.2. The results for the ink 5.3.1 samples were unusable, with a negative mean height of -301 nm without annealing, and -63 nm after a 160 minute anneal at 200°C. As such, they will not be discussed further. Figures 5.3.5.1, A.5.3.5.1, 5.3.5.2, and A.5.3.5.2 show the profiles obtained for the samples using ink 5.3.2 without annealing. All of the profiles show that a film has been formed, with very few heights approaching 0 nm within the bounds of the prints.

Figures 5.3.5.1 and A.5.3.5.1 show the left and right profiles, with the stylus moving perpendicular to the printed tracks that constitute the overall sample. Both figures show that the boundaries of the print are well defined and the print is of the correct size, with the sample scan length starting at approximately 1000 µm and ending at 11000 µm. The height is smaller at the edges of the print compared to the bulk, although the height does fluctuate considerably throughout the sample. There are several large peaks, similar to those obtained in Chapter 4. A few troughs are also present that tend towards the baseline but never meet or pass it, suggesting the base of the film is continuous. These troughs are often only a single measurement; they may have been caused by a transient interaction between the stylus tip and the sample rather than a true measurement.

The top and bottom profiles are shown in Figures 5.3.5.2 and A.5.3.5.2, where the stylus moved parallel to the direction of the sample printed tracks. There are a few differences between these profiles and the left and right profiles discussed above; most notably is the larger size of the print boundaries, which show the print to be around 1000 µm, or 1 mm larger than desired. The profiles parallel to the printed tracks also show a slightly lower average height and increased height fluctuation. A mean height of 1457 nm was calculated using the average height of each of the four profiles.

The calculated theoretical film thickness of a printed 1 cm^2 of ink 5.3.2 was 124 nm per printed pass, with a predicted 619 nm thickness for a 5 pass printed sample. In comparison with the theoretically calculated film thickness, the experimentally observed thickness is 135 %, or 2.35 times thicker. As with the previously analysed samples in Chapter 4, this discrepancy is likely due to the number of assumptions made in the theoretical calculation of the film thickness. The addition of nanoparticles somewhat alleviates the assumption of a uniform density, as the nanoparticle density is quoted by the manufacturer. However, it is also assumed in the calculation that the ink is homogeneously mixed and this is far less likely with the presence of nanoparticles that have a high likelihood of sedimentation.

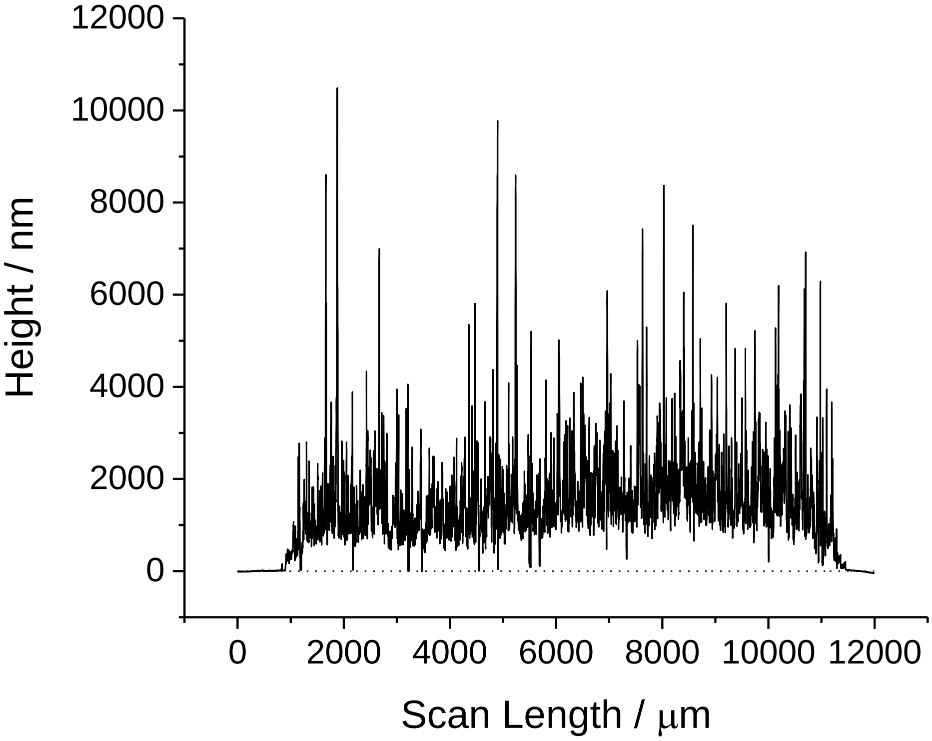

Figure 5.3.5.1 Left profile of 5 pass 1 cm^2 print using ink 5.3.2 on a glass substrate without annealing (average height of 1503 nm)

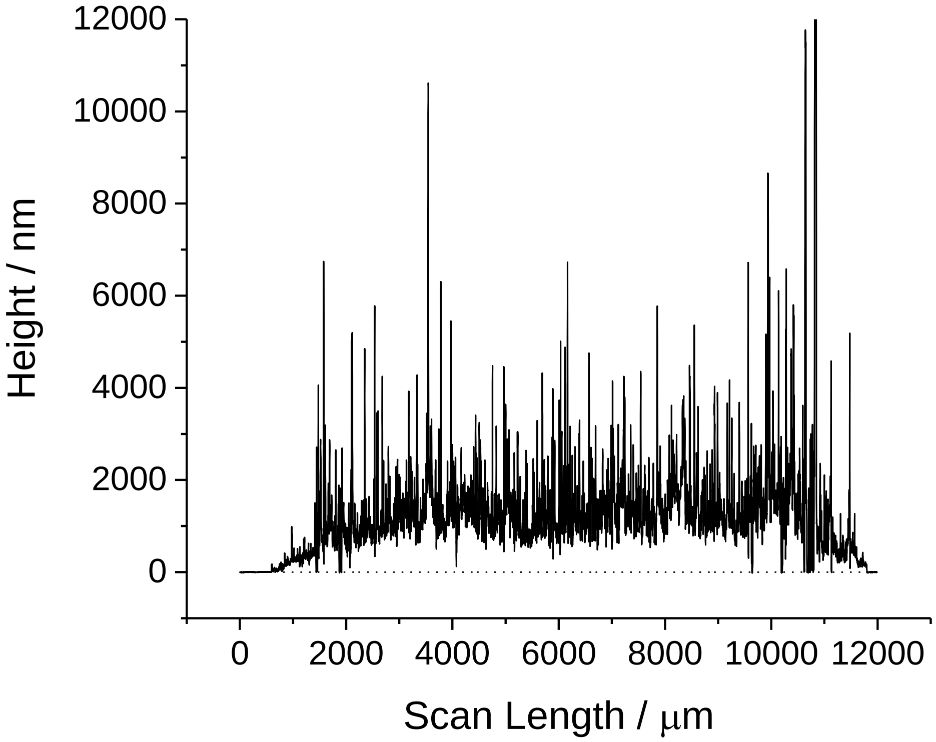

Figure 5.3.5.2 Top profile of 5 pass 1 cm^2 print using ink 5.3.2 on a glass substrate without annealing (average height of 1307 nm)

Another printed 5 pass 1 cm^2 sample using ink 5.3.2 was annealed at 200°C for 160 minutes before being analysed using the profilometer. The results are shown in Figures 5.3.5.3, A.5.3.5.3, 5.3.5.4, and A.5.3.5.4. All of the prints are approximately the correct size, with the peaks belonging to the printed film appearing within a 10000 µm scan length. Similar to the samples without annealing, the annealed samples show that a film has been printed, with a height above 0 nm within the bounds of the print. The profiles taken perpendicular and parallel to the printed tracks appear similar, indicating a more uniformly deposited sample than those previously discussed.

Figure 5.3.5.3 shows the left profile of the printed sample. There is a reduced number of large and sharp peaks when compared to the ink 5.3.2 samples without annealing. This difference may indicate a more uniform surface. The profile difference could also be caused by densification and subsequently an increased hardness of the sample, reducing any unwanted physical stylus-tip interactions. However, the print boundary at 11000 µm consists of the largest peak in the profile; this suggests a large presence of deposited material or may have been caused by a bump in the stylus. The right profile shown in Figure A.5.3.5.3 does not exhibit this same large peak at 11000, indicating that whatever caused the peak in the left profile was transient in nature. Similar to the left profile, the right profile indicates the sample is comparably uniform to the samples without annealing.

The top profile, shown in Figure 5.3.5.4, is similar to the left and right profiles despite the stylus moving parallel to the printed tracks rather than perpendicular. There are fewer tall, sharp peaks than the profiles obtained for the samples without annealing, indicating a more consistent sample thickness. Again, this may also be explained by an increased sample hardness after annealing, resulting in less bumping of the stylus as it's dragged across the sample surface. In comparison, the bottom profile contains taller peaks that are distributed more throughout the sample (See Figure A.5.3.5.4); this suggests the beginning of the print varies more with respect to height than the end of the print. A reason for this increased height variation could be the decap time of the dispensing device moving between jetting the ink droplets prior to printing and beginning the print at the centre of the stage. This increased decap time could also explain the unusually large profile peak at the lower print boundary of the left profile shown in Figure 5.3.5.3.

A mean sample height of 1601 nm was obtained for the printed 5 pass 1 cm^2 sample using ink 5.3.2 after annealing at 200°C for 160 minutes, using all four average sample heights. This height is 144 nm larger than the 1457 nm mean thickness of the similar sample without annealing, a 9.9% increase. It was hypothesised that the annealing process would decrease the mean height of the film due to the evaporation of any residual organic ink components and the densification of the deposited film. This decreased mean height was not observed in the two samples analysed, although there may have been a variation in height between the two samples after printing.

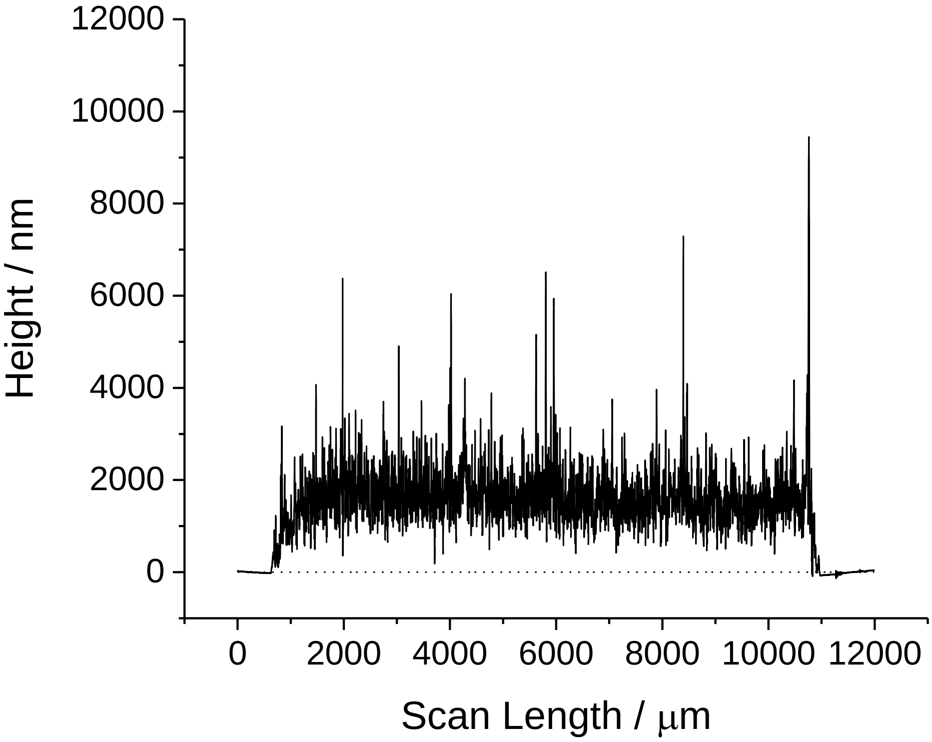

Figure 5.3.5.3 Left profile of 5 pass 1 cm^2 print using ink 5.3.2 on a glass substrate after 200°C for 160 minutes (average height of 1611 nm)

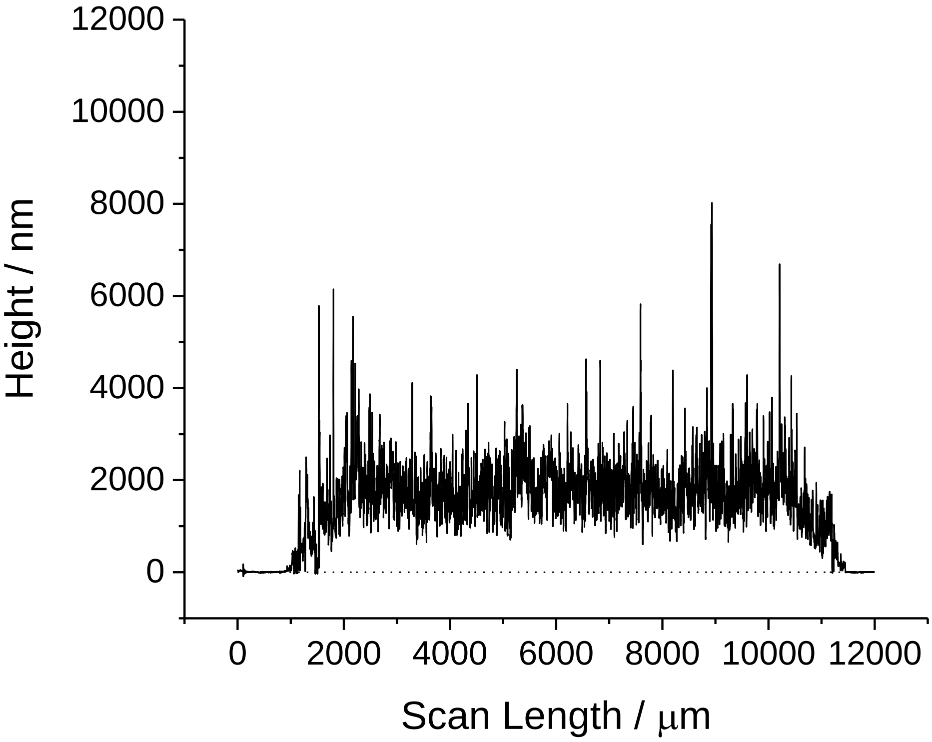

Figure 5.3.5.4 Top profile of 5 pass 1 cm^2 print using ink 5.3.2 on a glass substrate after 200°C for 160 minutes (average height of 1683 nm)

Transmittance spectra were obtained for printed 5 pass 1 cm^2 samples of inks 5.3.1 and 5.3.2. Figure 5.3.5.5 shows the overlay of two samples using ink 5.3.1, one without annealing and one after a 200°C anneal for 160 minutes. The two spectra are similar, with a non-linear decrease in transmittance as wavelength decreases from 900 nm to 350 nm. Below ca. 350 nm, the transmittance begins to increase slightly. A small jump in transmittance is observed at 300 nm due to the change in emission source and is seen in most of the spectrophotometric results. Transmittance is higher in the annealed sample, although the difference between the two does decrease with decreasing wavelength; the greatest difference is 7.5 % at 900 nm. It is proposed that the increased transmittance in the annealed sample is due to a reduction in scattering of incident light by the annealed sample due to its increased crystallinity. However, the transmittance may also have been increased by the removal of residual organic impurities from the ink after the annealing process.

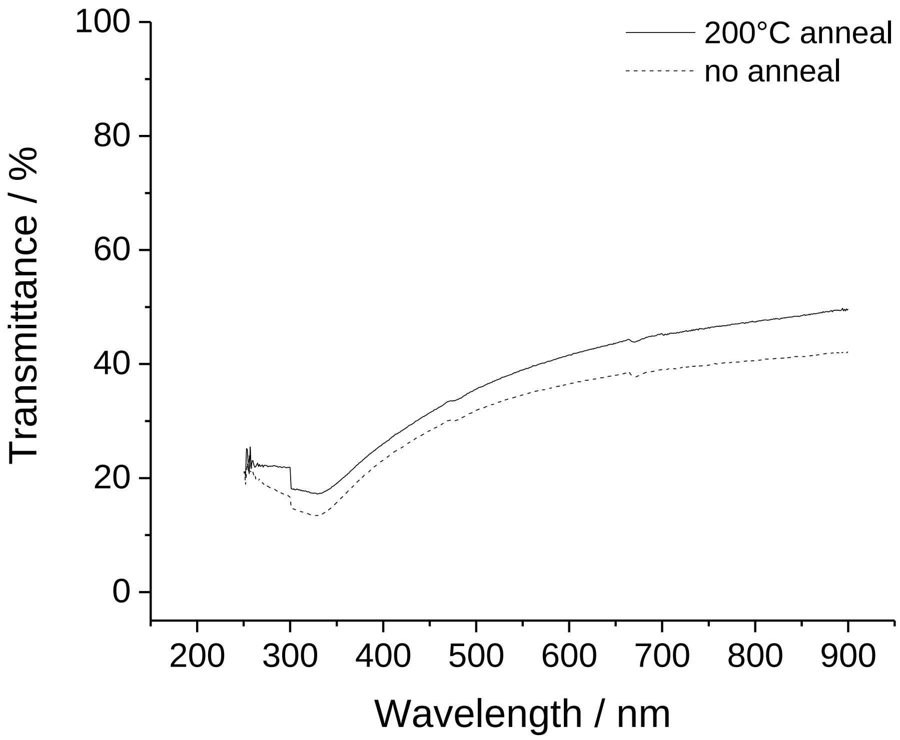

Figure 5.3.5.5 Optical transmittance of printed 5 pass 1 cm^2 using ink 5.3.1 on a glass substrate with and without annealing

Figure 5.3.5.6 shows the spectra obtained for the two printed samples using ink 5.3.2, one without annealing and the other after annealing at 200°C for 160 minutes. Both spectra show the samples to exhibit optical transmittance below 10 % at all wavelengths. Similar to the sample using ink 5.3.1, the general trend is for transmittance to decrease with a decreasing wavelength of light. The annealed sample exhibits a higher transmittance than the sample without annealing. Transmittance of the sample without annealing falls to almost zero at the lower wavelengths.

As the difference between inks 5.3.1 and 5.3.2 is the addition of TTIP as an additional titanium source, it can be deduced that the greatly reduced transmittance between Figures 5.3.5.5 and 5.3.5.6 is caused by the presence of TTIP. This is logically consistent with a thicker, more uniform, and more dense film being produced when using ink 5.3.2. Furthermore, as the optical transmittance is very low for the samples using ink 5.3.2, it is proposed that the alkoxide-derived TiO_2 forms a connective matrix between the anatase nanoparticles and thereby decreases transmittance significantly.

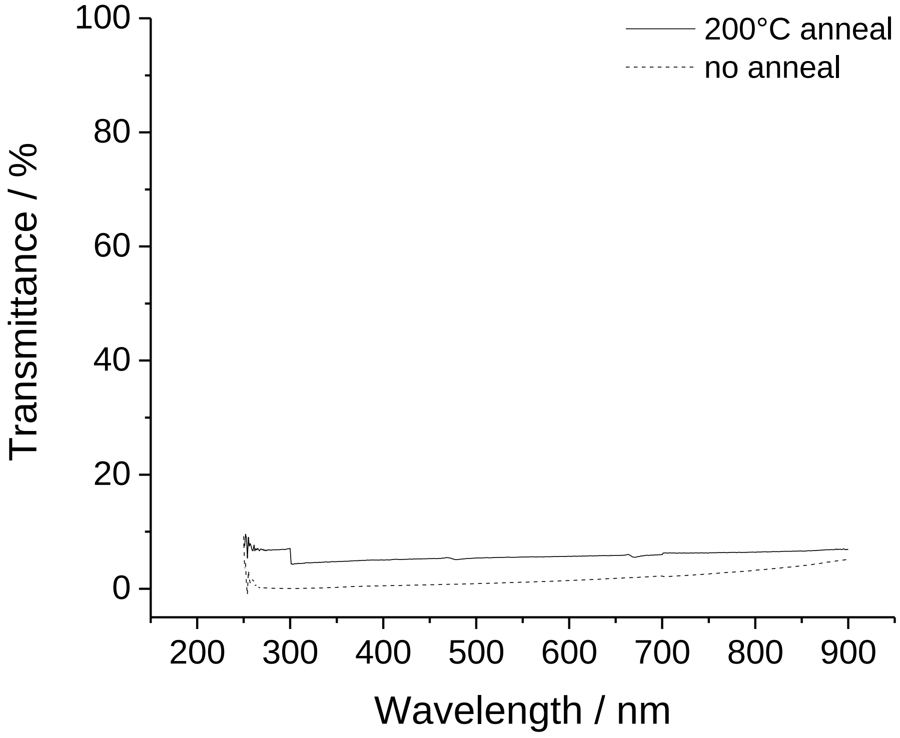

Figure 5.3.5.6 Optical transmittance of printed 5 pass 1 cm^2 using ink 5.3.2 on a glass substrate with and without annealing

The contact angle of distilled H_2O on inkjet printed 5 pass 1 cm^2 TiO_2 samples using ink 5.3.2 was investigated (see Figure 5.3.5.7). A mean contact angle of 104° was found for the sample without any thermal processing. A mean contact angle of 119° was found for the sample that had been annealed at 200°C for 160 minutes; an increase of 13.8 % compared to the sample that was not annealed. Both contact angles are relatively high when compared to other samples of anatase TiO_2. Wang et al. report a contact angle of 70°,[19] Isaifan et al. report a contact angle of 43°,[20] and Adachi et al. report a contact angle of ca. 48°.[21] This increased contact angle is likely caused by a high surface roughness and a Cassie-Baxter model of wettability.

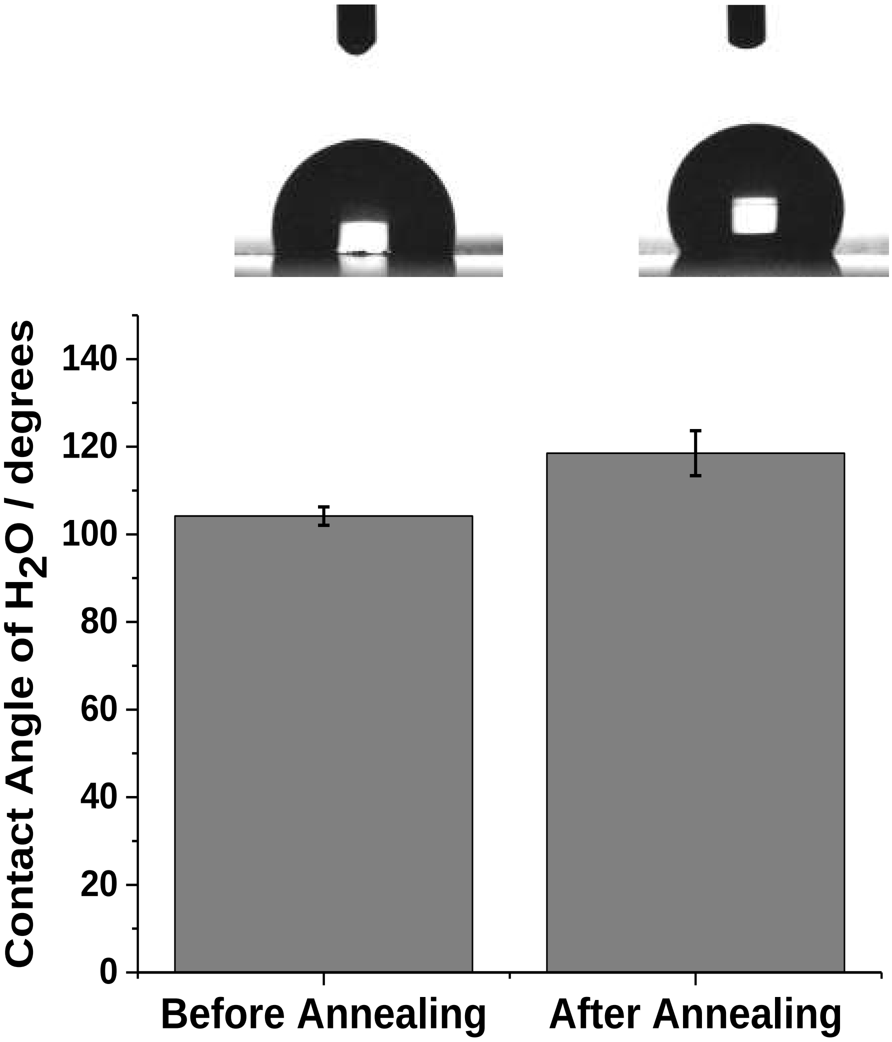

Figure 5.3.5.7 Contact angles of distilled H_2O on 5 pass 1 cm^2 prints using ink 5.3.2 on a glass substrate with and without annealing at 200°C for 160 minutes. Error bars show standard contact angle deviation. Inset images show one of the imaged sessile H_2O droplets

5.3.6 SEM and TEM

The surface topography of 5 pass 1 cm^2 inkjet printed films using ink 5.3.2 were analysed using SEM (See Figure 5.3.6.1). At low magnification, the film appears fairly homogeneous with a few areas of thicker deposit that are likely caused by aggregated nanoparticles on the surface. Increasing the magnification shows that the film is cracked rather than smooth, with crevasses throughout. The nanoparticles are glued together by a connective matrix of the TTIP-derived amorphous TiO_2, forming irregularly shaped and sized plates of material.

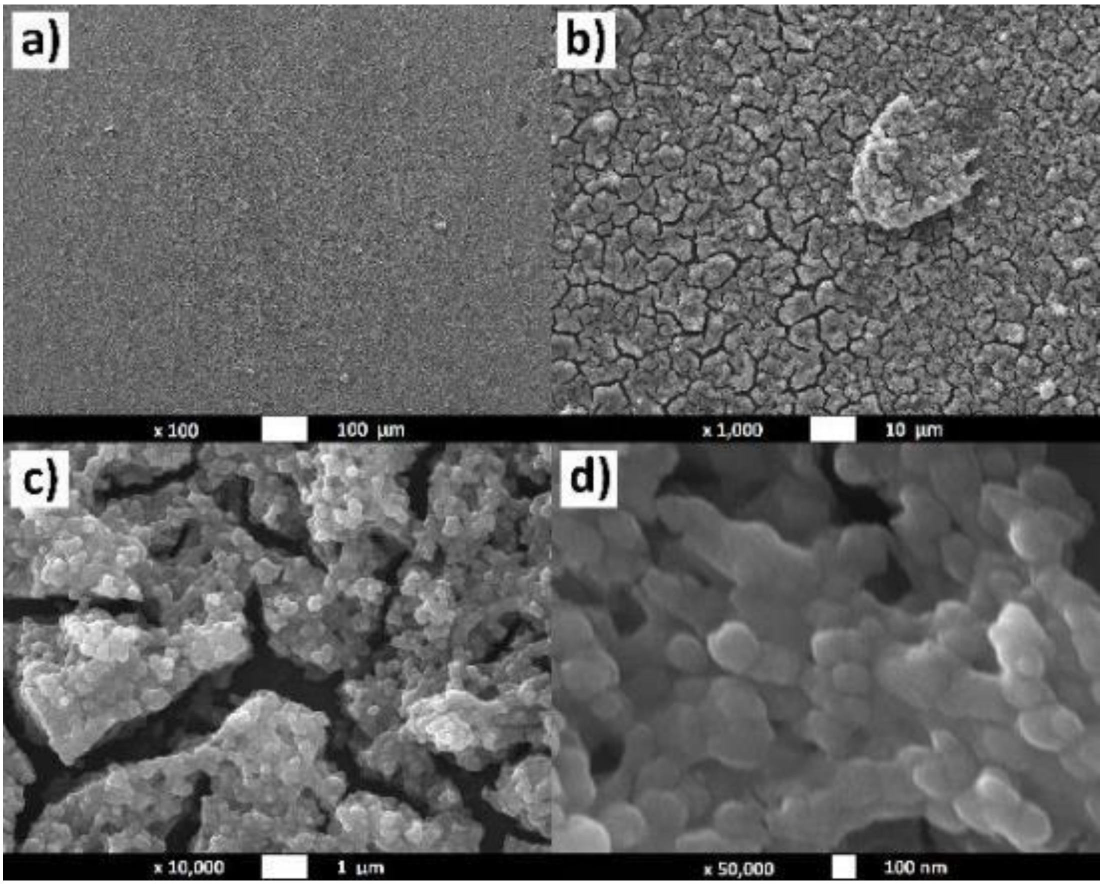

Figure 5.3.6.1 SEM of inkjet printed 5 pass ink 5.3.2 on a glass substrate without thermal treatment

Figure 5.3.6.2 shows the surface topography of a 5 pass 1 cm^2 inkjet printed film using ink 5.3.2 after annealing at 200°C for 160 minutes. The topography does not appear to be significantly affected by the annealing process. There appears to be less cracking when comparing Figure 5.3.6.2.b with Figure 5.3.6.1.b, although this is likely due to the variation displayed by each region of the sample. Increasing the magnification shows that the film is similarly cracked, the nanoparticles being glued together by a connective matrix of the TTIP-derived TiO_2.

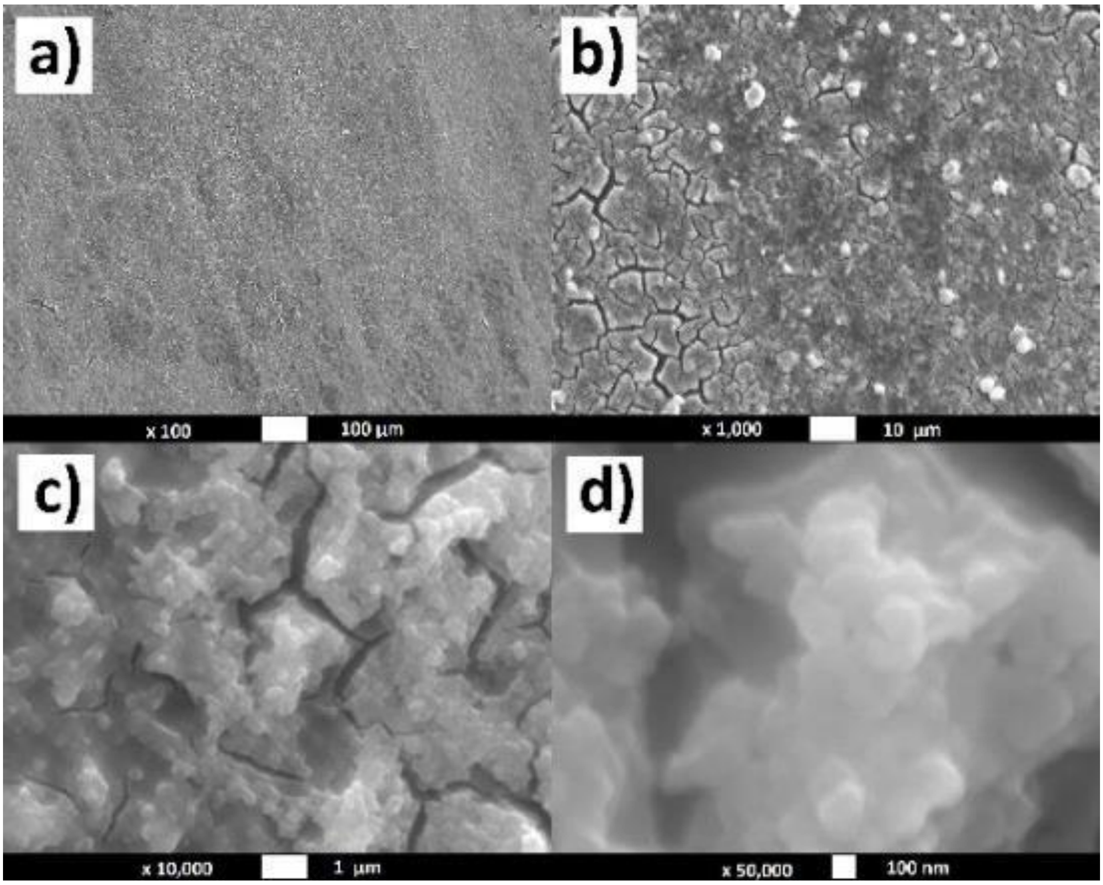

Figure 5.3.6.2 SEM of inkjet printed 5 pass ink 5.3.2 on a glass substrate after annealing at 450°C for 40 minutes

TEM was used to obtain high resolution images of the sample surface, with an emphasis on the seeding effect of the crystalline anatase nanoparticles when using ink 5.3.2. Figure 5.3.6.3.a shows a highly ordered nanoparticle with a clean surface, surrounded by disordered and chaotic amorphous TiO_2 sourced from the TTIP. It was noted that irradiation with the X-rays caused the TTIP-sourced TiO_2 to crystallise both near and away from the anatase nanoparticles. Figure 5.3.6.3.b shows the distribution of crystallised and amorphous material within the deposited ink 5.3.2. The top layer is primarily amorphous, whilst ordered crystalline material is clearly visible in the troughs of the image. This suggests that the nanoparticles are likely coated and connected by amorphous TiO_2.

Figure 5.3.6.4 shows a TEM of drop-tested ink 5.3.2 after annealing at 200°C for 160 minutes. Three distinct regions can be identified in the image; the crystalline anatase nanoparticles present in the ink formulation (denoted Sigma NPs), crystallised nanoparticles that have been formed from the TTIP-sourced amorphous TiO_2 (denoted formed NPs), and TTIP-sourced amorphous TiO_2 that has not crystallised (denoted precursor material). This confirms that the phase pure anatase nanoparticles are behaving as a seed for the amorphous TiO_2. It is also indicated that the annealing conditions for complete crystallisation of the amorphous TiO_2

requires further optimisation. This could potentially be achieved by increasing the duration or temperature of the annealing step, or increasing the loading of anatase nanoparticles to increase the presence of seed sites and promote more crystallisation.

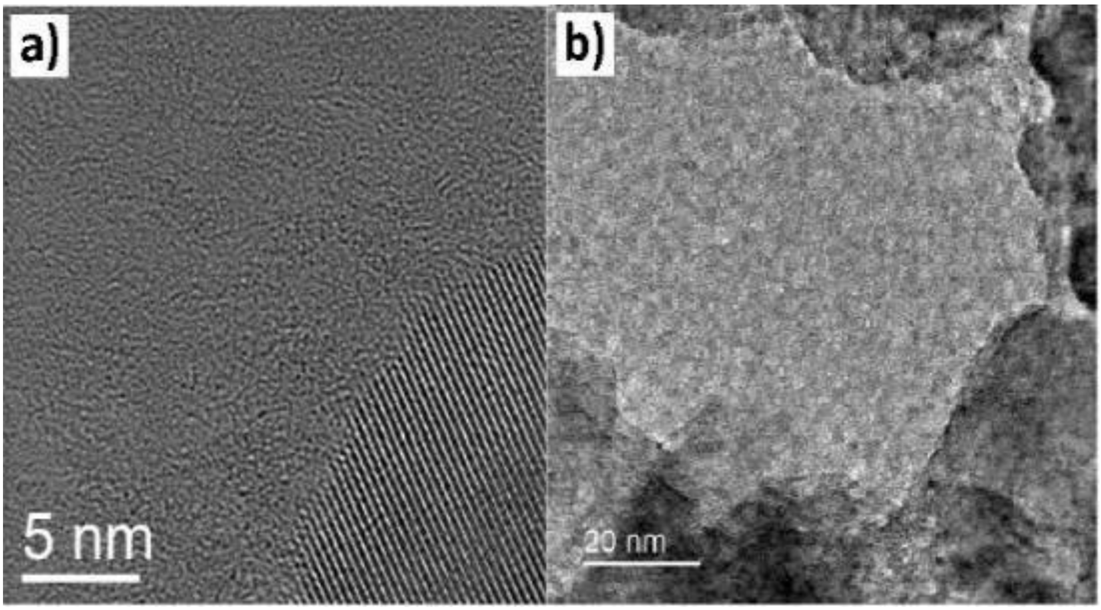

Figure 5.3.6.3 TEM image of drop-tested ink 5.3.2 without thermal treatment. Image a) highlights the crystalline nature of the nanoparticle and disordered amorphous TiO_2. Image b) shows the distribution of material in the deposit

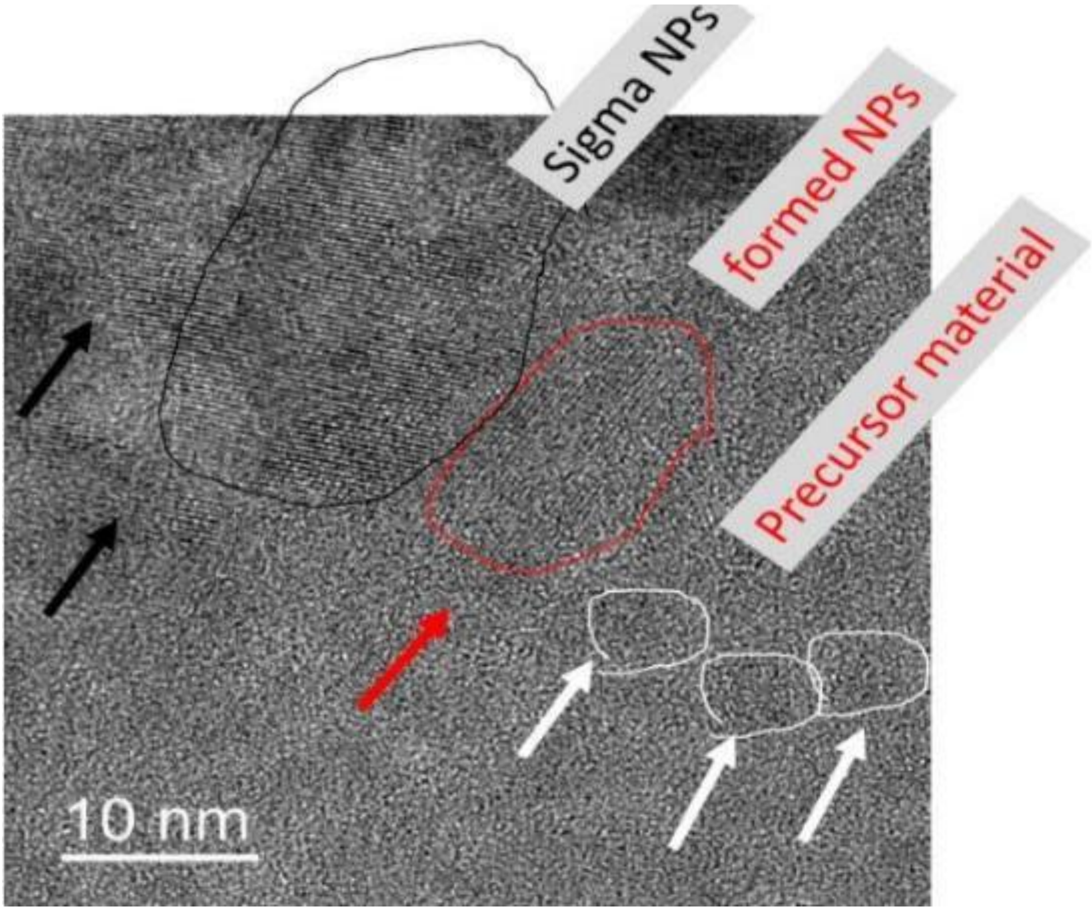

Figure 5.3.6.4 TEM image of drop-tested ink 5.3.2 after annealing at 200°C for 160 minutes, with representative regions of sample highlighted for clarity

5.3.7 Printing on PET

Although TEM indicates that the annealing conditions of 200°C for 160 minutes are insufficient for complete crystallisation of the precursor material, these conditions do result in a partial crystallisation of the amorphous TiO_2. As such, the inkjet printing of ink 5.3.2 and subsequent annealing of the sample was performed on PET. PET is a flexible plastic substrate that can withstand temperatures up to 255°C. Figure 5.3.6.1 shows the print track obtained at the identified optimum conditions, with an average track width of 360.3 µm. Although the track is not perfectly straight, there appears to be a uniform distribution of material with a slight granular appearance.

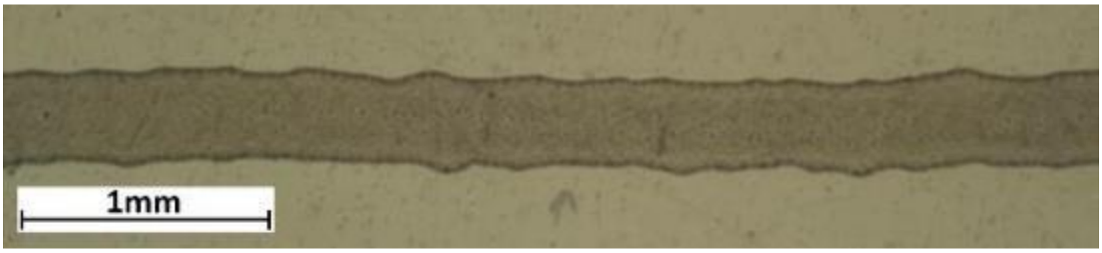

Figure 5.3.7.1 Printed track using ink 5.3.1 at 10 mm s^{-1} print speed and 0.1 mm step size on a PET substrate

Printed 1 and 5 pass 1 cm^2 samples were also obtained on a PET substrate, as shown in Figure 5.3.7.2.a and b. In the single pass print, the tracks are clearly defined and have well-defined edges. There is a slight overlap between the edges of the tracks, likely to result in a transient increase in the sample thickness. The 5 pass print has less well-defined edges, with a clear displacement in consecutive printed passes due to the changing thickness at the left edge of the image. The bulk of the deposit appears to be relatively uniform, with small regions of reduced thickness.

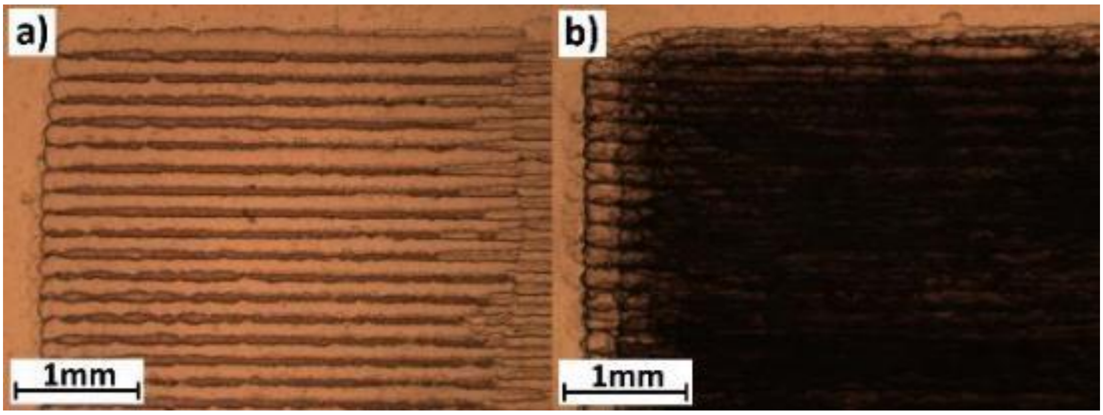

Figure 5.3.7.2 Printed 1 cm^2 using ink 5.3.2 at optimised print conditions on a PET substrate. Image a) is 1 pass and b) is 5 passes

Figure 5.3.7.3 Printed 3 pass 'TiO$_2$' using ink 5.3.2 at optimised print conditions on a PET substrate

A 3 pass sample of ink 5.3.2 was printed onto a PET substrate, using the word 'TiO$_2$' as the deposition pattern. Figure 5.3.7.3 shows a macroscopic image of the printed 'TiO$_2$' with the PET substrate under flexion. Adhesion of the deposit was shown, with no visible flaking or material loss after an extended number of manual flexion cycles.

Phase analysis was performed on ink 5.3.2 after it was drop-tested onto a PET substrate. Figure 5.3.7.4 shows that the large anatase E_g peak at ca. 146 cm^{-1} is present in the sample before annealing, due to the addition of anatase nanoparticles in the ink formulation. After annealing at 200°C for 160 minutes, the intensity of the peaks associated with anatase phase increase significantly. This increased intensity suggests the formation of additional anatase phase from the precursor material, supporting the behaviour of the nanoparticles as a seed on a PET template. The E_g peak at ca. 146 cm^{-1} increases by a factor of 6.5. This is roughly half the intensity increase observed for the same ink when drop-tested onto a glass substrate, which may indicate that the substrate identity has an influence on the crystallisation behaviour of the amorphous TiO$_2$. However, as the drop-tested samples will exhibit a large sample-to-sample variation, this would require further investigation.

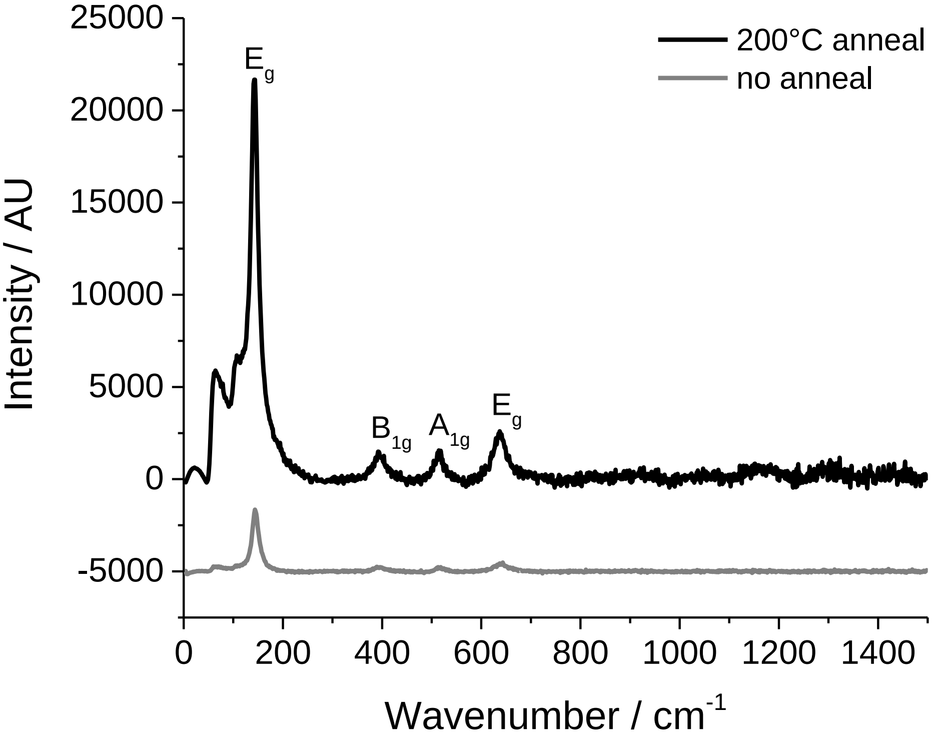

Figure 5.3.7.4 Overlaid Raman spectra of drop-tested ink 5.3.2 on a PET substrate before and after annealing at 200°C for 160 minutes

5.4 Nanoparticle and Hybrid Ink Discussion & Conclusion

After the ink formulation development in Chapter 4 it was decided that increasing the loading of titanium further would be beneficial. As the ink stability became unacceptable with higher concentrations of TTIP, the use of nanoparticles was investigated as an alternative method for increasing titanium loading. Initial attempts to synthesise TiO_2 nanoparticles and formulate them into an ink were unsuccessful. Phase pure anatase nanoparticles were then purchased and then formulated successfully into inks.

Through the addition of purchased anatase nanoparticles, titanium loading of the alkoxide inks discussed in Chapter 4 was increased from a total concentration of 0.15 to 0.25 M with respect to titanium. Ink stability was demonstrated over a 28 day maturation period, with a viscosity increase of only 1.55 % being observed. Although the loading of titanium had been increased, the printed samples still proved difficult to characterise and so drop-tested samples were used for annealing studies and phase analysis. A seeding or templating effect was observed for the drop-tested nanoparticle-containing hybrid ink after annealing at temperatures of 200°C, allowing an observable increase in anatase peak intensities in both Raman and XRD spectra. TEM studies, performed by Dr Leonardo Lari, confirmed the seeding behaviour of the nanoparticles.

As was found for ink 4.3.2 in Chapter 4, both profilometry and SEM indicated that the deposited films were inhomogeneous but continuous. The sample continuity is shown in the profilometry, despite the extreme fluctuations in measured sample height, by the apparent increase to the ‘baseline’ in the confines of the sample area. Although less evident in the higher magnification SEM images due to the high contrast, the lower magnification images show the samples to be continuous. Although the profilometry and SEM data agree on the sample continuity, the profilometry results again exhibit a spiky appearance likely due to unfavourable stylus-sample interactions and provide unreliable sample profiles. It is noted no distorted or curved profilometry baselines were obtained for printed samples of ink 5.3.2. Sample thickness was also shown by the low optical transmittance of printed ink 5.3.2.

After identifying a reduced annealing temperature requirement, printing was also performed successfully using a flexible plastic, PET, as a substrate. Annealing a drop-tested sample of the hybrid alkoxide / nanoparticle ink on PET at 200°C resulted in a notable increase to Raman peaks belonging to the anatase phase, indicating that the seeding effect of the nanoparticles was also occurring on the PET substrate. This finding is significant in the use of inkjet printing as a direct patterning deposition technique for MO thin films on flexible substrates.

5.5 Experimental Procedure

5.5.1 Hydrothermal Synthesis

To a Schlenk flask was added dried ^{i}PrOH (52.5 ml, 0.682 mol) and TTIP (2.5 ml, 8.44 mmol) under stirring. The resulting TTIP solution was cooled using an ice bath. To another Schlenk flask was added ^{i}PrOH (52.5 ml, 0.682 mol) and H_2O (0.57 ml, 31.6 mmol, 3.75 molar equivalents) under stirring. After allowing each solution to stir for 10 minutes, the H_2O solution was added dropwise to the stirring TTIP solution over 10 minutes. The ice bath was then removed and the mixture allowed to reach room temperature while stirring over 24 hours. After stirring the solution for 24 hours the stirring was terminated and the solution left for 48 hours, forming a white precipitate of TIO_2.

The crude product (0.868 g) was collected *via* Buchner filtration and washed with cold ^{i}PrOH (3x 20 ml). To a 17 ml Teflon lined autoclave was added washed product (0.2 g) and glacial acetic acid (8.35 ml, 1.5 M). The autoclave was then heated to 200°C for 6 hours at a ramp rate of 2.5°C min^{-1}. The resulting mixture was then concentrated *in vacuo* at 55°C, producing a fine off-white powder (0.1788 g, 2.24 mmol, 26.50 % yield). Found C: 1.85 %, H: 0.57 %. ν_{max}: 2981 (OH), 1523 (COO^-), 1415 (COO^-), and 1338 (COO^-) cm^{-1}.

The first nanoparticle synthesis performed was via a hydrothermal route, reported by Reyes-Coronado et al. In the paper, it is shown that the anatase nanoparticles synthesised by this method had a radius of between 3 and 6 nm, increasing by hydrothermal treatment time at 200°C. Performing the synthesis according to the literature yielded a pale white powder, confirmed to be crystalline anatase by Raman spectroscopy (See Figure 5.5.1.1). The high intensity E_g stretch, along with the B_{1g}, A_{1g}, and less intense E_g stretches are all present at the expected Raman shifts. With no discernible line broadening or frequency shifts, it was determined no phonon confinement effects were displayed by the nanoparticles.

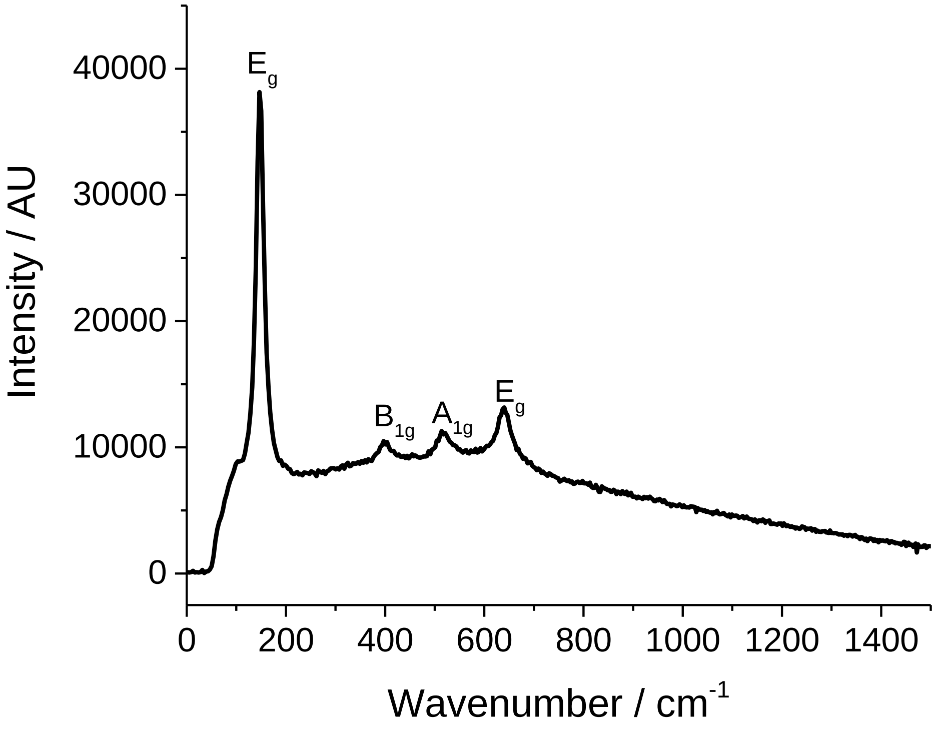

Figure 5.5.1.1 Raman spectrum of hydrothermally synthesised nanopowder

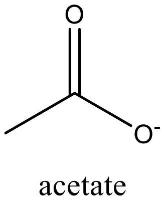

Figure 5.5.1.2 Acetate ligand

Elemental CHN and IR analyses were performed on the nanoparticles. The results suggest the surface hydroxyls of the TiO_2 had been peptised to an extent by the acetic acid solvent the TiO_2 was refluxed in during the hydrothermal treatment, behaving as acetate ligands. CHN results confirmed the presence of C (1.85 %) and H (0.57 %), both of which are contained in acetate (See Figure 5.5.1.2). The IR spectra shows the expected acetate peaks (cm^{-1} of 2981 [OH], 1523 [COO$^-$], 1415 [COO$^-$], and 1338 [COO$^-$]), confirming the presence of acetate caps.

5.5.2 Reflux Synthesis

A round bottom flask was charged with ^{n}BuOH (4.58 ml, 50 mmol) and TTIP (7.41 ml, 25 mmol). The mixture was cooled and stirred on an ice bath for 20 minutes. HCl (4.16 ml, 12 M) was then added dropwise over 5 minutes to the TTIP solution, and then stirred for a further 5 minutes. H_2O (0.9 ml, 50 mmol) was added and the mixture allowed to reach room temperature. The resulting solution was refluxed for 5 hours, forming a white precipitate. Precipitate was isolated *via* centrifugation and the yellow organic layer was discarded. The white powder extracts were combined and dried in a desiccator to yield a fine white powder (1.486 g, 18.6 mmol, 74.42 % yield). Found C: 1.08 %, H: 1.93 %. ν_{max}: 1614 (OH, adsorbed H_2O), 873 (Ti-O), 702 (Ti-O) cm^{-1}.

A reflux synthesis reported by Burunkaya et al. was also identified as a promising route to anatase nanoparticles. The anatase nanoparticles produced when refluxing in ^{n}BuOH with HCl were stated to have an average particle size of ~3.5 nm. Substituting TTIP in place of the Ti(OEt)$_4$, the synthesis was repeated to yield a fine white powder which was analysed by Raman spectroscopy (See Figure 5.5.2.1). The smaller B_{1g}, A_{1g}, and E_g stretch peaks are not as sharp as those found for the hydrothermally synthesised nanopowder (See Figure 5.5.1.1) The A_{1g} peak is almost indistinguishable from the baseline noise. The large E_g peak is present at a blue-shifted Raman shift of 153.87 cm^{-1}. A typical Raman shift of 144 cm^{-1} is observed for the large peak associated with the E_g stretching mode. Blueshift of almost 10 cm^{-1} for the measured E_g mode could be explained by the phonon confinement within the small nanoparticles (quoted as ~3.5 nm). The small size of the nanoparticles could also explain the broadness of the lower intensity stretching modes.

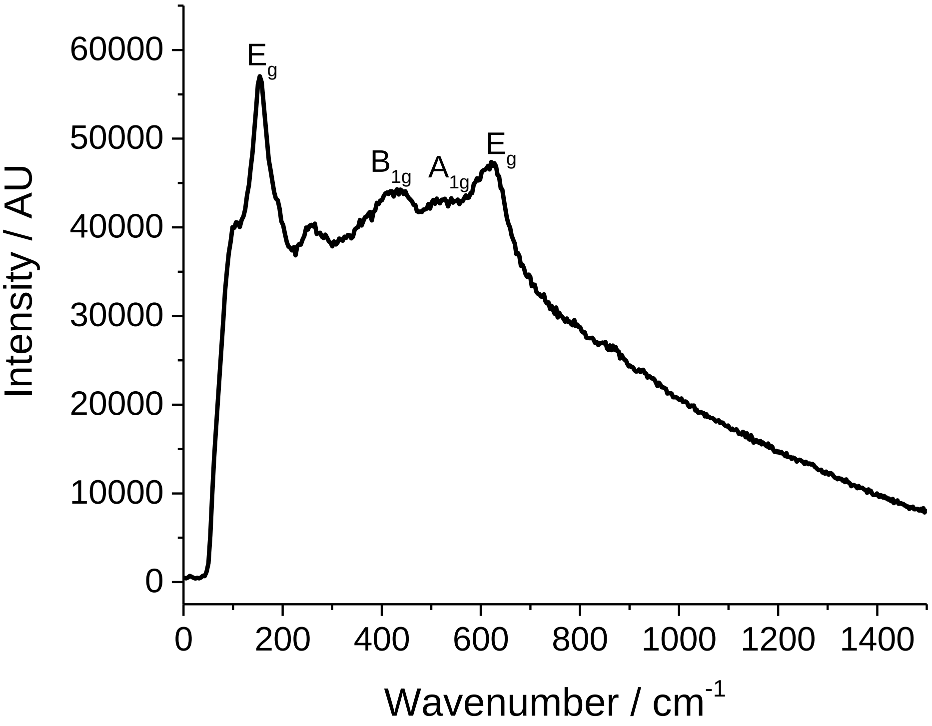

Figure 5.5.2.1 Raman spectrum of reflux synthesised nanopowder

Further analysis was performed using an XRD (See Figure 5.5.2.2). Similar to the Raman spectrum, the expected anatase peak intensities were very low. The A(101) peak is just distinguishable above the noise. There are no other significant peaks visible. Due to the poor XRD trace obtained, the Scherrer equation could not be used to calculate the crystallite size with any degree of precision. Elemental CHN and IR spectroscopy were used to investigate the sample purity. C (1.08 %) and H (1.93 %) were present, suggesting a small impurity of

^{n}BuOH and/or ^{i}PrOH, along with some H_2O. The IR spectrum showed only the presence of absorbed H_2O and Ti-O bonds.

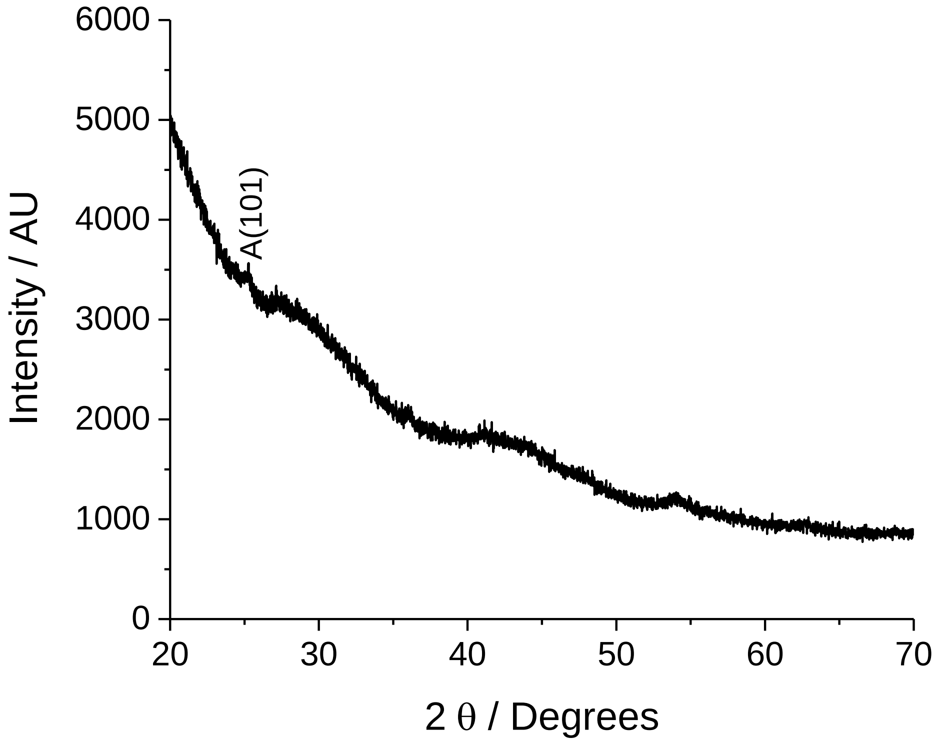

Figure 5.5.2.2 XRD pattern of reflux synthesised nanopowder

5.5.3 FTIR Spectra

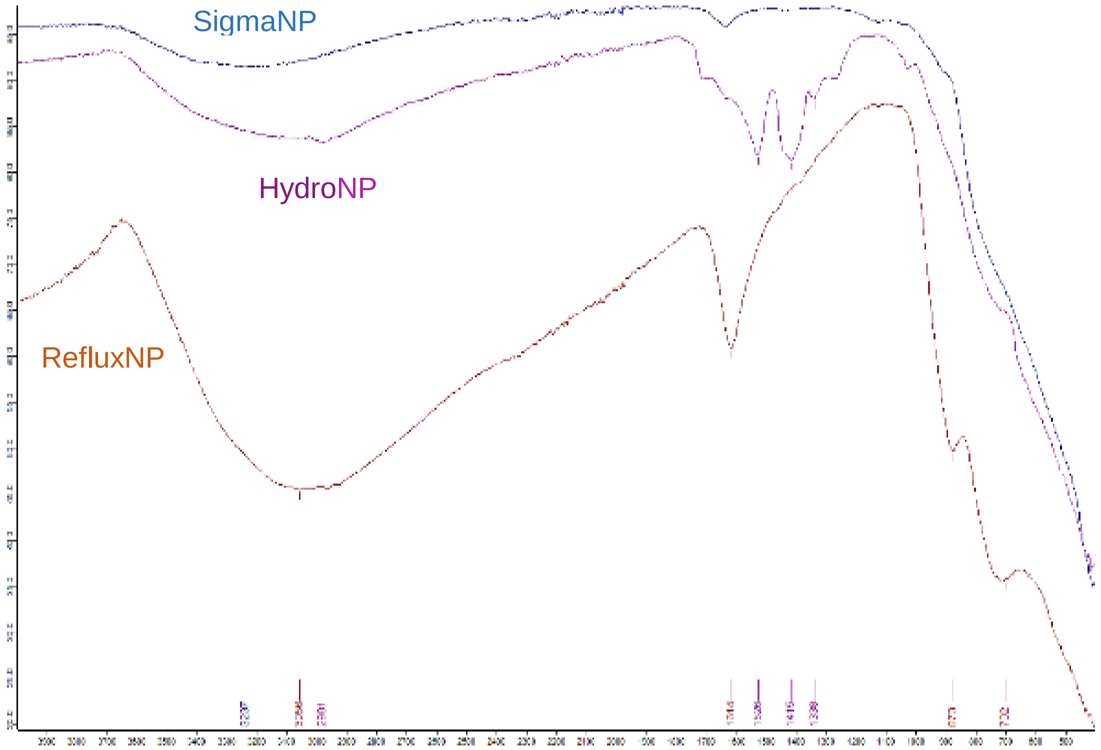

FTIR spectra were obtained using a Bruker Alpha spectrometer.

5.5.4 Preparation of Nanoparticle and Hybrid Alkoxide / Nanoparticle Inks

To a clean, oven dried Schlenk flask (100 cm^3) was accurately weighed titanium(IV) oxide (anatase nanopowder, <25 nm particle size) using a 4-figure analytical balance. To this was then added dry ^{i}PrOH, DME, and finally TTIP if required, via syringes purged in triplicate with N_2. The resulting solution was then sonicated for 60 minutes to ensure homogeneity. All inks were prepared to a total volume of 40 mL. An example ink formulation for the 0.15M TTIP ink stabilised with 10 molar equivalents of DME and containing 0.1 M of Ti from nanoparticles, discussed in 5.3.2, is given below.

To a clean, oven dried Schlenk flask (100 cm^3) was accurately weighed anatase nanopowder (0.3200 g, 0.004 mol with respect to titanium). The flask was then charged with dry ^{i}PrOH (32.0 mL) and DME (6.24 mL, 0.06 mol). To the resulting solution was added TTIP (1.76 mL, 0.006 mol). After 60 minutes of sonication, the white and cloudy ink suspension was ready for analysis and printing.

5.5.5 Dynamic Light Scattering

Hydrodynamic radius of nanoparticulate suspensions were measured using a Malvern Instruments Zetasiser Nano ZS set to 25°C, a scattering angle of 176°, and a solution refractive index set to 1.377 (that of bulk ^{i}PrOH). Samples were analysed in triplicate and a number average was calculated.

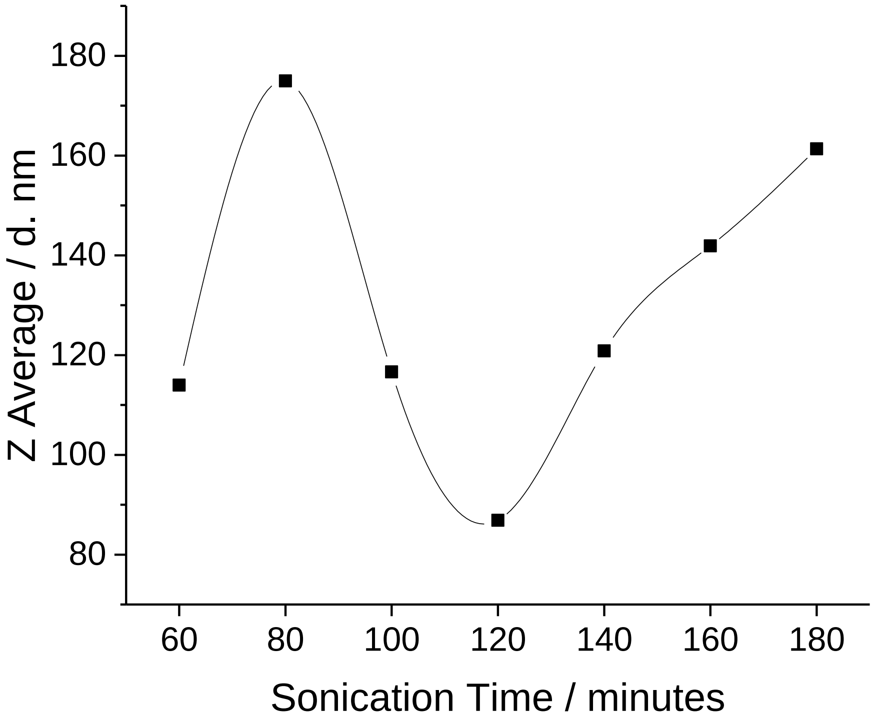

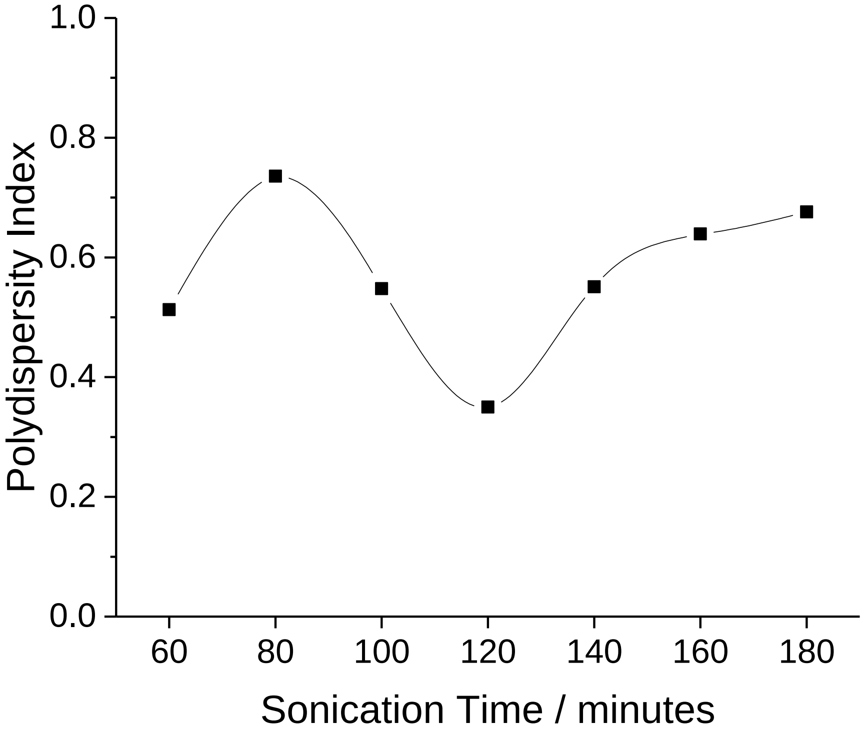

5.6 References

1. Y. Kunugi, Y. Kato, H. Uematsu and Y. Shimoyama, *Journal of Photopolymer Science and Technology*, 2015, **28**, 403-406.
2. H. Tomáš, S. Masoud, D. Petr, K. Richard, Ď. Zuzana, V. Michal and Č. Mirko, *Flexible and Printed Electronics*, 2017, **2**, 035010.
3. J. S. Gebauer, V. Mackert, S. Ognjanović and M. Winterer, *Journal of Colloid and Interface Science*, 2018, **526**, 400-409.
4. V. Sygouni and C. V. Chrysikopoulos, *Chemical Engineering Journal*, 2015, **262**, 823-830.
5. Y. Li, Y. Fan and Y. Chen, *Journal of Materials Chemistry*, 2002, **12**, 1387-1390.
6. G. Li, L. Li, J. Boerio-Goates and B. F. Woodfield, *Journal of the American Chemical Society*, 2005, **127**, 8659-8666.
7. S. Mahshid, M. Askari and M. S. Ghamsari, *Journal of Materials Processing Technology*, 2007, **189**, 296-300.
8. T. Kotsokechagia, F. Cellesi, N. Tirelli, A. Thomas and M. Niederberger, *Langmuir*, 2008, **24**, 6988-6997.
9. A. Teleki, R. Wengeler, L. Wengeler, H. Nirschl and S. E. Pratsinis, *Powder Technology*, 2008, **181**, 292-300.

10. J. Stotzel, D. Lutzenkirchen-Hecht, R. Frahm, C. V. Santilli, S. H. Pulcinelli, R. Kaminski, E. Fonda, F. Villain and V. Briois, *Journal of Physical Chemistry C*, 2010, **114**, 6228-6236.
11. S. M. Gupta and M. Tripathi, *Central European Journal of Chemistry*, 2012, **10**, 279-294.
12. M. M. Byranvand, A. N. Kharat, L. Fatholahi and Z. M. Beiranvand, *Journal of Nanostructures, Vol 3, Iss 1, Pp 1-9 (2013)*, 2013, DOI: 10.7508/jns.2013.01.001, 1.
13. M. Sasani Ghamsari, S. Radiman, M. Azmi Abdul Hamid, S. Mahshid and S. Rahmani, *Materials Letters*, 2013, **92**, 287-290.
14. L. Sang, Y. Zhao and C. Burda, *Chemical Reviews*, 2014, **114**, 9283-9318.
15. D. Reyes-Coronado, G. Rodríguez-Gattorno, M. E. Espinosa-Pesqueira, C Cab, R. d. Coss and G. Oskam, *Nanotechnology*, 2008, **19**, 10.
16. J. I. Langford and A. J. C. Wilson, *Journal of Applied Crystallography*, 1978, **11**, 102-113.
17. A. L. Patterson, *Physical Review*, 1939, **56**, 978-982.
18. E. Burunkaya, M. Akarsu, H. Erdem Çamurlu, Ö. Kesmez, Z. Yeşil, M. Asiltürk and E. Arpaç, *Applied Surface Science*, 2013, **265**, 317-323.
19. R. Wang, K. Hashimoto, A. Fujishima, M. Chikuni, E. Kojima, A. Kitamura, M. Shimohigoshi and T. Watanabe, *Nature*, 1997, **388**, 431-432.
20. R. J. Isaifan, A. Samara, W. Suwaileh, D. Johnson, W. Yiming, A. A. Abdallah and B. Aïssa, *Scientific Reports*, 2017, **7**, 9466.
21. T. Adachi, S. S. Latthe, S. W. Gosavi, N. Roy, N. Suzuki, H. Ikari, K. Kato, K.-i. Katsumata, K. Nakata, M. Furudate, T. Inoue, T. Kondo, M. Yuasa, A. Fujishima and C. Terashima, *Applied Surface Science*, 2018, **458**, 917-923.

Chapter 6

Titanium Oxo-cluster Inks

6.1 Background and Introduction

6.1.1 Previous Work

During an alkoxide ink stability investigation, a previous member of the research group inadvertently formed a titanium oxo-cluster; [$Ti_{12}O_{16}(O^iPr)_{16}$]. The experimental conditions involved stirring a solution of TTIP (2.0 mL, 6.8 mmol) and tetraglyme (7.4 mL, 34 mmol) for 2 hours in a purged Schlenk flask. To this was added ^{i}PrOH (7.6 mL, 99 mmol). As the aim of the experiment was to test the ability of tetraglyme to stabilise the TTIP with respect to hydrolysis by ambient H_2O, the Schlenk flask tap was then left open to the atmosphere and the time taken for hydrolysis to occur was recorded. After 5 days, instead of the expected formation of a white precipitate of TiO_2, colourless crystals had formed. The resulting colourless crystals were characterised using elemental CHN analysis. Table 6.1.1 shows that the CHN analysis strongly suggests the crystals identify as the dodecatitanate cluster, [$Ti_{12}O_{16}(O^iPr)_{16}$]. The CHN analysis is also very close to that obtained in the literature, in which Day et al. synthesise and characterise the dodecatitanate cluster.[1]

Table 6.1.1 Predicted, Experimental, and Literature values for CHN analysis of [$Ti_{12}O_{16}(O^iPr)_{16}$]

Element	Predicted %	Experimental %	Literature[1] %
Carbon	32.46	32.21	32.46
Hydrogen	6.31	6.32	6.36

Figure 6.1.1 shows the single crystal structure obtained for the synthesised crystals, confirming their identity as [$Ti_{12}O_{16}(O^iPr)_{16}$]. The structure consists of titanium atoms interconnected with μ-oxo bridges and a periphery of isopropoxy ligands. After confirming the identity of the crystals, it was found that toluene was a suitable solvent. Toluene-d_8 (2.0 mL) was used to dissolve a sample of [$Ti_{12}O_{16}(O^iPr)_{16}$] (0.095 g, mmol), resulting in a 0.026 M concentration, or 0.312 M concentration with respect to titanium atoms. The deuterated solution was then submitted for ^{13}C-NMR analysis; the resulting spectrum was comparable to that reported in the literature. With only 12 individual carbon peaks, it was deduced that some of the carbon environments were equivalent.

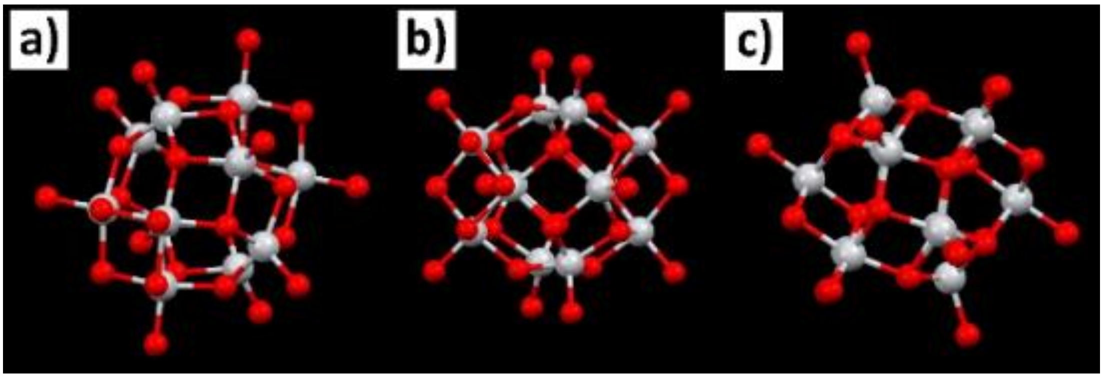

Figure 6.1.1 Single crystal structure of the colourless crystals at three different orientations. Red = Oxygen, Grey = Titanium atoms

This unintended synthesis of the dodecatitanate cluster instigated further research into the subject area of titanium oxo-clusters. Reported literature syntheses were repeated for $[Ti_4O_2(OAc)_2(O^iPr)_{10}]$ and $[Ti_{11}O_{13}(O^iPr)_{18}]$, according to reports by Boyle et al.[2] and Day et al.[1] Unfortunately, the syntheses were unsuccessful and the project came to an end before an ink could be tested.

6.1.2 Titanium Oxo-clusters Literature Search

Before beginning my contribution to the work on titanium oxo-clusters, a literature search was performed with the aim of identifying suitable cluster syntheses. The ultimate aim of this was to formulate an ink containing these titanium oxo-clusters that would be suitable for TiO_2 deposition via inkjet printing. It is proposed that the use of titanium oxo-cluster inks may yield beneficial results in comparison with the alkoxide ink discussed in Chapter 4. The structure of titanium oxo-clusters is in-between that of a titanium alkoxide and TiO_2; potentially increasing the stability of the titanium atoms with respect to hydrolysis, or reducing the thermal budget required for a specific polymorph of TiO_2 after deposition.

Rozes and Sanchez published a critical review on titanium oxo-clusters in 2011, compiling an extensive library of the various clusters present within the literature.[3] Several properties are used to describe these titanium oxo-clusters. Most important are the titanium coordination numbers (CN, typically ranging from 4 to 6), degree of condensation (O/Ti ratio), the bridging behaviour of the oxo ligands (μ_2-O, μ_3-O, μ_4-O, and in some cases μ_5-O) and the behaviour of the peripheral alkoxy moieties (terminal OR ligands or bridging μ_2-OR). Cluster stability is expected to increase as titanium coordination number increases towards 6 and degree of condensation increases towards 2, as observed for pure TiO_2.

Stabilisation of the cluster structure is achieved with μ-oxo bridges, in which a single oxygen atom is bonded to two (or more) of the titanium atoms to create a ‘bridging’ structure. This increases coordination to the unsaturated, reactive titanium atoms and should hinder subsequent reactivity. The presence of μ-oxo bridges is essential within the titanium oxo-clusters, forming the core of the structure. Peripheral ligands, either monodentate or multidentate, encapsulate the core structure. Common peripheral ligands are the alkoxides from the titanium alkoxide precursor or alcohol solvent, bonding at the oxygen.

Synthesis of titanium oxo-clusters typically involves solvothermal treatment of a solution containing a titanium alkoxide in its parent alcohol and a stoichiometric addition of water, as shown in Figure 6.1.2.1. The degree of condensation (O/Ti) in this reaction is given by m/n. There are also several differing synthetic methods for the formation of titanium oxo-clusters which involve the addition of other chemical species, which may be incorporated into the structure.

$$n\mathrm{Ti(OR)_4} + m\mathrm{H_2O} \longrightarrow [\mathrm{Ti}_n\mathrm{O}_m\mathrm{(OR)}_{4n-2m}] + 2m\mathrm{ROH}$$

Scheme 6.1.2.1. Reaction pathway of TTIP and H_2O to form a titanium oxo-cluster

Many titanium oxo-clusters have been reported.[2, 4-15] Figure 6.1.2.1 shows the polyhedral arrangements for 9 different core structures of titanium oxo-alkoxide clusters for n = 3 – 18. The majority of the polyhedra are blue, indicating the preference of the titanium atoms to adopt a coordination number of 6. Some of the polyhedra are green, suggesting that the titanium atoms can also adopt a coordination number of 5. There are very few yellow polyhedra, signifying the aversion of the titanium atoms to adopt a coordination number of 4.

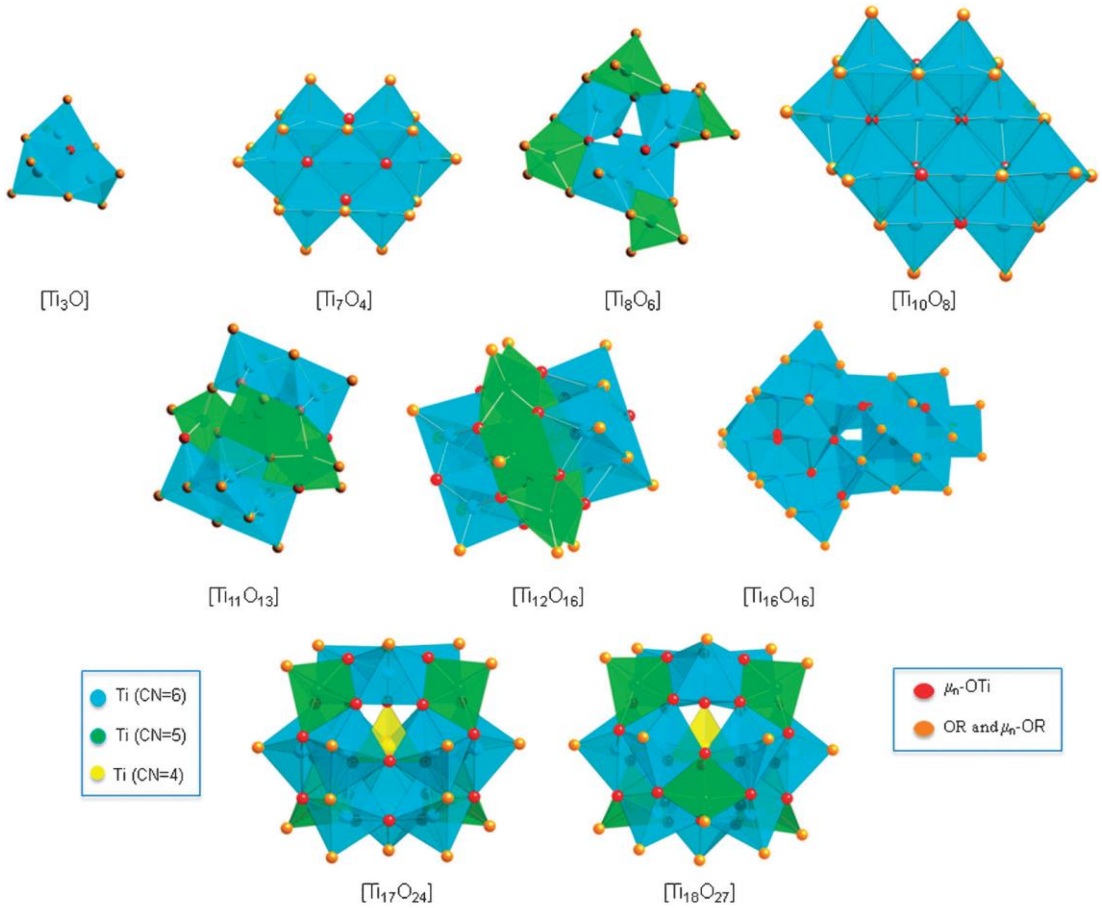

Figure 6.1.2.1 Polyhedral core structures for 9 different titanium oxo-clusters, adapted from Rozes et al.[3] *Reproduced by permission of The Royal Society of Chemistry*

$[Ti_{12}O_{16}(O^iPr)_{16}]$ was identified as a potential titanium oxo-cluster for use in inkjet inks due to the simple synthesis and known solubility in toluene. A modest hydrolysis ratio of 1.33 and titanium coordination numbers of 5 and 6 suggest an intermediate stability for the $[Ti_{12}O_{16}(O^iPr)_{16}]$ cluster. A simple synthesis is reported by Day et al. whereby TTIP is reacted with 1 molar equivalent of H_2O in an ^{i}PrOH solvent at 100°C for 3 days.[1] Despite the 1:1 molar ratio of H_2O to titanium, the cluster exhibits a condensation ratio of 1.33. Good solubility was reported in toluene. It was also reported that treatment with EtOH leads to selective ligand substitution of the alkoxy groups bonded to the 5 coordinate titanium atoms, resulting in formation of a $[Ti_{12}O_{16}(O^iPr)_{10}(OEt)_6]$ cluster.

The dodecatitanate ball and stick structure is shown in Figures 6.1.2.2 and 6.1.2.3. Figure 6.1.2.2 shows the low steric repulsion of the ^{i}PrOH ligands as they are all located at the periphery of the spherical cluster. The polyhedral array of the $[Ti_{12}O_{16}]$ core in Figure 6.1.2.1 and the coloured ball and stick structure in Figure 6.1.2.3 show the three distinct structural sub-units: a central heaxanuclear crown of 5-coordinate titanium atoms with caps at the top and bottom consisting of Ti_3O_{13} trimers in which the titanium atoms are 6-coordinate. Figure 6.1.2.3 also highlights the different oxo and alkoxo environments present within the $[Ti_{12}O_{16}(O^iPr)_{16}]$ cluster. The dodecatitanate cluster is isostructural to the organostannate $[(RSn)_{12}O_{14}(OH)_6]^{2+}$ and fluorovanadate $[V_{12}O_{24}F_2(OH)_6]^{2-}$ frameworks.[16-18]

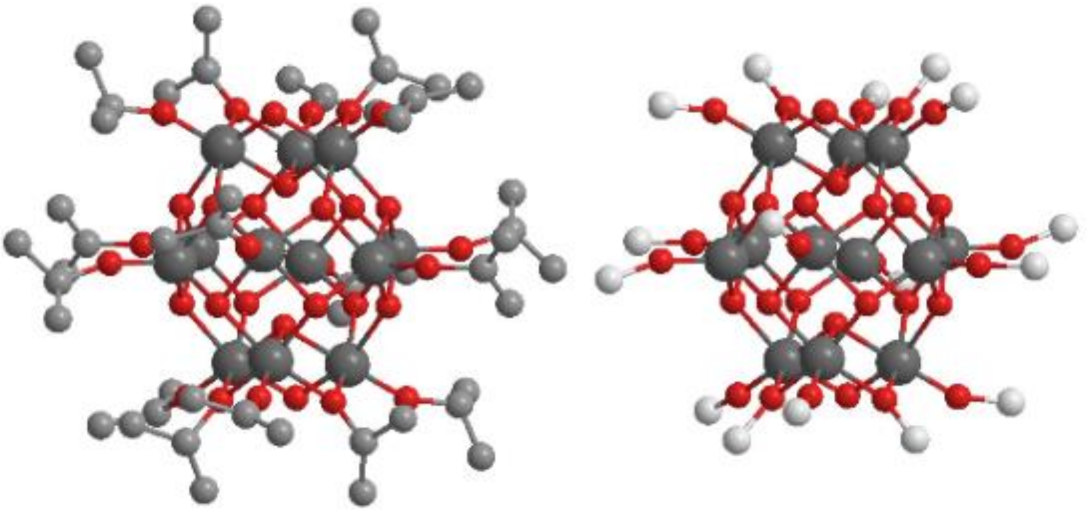

Figure 6.1.2.2 Ball and stick structures of $[Ti_{12}O_{16}(O^iPr)_{16}]$ with hydrogen atoms omitted. The grey atoms are titanium, the red atoms are oxygen, and the smaller grey atoms are carbons. The right image substitutes the isopropyl chains for a single white ball for clarity.

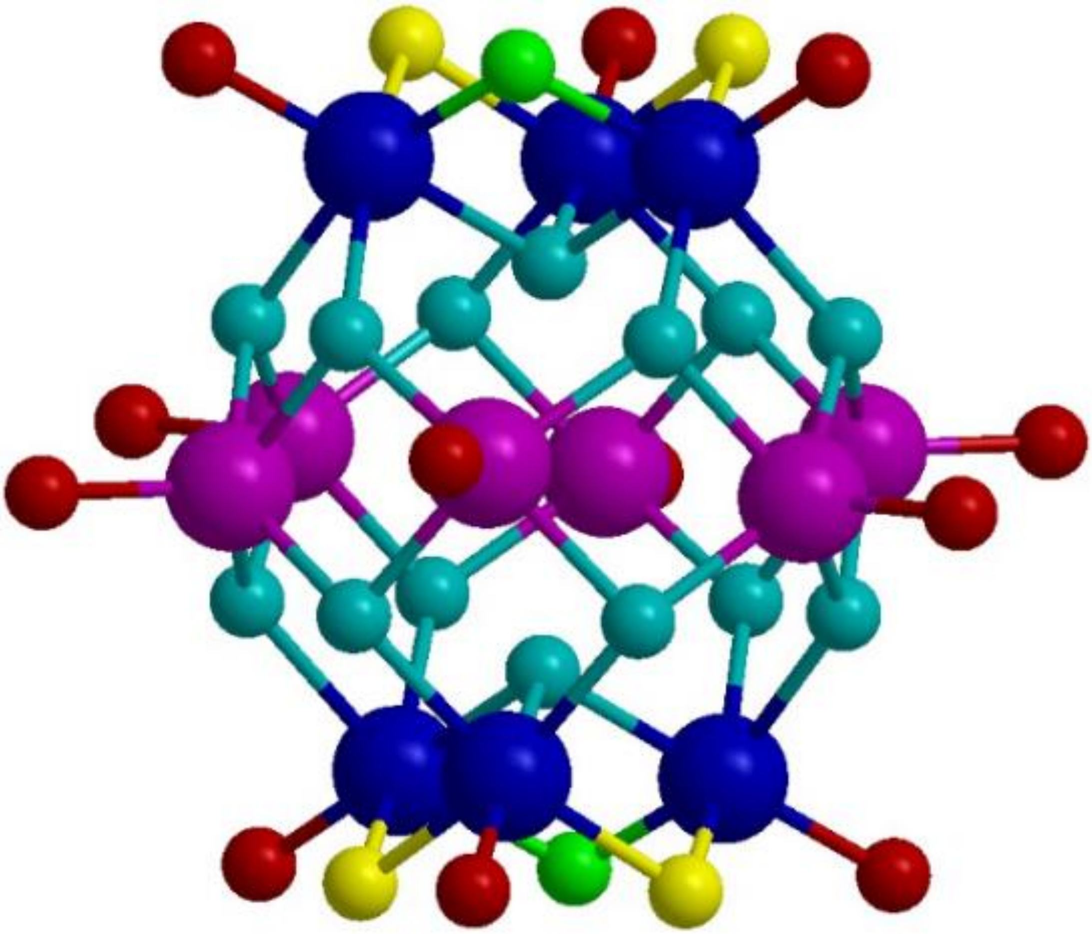

Figure 6.1.2.3 Ball and stick structure of [$Ti_{12}O_{16}(O^iPr)_{16}$] with carbon and hydrogen atoms omitted for clarity. Dark blue atoms represent 6 co-ordinate titanium, purple atoms represent 5 co-ordinate titanium, cyan atoms represent 3 co-ordinate core oxygen, green atoms represent 2 co-ordinate core oxygen, yellow atoms represent 3 co-ordinate alkyl oxygen, and red atoms represent 2 co-ordinate alkyl oxygen.

Closely related to the [$Ti_{12}O_{16}(O^iPr)_{16}$] cluster in both formula and structure is [$Ti_{11}O_{13}(O^iPr)_{18}$], also reported by Day et al.[1] The reported synthesis of this cluster involved the reaction of TTIP with 0.3 – 0.8 molar equivalents of H_2O in ^{i}PrOH under ambient conditions. [$Ti_{11}O_{13}(O^iPr)_{18}$] has a condensation ratio of 1.18, with the same titanium coordination numbers as the [$Ti_{12}O_{16}(O^iPr)_{16}$] cluster. Similar to [$Ti_{12}O_{16}(O^iPr)_{16}$], the [$Ti_{11}O_{13}(O^iPr)_{18}$] cluster was demonstrated to be soluble in toluene, and could undergo selective ligand substitution with EtOH to form [$Ti_{11}O_{13}(O^iPr)_{13}(OEt)_5$].

Figure 6.1.2.4 shows the ball and stick structure of the [$Ti_{11}O_{13}(O^iPr)_{18}$] cluster, which at first glance appears to be the same as [$Ti_{12}O_{16}(O^iPr)_{16}$]. Further analysis of the [$Ti_{11}O_{13}(O^iPr)_{18}$] atomic environments, shown in Figure 6.1.2.5, highlights the differences between the two closely related structures. The brown atoms show the titanium environments with an occupation of less than 1, indicating that these atoms are not always present within the crystal structure and reducing the number of titanium atoms from 12 to 11. The green μ$_2$-oxo atoms in the [$Ti_{12}O_{16}(O^iPr)_{16}$], shown in Figure 6.1.2.3 are replaced by yellow μ$_2$-alkoxy ligands in the [$Ti_{11}O_{13}(O^iPr)_{18}$] cluster, shown in Figure 6.1.2.5. This results in the increased number of O^iPr ligands and reduced number of core oxygen atoms by 2. Not represented in Figure 6.1.2.5 are the partially occupied core bridging oxygen atoms, resulting in the reduction of oxo atoms further from 14 to 13.

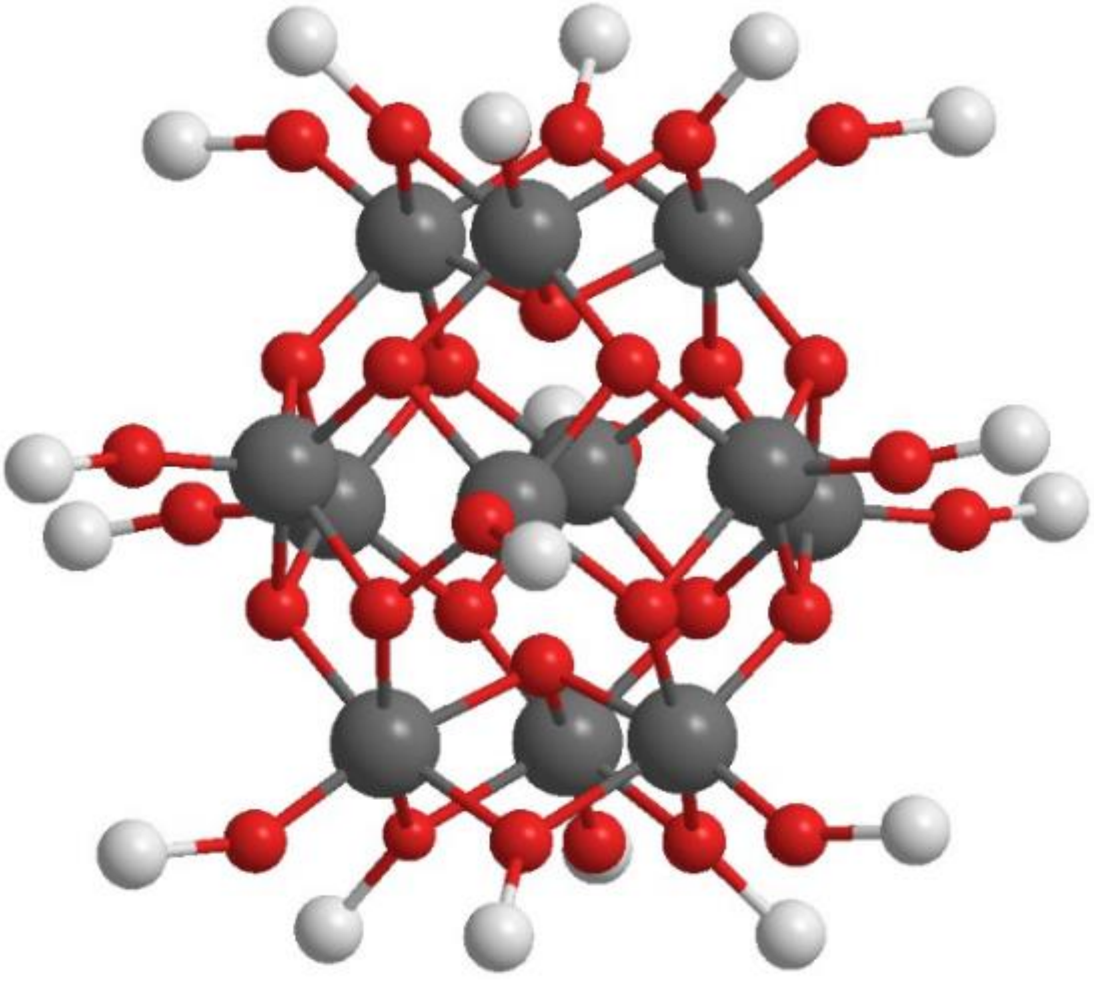

Figure 6.1.2.4 Ball and stick structure of the [$Ti_{11}O_{13}(O^iPr)_{18}$] cluster with hydrogen omitted. The grey atoms are titanium, the red atoms are oxygen, and the alkyl groups are represented by a single white ball for clarity.

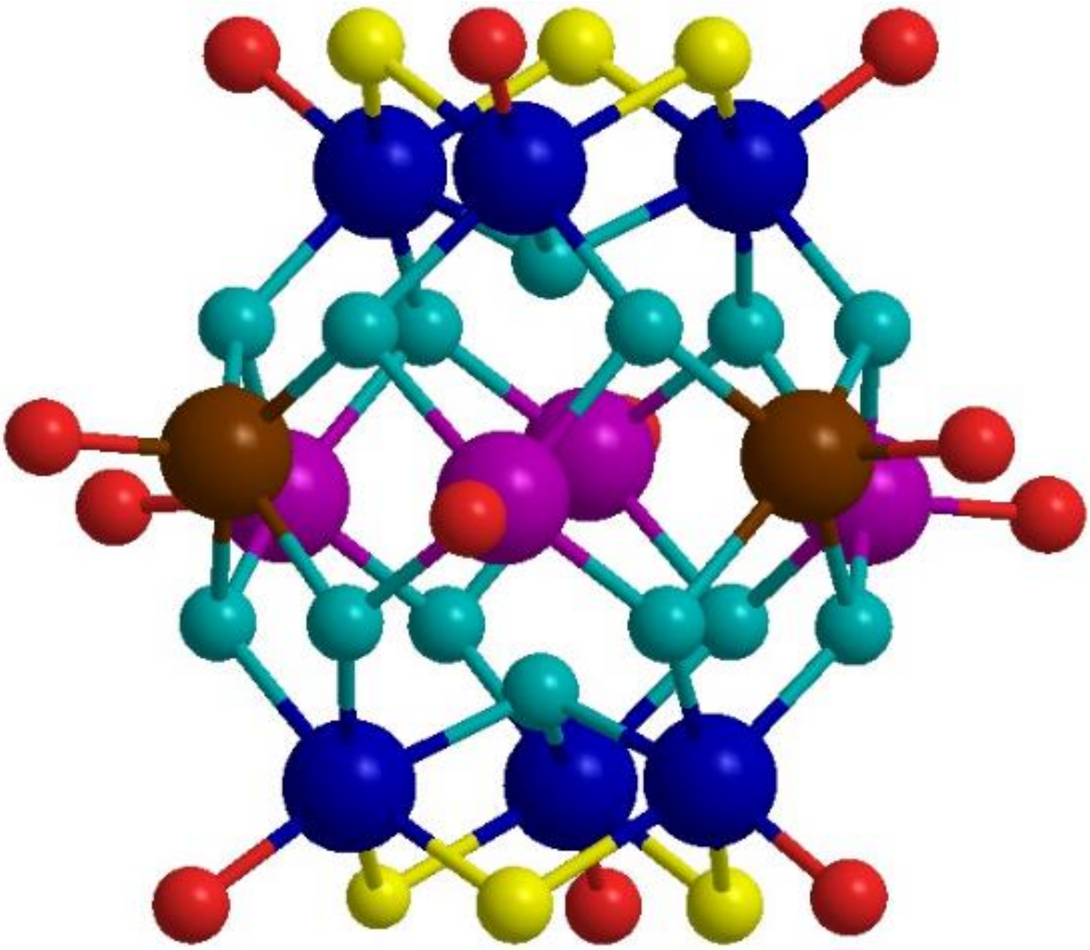

Figure 6.1.2.5 Ball and stick structure of the [$Ti_{11}O_{13}(O^iPr)_{18}$] cluster with hydrogen and carbon omitted for clarity. Dark blue atoms represent 6 co-ordinate titanium, purple atoms represent 5 co-ordinate titanium, brown atoms represent partially occupied 5 co-ordinate titanium, cyan atoms represent 3 co-ordinate core oxygen, yellow atoms represent 3 co-ordinate alkyl oxygen, and red atoms represent 2 co-ordinate alkyl oxygen.

The [$Ti_{28}O_{40}(O^tBu)_{20}(OAc)_{12}$] cluster synthesised by Benedict et al.[11] is reported to be the largest cluster synthesised to date with a metal oxide core measuring 2.0 nm in width and a maximum particle dimension of nearly 2.4 nm. The synthesis is achieved by mixing ^tBuOH, AcOH and $Ti(O^tBu)_4$, forming H_2O *in situ* via an esterification reaction between the alcohol and the acid. Although the AcOH is effectively the H_2O source for the reaction, as the alcohol is in a large molar excess, the AcOH is also incorporated into the [$Ti_{28}O_{40}(O^tBu)_{20}(OAc)_{12}$] cluster. A condensation ratio of 1.43 was calculated for the cluster. It is claimed that the reaction solutions that produce the [$Ti_{28}O_{40}(O^tBu)_{20}(OAc)_{12}$] cluster form pure anatase powder at just 160°C.[11] If this behaviour is replicated by the printed inks of the [$Ti_{28}O_{40}(O^tBu)_{20}(OAc)_{12}$] cluster, then directly patterned anatase TiO_2 may be accessible at temperatures low enough for a wider range of thermally sensitive susbtrates.

Structurally, [$Ti_{28}O_{40}(O^tBu)_{20}(OAc)_{12}$] contains two [$Ti_{14}O_{19}(O^tBu)_{10}(OAc)_6$] clusters connected by two bridging oxygen atoms, which can be seen clearly in Figure 6.1.2.6. The cluster contains 20 titanium atoms that are 6 co-ordinate, and 8 that are 5 co-ordinate. Unusually, each [$Ti_{14}O_{19}(O^tBu)_{10}(OAc)_6$] fragment contains an orange μ_4-oxo atom, as shown in Figure 6.1.2.7.

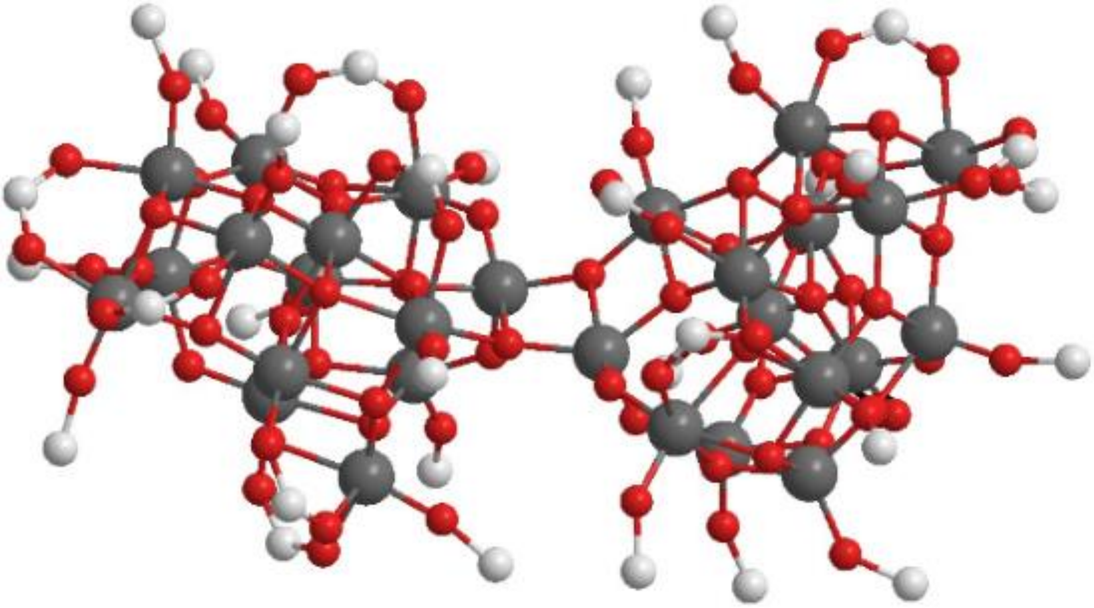

Figure 6.1.2.6 Ball and stick structure of the [$Ti_{28}O_{40}(O^tBu)_{20}(OAc)_{12}$] cluster with hydrogen omitted. The grey atoms are titanium, the red atoms are oxygen, and the alkyl groups are represented by a single white ball for clarity.

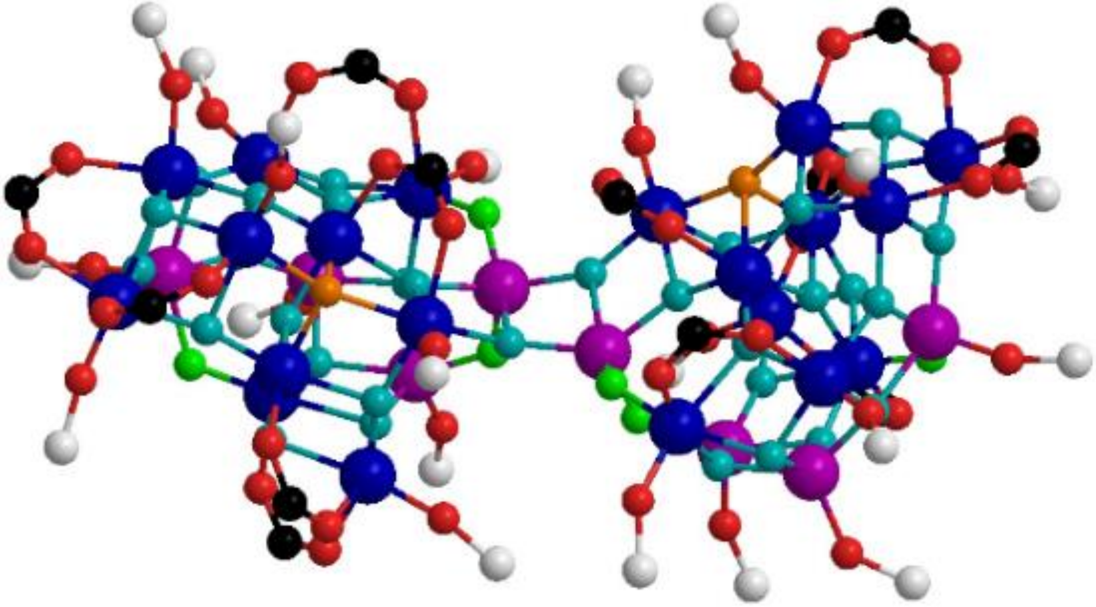

Figure 6.1.2.7 Ball and stick structure of the [$Ti_{28}O_{40}(O^tBu)_{20}(OAc)_{12}$] cluster with hydrogen omitted for clarity. Dark blue atoms represent 6 co-ordinate titanium, purple atoms represent 5 co-ordinate titanium, orange atoms

represent 4 co-ordinate core oxygen, cyan atoms represent 3 co-ordinate core oxygen, green atoms represent 2 co-ordinate core oxygen, red atoms represent 2 co-ordinate alkyl oxygen, white balls represent the ^{t}Bu groups, and black balls represent the CCH_3 from the OAc ligands.

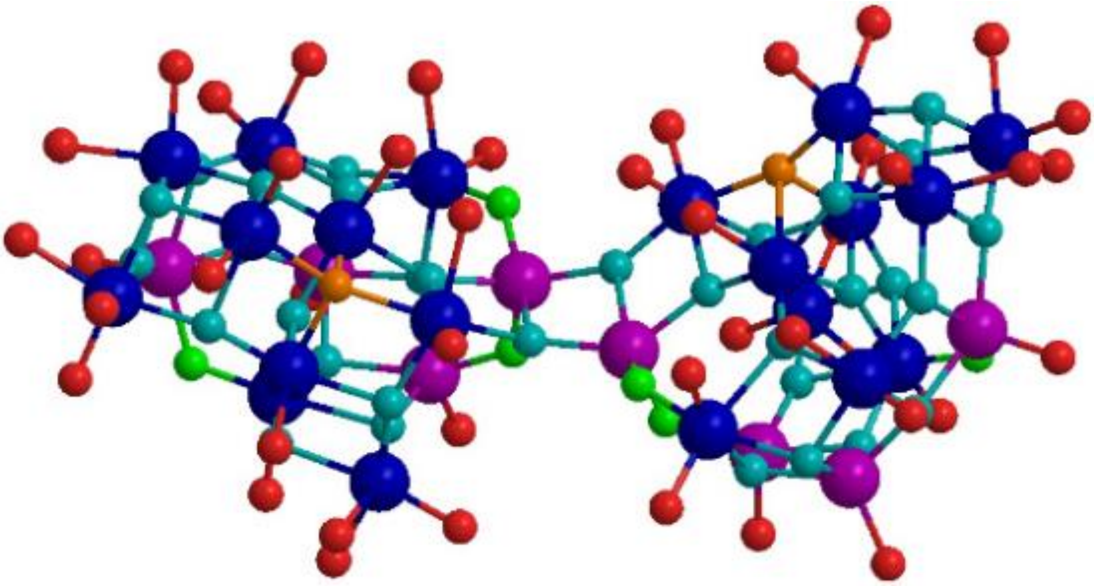

Figure 6.1.2.8 Ball and stick structure of the $[Ti_{28}O_{40}(O^{t}Bu)_{20}(OAc)_{12}]$ cluster with hydrogen and carbon omitted for clarity. Dark blue atoms represent 6 co-ordinate titanium, purple atoms represent 5 co-ordinate titanium, orange atoms represent 4 co-ordinate core oxygen, cyan atoms represent 3 co-ordinate core oxygen, green atoms represent 2 co-ordinate core oxygen, and red atoms represent 2 co-ordinate alkyl oxygen.

A simple synthesis of the $[Ti_{16}O_{16}(OEt)_{32}]$ cluster is reported by Schmid et al. yielding colourless crystals which are stable in air.[5] This stability with respect to reaction with ambient moisture is likely due to each titanium atom having a complete coordination sphere with a coordination number of 6. Synthesis involves mixing equal volumes of $Ti(OEt)_4$ and EtOH and heating the mixture to 100°C for 2 weeks. The $[Ti_{16}O_{16}(OEt)_{32}]$ cluster is stated to be stable in both toluene and EtOH.[5] The ball and stick structure of $[Ti_{16}O_{16}(OEt)_{32}]$ is shown in Figures 6.1.2.9 and 6.1.2.10. Containing only 6 coordinate titanium atoms and small OEt ligands, the $[Ti_{16}O_{16}(OEt)_{32}]$ cluster has a compact structure consisting of two orthogonal blocks of eight TiO_6 octahedra.

Fornasieri et al. present the ease with which the labile ethoxy groups can be transalcoholyzed, leaving the titanium oxo core intact.[19] A general formula of $[Ti_{16}O_{16}(OEt)_{32-x}(OR)_x]$ is obtained, with substitution values of x varying between 4, 8 and 16 and the identities of the substitute groups R including, but not limited to: Me, ^{n}Pr, ^{i}Pr, ^{n}Bu, and Ph. The substitution value is highly dependent on the identity of R. Through alcohol substitution, the properties of the cluster are likely to be modified. Formulation of substituted

$[Ti_{16}O_{16}(OEt)_{32-x}(OR)_x]$ inks could result in finely tuned deposits with properties dependant on the nature of the identity of the cluster used.

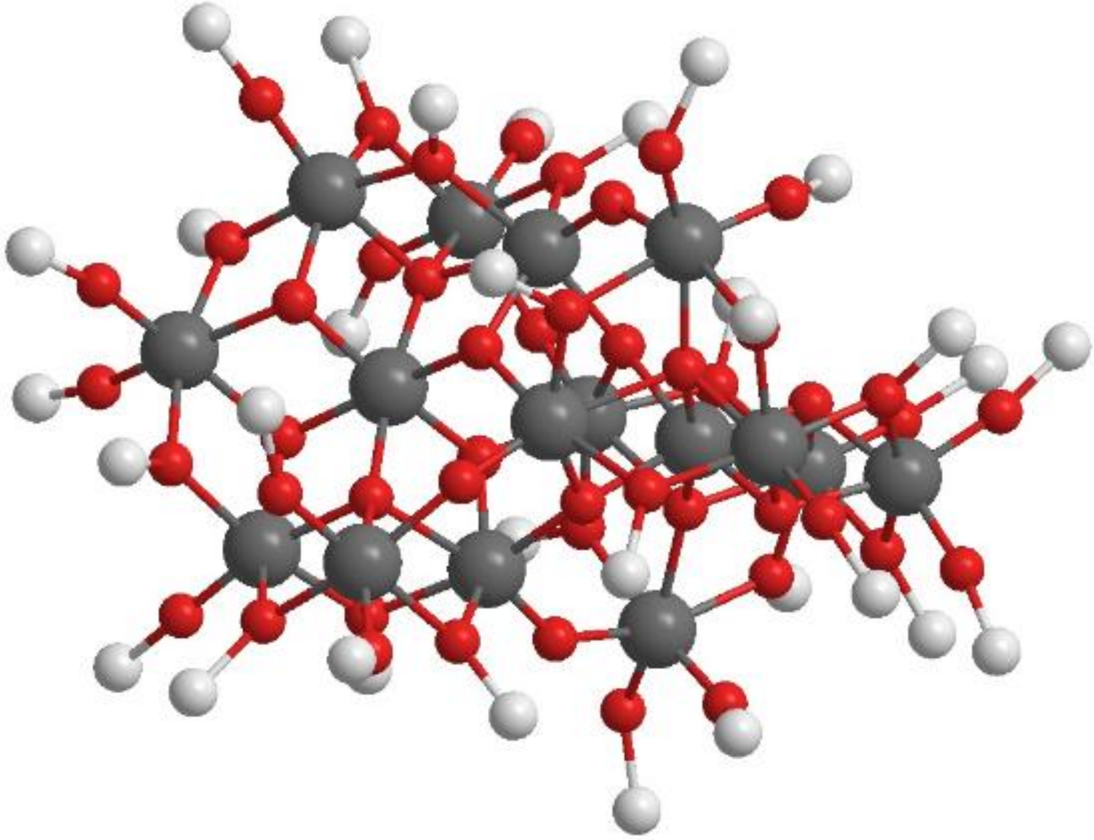

Figure 6.1.2.9 Ball and stick structure of the $[Ti_{16}O_{16}(OEt)_{32}]$ cluster with hydrogen omitted. The grey atoms are titanium, the red atoms are oxygen, and the alkyl groups are represented by a single white ball for clarity.

Table 6.1.2 Summary of the titanium and oxygen atom co-ordination numbers and environments

Atom	**Titanium**			**Core Oxygen**			**Alkyl Oxygen**	
Co-ordination Number & Atom Colour	**CN 6 Blue**	**CN 5 Purple**	**CN 5 Brown**	**CN 4 Orange**	**CN 3 Cyan**	**CN 2 Green**	**CN 3 Yellow**	**CN 2 Red**
$[Ti_{12}O_{16}(O^iPr)_{16}]$	6	6	0	0	14	2	4	12
$[Ti_{11}O_{13}(O^iPr)_{18}]$	6	4	2	0	14	0	6	12
$[Ti_{28}O_{40}(O^tBu)_{20}(OAc)_{12}]$	20	8	0	2	32	6	0	44
$[Ti_{16}O_{16}(OEt)_{32}]$	16	0	0	4	8	4	16	16

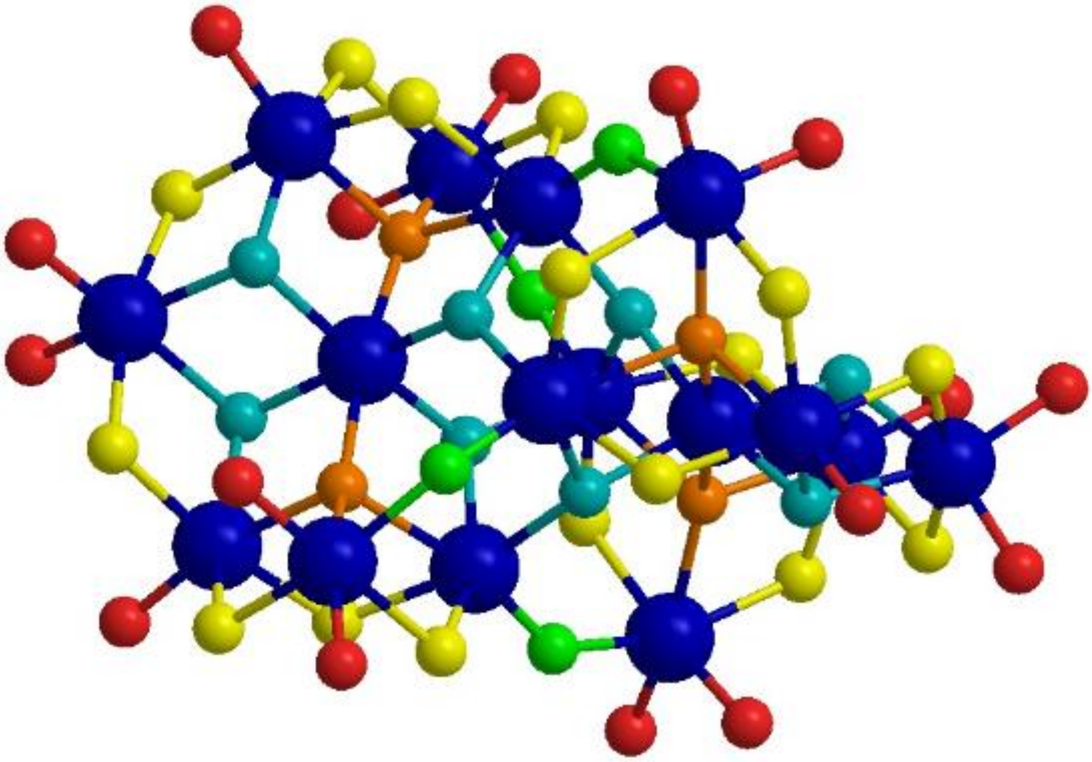

Figure 6.1.2.10 Ball and stick structure of the [$Ti_{16}O_{16}(OEt)_{32}$] cluster with hydrogen and carbon omitted for clarity. Dark blue atoms represent 6 co-ordinate titanium, orange atoms represent 4 co-ordinate core oxygen, cyan atoms represent 3 co-ordinate core oxygen, green atoms represent 2 co-ordinate core oxygen, yellow atoms represent 3 co-ordinate alkyl oxygen, and red atoms represent 2 co-ordinate alkyl oxygen.

After identifying suitable titanium oxo-cluster candidates for synthesis and possible ink formulation, summarised in Table 6.1.2, the next step was to attempt to repeat the literature syntheses; this will be the focus of section 6.2. [$Ti_{12}O_{16}(O^iPr)_{16}$], [$Ti_{28}O_{40}(O^iBu)_{20}(OAc)_{12}$], and [$Ti_{16}O_{16}(OEt)_{32}$] were all synthesised by following synthetic routes from the literature.[1, 5, 11] [$Ti_{11}O_{13}(O^iPr)_{18}$] was synthesised using two novel methods. The primary characterisation of the titanium clusters was elemental CHN. Ink formulations containing the synthesised titanium oxo-clusters are discussed in section 6.3, along with the characterisation of the resulting printed samples. Annealing studies were performed to deduce the minimum temperature at which anatase phase was formed. Section 6.4 summarises the findings and concludes the discussion of the titanium oxo-cluster ink chapter, with Section 6.5 containing the experimental procedures specific to this chapter.

6.1.3 Rationale Behind Titanium Oxo-cluster Inks

Titanium oxo-clusters are formed as transient intermediates in the sol-gel process (See Figure 6.1.3.1). To isolate them, a controlled hydrolysis must instead be performed in which there is insufficient H_2O for consumption of the highlighted reactive molecular cluster (RMC) through further hydrolytic steps. Once these RMCs have been synthesised and isolated, an ink can be formulated which will allow them to be deposited and subsequently finish hydrolysis to form the bulk metal oxide, TiO_2. It was anticipated that the RMC inks may exhibit different behaviour to the solution-based TTIP inks discussed in Chapter 4 as an extensively bridged metal oxide core had already been pre-formed. An example of the anticipated behaviour included a lower temperature requirement for the formation of anatase or rutile TiO_2, due to the presence of a bridged metal oxide core.

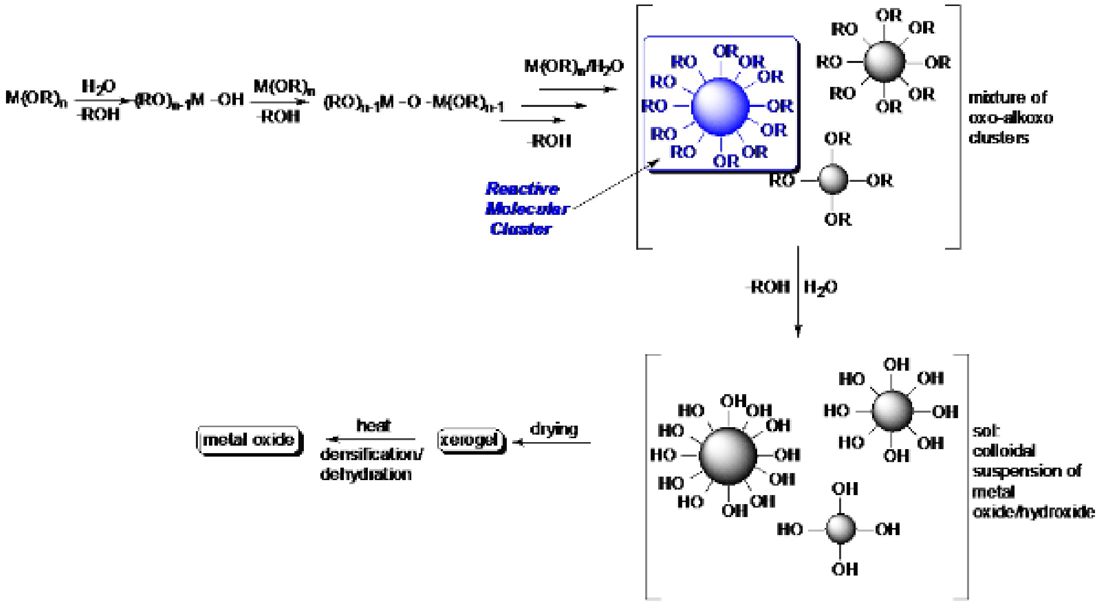

Figure 6.1.3.1 Reactive pathway of the sol-gel process, highlighting the formation of a reactive molecular cluster

After formulating and depositing basic titanium-oxo cluster inks, the functionalisation of the reactive alkoxy groups could then be explored. Some examples of the potential RMC modifications are shown in Figure 6.1.3.2. Similar to the TTIP inks, reaction with hydroxyl groups present on the substrate surface could be envisaged to form a covalent bond to the surface and thereby increasing the film adhesion and durability. Through addition of a reactive metal dopant to an RMC ink, it would be possible to incorporate the dopant into the forming metal oxide structure and ultimately result in a doped oxide material. The topic of doping will be discussed further in Chapter 7. Non-hydrolytic routes to the formation of a metal oxide film could also be achieved through the use of appropriate reactive moieties. This would enable air and moisture sensitive systems to be inkjet printed, and therefore directly patterned, without the requirement for atmospheric moisture to be present post-deposition.

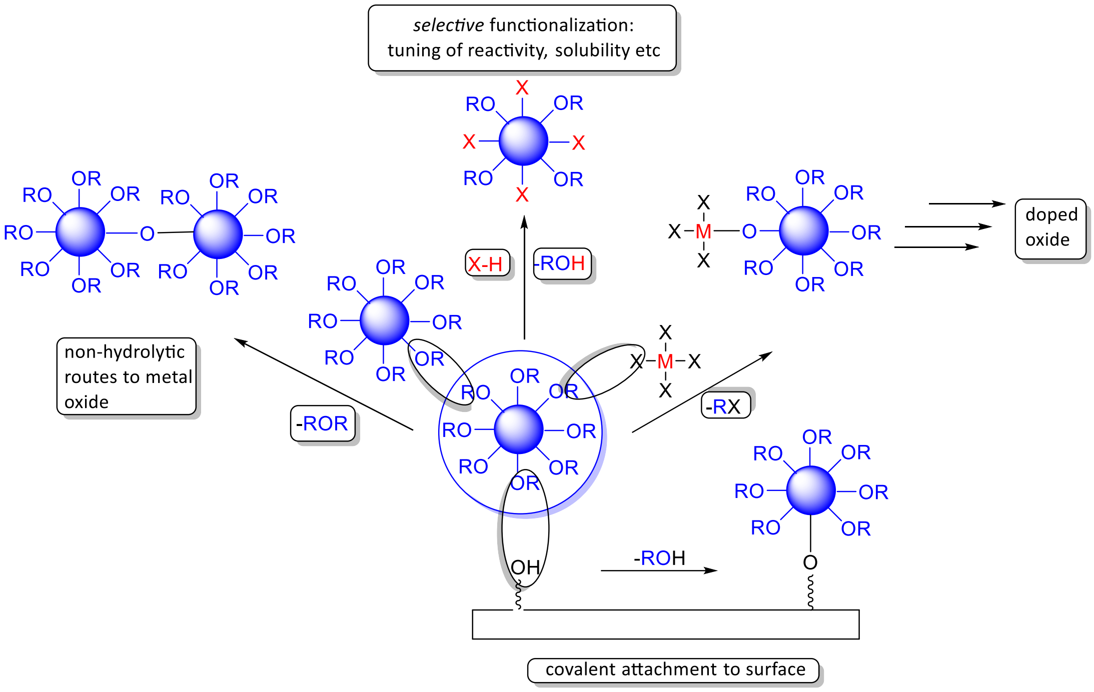

Figure 6.1.3.2 Overview of potential modifications of a reactive molecular cluster

Of particular note is the potential for selective functionalisation of the reactive moieties of the RMC. Selective functionalisation could yield several benefits to the RMC inks, including: increased stability of the cluster with respect to hydrolysis, increased reactivity for rapid film formation post-deposition, improved solubility with the use of hydrophobic or hydrophilic functional groups, and an altered film property such as conductivity or optical transparency. Many of the reported titanium oxo-clusters display selective substitution when in the presence of nucleophilic molecules. Most of this data shows ligand substitution between different alcohols, although some other molecules are also shown.

6.2 Titanium Oxo-cluster Syntheses

6.2.1 $[Ti_{12}O_{16}(O^iPr)_{16}]$ Solvothermal Synthesis

$[Ti_{12}O_{16}(O^iPr)_{16}]$ was synthesised using a scaled down repeat of the reaction reported by Day et al.[1] whereby TTIP is reacted with a 1:1 molar equivalent of H_2O in an ^{i}PrOH solvent and heated to 100°C for 3 days. The isolated crystalline powder product was washed, dried, and analysed by elemental CHN analysis. A carbon content of 34.27 % was found, along with a hydrogen content of 6.70 %. Although this analysis does somewhat suggest the formation of the $[Ti_{12}O_{16}(O^iPr)_{16}]$ cluster, the results are further from the calculated carbon and hydrogen contents (C: 32.47 %, H: 6.36 %) than those reported by Day et al. (C: 32.46 %, H: 6.36 %)[1] and those obtained during the previous alkoxide ink stability investigation (C: 32.21 %, H: 6.32 %).

6.2.2 [$Ti_{28}O_{40}(O^tBu)_{20}(OAc)_{12}$] Solvothermal Synthesis

A repeat synthesis of the [$Ti_{28}O_{40}(O^tBu)_{20}(OAc)_{12}$] cluster was performed, as reported by Benedict et al.[11] A mixture of ^tBuOH, AcOH, and $Ti(O^tBu)_4$ was heated to 130°C for 5 days in a digestion bomb. With a molar ratio of 1.3 AcOH per $Ti(O^tBu)_4$, there is a maximum formation of 0.88 molar equivalents of H_2O per $Ti(O^tBu)_4$ assuming complete conversion of $Ti(O^tBu)_4$ to [$Ti_{28}O_{40}(O^tBu)_{20}(OAc)_{12}$] and complete esterification of every AcOH not incorporated into the [$Ti_{28}O_{40}(O^tBu)_{20}(OAc)_{12}$] cluster. The small colourless crystals isolated from the reaction mixture were analysed by elemental CHN. A carbon content of 7.85 % and a hydrogen content of 5.24 % was found. The CHN results are far from the calculated results (C: 30.09 %, H: 5.24 %), suggesting that the synthesis was either unsuccessful or the formed cluster had rapidly decomposed during the transport and time before the elemental analysis was performed.

6.2.3 [$Ti_{16}O_{16}(OEt)_{32}$] Solvothermal Synthesis

Although the synthesis of the [$Ti_{16}O_{16}(OEt)_{32}$] cluster reported by Schmid et al. was simple, the reaction mixture of $Ti(OEt)_4$ and EtOH required 2 weeks in an autoclave at 100°C.[5] However, this long synthesis was offset by the stated stability of the cluster product both as a solid crystal and as a solution with a toluene solvent, and so the [$Ti_{16}O_{16}(OEt)_{32}$] cluster was investigated. True to the literature, the large colourless crystals were found to be stable in air.

6.2.4 [$Ti_{11}O_{13}(O^iPr)_{18}$] Syntheses

Taking inspiration from the inadvertent [$Ti_{12}O_{16}(O^iPr)_{16}$] synthesis during the alkoxide ink stability investigation mentioned in section 6.1.1, more controlled methods of slow H_2O introduction to a stabilised TTIP solution were investigated. Initial thoughts were to flow dry nitrogen gas over an aqueous solution and into a Schlenk flask containing a TTIP solution, although the practical implications of controlling the nitrogen flow over a prolonged period of time prevented this. An unusual piece of glassware was found (See Figure 6.2.4.1) that could be fully purged using standard Schlenk techniques and the capillary-like tubes charged with two different solutions.

To one tube was added a stabilised TTIP solution, to the other was added a H_2O / ^iPrOH solution. It was found that over time, crystals formed at the meniscus of the TTIP solution and then fell into the solution. This indicates that some of the “wet” ^iPrOH solution has evaporated and travelled through to the surface of the TTIP solution and caused hydrolysis to occur. As crystals were formed rather than TiO_2, a white powder, it is suggested hydrolysis has only partially occurred to form a titanium oxo-cluster intermediate. Once the titanium oxo-cluster is formed and becomes denser than the surrounding medium, the crystal falls from the solution surface and is then protected from further hydrolysis reactions with H_2O. This suggests that kinetic control of hydrolysis has been achieved such that titanium oxo-clusters can be formed.

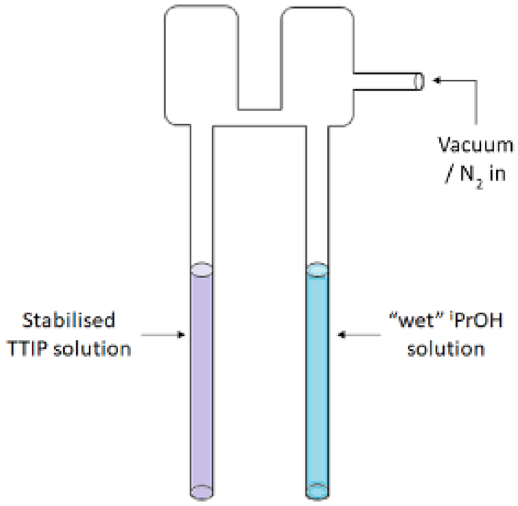

Figure 6.2.4.1 Capillary $[Ti_{11}O_{13}(O^iPr)_{18}]$ *synthesis*

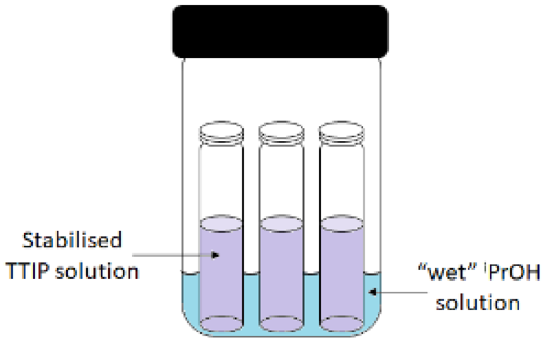

Figure 6.2.4.2. TLC jar $[Ti_{11}O_{13}(O^iPr)_{18}]$ *synthesis*

Due to time constraints, another synthetic apparatus was also considered. Taking inspiration from the twin capillary method described above, this method utilised a standard thin-layer chromatography (TLC) jar and five 12 mL sample vials (See Figure 6.2.4.2). The TLC jar contained the "wet" ^{i}PrOH solution, whereas the sample vials were charged with the stabilised TTIP solution. The sample vials were left open to the "wet" ^{i}PrOH atmosphere contained within the closed TLC jar. After a few days, crystals were found to have formed in the sample vials. A similar mechanism is occurring to that observed in the twin capillary method, whereby the TTIP is partially hydrolysed to form a titanium oxo-cluster intermediate which then falls into the TTIP solution and is protected from further reaction with H_2O.

6.3 Titanium Oxo-cluster Inks

Toluene was identified as the most common solvent for the titanium oxo-clusters. A waveform was generated for neat toluene (See Table 6.3.1.1), following the same procedure as the previously identified waveforms. After imaging 50 droplets, an average droplet diameter of 74.75 µm and a moving range of 2.01 µm was calculated. Following the successful jetting of toluene, anhydrous toluene was added to each of the isolated titanium oxo-clusters and the use of the resulting solutions as inks for inkjet printing was assessed. Table 6.3.0.2

summarises the ink compositions, their effective concentrations with respect to titanium, and their ink designations. Table 6.3.0.3 shows the measured and optimised print properties of the titanium oxo-cluster inks.

Table 6.3.0.1 Toluene Waveform

Parameter	Value
Rise Time 1 (µs)	17
Dwell Time (µs)	17
Fall Time (µs)	17
Echo Time (µs)	34
Rise Time 2 (µs)	17
Idle Voltage (V)	0
Dwell Voltage (V)	45
Echo Voltage (V)	-45

Table 6.3.0.2 Ink Compositions and Designations

Ink Composition and concentration of Ti	Ink Designation
$[Ti_{12}O_{16}(O^iPr)_{16}]$, toluene, 0.1 M	6.3.1
$[Ti_{28}O_{40}(O^tBu)_{20}(OAc)_{12}]$, toluene, 0.09 M	6.3.2
$[Ti_{28}O_{40}(O^tBu)_{20}(OAc)_{12}]$, toluene reflux, 0.09 M	6.3.3
$[Ti_{16}O_{16}(OEt)_{32}]$, toluene, 0.15 M	6.3.4
$[Ti_{11}O_{13}(O^iPr)_{18}]$, toluene, 0.14 M	6.3.5
$[Ti_{11}O_{13}(O^iPr)_{18}]$, 1.5 M diglyme, toluene, 0.14 M	6.3.6

Table 6.3.0.3 Measured and optimised print properties of titanium oxo-cluster inks

Ink Designation	Droplet Diameter µm	Print Speed mm s^{-1}	Step Size mm	Track Width µm
Toluene	74.8 ± 2.0	-	-	-
6.3.1	63.1 ± 1.3	6	0.1	228.3
6.3.2	77.3 ± 1.2	12	0.1	220.2
6.3.3	63.1 ± 1.3	10	0.1	267.6
6.3.4	-	-	-	-
6.3.5	75.1 ± 2.7	10	0.1	189.1
6.3.6	107.3 ± 11.6	10	0.1	290.3

6.3.1 $[Ti_{12}O_{16}(O^iPr)_{16}]$, $[Ti_{28}O_{40}(O^tBu)_{20}(OAc)_{12}]$ & $[Ti_{16}O_{16}(OEt)_{32}]$ Inks

Ink 6.3.1 was the first cluster ink to be investigated. True to the findings of Day et al. the cluster was soluble in toluene and required nothing more than a gentle agitation. The resulting solution was loaded into the printer. After imaging 50 droplets, the print parameters were optimised to yield the track shown in Figure 6.3.1.1. The track is straight, with parallel edges. Material deposition is continuous, with a somewhat granular appearance suggesting a fluctuating sample thickness.

Figure 6.3.1.1 Printed track using ink 6.3.1 at 6 mm s^{-1} print speed and 0.1 mm step size on a glass substrate

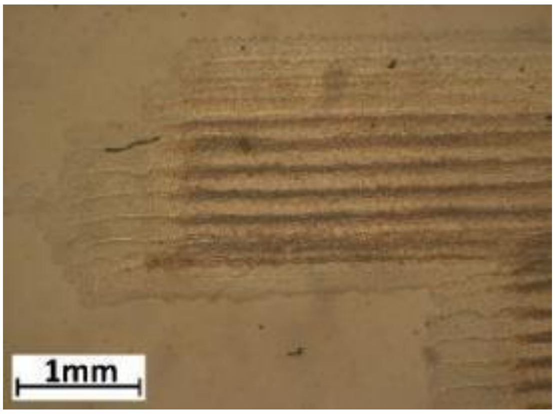

Figure 6.3.1.2 shows a multiple pass printed sample of the text 'TiO$_2$' using ink 6.3.1. This increased print complexity has increased the dispensing device decap time, resulting in the printed layers being offset. Offset layers indicate that the ink is susceptible to blocking the dispensing device.

Figure 6.3.1.2 Printed 3 pass TiO$_2$ using ink 6.3.1 at optimised conditions on a glass substrate

Toluene was first added to the $[Ti_{28}O_{40}(O^tBu)_{20}(OAc)_{12}]$ cluster and agitated gently to formulate ink 6.3.2. Figure 6.3.1.3 shows the optimised print track when using ink 6.3.2. The track consists of discrete particulates with a diameter of ~ 60 µm between two parallel edges likely belonging to the evaporated solvent front. There are appears to be no material deposited aside from the discrete particulates. With a maximum dimension of 2.4 nm for the individual $[Ti_{28}O_{40}(O^tBu)_{20}(OAc)_{12}]$ cluster, the discrete particulates observed within the printed track must either be aggregates of the clusters or resulting hydrolysis products of the titanium cluster.

Figure 6.3.1.3 Printed track using ink 6.3.2 at 10 mm s^{-1} print speed and 0.1 mm step size on a glass substrate

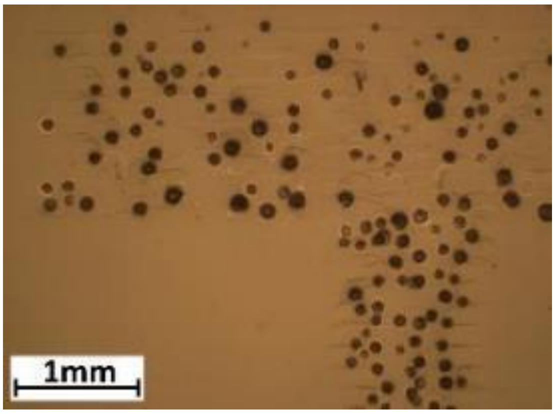

Figure 6.3.1.4 Printed 3 pass TiO_2 using ink 6.3.2 at optimised conditions on a glass substrate

A more complex, multiple pass print was obtained using ink 6.3.2, shown in Figure 6.3.1.4. The discrete particulates are also exhibited by this print, although the size of the particles and particle spacing varies significantly. This variation in size may be due to increasing aggregation or hydrolysis occurring with the lifetime of the ink. Although there appears to be no continuous deposit, the material all appears to be contained within the print boundaries.

As the $[Ti_{28}O_{40}(O^tBu)_{20}(OAc)_{12}]$ cluster did not initially appear to be as soluble in toluene as the $[Ti_{12}O_{16}(O^iPr)_{16}]$ cluster, another ink formulation was prepared. Ink 6.3.3 was prepared by adding toluene to the $[Ti_{28}O_{40}(O^tBu)_{20}(OAc)_{12}]$ cluster and then refluxing the resulting solution for 60 minutes. After identifying the optimum printing conditions for ink 6.3.3, a single pass 1 cm^2 and 3 pass text 'TiO$_2$' was printed (See Figures 6.3.1.5.a and b). It is immediately apparent that refluxing has facilitated a more even distribution of the $[Ti_{28}O_{40}(O^tBu)_{20}(OAc)_{12}]$ cluster in the toluene carrier solvent. This suggests the process of dissolving the $[Ti_{28}O_{40}(O^tBu)_{20}(OAc)_{12}]$ cluster in toluene is kinetically or thermodynamically hindered under standard conditions, requiring an input of energy to occur. The individual tracks can be distinguished in both images, yielding a continuous albeit granular deposit. Figure 6.3.1.5.a shows the presence of some large particles within the print. Figure 6.3.1.5.b shows the print exhibits neat and well-defined edges, aside from a few satellite droplets. The deposit of the 3 pass print is darker than the single pass print, indicating an increased material thickness.

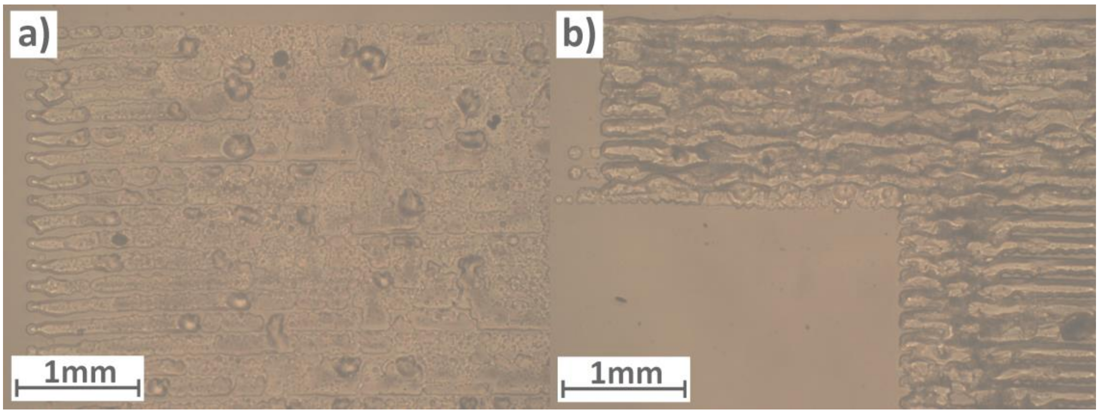

Figure 6.3.1.5 Printed samples using ink 6.3.3 at optimised conditions on a glass substrate. Image a) is 1 pass 1 cm^2 and b) is 3 pass. Image brightness has been increased by 40 % for clarity.

The large gravel-like crystals of the [$Ti_{16}O_{16}(OEt)_{32}$] cluster were found to be soluble in toluene after gentle agitation for 60 minutes, yielding ink 6.3.4. However, the resulting solution was found to degrade after just a few days and form a white powdery sediment likely to be TiO_2. Despite this relatively short shelf-life, ink 6.3.4 was still loaded into the printer to assess its viability as an inkjet ink. It was found to be too reactive as 50 consecutive images of droplets could not be taken without the dispensing device blocking. As such, no printed samples were achieved with ink 6.3.4.

6.3.2 [$Ti_{11}O_{13}(O^iPr)_{18}$] Ink

Table 6.3.2.1 Rheological properties of [$Ti_{11}O_{13}(O^iPr)_{18}$] inks

Ink Designation	Viscosity mPa s	Density g cm^{-3}	Surface Tension mN m^{-1}
Toluene	0.737	0.8619	26.94
Diglyme	1.045	0.9435	27.57
6.3.5	0.759	0.8655	24.93
6.3.6	0.797	0.8689	25.03

Toluene was also found to be a suitable solvent for the [$Ti_{11}O_{13}(O^iPr)_{18}$] cluster, yielding ink 6.3.5. After successfully imaging 50 droplets, optimised print parameters of 10 mm s^{-1} print speed and 0.1 mm step size were identified when using ink 6.3.5. The optimised track is shown in Figure 6.3.2.1. The printed track contains discrete particulates, similar to when using ink 6.3.2. Unlike the printed track in Figure 6.3.1.3, the particles vary in size and are less evenly spaced. Furthermore, the printed track is less straight and has a large variation in thickness. There is a difference in colour between the printed track and the glass substrate, suggesting that a film has been deposited in addition to the discrete particles. Figures 6.3.2.2.a and b show the printed 1 and 5 pass 1 cm^2 samples when using ink 6.3.5 to exhibit different phenomenon to the single printed track. The particles appear to have aggregated to form larger regions of deposit. Individual droplets can be seen at the top edge of Figure 6.3.2.2.b that show individual particles. There are also fluidic patterns present within the print, indicative of an insufficient substrate temperature for a fast evaporation of the toluene carrier. Elevation of the stage temperature to 60°C was investigated.

Figure 6.3.2.1 Printed track using ink 6.3.5 at 10 mm s^{-1} print speed and 0.1 mm step size on a glass substrate

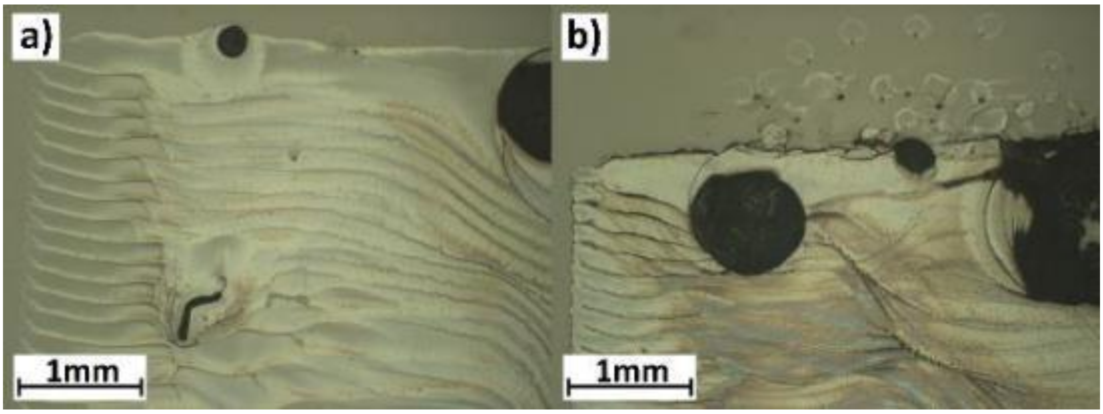

Figure 6.3.2.2 Printed 1 cm^2 using ink 6.3.5 at optimised print conditions on a glass substrate. Image a) is 1 pass and b) is 5 passes

Figure 6.3.2.3 shows the optimised printed track using ink 6.3.5 with a stage temperature of 60°C. In comparison to Figure 6.3.2.1, the borders of the track are far less uniform. Increasing the stage temperature appears to have had a negative effect on the optimised printed tracks. However, this was not the case for larger printed samples.

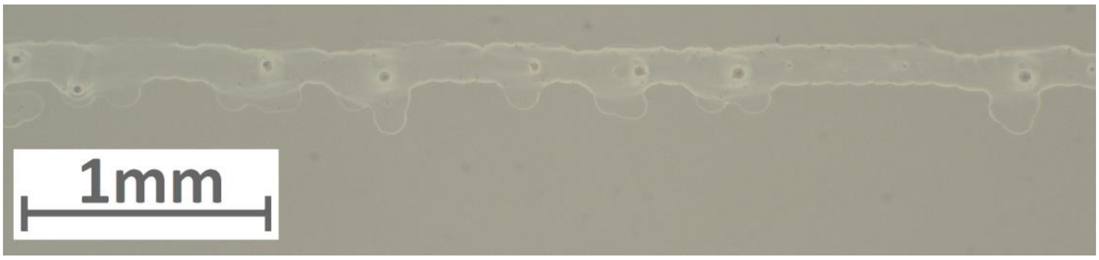

Figure 6.3.2.3 Printed track using ink 6.3.5 at 10 mm s^{-1} print speed and 0.1 mm step size on a glass substrate at 60°C stage temperature. Image brightness has been increased by 40 % for clarity.

1 and 5 pass prints of 1 cm^2 were printed using ink 6.3.5 at a stage temperature of 60°C, shown in Figures 6.3.2.4.a and b. Similar to the printed track, discrete particulates can be identified in both samples. The samples exhibit a well-defined printed edge and a continuous film. Increasing the number of printed passes from 1 to 5 yields an increase in homogeneity of the deposit in addition to an increased thickness. There was a marked improvement to the larger printed samples after increasing the stage temperature to 60°C.

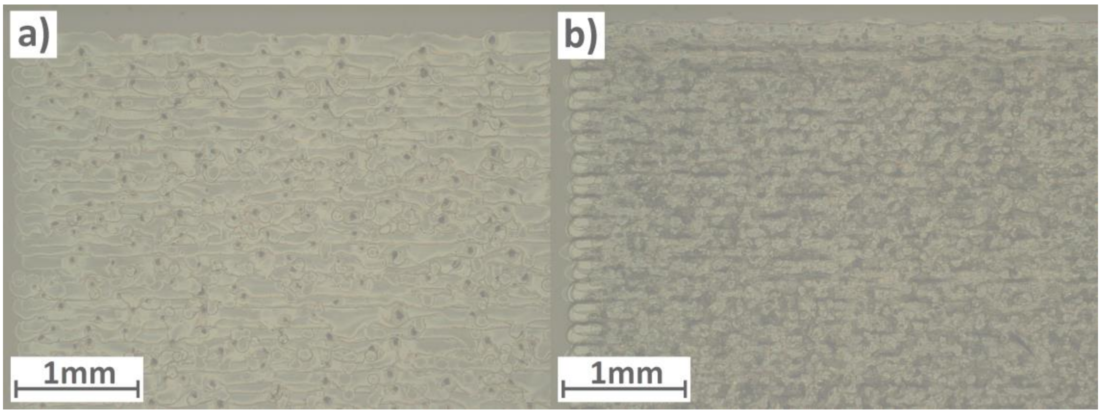

Figure 6.3.2.4 Printed 1 cm^2 using ink 6.3.5 at optimised print conditions on a glass substrate at 60°C stage temperature. Image a) is 1 pass and b) is 5 passes. Image brightness has been increased by 40 % for clarity.

Addition of a diglyme stabiliser to ink 6.3.5 was investigated, yielding ink 6.3.6. It was suspected that the addition of a glycol ether would inhibit the formation of discrete particulates if they were the product of cluster hydrolysis. This ink was also printed at an elevated substrate temperature of 60°C to allow direct comparisons to be made with the previous prints. Figure 6.3.2.5 shows the optimised track obtained with ink 6.3.5. Instead of discrete particulates, the track instead displays regions of iridescence connected by a continuously deposited film. As the track does not contain discrete particulates, the diglyme is inhibiting the hydrolysis of the $[Ti_{11}O_{13}(O^iPr)_{18}]$ cluster or preventing the formation of large cluster aggregates. However, the diglyme is not facilitating the formation of a uniformly deposited film. The track is comparatively straighter and more uniform than that obtained for ink 6.3.5. This improved performance of the ink on the substrate may be attributed to the diglyme behaving as a viscosity and surface tension modifier.

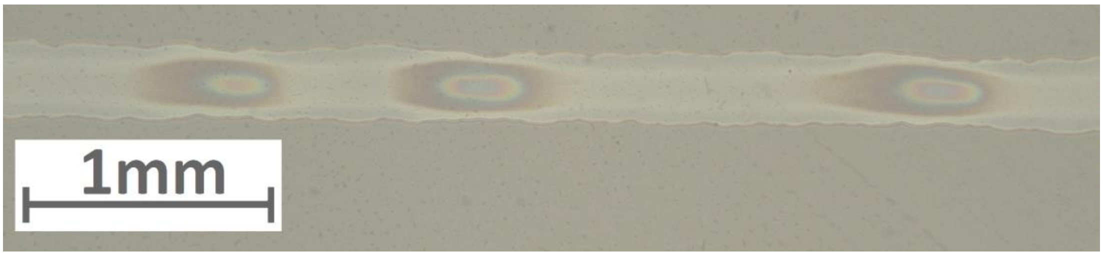

Figure 6.3.2.5 Printed track using ink 6.3.6 at 10 mm s^{-1} print speed and 0.1 mm step size on a glass substrate at 60°C stage temperature. Image brightness has been increased by 40 % for clarity.

Figures 6.3.2.6.a and b show the 1 and 5 pass 1 cm^2 prints using ink 6.3.6. Both prints exhibit an inhomogeneous material distribution over a continuous film deposit. In the single pass print there are many regions of differing appearance, suggesting a varying film thickness. The curved shapes of the different regions are indicative of droplet or evaporation driven effects.

There is a sparse distribution of darker deposits at the far right of Figure 6.3.2.6.a which strongly resembles a significant portion of the 5 pass deposit in Figure 6.3.2.6.b. The dark deposit is likely a relatively thick area of TiO_2, indicating the darker 5 pass sample consists of a larger quantity of deposited TiO_2. Unlike the single pass print, the 5 pass print exhibits a more localised distribution of material with several large dark regions consisting of the bulk of the deposited TiO_2. These dark regions are connected by the continuous and relatively thinner film that spans the printed area. At the far left of Figure 6.3.2.6.b, there is a line down the edge of the print that indicates a difference in material distribution likely caused by a partial blockage of the dispensing device and resulting in a small shift in the placement of a printed layer.

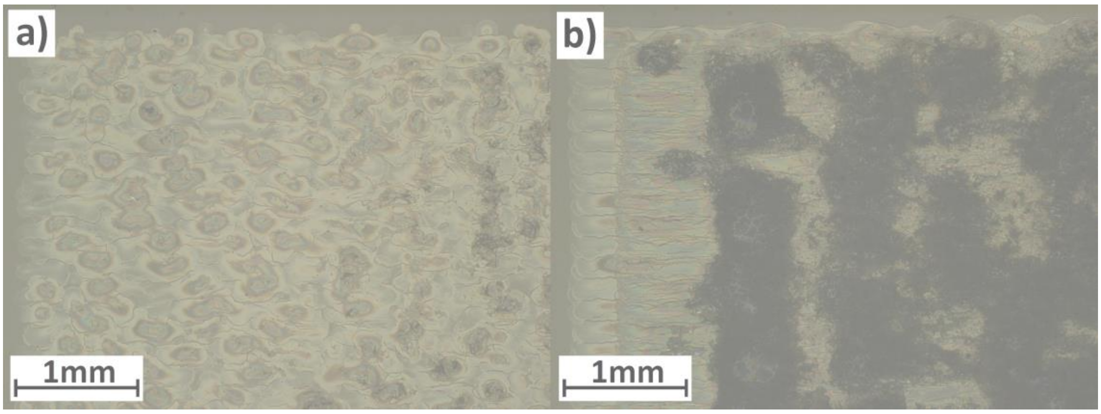

Figure 6.3.2.6 Printed 1 cm^2 using ink 6.3.6 at optimised print conditions on a glass substrate at 60°C stage temperature. Image a) is 1 pass and b) is 5 passes. Image brightness has been increased by 40 % for clarity.

6.3.3 $[Ti_{11}O_{13}(O^iPr)_{18}]$ Ink Ageing Study

The stability of ink 6.3.5 was investigated by measuring the change in viscosity of the ink over 28 days (See Figure 6.3.3.1). Viscosity was found to increase over time, likely caused by a small presence of H_2O within the ink formulation causing hydrolysis and further condensation reactions to take place. Despite the general trend of increasing viscosity, an increase of only 0.028 mPa s was measured over the 28 day ageing study. This would suggest that the ink displayed reasonable stability, although as the ink viscosity as a whole is relatively low the small increase results in a difference of 3.68 %. The difference in viscosity as a percentage is larger than the other samples discussed in Chapters 4 and 5. It was noted that after 3 months of storage, ink 6.3.5 had formed a gelatinous solid and the carrier solvent had mostly or entirely evaporated. The formation of a gel indicates that a stabiliser would be required in the ink formulation if the ink was to be stored over longer periods of time.

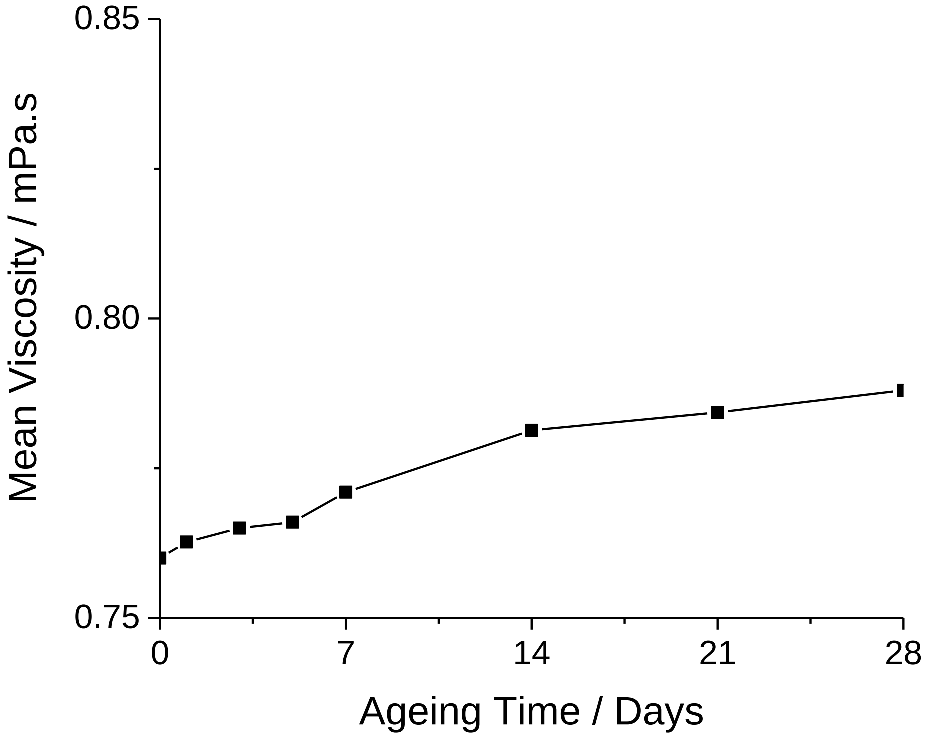

Figure 6.3.3.1 Ageing data for ink 6.3.5 over a 28 day maturation time

6.3.4 Discussion of Titanium Oxo-cluster Prints

Mixed success was found in printing titanium oxo-cluster containing inks. Although the [$Ti_{16}O_{16}(OEt)_{32}$] cluster was observed to be stable as a solid, it was unstable once dissolved in toluene and ink 6.3.4 could not be jetted through the inkjet dispensing device without an unacceptable prevalence of blockages. When dissolved in toluene, both the [$Ti_{28}O_{40}(O^tBu)_{20}(OAc)_{12}$] and [$Ti_{11}O_{13}(O^iPr)_{18}$] clusters displayed discrete particulates in their printed tracks. These particulates are likely caused by large aggregates of their respective clusters. For the [$Ti_{28}O_{40}(O^tBu)_{20}(OAc)_{12}$] cluster, this phenomenon was overcome by refluxing the cluster in toluene to facilitate its dissolving. The [$Ti_{12}O_{16}(O^iPr)_{16}$] cluster was also found to dissolve in toluene, yielding satisfactory single pass prints with ink 6.3.1. However, the stability of ink 6.3.1 was insufficient for complex multiple pass prints, as evidenced by the offset printed layers in Figure 6.3.1.2.

After increasing the substrate temperature to 60°C, the 5 pass 1 cm^2 shown in Figure 6.3.2.4.b is the most promising sample obtained with the titanium oxo-cluster containing inks. The edges are well-defined, forming a clear printed boundary. Material deposition is uneven, but distributed well throughout the sample. The formation of a gel after the ageing study of ink 6.3.5 indicated a stabilising agent should be added to the ink. The optical micrographs of ink 6.3.6 showed that the addition of diglyme did not improve the prints. As such, prints obtained with ink 6.3.5 will be studied further. It is noted that this ink formulation could be optimised further.

6.3.5 Annealing, XRD, and Raman Investigation

No useful XRD data could be obtained for printed or drop-tested samples of ink 6.3.5 as the signal to noise ratio was unusually low and there were no discernible peaks in any of the analysed samples. A low signal was also observed for the samples analysed by Raman spectroscopy. Peaks could be identified above the baseline, especially in the case of the sample after annealing at 450°C for 40 minutes (See Figure 6.3.5.1). Unlike the Raman spectra analysed so far, the annealed sample displays peaks belonging to the rutile polymorph in addition to those of anatase. The rutile peaks are of higher intensity than those of anatase, especially the large rutile E_g peak at ca. 418 cm^{-1}. The large rutile E_g peak, along with the rutile B_{2g} peak, may also be present in the sample before annealing although the intensity is low enough that this is uncertain. Interestingly, the anatase E_g peak is shifted to ca. 158 cm^1. A typical wavenumber for this peak is between 143 and 146 cm^{-1}, with the sample exhibiting a 10 – 15 cm^1 blue-shift. Such a large blue-shift is indicative of phonon confinement, which suggests the drop-tested sample consists of small nanoparticles or discreet molecular clusters. The blue-shift is larger than that observed for the reflux synthesised nanoparticles discussed in Chapter 5.

An annealing temperature of 450°C is low for the formation of rutile. Further investigation of annealed ink 6.3.5 samples to identify the conditions for pure rutile may indicate a potential application of ink 6.3.5 as a rutile deposition ink. Longer annealing times or an increased temperature are likely to reduce the presence of anatase and increase the abundance of rutile within the samples.

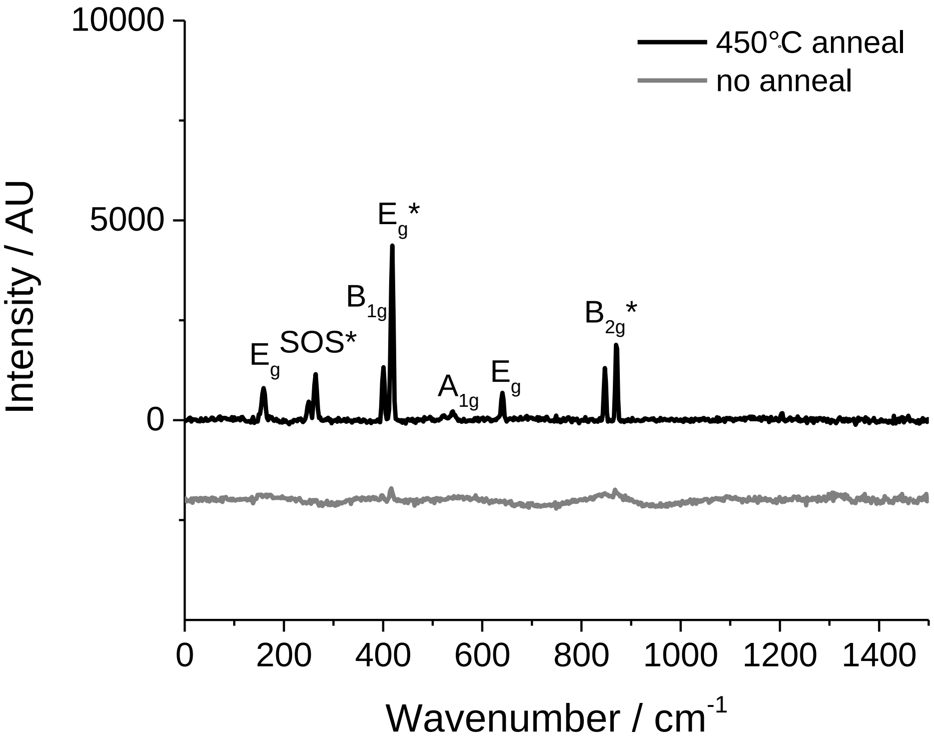

*Figure 6.3.5 Raman spectra of drop-tested samples using ink 6.3.5 on a glass substrate before and after annealing at 450°C for 40 minutes. A * indicates a peak belonging to the rutile polymorph*

6.3.6 Optical Transmittance and Wettability of the Printed Film

Profilometry was not performed for any printed samples of cluster containing inks, due to their discontinuous nature and unusual interactions with the stylus tip during preliminary testing. Optical transmittance was performed on a printed 5 pass 1 cm^2 using ink 6.3.5 (See Figure 6.3.6.1). Within the visible region (380 – 740 nm), an optical transmittance of between 46 and 59 % was measured. A sharp decrease beginning at 350 nm was measured, dropping to 2 % optical transmittance at 300 nm and continuing to fall towards 0 % below 300 nm. This is a similar observation to the printed samples in Chapter 4, and is likely a result of an increased absorbance due to the wavelength of the incident light corresponding to the energies of the TiO_2 band gap.

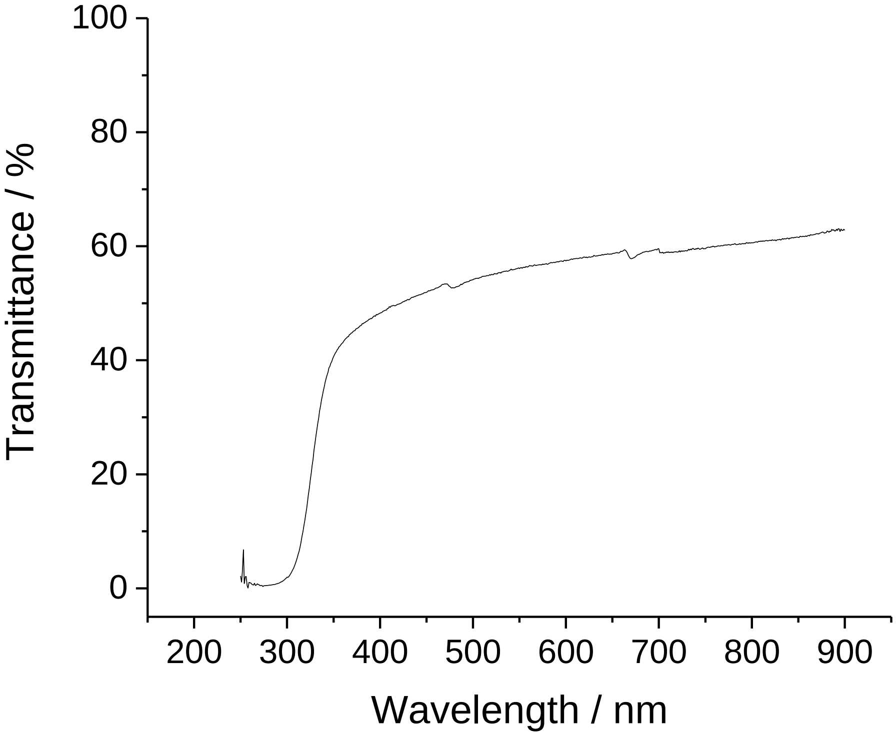

Figure 6.3.6.1 Optical transmittance of printed 5 pass 1 cm² using ink 6.3.5 on a glass substrate without annealing

Droplets of distilled H_2O were deposited onto a printed 5 pass 1 cm² sample of ink 6.3.5. The contact angle of the H_2O was measured after deposition (See Figure 6.3.6.2). A mean contact angle of 81° was measured, which is comparable to the 83° that was measured for ink 4.3.2. The data displayed a moderate range of 8°.

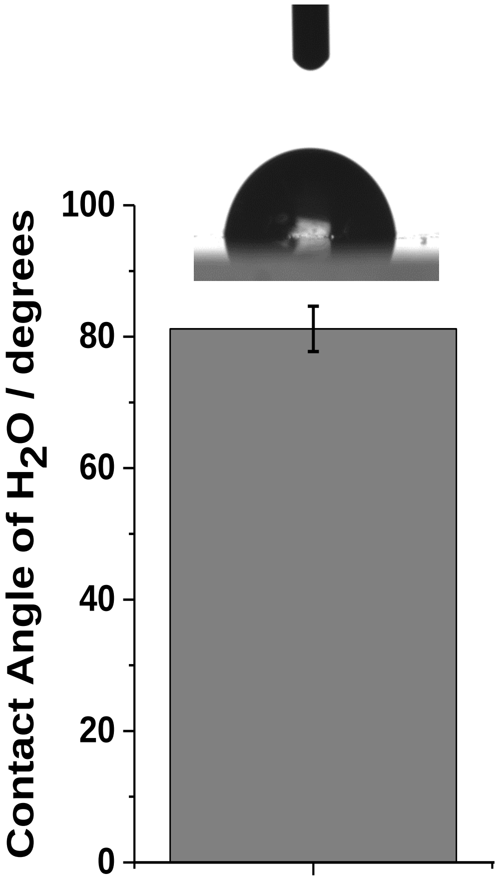

Figure 6.3.6.2 Contact angle of distilled H_2O on 5 pass 1 cm² print using ink 6.3.5 on a glass substrate without annealing. Error bar shows standard contact angle deviation. Inset image shows one of the imaged sessile H_2O droplets

6.3.7 SEM

Figure 6.3.7.1 shows SEM images of an inkjet printed 5 pass 1 cm^2 sample of ink 6.3.5 without any thermal treatment. At low magnification, the sample appears to consist of a thin film with a large number of cracks, resulting in an uneven distribution of material. Figure 6.3.7.1.b shows the bias of material deposition to be at and near the cracks of the film surface. Evaporation of residual solvent after the film has partially formed is the likely cause of the film cracking. Higher magnification images indicate the uncracked regions of the film to be smooth and homogeneous (See Figures 6.3.7.1.a and b).

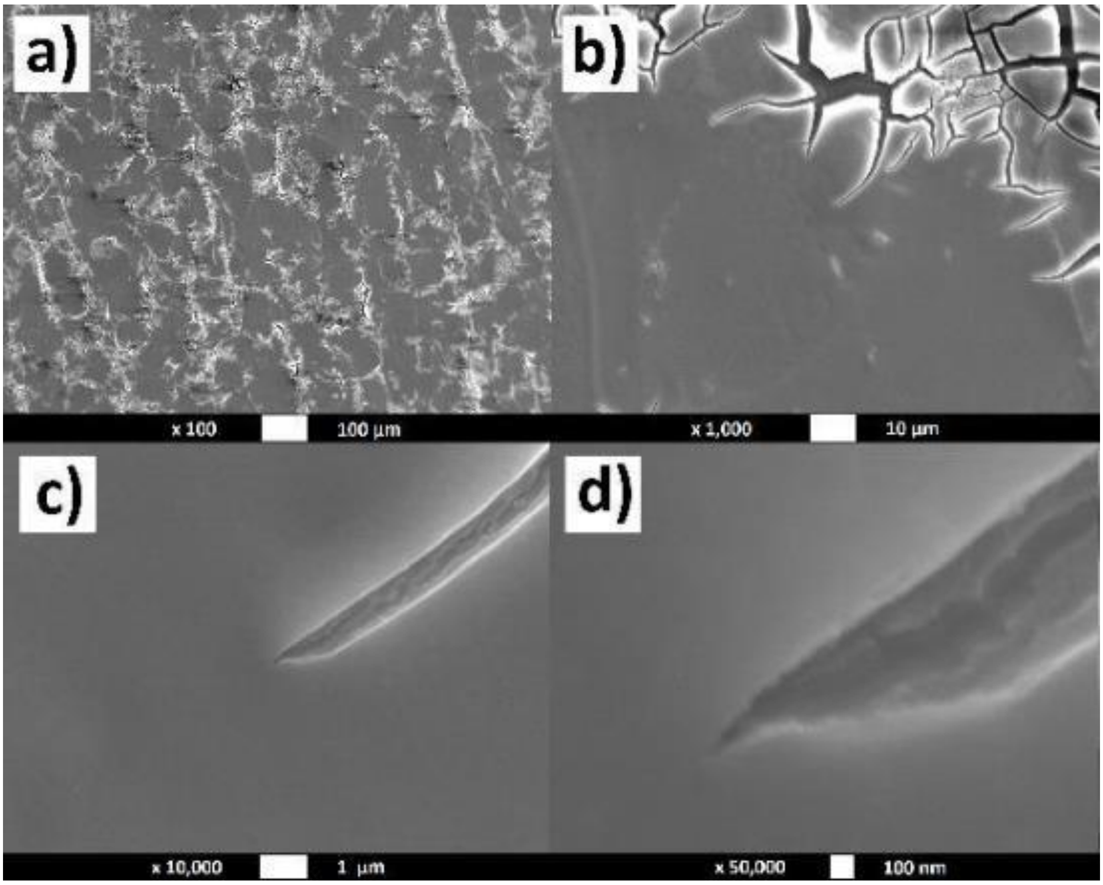

Figure 6.3.7.1 SEM of inkjet printed 5 pass ink 6.3.5 on a glass substrate without thermal treatment

SEM images were also taken for printed 5 pass 1 cm^2 samples of ink 6.3.6 to further investigate the effect of adding a diglyme stabiliser to the $[Ti_{11}O_{13}(O^iPr)_{18}]$ cluster ink. Figure 6.3.7.2.a shows that at low magnification it is clear that the sample of ink 6.3.6 consists of a less cracked film than that of ink 6.3.5. There are large lumps of material on the sample surface, which likely consist of TiO_2 that were not incorporated in the film. This may have been caused by the initial stabilisation of some clusters by diglyme, that are no longer stabilised after the evaporation of diglyme and subsequently form discreet particles of TiO_2 on the surface of the film. The film damage in Figure 6.3.7.2.b resembles a shattering, rather than a crack induced by solvent evaporation and escape. Higher magnifications indicate the undamaged film to be smooth and homogeneous. There appears to be small particles within the bulk of the film in Figure 6.3.7.2.d, although the drift in the image makes this uncertain.

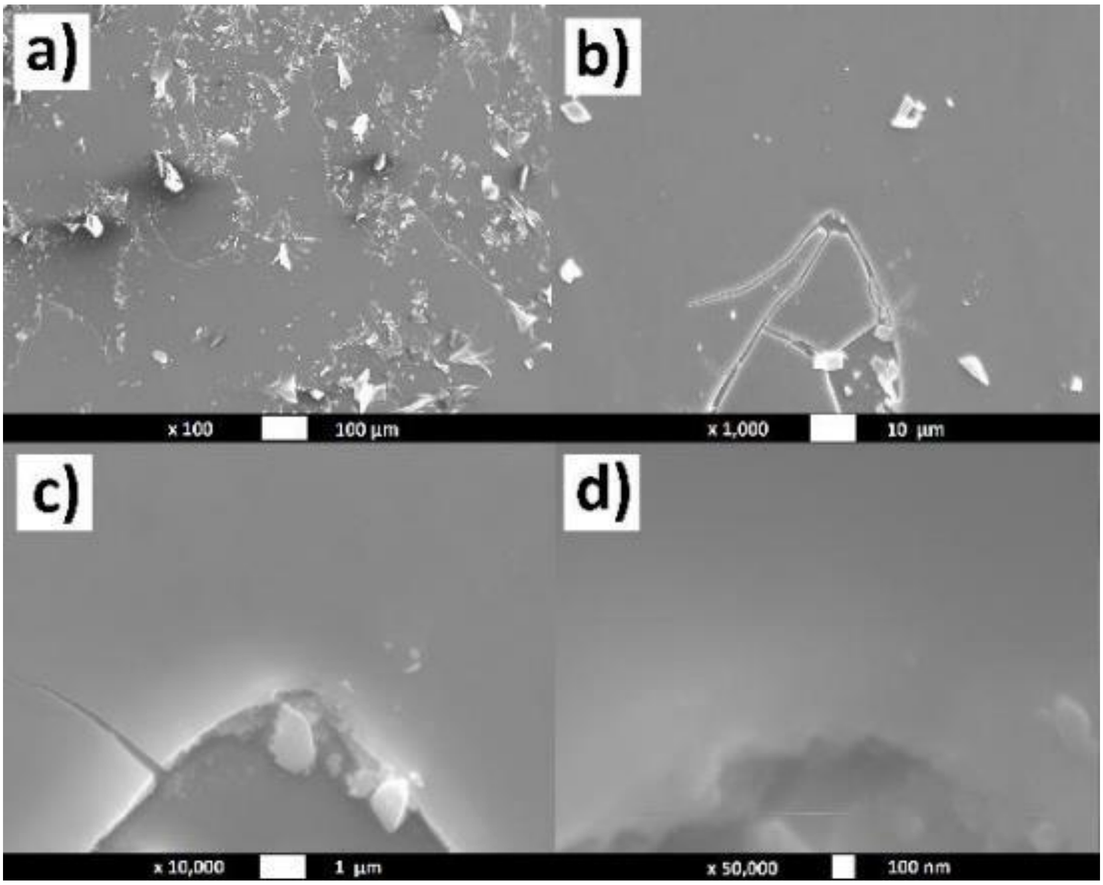

Figure 6.3.7.1 SEM of inkjet printed 5 pass ink 6.3.6 on a glass substrate without thermal treatment

6.4 Titanium Oxo-cluster Ink Discussion & Conclusion

Titanium oxo-clusters were identified as potential TiO_2 precursors for use in inkjet printing formulations. With an intermediate structure between that of a titanium alkoxide and TiO_2, it was believed that a reduction in thermal requirements or interesting phase selectivity would be observed when depositing titanium oxo-cluster containing inks. To this end, several titanium oxo-cluster syntheses were repeated according to the literature, along with a novel in-house synthesis of a cluster identifying closely as $[Ti_{11}O_{13}(O^iPr)_{18}]$ by elemental analysis.

A printable ink was not obtained with the $[Ti_{16}O_{16}(OEt)_{32}]$ cluster due to the relative instability of the cluster in solution. Toluene was found to be a suitable carrier solvent for the other synthesised clusters. Initial progress was made with ink 6.3.1 containing the dodecatitanate cluster, $[Ti_{12}O_{16}(O^iPr)_{16}]$, obtaining acceptable printed tracks. Unfortunately, the dispensing device was susceptible to blockage when jetting ink 6.3.1 for more complex print patterns.

Printing with the $[Ti_{28}O_{40}(O^tBu)_{20}(OAc)_{12}]$ containing cluster ink 6.3.2 yielded an unusual pattern of fairly regularly sized and spaced circles of material in the middle of the printed tracks. This phenomenon was somewhat alleviated by refluxing the ink.

Ink 6.3.5, containing the $[Ti_{11}O_{13}(O^iPr)_{18}]$ cluster, also displayed unusual circles of material when printed. Addition of diglyme to ink 6.3.5, giving ink 6.3.6, resulted in some inhibition to the circular deposits of material. However, material deposition was found to be more homogeneous without the presence of diglyme and so ink 6.3.5 was investigated further. Ink stability of ink 6.3.5 was demonstrated over a 28 day maturation period, with a 3.68 % increase to viscosity. It was noted that after 3 months of storage the ink had formed a gel, indicating that long-term stability was unacceptable and inks would need to be formulated relatively close to their dates of intended use.

Raman analysis demonstrated that annealing a drop-tested sample of ink 6.3.5 at 450°C for 40 minutes gave a mixture of anatase and rutile TiO_2. This was unexpected as 450°C is a relatively low temperature for the formation of rutile. Pending further investigation, this could suggest ink 6.3.5 or other $[Ti_{11}O_{13}(O^iPr)_{18}]$ containing inks have a potential application as a lower temperature rutile source. SEM analysis showed that although the unbroken films of printed samples using ink 6.3.5 and 6.3.6 were smooth and homogeneous, there was a significant presence of cracking that led to an overall uneven material distribution. Large particles were present on the surface of the printed ink 6.3.6 sample. This discontinuity and uneven distribution of material was shown by the relatively high optical transmittance in the visible range of the printed ink 6.3.5 samples.

Overall, the synthesis of titanium oxo-clusters and subsequent formulation into RMC inks was achieved. Some promising initial results have been obtained, such as the potential identification of $[Ti_{11}O_{13}(O^iPr)_{18}]$ as a low temperature rutile precursor. However, the formulation of RMC inks is still in its infancy and requires further optimisation before the scope of such inks is revealed.

6.5 Experimental Procedure

6.5.1 $[Ti_{12}O_{16}(O^iPr)_{16}]$ Solvothermal Synthesis

To a freshly purged Schlenk flask was added dry ^iPrOH (9.29 mL, 0.12 mol) and TTIP (7.26 mL, 25 mmol) under stirring. H_2O (0.45 mL, 25 mmol) was then added dropwise over 30 seconds while stirring. Each addition of H_2O caused a small amount of white precipitate to form. The resulting cloudy, white solution was left to stir for a further 5 minutes, then transferred into a polytetrafluoroethylene (PTFE) lined acid digestion vessel and placed in an autoclave for 3 days at 100°C. Once the vessel had cooled to room temperature, the solution was transferred to a freshly purged Schlenk flask. The solution was less cloudy, although there was some residual white precipitate lost in the solution transfer. Volatiles were removed *in vacuo*. Dried MeCN (3.0 mL, 75 mmol) was then added to the solution, causing precipitate to form. To a second purged Schlenk flask was transferred the liquid from the reaction mixture. MeCN (3.0 mL) was then used to wash the solid residue and combined with the other liquid extracts to yield a solid crystalline powder (1.482 g, 40 %). Found C: 34.27 %, H: 6.70 % (Calculated C: 32.47 %, H: 6.36 %).

6.5.2 $[Ti_{28}O_{40}(O^tBu)_{20}(OAc)_{12}]$ Solvothermal Synthesis

A freshly purged Schlenk flask was charged with ^tBuOH (5.0 mL, 52 mmol) and acetic acid (0.62 mL, 11 mmol). $Ti(O^tBu)_4$ (3.2 mL, 8.3 mmol) was added to the clear solution, which was then immediately transferred to a PTFE lined acid digestion vessel. The vessel was heated in an oven set to 130°C for 5 days. After the vessel had cooled to room temperature, the solution was transferred to a freshly purged Schlenk flask. Volatiles were removed *in vacuo* to yield small white crystals (0.32 g, 26 %). Found C: 7.85 %, H: 3.15 % (Calculated C: 30.09 %, H: 5.24 %).

6.5.3 $[Ti_{16}O_{16}(OEt)_{32}]$ Solvothermal Synthesis

To a PTFE lined acid digestion vessel was added ethanol (3.5 mL, 60 mmol), titanium ethoxide (3.5 mL, 17 mmol), and H_2O (0.15 mL, 8.3 mmol). The vessel was then heated in an oven to 100°C for 12 days. Once removed the vessel was allowed to cool under ambient conditions for 24 hours. Large, clear crystals (1.73 g, 66 % yield) were isolated from the reaction mixture and dried under nitrogen. It was found that the crystals were stable in air, as stated in the literature.

6.5.4 $[Ti_{11}O_{13}(O^iPr)_{18}]$ Syntheses

The glassware depicted in Figure 1 was dried and purged using standard Schlenk techniques. Under a N_2 atmosphere, one tube was charged with ^iPrOH (0.6 mL, 7.8 mmol), tetraglyme (1.5 mL, 6.8 mmol) and TTIP (0.6 mL, 2.0 mmol). To the other tube was added ^iPrOH (2.1 mL, 27 mmol) and H_2O (0.7 mL, 39 mmol). The reaction was then monitored over the course of a week. At the first hint of TiO_2 formation, indicated by the presence of a white powder, the "wet" ^iPrOH was removed and the reaction terminated. Using a syringe, the supernatant stabilised TTIP solution was then removed and the resultant clear crystals (0.105 g, 32 % yield) were washed several times with dried ^iPrOH and drying under nitrogen.

To increase the productivity of the $[Ti_{11}O_{13}(O^iPr)_{18}]$ cluster, a new synthetic method was devised. A TLC jar (175 cm^3) and five sample vials (12 cm^3) were dried in an oven. After drying, the TLC jar was charged with ^{i}PrOH (15 mL, 0.2 mol) and the five sample vials placed within. The TLC jar was then sealed and left for 24 hours to create an environment saturated in the solvent. To each sample vial was then added ^{i}PrOH (2.0 mL, 26 mmol), glycol ether stabiliser (See Table 1), and TTIP (2.0 mL, 6.8 mmol). See Figure 2 for a schematic of the experimental set-up. H_2O (1.0 mL, 56 mmol) was then added to the ^{i}PrOH at the base of the TLC jar. The TLC jar was resealed and stored in a laboratory cupboard for 5-7 days.

Table 6.5.4 Stabilised TTIP Solution Reaction Quantities

Glycol ether stabiliser	Volume (mL)	Moles (mmol)
DME	4.0	18
Diglyme	4.5	25
Triglyme	3.0	21
Tetraglyme	5.0	48

During the storage time clear crystals had formed within the stabilised TTIP solution containing sample vials. The crystals were then isolated by transferring the sample vials into a Schlenk flask, collecting the the supernatant solution with a syringe, washing the crystals with ^{i}PrOH, and drying under nitrogen. A maximum yield of 34 % was isolated for this process, equating to 0.38 g per sample vial. Unreacted supernatant solution could be recycled to further increase yield to 62 %, close to 0.69 g per sample vial.

Table 6.5.5 Reaction Product Elemental Analyses

Glycol Ether Stabiliser	Carbon %	Hydrogen %
DME	36.56	7.22
Diglyme	36.28	7.16
Triglyme	36.44	7.08
Tetraglyme	35.65	7.04
$[Ti_{11}O_{13}(O^iPr)_{18}]$ Calculated	36.07	7.06

6.5.5 Preparation of Titanium Oxo-cluster Inks

To a previously synthesised cluster, stored in a Schlenk flask (100 cm^3) under N_2, was added toluene according to Table 6.5.5. Ink 6.3.2 was refluxed for 1 hour to give ink 6.3.3. Diglyme

(8.60 mL, 60 mmol) was added to ink 6.3.6. The inks were then ready for analysis and printing according to Chapter 3.

Table 6.5.5 Stabilised TTIP Solution Reaction Quantities

Ink Designation	Mass of Cluster / g	Volume of Toluene / mL	Notes
6.3.1	0.4441	30.0	-
6.3.2	0.2615	20.0	-
6.3.3	0.2615	40.0	Refluxed
6.3.4	0.9200	40.0	-
6.3.5	0.9000	40.0	-
6.3.6	0.9000	31.40	8.60 mL Diglyme

6.6 References

1. V. W. Day, T. A. Eberspacher, W. G. Klemperer and C. W. Park, *Journal of the American Chemical Society*, 1993, **115**, 8469-8470.
2. T. J. Boyle, T. M. Alam, C. J. Tafoya and B. L. Scott, *Inorganic Chemistry*, 1998, **37**, 5588-5594.
3. L. Rozes and C. Sanchez, *Chemical Society Reviews*, 2011, **40**, 1006-1030.
4. V. W. Day, T. A. Eberspacher, W. G. Klemperer, C. W. Park and F. S. Rosenberg, *Journal of the American Chemical Society*, 1991, **113**, 8190-8192.
5. R. Schmid, A. Mosset and J. Galy, *Journal of the Chemical Society, Dalton Transactions*, 1991, DOI: 10.1039/DT9910001999, 1999-2005.
6. C. F. Campana, Y. Chen, W. G. Klemperer, V. W. Day and R. A. Sparks, *Journal of the Chemical Society - Dalton Transactions*, 1996, DOI: 10.1039/dt9960000691, 691-702.
7. N. Steunou, F. Robert, K. Boubekeur, F. Ribot and C. Sanchez, *Inorganica Chimica Acta*, 1998, **279**, 144-151.
8. N. Steunou, G. Kickelbick, K. Boubekeur and C. Sanchez, *Journal of the Chemical Society, Dalton Transactions*, 1999, DOI: 10.1039/A906198C, 3653-3655.
9. L. Rozes, N. Steunou, G. Fornasieri and C. Sanchez, *Monatshefte für Chemie / Chemical Monthly*, 2006, **137**, 501-528.
10. R. Azouani, A. Soloviev, M. Benmami, K. Chhor, J. F. Bocquet and A. Kanaev, *Journal of Physical Chemistry C*, 2007, **111**, 16243-16248.

11. J. B. Benedict, R. Freindorf, E. Trzop, J. Cogswell and P. Coppens, *Journal of the American Chemical Society*, 2010, **132**, 13669-13671.
12. P. Coppens, Y. Chen and E. Trzop, *Chemical Reviews*, 2014, **114**, 9645-9661.
13. M. Czakler, C. Artner and U. Schubert, *Monatshefte fur Chemie*, 2015, **146**, 1249-1256.
14. N. Li, P. D. Matthews, J. J. Leung, T. C. King, P. T. Wood, H.-K. Luo and D. S. Wright, *Dalton Transactions*, 2015, **44**, 19090-19096.
15. M.-Y. Gao, F. Wang, Z.-G. Gu, D.-X. Zhang, L. Zhang and J. Zhang, *Journal of the American Chemical Society*, 2016, **138**, 2556-2559.
16. H. Puff and H. Reuter, *Journal of Organometallic Chemistry*, 1989, **373**, 173-184.
17. F. O. Ribot, F. Banse and C. Sanchez, *MRS Proceedings*, 1994, **346**, 121.
18. A. Müller, R. Rohlfing, E. Krickemeyer and H. Bögge, *Angewandte Chemie International Edition in English*, 1993, **32**, 909-912.
19. G. Fornasieri, L. Rozes, S. Le Calve, B. Alonso, D. Massiot, M. N. Rager, M. Evain, K. Boubekeur and C. Sanchez, *Journal of the American Chemical Society*, 2005, **127**, 4869-4878.

Chapter 7

Niobium Doped Inks

7.1 Background and Introduction

Electrical conductivity is an important property for materials and their potential uses for many applications. There are three main types of material with respect to electrical conductivity: metallic conductors, semiconductors, and insulators. Before discussing semiconductors and doping, the basics of electrical conductivity and the electronic band theory is covered. Electronic conductivity is the measure of how freely an electric current can flow through a specific material. The most common form of an electric current is electrons, although any moving charged species can be considered as a current. In a highly conductive material there is very little or no resistance to the flow of these electron charge carriers and so a large current can be achieved. Conversely, a material that is highly resistive to the flow of charge carriers inhibits and diminishes current. The conductivity of a material is defined as the inverse of its resistance.

Quantum mechanics dictates that the energy levels that an electron can occupy are quantised. For electrons in a large enough system, these allowed energy levels are infinitesimally small increments apart and so can be effectively treated more as a continuous energy band than as discrete energy levels. The Pauli exclusion principle, stating that no two electrons can simultaneously occupy the same quantum states within a system, is still applied to the resulting band structure. Application of the Pauli exclusion principle, in addition to energy minimisation, causes the bands to fill upwards with electrons from the bottom of the band.

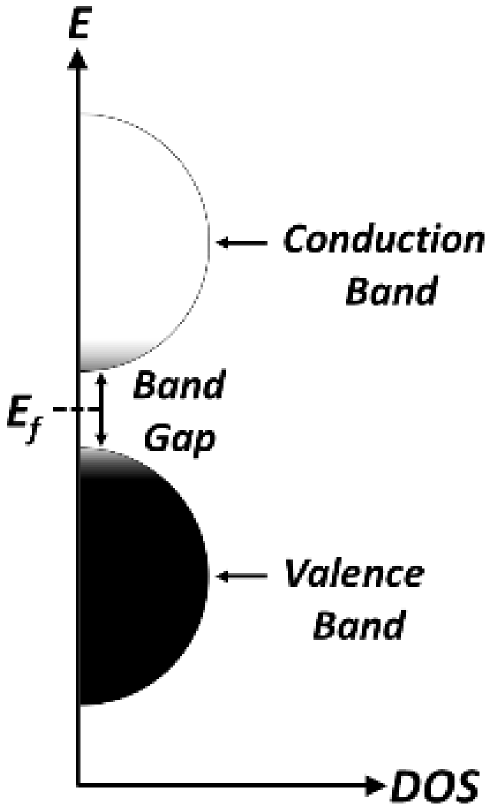

Figure 7.1.0.1 Band model of a semiconductor material

A generic semiconductor band model is shown in Figure 7.1.0.1. Along the x-axis is the density of states (DOS), a description of the number of states available to be occupied by the system at a given energy level. Energy is shown by the y-axis. The Fermi-Dirac distribution is used to show the population of each band using a shading system: black indicates all energy states are filled, grey indicates partial occupation of energy states, white indicates no energy states are filled. The valence band is the highest energy band that is occupied by the outermost electrons of the material. Conversely, the conduction band is the lowest energy band that is unoccupied by electrons. The energy difference between the end of the valence band and the start of the conduction band is known as the band gap; this energy is the minimum energy required to excite an electron into the conduction band.

Another important property of a material is the Fermi level, denoted by E_F, which is defined as the thermodynamic work required to add one electron to the material. Within band theory the Fermi level may be considered to be a hypothetical energy level that has a 50 % probability of being occupied by an electron at equilibrium. The Fermi level does not always correspond to an allowed energy level and therefore does not always lie within a band. Different types of materials are shown in Figure 7.1.0.2 in terms of band theory.

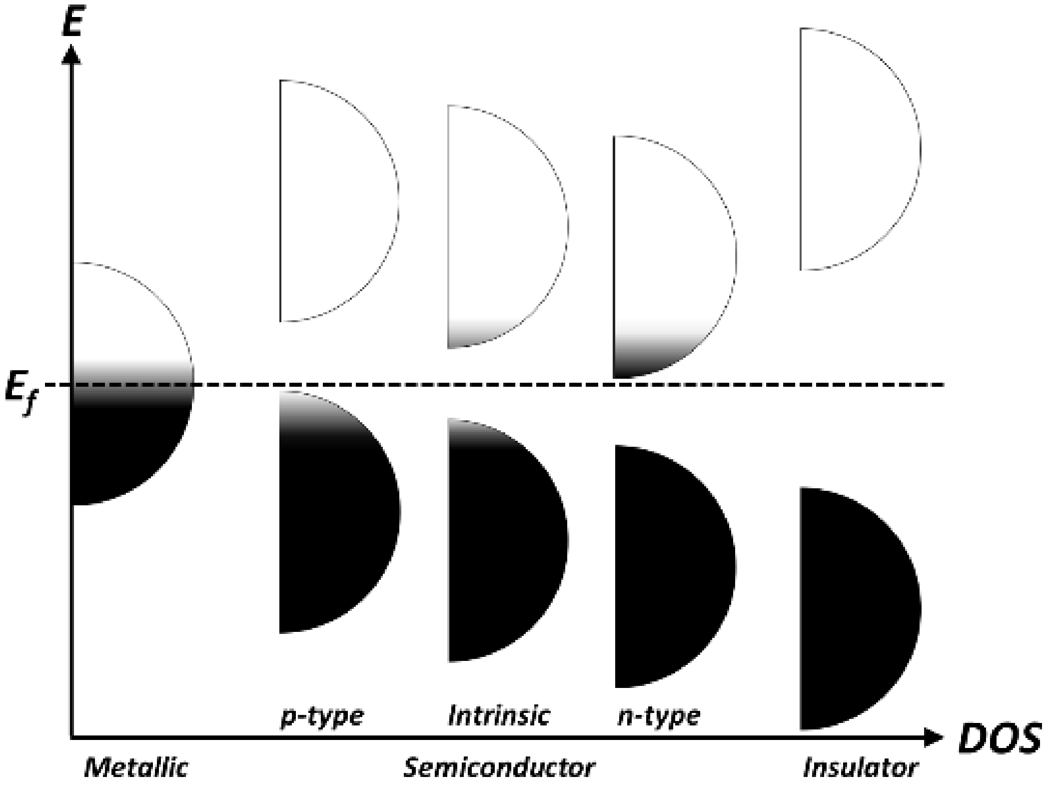

Figure 7.1.0.2 Fermi-Dirac representation of different types of materials at equilibrium.

Metallic conductors are highly conductive materials, allowing electrons to flow through them. This flow of electrons is facilitated by a partially filled band and high density of available states, shown in Figure 7.1.0.2. The traditional valence and conduction bands are overlapped in a conductor, and the Fermi level is in the middle of the band structure. There is no band gap in metallic conductors. Electrons may move quickly through the material by transiently occupying any of the allowed energy levels. There are also many electrons found at the Fermi level, allowing multiple electrons to flow simultaneously. Insulators are highly resistive materials, retarding the movement of electrons as there are no permitted energy states available for electrons to occupy. This is shown in Figure 7.1.0.2 by a Fermi level between a fully occupied valence band and an empty conduction band, along with a large band gap. The band gap is large enough in an insulator that excitation of an electron from the valence band into the conduction band is negligible.

Semiconductors are a diverse range of materials that have intermediate conductivities, with several different semiconductor types available. In a semiconductor, the band gap is sufficiently small that electrons can be promoted to the conduction band from the valence band under mild conditions such as room temperature. The conductivity of semiconductors increases with increasing temperature, unlike metallic conductors. This increased conductivity with increased temperature is due to the increased promotion of electrons into the conduction band, increasing the number of free electrons and holes. A hole is left when an electron is moved, holding an effectively positive charge relative to its previous state. Holes can also be utilised as charge carriers within a semiconductor, although they move much slower than electrons and are often removed by recombination with an electron.

7.1.1 Doping of Semiconductors

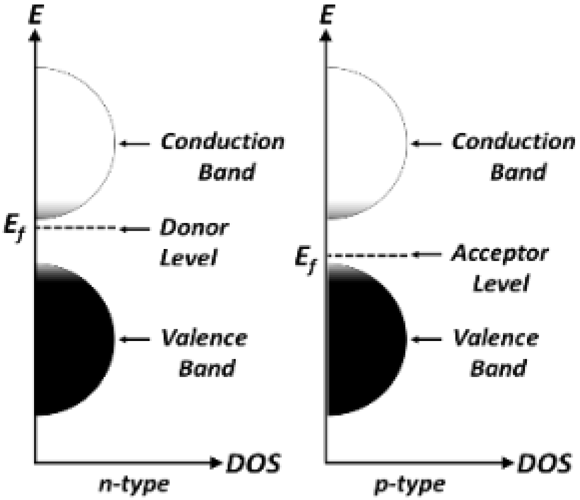

Figure 7.1.1.1 Band model of n-type and p-type doped semiconductors

Pure semiconductors, containing no impurities, are known as intrinsic semiconductors. Impurities can be introduced deliberately into the system to modify the conductivity of the material; these impurities are known as dopants. The conductivity is generally modified by either n-type or p-type doping (See Figure 7.1.1.1). Through introducing a dopant with an additional valence electron, n-doping is achieved. This dopant element is integrated into the semiconductor crystal lattice, in place of one of the original atoms, resulting in the introduction of a free electron charge carrier. The dopant element is known as an electron donor. In n-doped semiconductors, electrons are the primary charge carriers. Introduction of a dopant with one fewer electron than the original semiconductor atom is known as p-type doping. This dopant accepts electrons from the semiconductor atoms, resulting in the formation of positively charged electron holes and increasing mobility of the electrons in the valence band. In p-doped semiconductors, holes are the primary charge carriers.

An industrially significant semiconductor is indium tin oxide (ITO).[1-3] In addition to being an n-doped semiconductor with a high conductivity, thin films of ITO are also transparent to visible light. ITO is one of the most commonly used transparent conducting oxides (TCOs) as it can be easily deposited as a thin film with several advantageous properties in addition to its optical transparency and high conductivity. With a large band gap of approximately 4 eV (depending on composition), ITO is strongly absorbing of UV-A and UV-B electromagnetic radiation. It is also highly reflective of infrared emissions and anti-reflective of visible light, leading to use as hot mirrors (infrared-reflective coating) and anti-reflective coatings.

Common uses of ITO include: touch-screen applications, flat-panel and liquid crystal displays, organic light-emitting diodes, solar cells, and gas sensors.

There are issues associated with the use of ITO thin film coatings. As with most TCO coatings, a compromise is made between the properties of optical transparency and electrical conductivity. To improve the electrical conductivity the film thickness is increased; this increase in thickness causes a decrease in optical transparency, and vice versa. ITO also suffers from the issue of indium supply, relative to its demand, and has been identified as a technology-critical element. This has in turn increased the cost of indium and therefore ITO. Alternatives to ITO have been identified and are under further investigation, including aluminium-doped zinc oxide and gallium-doped zinc oxide, although these materials generally offer a lower performance.[4]

7.1.2 Doping TiO_2 with Niobium

Through the use of a dopant, such as niobium, TiO_2 can exhibit improved optical transparency and electrical conductivity. There are many ways to dope TiO_2 including the use of higher valence cations such as W^{6+}, Ta^{5+}, and Nb^{5+}, or lower valence cations such as In^{3+}, Zn^{2+}, and Li^{+}.[5] Doping can also be achieved in the anionic sites, using elements such as N, C, and S. Formation of Ti^{3+} can also be favoured under vacuum conditions, effectively resulting in a p-doped TiO_2.[6, 7] This chapter will focus on the investigation of niobium-doped titanium oxide as a TCO and potential alternative to ITO. Niobium is a promising dopant for TiO_2 systems as the size of the Nb^{5+} ion is similar to that of Ti^{4+} (~0.64 Å vs ~0.61 Å), allowing a successful substitution into the TiO_2 lattice. Substitution of a Ti^{4+} site with Nb^{5+} results in n-type doping as the niobium dopant has a valency one higher than titanium.

Niobium-doped titanium dioxide has seen extensive investigation within the literature.[8-15] Furubayashi et al. report on the synthesis of a transparent and conductive film of niobium-doped anatase TiO_2, with a formula $Ti_{1-x}Nb_xO_2$ for $x = 0.002 – 0.2$.[10] The films were produced to typically 40 nm thick by pulsed laser deposition. Resistivity was reported to be comparable to that of ITO, with an estimated sheet resistance of 60-80 Ω / □. A transmittance as high as 97 % was also found for visible light. The optimum electrical and optical properties were achieved with a dopant level $x \approx 0.03$.

Liu et al. report on the solvothermal synthesis of niobium-doped TiO_2 nanoparticles with a niobium incorporation in excess of 20 mol %.[16] The synthesised nanoparticles were dispersed into a solution of THF and polymer, after which the resulting solution was dip coated onto a silicon wafer or glass substrate to yield an average film thickness of 200 nm. In comparison to the un-doped samples, the niobium-doped TiO_2 was reported to drastically increase the electrical conductivity of the nanoparticles. An enhancement of the mesostructured uniformity, surface area, and pore volume were also observed.

Doping of TiO_2 with niobium also modifies the properties associated with common TiO_2 applications, with one such application being photocatalytic pollutant and dye degradation. Through niobium doping the optical absorption properties of TiO_2 can be red-shifted to improve absorption of the visible wavelengths. This improved absorption is shown by Wu et al. with the improved photocatalytic activity of various niobium-doped TiO_2 samples relative to the pure anatase TiO_2 they were derived from.[13] A 0.50 mol % level of niobium doping was found to produce the highest activity of catalysed photodegradation of methyl orange under UV and visible light.

It is apparent that there is no ideal level of niobium doping for all possible applications of niobium-doped TiO_2; the level of doping allows for the tuning of the sample towards its intended application. Wang et al. report on the niobium doping of spin-coated TiO_2 films .[11] A difference in the phase analysis after annealing indicated a reduction in required annealing temperature for the complete anatase to rutile transformation. A lower transmittance was observed for the films containing niobium, particularly around 500 nm. The optical band gap was also shown to reduce with the addition of a niobium dopant. Cirera et al. reported a large dependence of the anatase to rutile transformation on the loading of the niobium dopant.[8]

This chapter will continue in section 7.2 by discussing the different inks that were formulated using a solution provided by EpiValence as the titanium and niobium source. Another ink will then be discussed that is comparable to ink 4.3.2 with an equivalent doping level of niobium to the final EpiValence ink formulation. The prints of these two inks will be annealed and characterised. Concluding remarks will then be given in section 7.3.

7.2 Niobium Doped Inks

Preliminary work on niobium doped titanium inks utilised chemical solutions provided by EpiValence; a company focused on the deisgn, manufacture, and supply of specialty chemicals to the electronics industry. One solution consisted of $Ti(OEt)_4$ with a $Nb(OEt)_5$ dopant and a 2-methoxyethanol solvent, although limited success was found with this solution. Another solution consisting of $Ti(OEt)_4$ with a $Nb(OEt)_5$ dopant was also used, instead containing a 2-isopropoxyethanol (^{i}PPE) solvent. Both of these solutions have been reported on.[17] All of the work described below that utilises a solution from EpiValence uses the niobium doped titanium ink in ^{i}PPE. It was believed that use of the 2-alkyloxyethanols would be multifunctional, behaving as both the bulk solvent for the solutions and a stabilising component for the metal alkoxides with respect to hydrolysis with H_2O. The structure of the 2-alkyloxyethanols is similar to that of DME (See Figure 7.2.0.1), which was used as a TTIP stabiliser in Chapters 4 and 5. In-house testing of the solutions by EpiValence showed ^{i}PPE to be suitable for the stabilisation of the $Ti(OEt)_4$ and $Nb(OEt)_5$ components.

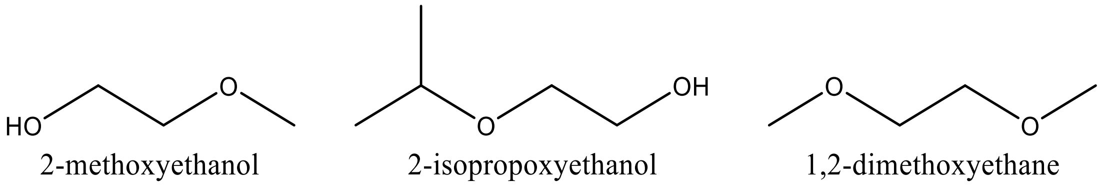

Figure 7.2.0.1 Structures of 2-methoxyethanol, 2-isopropoxyethanol (^{i}PPE), and 1,2-dimethoxyethanol (DME)

Table 7.2.0.1 Niobium doped ink compositions

Ink Designation	^{i}PrOH	^{i}PPE	DME	TTIP	$Ti(OEt)_4$	$Nb(OEt)_5$
EpiValence	-	7.47 M	-	-	0.61 M	0.039 M
7.2.1	-	8.47 M	-	-	0.10 M	0.0065 M
7.2.2	7.85 M	1.49 M	1.93 M	-	0.12 M	0.0079 M
7.2.3	7.83 M	1.83 M	1.50 M	-	0.15 M	0.0097 M
7.2.4	10.43 M	-	1.50 M	0.15 M	-	0.0097 M

Table 7.2.0.2 Rheological properties of niobium doped inks

Ink Designation	Viscosity mPa s	Density g cm^{-3}	Surface Tension mN m^{-1}
^{i}PrOH	2.529	0.7870	19.27
^{i}PPE	2.389	0.9056	24.42
DME	0.445	0.8630	23.41
7.2.1	2.457	0.8912	24.04
7.2.2	1.839	0.8226	22.29
7.2.3	1.964	0.8290	21.85
7.2.4	1.889	0.8030	20.18

It became apparent that whilst the ^{i}PPE was capable of stabilising the metal alkoxides with respect to hydrolysis, the concentration at which the solution was supplied was too high; immediately after attempting to jet the as-supplied solution a blockage would form. As such, the first ink to be discussed consists of the EpiValence solution diluted further with ^{i}PPE (Ink 7.2.1). Another approach to formulating an EpiValence ink was also investigated, where the as-supplied solution was diluted with DME and ^{i}PrOH (Ink 7.2.2).

Following the success of the DME and ^{i}PrOH additions, another ink was formulated to make the final concentrations comparable to ink 4.3.2 with a 0.15 M concentration of titanium (Ink 7.2.3). A final ink was formulated that did not contain the EpiValence solution. Instead, it was a variation of ink 4.3.2 with the inclusion of 0.0097 M $Nb(OEt)_5$; the same dopant ratio as the EpiValence solution for direct comparisons (Ink 7.2.4).

Table 7.2.0.3 Measured and optimum print properties of niobium doped inks

Ink Designation	Droplet Diameter µm	Print Speed mm s^{-1}	Step Size mm	Track Width µm
^{i}PPE	65.7 ± 1.1	-	-	-
7.2.1	61.6 ± 3.6	10	0.2	-
7.2.2	86.3 ± 8.9	6	0.2	251.5
7.2.3	88.5 ± 5.3	10	0.1	205.2
7.2.4	93.8 ± 3.9	10	0.1	313.9

7.2.1 EpiValence Inks

A niobium doped titanium solution was supplied by EpiValence, the formulation of which is included in Table 7.2.0.1.[17] The ^{i}PPE was chosen as a multi-purpose additive that is both the carrier solvent and stabilising agent. There was a 15.5 : 1 molar ratio of titanium to niobium, and a 12.2 : 1 molar ratio of ^{i}PPE to titanium. Despite the larger ratio of stabiliser to active component in this solution when compared to ink 4.3.2, the solution was found to be too reactive as an ink within an inkjet system. Attempting to jet the solution caused immediate blockages to occur due to the hydrolysis of the $Ti(OEt)_4$ at the dispensing device orifice.

With a concentration of 0.61 M with respect to titanium, this ink is just over four times as concentrated as the 0.15 M TTIP ink 4.3.2. It is was therefore decided to reduce the concentration of the EpiValence solution down to 0.1 M with respect to titanium by diluting with ^{i}PPE, yielding ink 7.2.1. Ink 7.2.1 was found to jet a consistent stream of droplets. None of the printed tracks were acceptable, with wildly fluctuating and discontinuous lines being deposited. Figures 7.2.1.1.a and b show optical micrographs of the top left and middle of a single pass 1 cm^2 print obtained with ink 7.2.1. It is immediately apparent that the print is of poor quality, with little to no deposited material at the edges of the print boundaries. The material has gathered towards the middle of the print, exhibiting an unusual pattern of radial expansion.

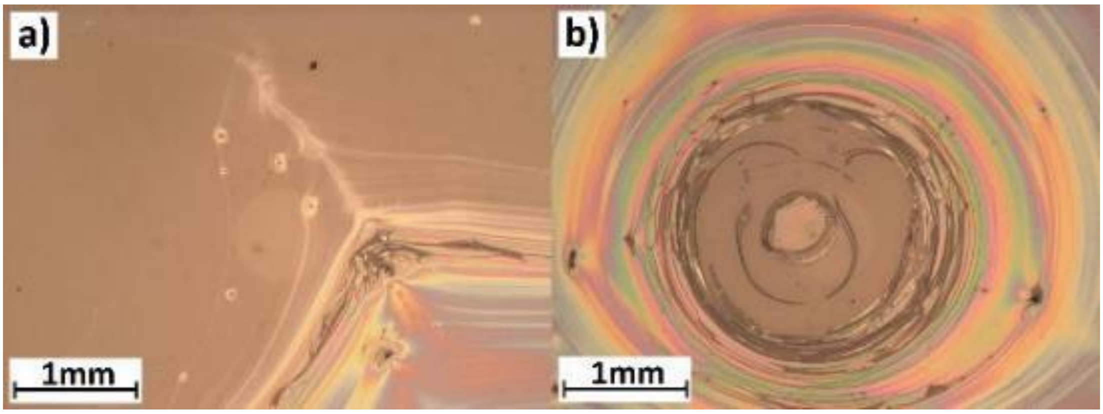

Figure 7.2.1.1 Printed 1 pass 1 cm^2 using ink 7.2.1 at 10 mm s^{-1} print speed and 0.2 mm step size on a glass substrate. Image a) is top left, b) is middle of print

Iridescence is also exhibited radially by the sample, except at the very centre and edges; the iridescence is likely due to the mechanism of thin-film interference, whereby the photons reflected by the upper and lower boundaries of the thin film interfere with one-another. This interference causes varying increases or decreases in the reflection and transmission of certain wavelengths of the incident light, resulting in intensifying certain colours and attenuating others. With a boiling point of 142 – 144°C, it is proposed that the ^{i}PPE is the primary cause of the unusual phenomena exhibited by the printed sample using ink 7.2.1. As the boiling point of the carrier solvent is high, relative to the stage temperature of 30°C, evaporation will occur very slowly. This slow evaporation reduces the pinning of the contact line, facilitating the flow of the metal alkoxides and any partially or fully formed hydrolysis products to the middle of the print as the solvent front slowly recedes (See Figure 7.2.1.2).

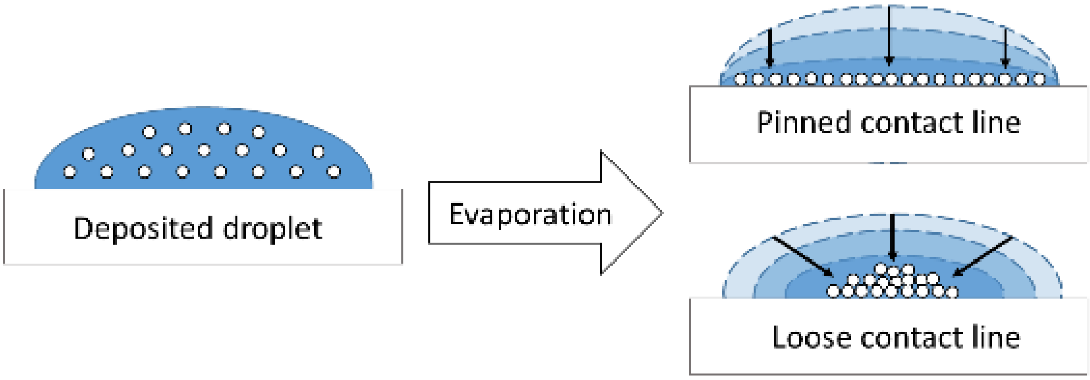

Figure 7.2.1.2 Schematic to show the difference between a pinned and loose contact line in an evaporating droplet

Due to the higher boiling point of ^{i}PPE relative to the other solvents used, the stage temperature was increased from 30 to 60°C. Figures 7.2.1.2.a and b show the resulting top left and middle optical micrographs of a single pass 1 cm^2 print obtained with ink 7.2.1 with a 60°C stage temperature. Whilst the print is still far from ideal, there is a marked improvement after increasing the stage temperature. The edges of the print can be identified, with the individual printed tracks distinguishable on the left edge as shown in Figure 7.2.1.3.a. However, the top edge is poorly defined and the film becomes discontinuous. Both Figures 7.2.1.3.a and b show that the deposit is iridescent and exhibits a distribution of material that appears to be dominated by the flow of liquid.

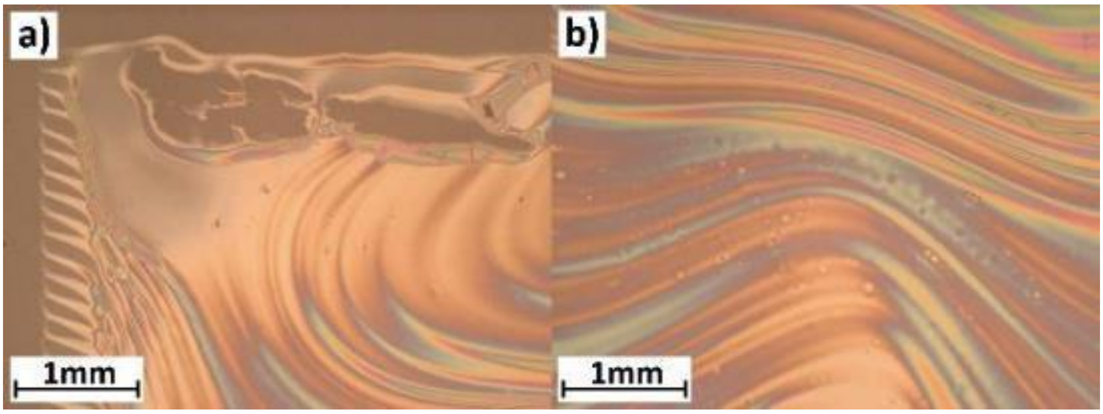

Figure 7.2.1.3 Printed 1 pass 1 cm^2 using ink 7.2.1. at 10 mm s^{-1} print speed and 0.2 mm step size on a glass substrate at 60°C stage temperature. Image a) is top left, b) is middle of print

Further modifications to the ink formulation were performed in an attempt to improve performance of the ink after jetting. Instead of diluting the original EpiValence solution with ^{i}PPE, as was done for ink 7.2.1, the solution was diluted with DME and dried ^{i}PrOH to yield ink 7.2.2. Using the ^{i}PrOH waveform a continuous stream of droplets was jetted from the dispensing device with a relatively large moving range of 8.86 µm, which is 10.2 % of the average droplet size at 86.25 µm. Figure 7.2.1.4 shows the printed track obtained when using ink 7.2.2 at the identified optimum print parameters and a stage temperature of 60°C. The track has two straight, parallel edges. Material deposition appears to be primarily in the middle of the track and at the very edges, with the inner edges of the track appearing to consist of a thinner deposit.

Figure 7.2.1.4 Printed track using ink 7.2.2 at 6 mm s^{-1} print speed and 0.2 mm step size on a glass substrate at 60°C stage temperature

Figures 7.2.1.5.a and b show the single and multiple pass printed 1 cm^2 samples obtained with ink 7.2.2 printed onto a substrate temperature of 60°C. The effects of liquid flow have been reduced compared to the previous sample using ink 7.2.1. Both the left and top edges are well defined. However, the prints using 7.2.2 are still not ideal. Figure 7.2.1.5.a shows the single pass sample to be discontinuous, consisting of individual or small groups of merged droplets rather than printed tracks. This is unusual as the printed track obtained under the same printing conditions was continuous. The difference between the individual printed track in Figure 7.2.1.4 versus the discontinuous tracks observed within the 1 cm^2 sample in Figure 7.2.1.5.a could be caused by the increased saturation of evaporated ink organics in the nearby atmosphere, retarding the rate of evaporation for the remaining organic ink components on the substrate surface.

The 5 pass sample, shown in Figure 7.2.1.5.b, also consists of individual or small groups of merged droplets. Increasing the number of printed passes will exacerbate the effects of increased partial pressures near the evaporating solvent front, further retarding the evaporation rate of the remaining organic ink components. Unlike the single pass print, the printed lines are neat and clearly defined in the 5 pass print. The left and top edges are also neat and well defined, with no stray droplets or satellites present. Furthermore, the droplets within the bulk of the print all appear to have overlapped well with the previous layers. Iridescence is displayed by the discrete sections of deposited material, similar to the samples obtained when printing ink 7.2.1.

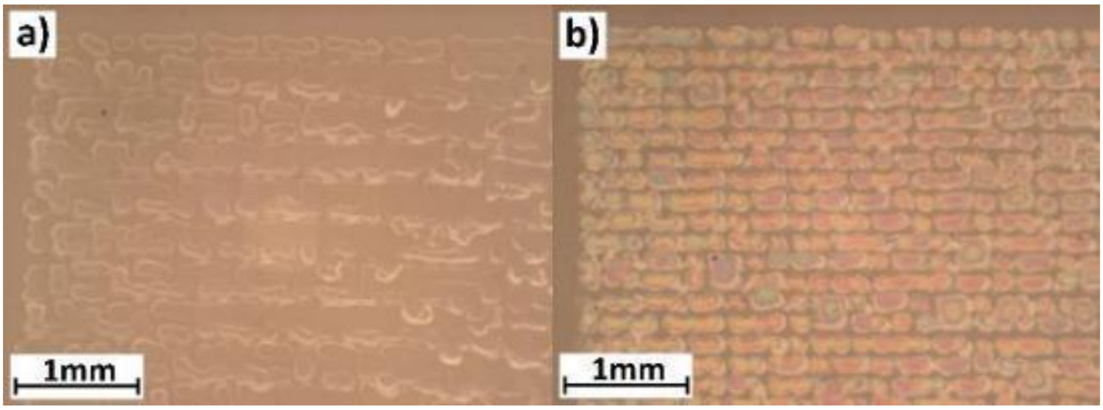

Figure 7.2.1.5 Printed 1 cm^2 using ink 7.2.2 at optimised print conditions on a glass substrate at 60°C stage temperature. Image a) is 1 pass and b) is 5 passes

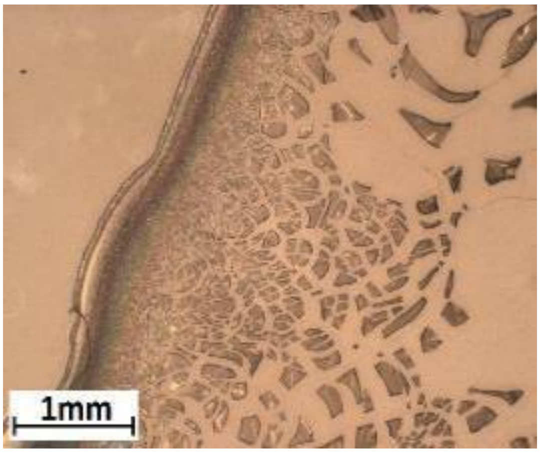

Figure 7.2.1.6 Drop-tested ink 7.2.2 on a glass substrate at 60°C stage temperature.

A sample of ink 7.2.2 was drop-tested onto a cleaned glass substrate heated to 60°C for analysis. Figure 7.2.1.6 shows the edge of the drop-test. It is immediately apparent that the deposit has not adhered to the substrate, evidenced by the majority of the deposit having flaked off. The size of the remaining flakes decreases closer to the edge of the drop. Near to the edge, the sample exhibits some iridescence. This lack of adhesion may be caused by the high boiling point of ^{i}PPE; the metal oxide deposit forming fully on top of a layer of residual ^{i}PPE, preventing an effective adhesion.

Following the improvements made to the original EpiValence ink, another ink was formulated using the EpiValence solution. Ink 7.2.3 was intended to be directly comparable with ink 4.3.2, and so was made to a 0.15 M concentration of titanium, stabilised by a 1.5 M concentration of DME. The ink also contained a 0.01 M concentration of niobium dopant, and a 1.83 M concentration of ^{i}PPE, with an ^{i}PrOH carrier solvent. Figure 7.2.1.7 shows the printed track obtained with ink 7.2.3 at the identified optimum print parameters and a stage temperature of 60°C. The track is somewhat straight, with parallel edges to one-another. The distribution of material appears uniform based on the even colour and tone of the print.

Figure 7.2.1.7 Printed track using ink 7.2.3 at 6 mm s^{-1} print speed and 0.2 mm step size on a glass substrate at 60°C stage temperature

After ascertaining the optimum print speed and step size when jetting with ink 7.2.3, single and multiple pass prints of 1 cm^{2} were generated. Figure 7.2.1.8.a shows the single pass sample to be a continuous deposit composed of discernible printed tracks. The left and top edges of the print are well defined. The track that forms the top edge appears to fluctuate in width. Material deposition appears uniform for the 5 pass sample, shown in Figure 7.2.1.8.b. However, the sample is thinner at the very edges of the print as shown by the increased apparent brightness of the deposit. This reduced thickness at the edge of the print is likely caused by a small deviation in the impact location of a single printed pass during the printing process; likely caused by turbulence or a partial blockage in the dispensing device. The feint lines down the middle of the image and along the bottom are signs of scraping caused by the profilometry stylus. This damage was not observed for most other samples, indicating the printed ink 7.2.3 sample is soft relative to the other prints.

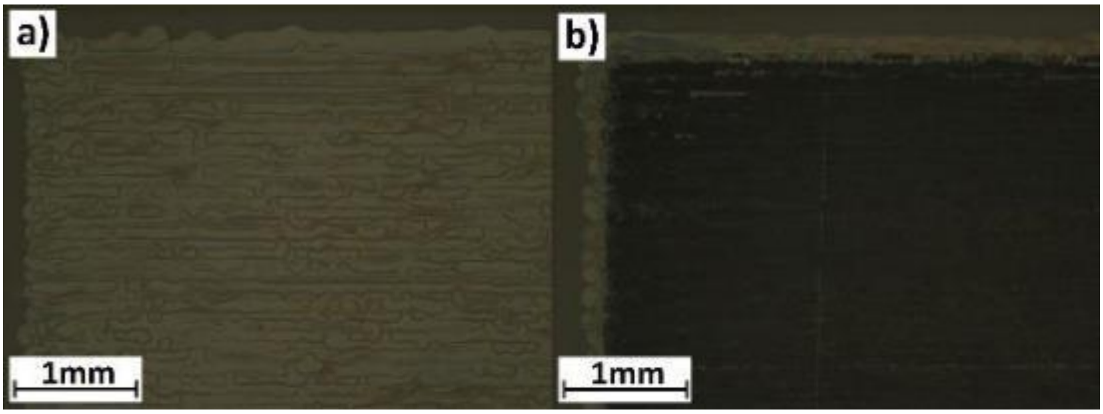

Figure 7.2.1.8 Printed 1 cm^2 using ink 7.2.3 at optimised print conditions on a glass substrate at 60°C stage temperature. Image a) is 1 pass and b) is 5 passes.

7.2.2 Niobium Doped 0.15 M TTIP Ink

A similar ink to 7.2.3 was formulated using off-the-shelf chemicals, rather than the EpiValence solution, resulting in an ink consisting of the following final concentrations: 0.15 M TTIP, 0.01 M $Nb(OEt)_5$, 1.5 M DME, all dispersed within an ^iPrOH carrier solvent. The differences between this new ink, designated ink 7.2.4, and ink 7.2.3 are the substitution of $Ti(OEt)_4$ with TTIP, and the exclusion of ^iPPE. Despite the absence of ^iPPE from the ink formulation, ink 7.2.4 was still printed at a substrate temperature of 60°C for a fair comparison to the other niobium doped prints. Figure 7.2.2.1 shows the printed track of ink 7.2.4 using the optimised print conditions. The edges of the track are straight and parallel to one-another. Just within the track boundaries the film appears to fluctuate in its distribution, leading to an unusual but consistent oscillatory pattern. The bulk of the printed track is uniform in nature.

Figure 7.2.2.1 Printed track using ink 7.2.4 at 6 mm s^{-1} print speed and 0.2 mm step size on a glass substrate at 60°C stage temperature

Figures 7.2.2.2.a and b show the 1 and 5 pass printed 1 cm^2 obtained when printing with ink 7.2.4 onto a cleaned glass slide substrate at 60°C. The top edges of both prints are well-defined, consisting of clear tracks that resemble the individual track shown in Figure 7.2.2.1. In the single pass print the left edge appears to suffer from the first droplet issue, whereby the first printed droplet of a new printed line is more difficult to form. This difficulty in formation is commonly caused by evaporation of solvent at the tip of the dispensing device and potentially causing a partial blockage that must be overcome. The rest of the print is continuous with an apparent homogeneous distribution of material. Individual printed track boundaries are prevalent throughout the print. Figure 7.2.2.2.b shows that the left edge of the 5 pass exhibits an unusual step approximately 1 mm away from the top, likely caused by a transient blockage causing the jetting to be offset. Somewhere along the last printed track of the step the dispensing device has unblocked, causing the top 1 mm of the left edge to be correctly positioned. Material deposition is not homogeneous, as shown by the darker and brighter sections of the print, but the print is continuous.

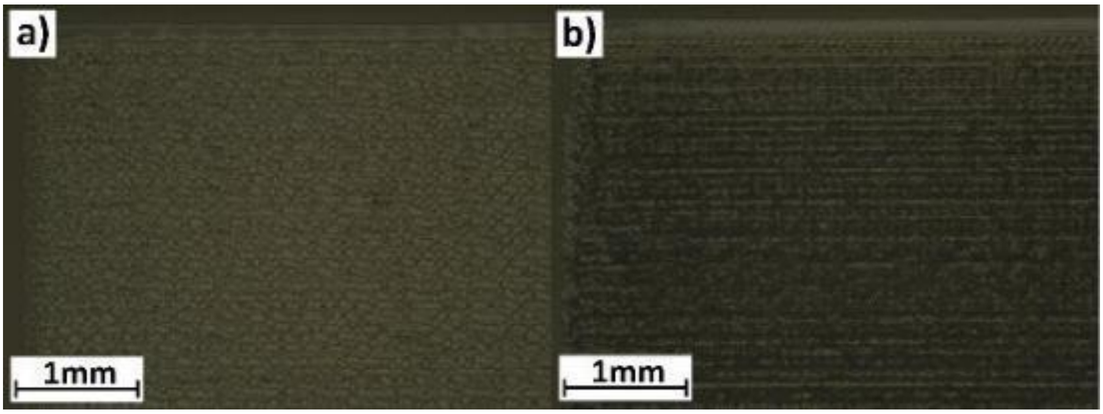

Figure 7.2.2.2 Printed 1 cm^2 using ink 7.2.4 at optimised print conditions on a glass substrate at 60°C stage temperature. Image a) is 1 pass and b) is 5 passes.

7.2.3 Niobium Doped Ink Ageing Studies

An ageing study was performed for inks 7.2.3 and 7.2.4. Ink 7.2.3 showed good stability over the 28 day maturation period (See Figure 7.2.3.1). The viscosity of the ink increases slightly as it ages, with a 0.86 % increase between the 1.975 mPa s measured at t = 0 and the 1.992 mPa s measured at t = 28 days. This negligible increase suggests that the ink is stable and the $Ti(OEt)_4$ and $Nb(OEt)_5$ had been stabilised with respect to hydrolysis during the storage process. Ink 7.2.4 displayed a larger increase in viscosity during the ageing study (See Figure 7.2.3.2). A total increase of 3.71 % was observed over the 28 days. The large increase between the t = 0 and t = 1 day measurements suggest the alkoxide ink components were not stabilised to hydrolysis. This large increase was not observed for ink 4.3.2, a similar ink without the $Nb(OEt)_5$, indicating that the $Nb(OEt)_5$ component is reacting with H_2O.

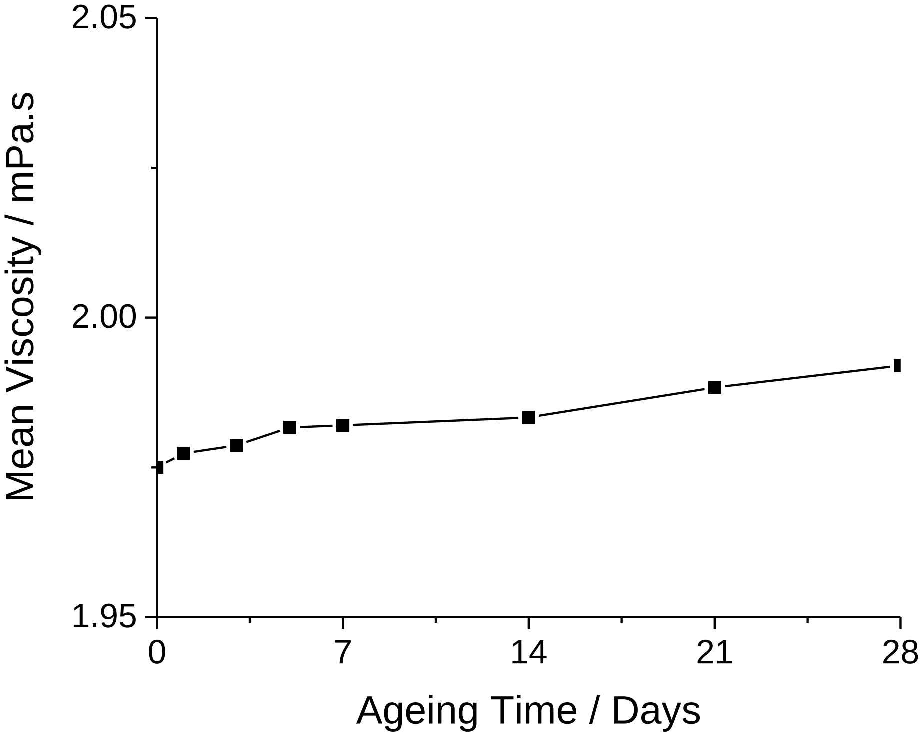

Figure 7.2.3.1 Ageing data for ink 7.2.3 over a 28 day maturation time

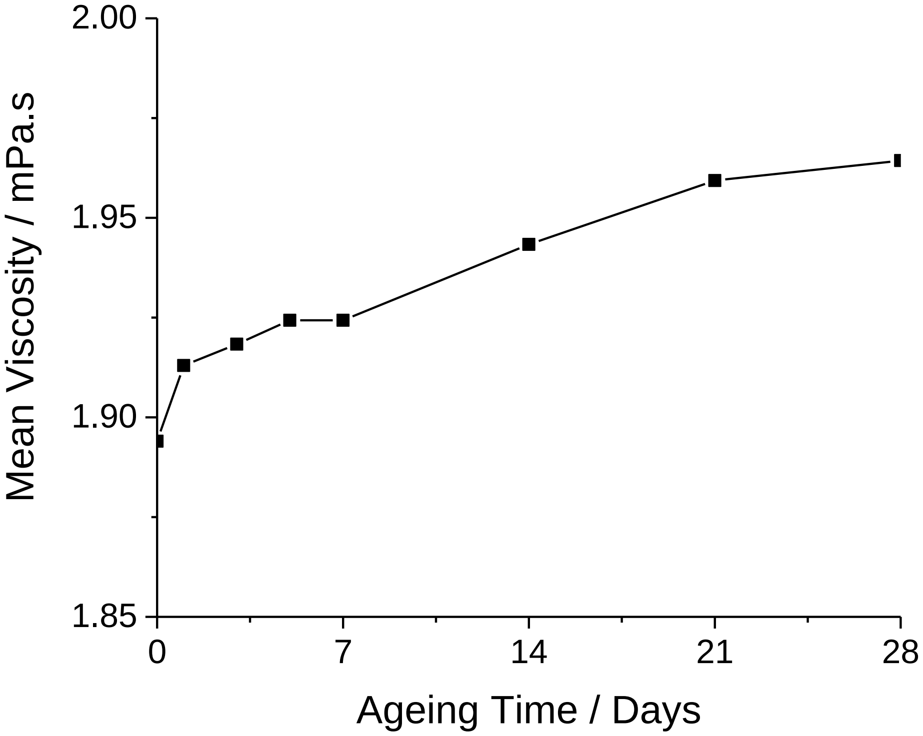

Figure 7.2.3.2 Ageing data for ink 7.2.4 over a 28 day maturation time

7.2.4 Discussion of Niobium Doped prints

After determining the as-supplied EpiValence solution was too reactive to pass through the printer, inks were formulated to facilitate inkjet printing of the EpiValence solution. Dilution of the solution with ^{i}PPE yielded ink 7.2.1. A substrate temperature of 30°C was identified as insufficient for satisfactory evaporation of ^{i}PPE during the printing process, so the substrate temperature was increased to 60°C. Figures 7.2.1.1 and 7.2.1.3 show the marked improvement in the quality of the printed films when using the same ink with an elevated substrate temperature. However, the printed samples shown in Figure 7.2.1.3 are still far from adequate, displaying a discontinuous film with unusual patterns indicative of fluidic flows. It was proposed that many of the issues encountered with printing ink 7.2.1 were due to the relatively high boiling point of ^{i}PPE.

To reduce the effect of the ^{i}PPE, ink 7.2.2 was formulated. This ink facilitates the printing of the EpiValence solution by adding DME and ^{i}PrOH. Still printing with a substrate temperature of 60°C, Figure 7.2.1.5 shows that the printed samples obtained when using ink 7.2.2 are significantly different to those obtained with ink 7.2.1. The issue of material flow appears to be reduced by changing the chemicals used for dilution. Film discontinuity is also observed when using ink 7.2.2, although it now manifests as discretely formed regions of deposit consisting of one droplet or a small group of merged droplets. Figure 7.2.1.6 shows the poor adhesion of a drop-tested sample of ink 7.2.2 to the heated glass substrate, likely caused by the presence of ^{i}PPE.

Final optimisation of the EpiValence ink formulation was performed by altering the composition of ink 7.2.2 to replicate the same concentrations of titanium and DME as ink 4.3.2. Figure 7.2.1.8 shows the prints obtained with the optimised ink 7.2.3. The printed films are continuous and do not exhibit material flow, indicating that the issues associated with the presence of ^{i}PPE have been alleviated. Both printed samples appear homogeneous in their distribution of material, aside from the very edges in the 5 pass sample.

Ink 7.2.4 was formulated to demonstrate how ink 7.2.3 would behave without the presence of ^{i}PPE from the original EpiValence solution. Figure 7.2.2.2.a shows that for the single pass print, the tracks within the print are more distinguishable than those obtained with ink 7.2.3 in Figure 7.2.1.7.a, likely leading to a decreased homogeneous thickness of the film. This difference is also clearly seen in the 5 pass samples, with Figure 7.2.1.7.b showing the print using ink 7.2.3 to be more homogeneous in material distribution than ink 7.2.4 as shown in

Figure 7.2.2.2.b. Ageing studies indicated that ink 7.2.3 was more stable than ink 7.2.4, likely caused by the additional ^{i}PPE stabiliser inhibiting the hydrolysis of the reactive $Nb(OEt)_5$.

7.2.5 Annealing, XRD, and Raman investigation

Unfortunately, as the XRD and Raman analytical instruments used for phase analysis did not have the sensitivity required for analysis of the printed films, drop-tested samples were required for XRD and Raman phase analysis. As shown in 7.2.1.6, the drop-tested samples of niobium doped inks exhibited extreme issues with substrate adhesion. Consequently, no meaningful annealing data could be obtained for ink 7.2.3. It was decided that an annealing temperature of 450°C for a duration of 40 minutes would still be used for inkjet printed samples of ink 7.2.3 to allow a fair comparison with ink 4.3.2. Figure A.7.2.5.1 shows the Raman spectra obtained with drop-tested ink 7.3.4, before and after annealing at 450°C for 40 minutes. The signal to noise ratio is relatively low, with a broad peak starting above a wavenumber of 1000 cm^{-1} due to the glass substrate. Some peaks associated with anatase and Nb_2O_5 can be identified. However, as drop-tested samples of ink 7.2.4 also displayed poor substrate adhesion, the Raman spectra showed extreme variation when analysing different parts of the deposit. As such, no conclusions can be drawn from the annealing and Raman study of ink 7.2.4.

7.2.6 Profilometry, Optical Transmittance, and Wettability

Using the average droplet diameter of 88.50 µm obtained for the imaged droplets of ink 7.2.3, the theoretical film thickness was calculated to be 121.97 nm per printed pass of a 100 x 100 square array. A moving range of 5.27 nm was calculated for the imaged droplets of ink 7.2.3. Using this moving range, a percentage spread of theoretical film thickness was calculated as 35.77 %. This spread is quite large, due to the relatively large moving range and droplet diameters involved. Multiplying the average theoretical film thickness of 121.97 nm for a single printed pass by 5 yields a theoretical film thickness of 609.86 nm for a 5 pass 1 cm^2 sample.

Film thickness measurements were obtained experimentally for 5 pass printed samples of ink 7.2.3 using a profilometer. A total of four profiles were taken, shown in Figures 7.2.6.1, A.7.2.6.1, 7.2.6.2, and A.7.2.6.2. The mean thickness was determined to be 603.50 nm, which is 98.96 % of the theoretically calculated value. However, there are large differences between the left and right profiles taken perpendicular to the direction of the printed tracks, and the top and bottom profiles taken parallel to the printed tracks. Figures 7.2.6.1 and A.7.2.6.1 show the left and right profiles with average heights of 741 and 766 nm, respectively. The sample profile occurs within a scan length of approximately 10000 µm, indicating that the print is the correct size. Both profiles suggest a continuous film has been printed as there is a small step up in the minimum height within the bounds of the print. There are several large peaks in each profile, indicating an inhomogeneous distribution of printed material.

Figures 7.2.6.2 and A.7.2.6.2 show the experimentally obtained profiles taken parallel to the direction of the printed tracks. As with the left and right profiles, both the top and bottom profiles occur within a scan length of approximately 10000 µm, reinforcing that the printed sample is the correct size. The average heights for the top and bottom profiles are 479 and 428 nm, respectively; lower than the average heights obtained for the profiles taken perpendicular to the printed tracks. The top profile shown in Figure 7.2.6.2 does not exhibit the same small step up in height that the left and right profiles do, suggesting that the material is not as continuous as initially proposed or is much thinner along the printed direction. However, the bottom profile in Figure A.7.2.6.2 does exhibit a very small step up in height. There are other differences between the top and bottom profiles too; most notably the top profile only has one large peak over 6000 nm in height, whereas the bottom profile has several large peaks. The different appearance of the two profiles indicates that the printed film varies significantly from top to bottom, although it is also suspected that there would be significant variation found with small changes in the scanning location of the stylus relative to the sample. This variation with stylus placement is especially true when taking the top and bottom profiles, due to the measurements being taken in parallel with the printed tracks.

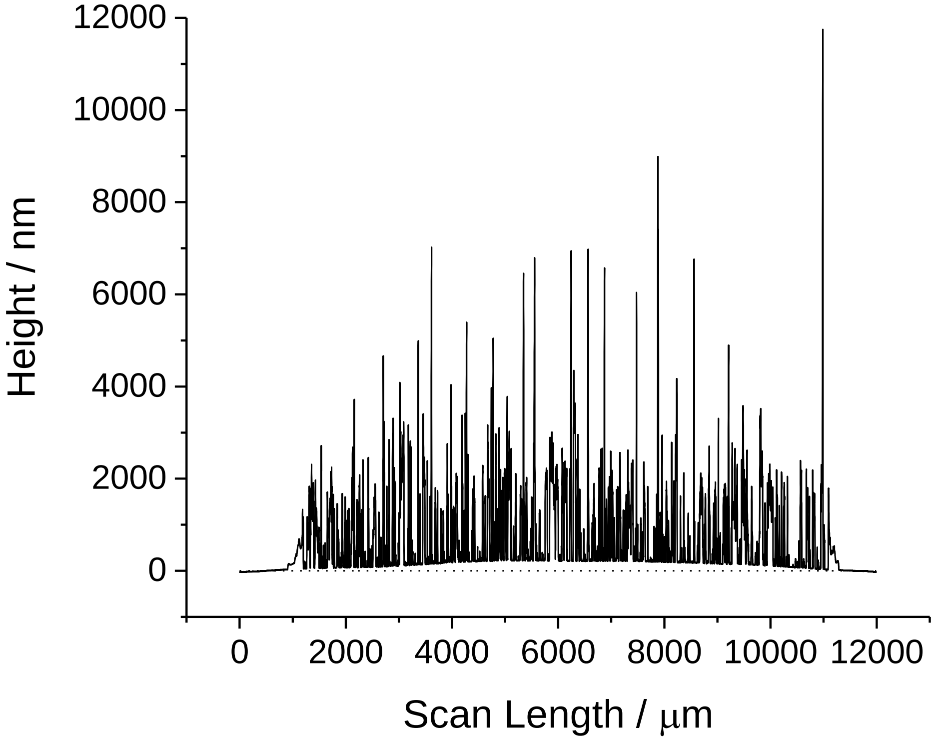

Figure 7.2.6.1 Left profile of 5 pass 1 cm² print using ink 7.2.3 on a glass substrate without annealing (average height of 741 nm)

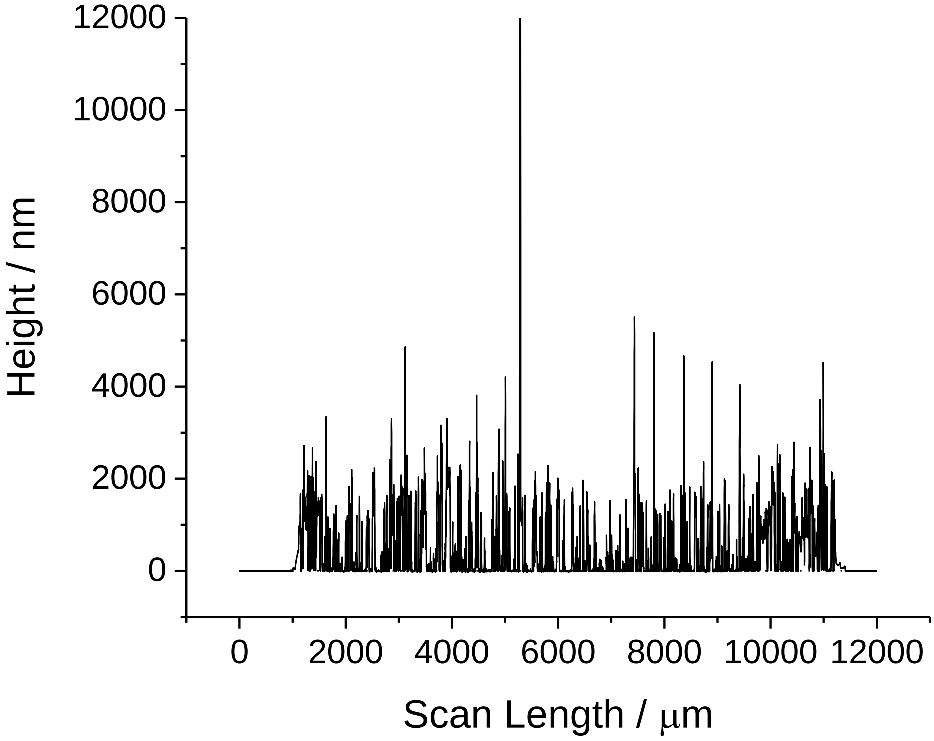

Figure 7.2.6.2 Top profile of 5 pass 1 cm² print using ink 7.2.3 on a glass substrate without annealing (average height of 479 nm)

In an attempt to ascertain the effects of annealing on the profiles of the printed samples, profilometry was performed on a printed 5 pass 1 cm^2 sample using ink 7.2.3 after annealing the sample to 450°C for 40 minutes. Figures 7.2.6.3, A.7.2.6.3, 7.2.6.4, and A.7.2.6.4 show the resulting left, right, top, and bottom measured height profiles. Unfortunately, all of the profiles exhibit a curved baseline that renders the absolute numerical height data unusable. The relative heights will still be briefly discussed. Unlike the curved baselines obtained in Figures 4.4.2.2 and A.4.4.2.2, these profiles exhibit an upwards curvature.

Aside from the top profile in Figure 7.2.6.3, the profiles appear to have a reduced number of large peaks relative to the profiles of the sample that was not annealed. This reduced number of large peaks, in addition to the relatively clustered nature of the smaller peaks, suggests that the annealed sample thickness is of increased uniformity. Without numerical average heights that are accurate, it cannot be deduced whether this increased sample uniformity is due to densification of the film. The profiles indicate that the sample is the correct size, as indicated by the sample peaks being within a scan length of approximately 10000 µm.

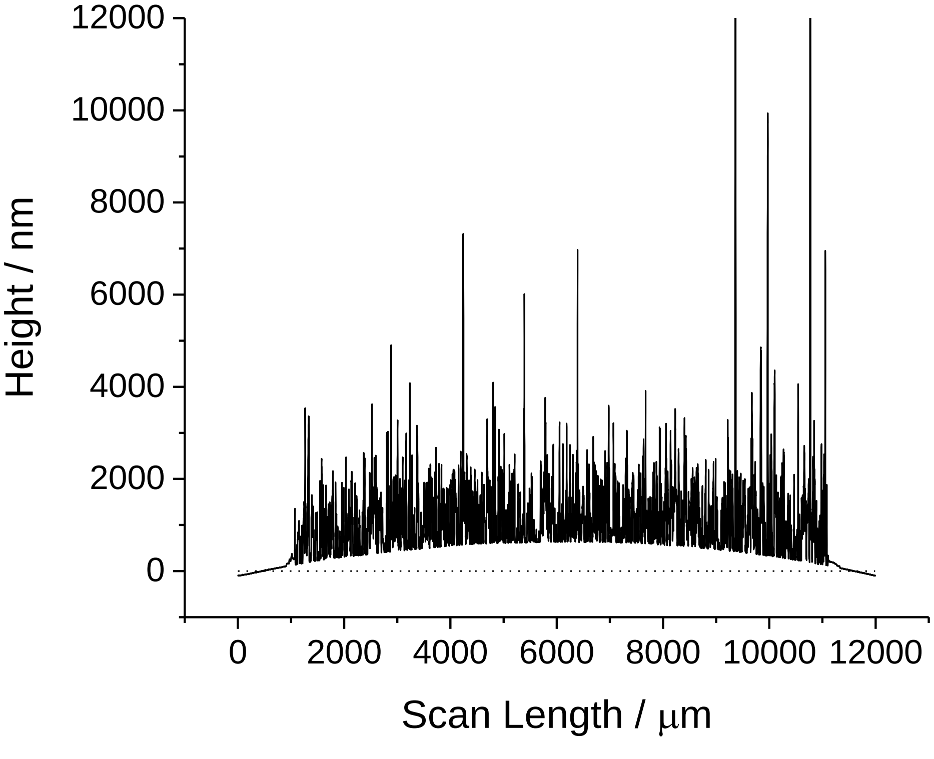

Figure 7.2.6.3 Top profile of 5 pass 1 cm^2 print using ink 7.2.3 on a glass substrate after annealing at 450°C for 40 minutes (average height of 1153 nm)

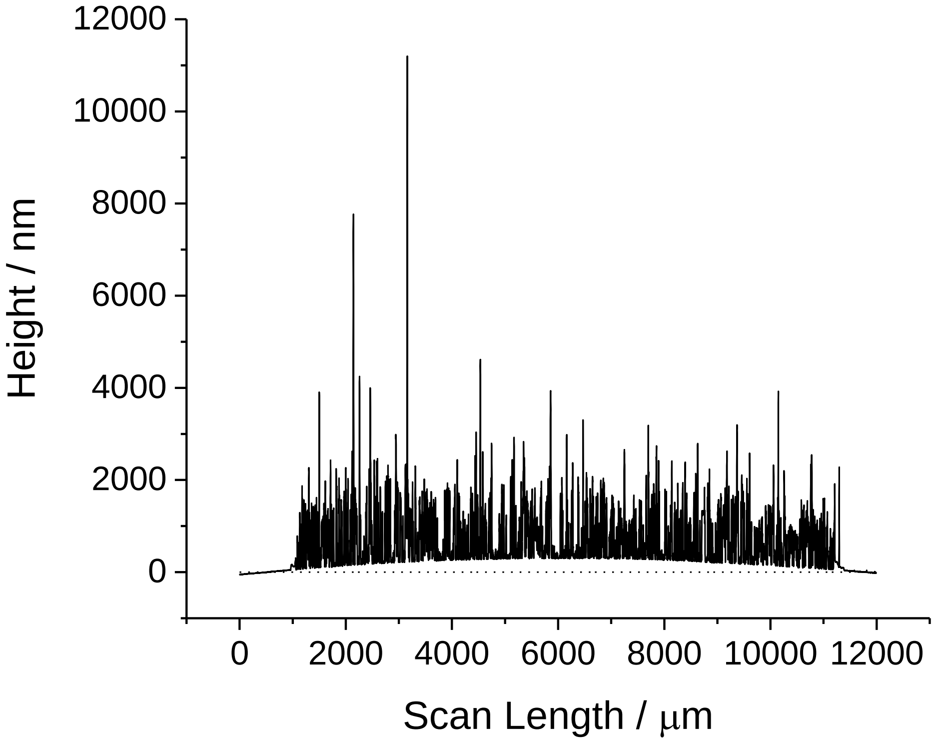

Figure 7.2.6.4 Top profile of 5 pass 1 cm^2 print using ink 7.2.3 on a glass substrate after annealing at 450°C for 40 minutes (average height of 722 nm)

Profilometry was also performed for printed samples using ink 7.2.4. Figures 7.2.6.5, A.7.2.6.5, 7.2.6.6, and A.7.2.6.6 show the profiles obtained for the printed 5 pass 1 cm^2 sample using ink 7.2.4. It is immediately apparent that, as proposed in section 7.2.3, the printed films when using ink 7.2.4 result in a less homogeneous material distribution than those obtained with ink 7.2.3. The height profile fluctuates wildly, giving an overall 'spikier' appearance, which corresponds well with the imaged sample in Figure 7.2.2.2.b. The left and right profiles both indicate that the sample size exceeds the expected scan length of 10000 μm, which also corresponds well with the left edge of the imaged sample. The top and bottom profiles indicate that the sample size is close to the expected 1 cm, with the sample peaks confined to a scan length of approximately 10000 μm. The average sample height was determined to be 757.75 nm.

Theoretical film thickness was calculated for ink 7.2.4 in the same way as ink 7.2.3. Per printed pass, a thickness of 145.36 nm was calculated. Multiplying the average theoretical film thickness of 145.36 nm for a single printed pass by 5 yields a theoretical film thickness of 726.81 nm for a 5 pass 1 cm^2 sample. This is very close to the average sample height of 757.75 nm as determined by profilometry.

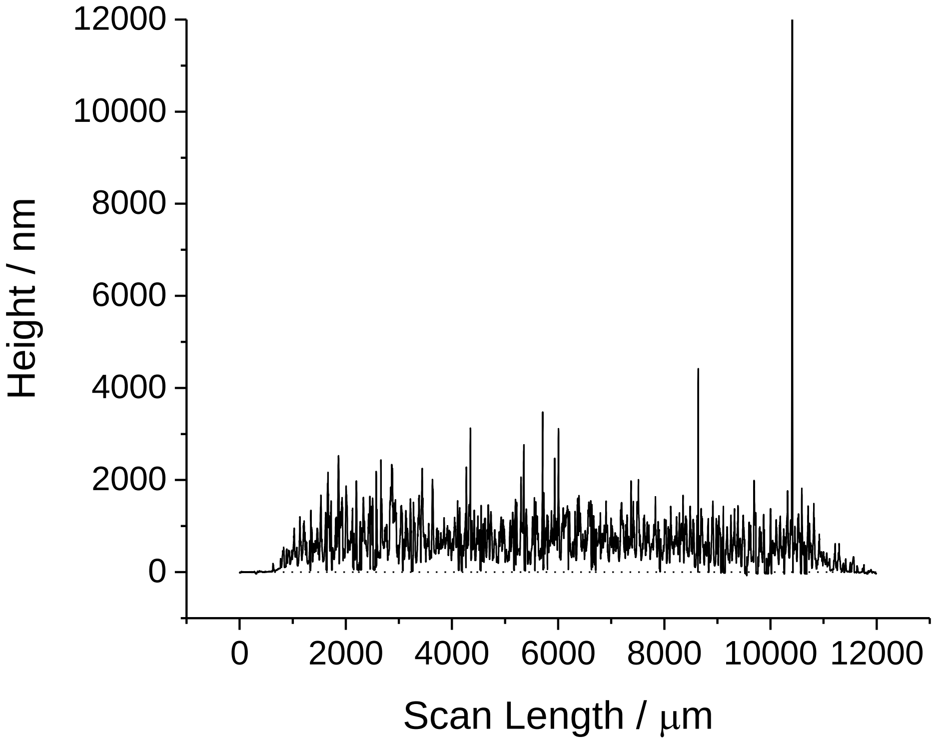

Figure 7.2.6.5 Left profile of 5 pass 1 cm^2 print using ink 7.2.4 on a glass substrate without annealing (average height of 663 nm)

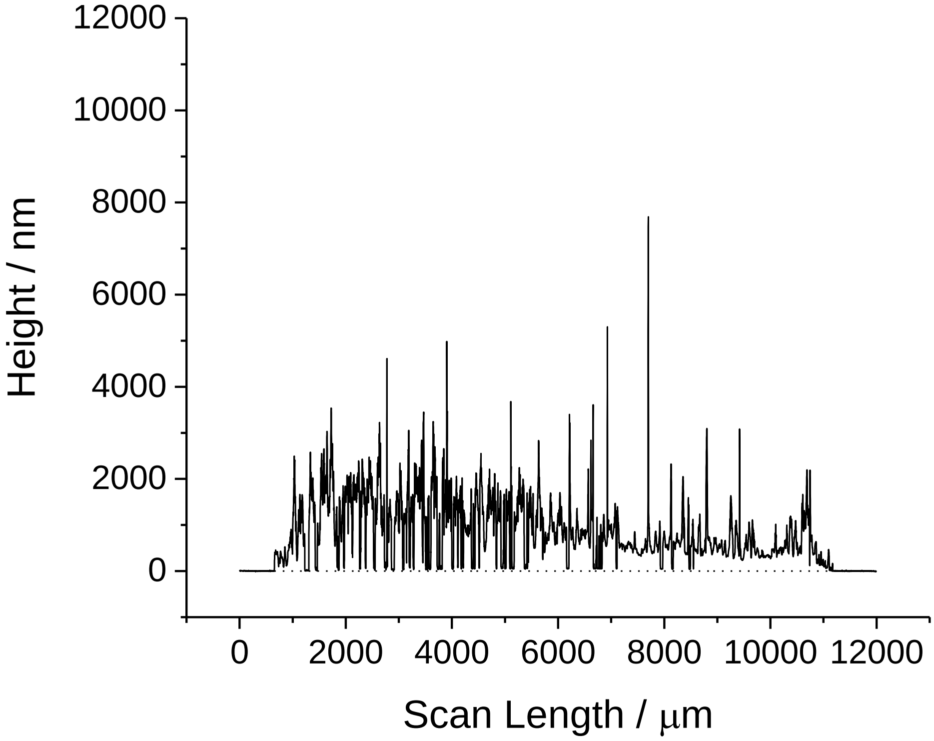

Figure 7.2.6.6 Top profile of 5 pass 1 cm^2 print using ink 7.2.4 on a glass substrate without annealing (average height of 885 nm)

Figures 7.2.6.7, A.7.2.6.7, 7.2.6.8, and A.7.2.6.8 show the profiles obtained for a printed 5 pass 1 cm^2 sample using ink 7.2.4 after the sample had been annealed at 450°C for 40 minutes. The profiles exhibit a curved baseline, similar to those obtained in Figures 4.4.2.2 and A.4.4.2.2, and so will not be discussed in any quantitative fashion. The profiles resemble those obtained for ink 7.2.3 more closely than they resemble the profiles obtained for the sample using ink 7.2.4 without annealing; they are less 'spiky' than the previously discussed ink 7.2.4 profiles, indicating a more even film thickness and therefore distribution. The annealing process may have caused this difference, or it may be due to an inherent variation between the two printed samples. All of the profiles show a good agreement with the intended sample size of 1 cm^2 as shown by the sample peaks appearing within a range of a roughly 10000 μm scan length.

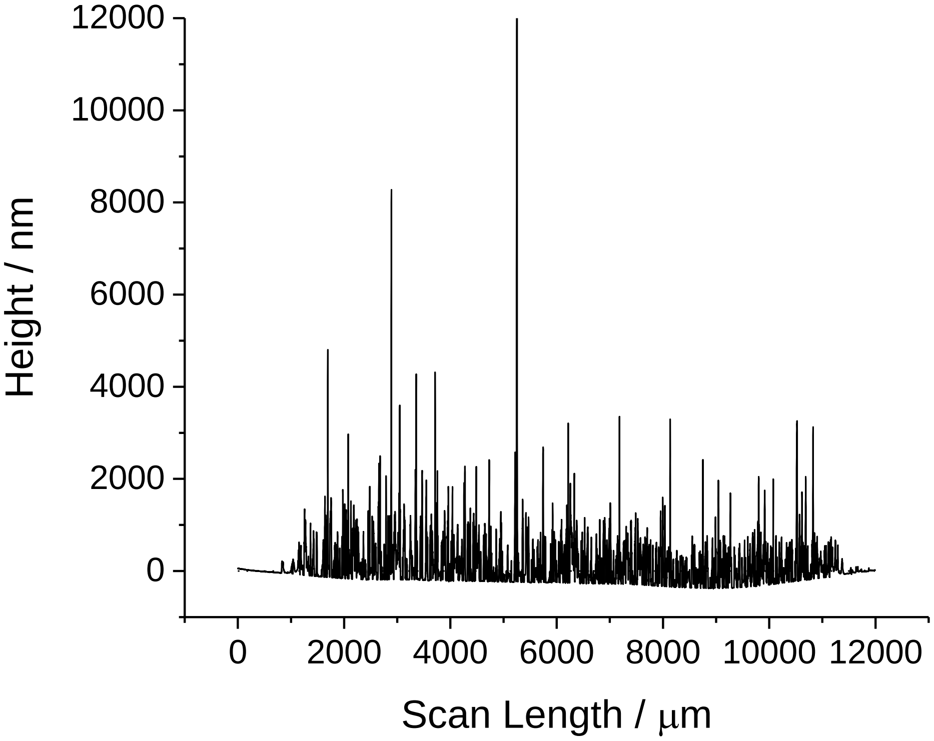

Figure 7.2.6.7 Left profile of 5 pass 1 cm^2 print using ink 7.2.4 on a glass substrate after annealing at 450°C for 40 minutes (average height of 180 nm)

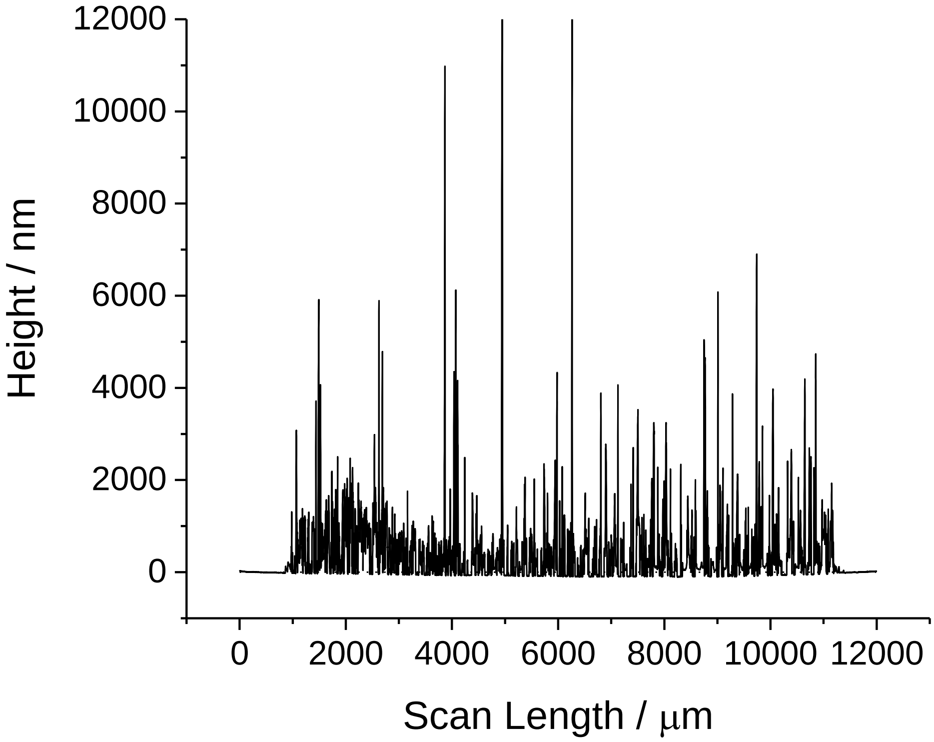

Figure 7.2.6.8 Top profile of 5 pass 1 cm² print using ink 7.2.4 on a glass substrate after annealing at 450°C for 40 minutes (average height of 474 nm)

As a potential TCO material, the optical transparency of the niobium-doped TiO_2 films was of particular interest. Figure 7.2.6.9 shows the transmittance spectrum obtained for two printed samples of ink 7.2.3, one had been heat treated and the other had not. It was expected that the transmittance would be higher than the un-doped printed samples. However, it was found that the transmittance was lower by 10 – 15 % than the ink 4.3.2 samples analysed in Chapter 4. This unexpected decrease in transmittance could be caused by an increased absorbance or reflectance by the sample, as the three optical properties of absorbance, reflectance, and transmittance are closely interlinked. Red-shift in the sudden drop in transmittance at ~350 nm was also expected to occur, as reported in the literature.

It is apparent that annealing the sample has a large effect on the behaviour of the sample. Without annealing, the transmittance of the sample varies between 32 and 40 % for wavelengths of 350 – 900 nm. Below 350 nm, there is a marked decrease that is likely due to absorption of the UV as the energies correspond closely to the band gap of TiO_2. The sample that had been annealed to 450°C for 40 minutes exhibits a constant transmittance of 34 % between wavelengths of 350 nm and 900 nm, decreasing gradually to 28 % below 350 nm.

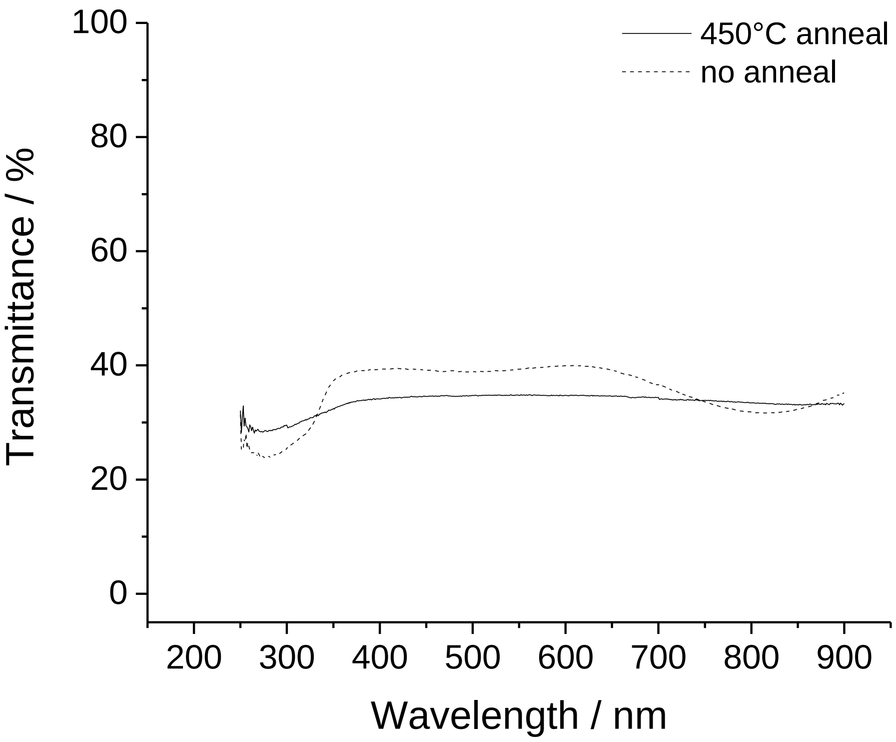

Figure 7.2.6.9 Optical transmittance of printed 5 pass 1 cm^2 using ink 7.2.3 on a glass substrate with and without annealing

Figure 7.2.6.10 shows the optical transmittance data obtained for printed samples of ink 7.2.4. The samples with and without annealing exhibit a similar transmittance of ~40 % within the visible wavelengths of 380 nm to 740 nm. Above 740 nm, the transmittance of the sample without annealing increases up to a maximum of 45 % whereas the transmittance of the annealed sample decreases to 38 % at 900 nm. Similar to the other samples, a decrease in transmittance was observed at and below 350 nm due to absorbance. This decrease in transmittance is much larger in the sample without annealing, decreasing rapidly down to a transmittance of just 4 %. The annealed sample exhibits a decrease from 34 % at 350 nm to 26 % at 301 nm, jumping up to 30 % at 300 nm due to the changing emission source.

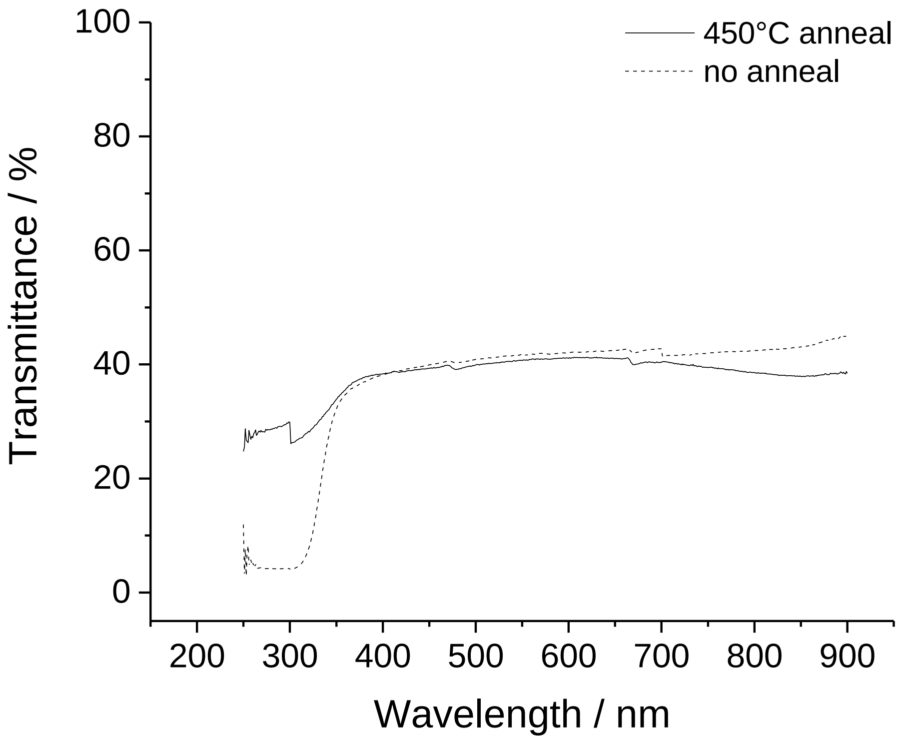

Figure 7.2.6.10 Optical transmittance of printed 5 pass 1 cm^2 using ink 7.2.4 on a glass substrate with and without annealing

Wettability of the printed films was investigated by measuring the contact angle of distilled H_2O immediately after deposition onto the printed samples. Figure 7.2.6.11 shows the mean contact angle of H_2O on inkjet printed 5 pass 1 cm^2 samples of ink 7.2.3. The contact angle of 90° is comparable to the contact angles obtained for ink 4.3.2. After annealing under the same conditions as the ink 4.3.2 samples, the mean contact angle of H_2O on the printed ink 7.3.2 sample decreases significantly to a contact angle of ca. 23°, lower than the 35° contact angle observed for the ink 4.3.2 sample. However, a large spread of data was collected for the contact angle of H_2O on the printed ink 7.2.3 samples. The minimum measurement was 14° and the maximum measurement was 39°, as shown in the insets of Figure 7.2.6.11. Several measurements were taken, with multiple contact angles observed near each extreme. It was deduced that the contact angle of H_2O on the printed samples of ink 7.2.3 after being annealed was very sensitive to the placement of the droplet onto the surface.

Figure 7.2.6.12 shows the wettability data for printed samples of ink 7.2.4. These samples display comparable measurements to those obtained with ink 4.3.2 both with and without annealing. This is unsurprising as the loading of niobium is small relative to that of titanium. The rest of the ink 7.2.4 formulation is also comparable to that of ink 4.3.2, unlike that of ink 7.2.3 which contains a $Ti(OEt)_4$ titanium precursor, rather than TTIP, and the presence of ^{i}PPE.

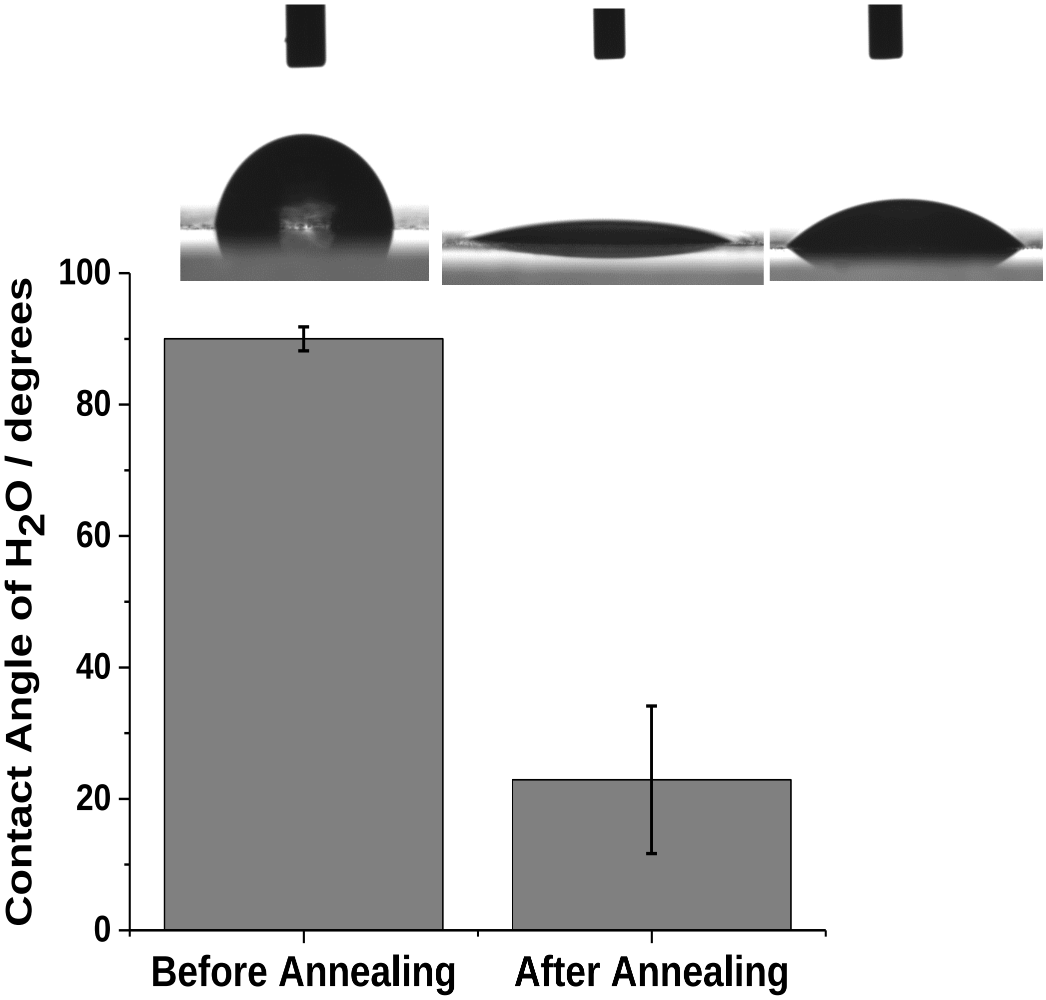

Figure 7.2.6.11 Contact angles of distilled H_2O on 5 pass 1 cm^2 prints using ink 7.2.3 on a glass substrate with and without annealing at 450°C for 40 minutes. Error bars show standard contact angle deviation. Inset images show one the imaged sessile H_2O droplets

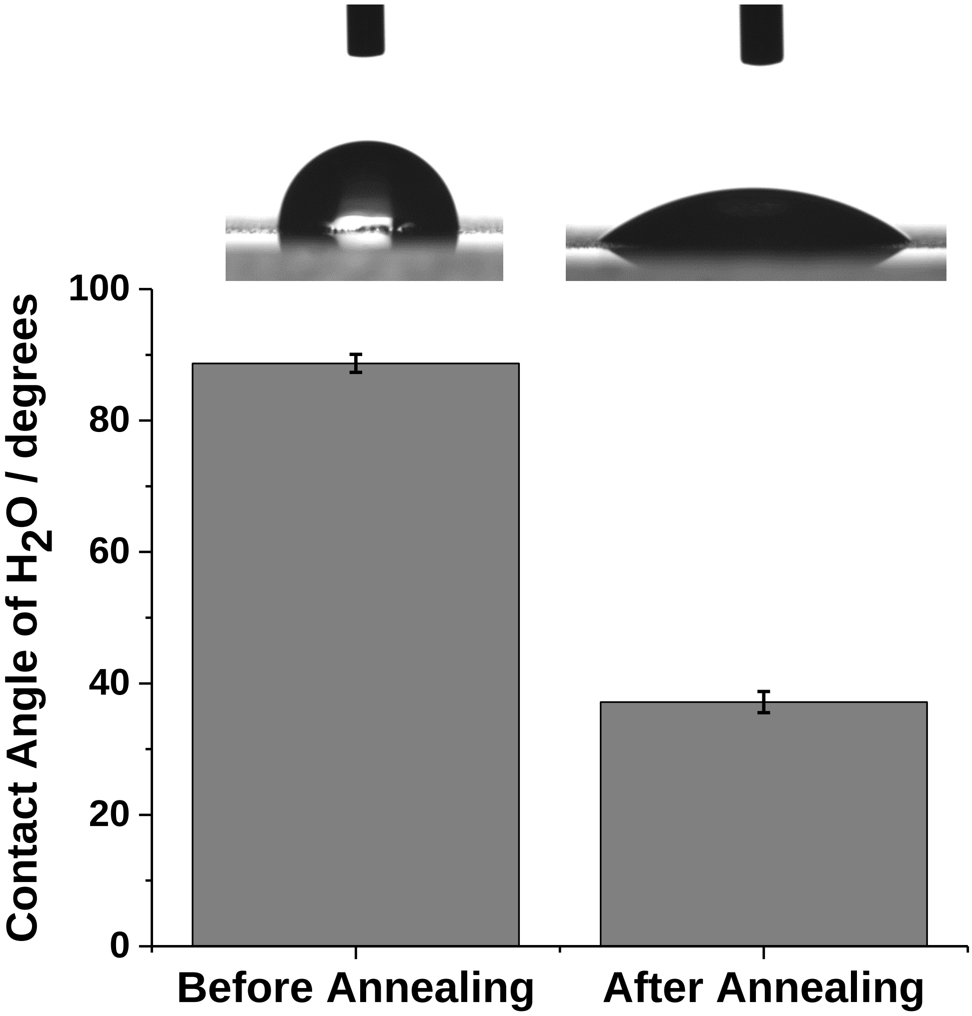

Figure 7.2.6.12 Contact angles of distilled H_2O on 5 pass 1 cm^2 prints using ink 7.2.4 on a glass substrate with and without annealing at 450°C for 40 minutes. Error bars show standard contact angle deviation. Inset images show one of the imaged sessile H_2O droplets

7.2.7 SEM

Surface topology of the inkjet printed 5 pass 1 cm^2 samples using inks 7.2.3 and 7.2.4 was investigated used SEM. Figure 7.2.7.1 shows SEM images of the sample using ink 7.2.3. At extremely low magnification it is clear that a continuous film has not been formed. Instead, a cracked film that consists of small plates of material is observed, with larger plates occurring at the boundaries of the printed tracks (See Figure 7.2.7.1.a). At higher magnifications, the size and shape discrepancy of the plates is shown. Furthermore, outlines of either solvent evaporation or discarded material can be seen between the adhered plates of material. This suggests that the adhesion issues displayed by the ink may be caused by trapped solvent evaporating and breaking through the film. At the highest magnification the surface of the plates appears smooth, whilst the edges are jagged and irregular (See Figure 7.2.7.1.d). The jagged edges may indicate mechanical stress or strain resulted in breakage of the deposited material.

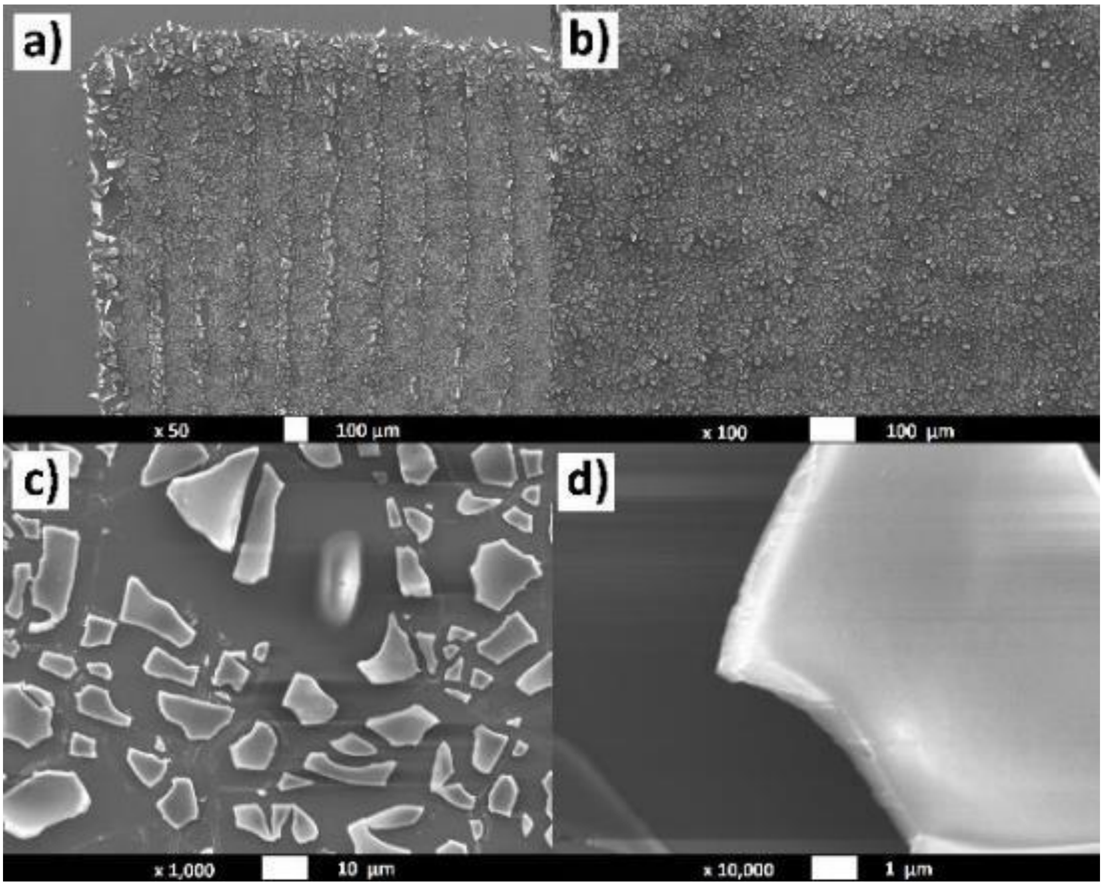

Figure 7.2.7.1 SEM of inkjet printed 5 pass ink 7.2.3 on a glass substrate without thermal treatment

Figure 7.2.7.2 shows the SEM images obtained of the inkjet printed 5 pass 1 cm^2 sample using ink 7.2.4. This sample also consists of plates of material rather than a continuous film. The plates are typically larger than those observed for the ink 7.2.3 sample shown in Figure 7.2.7.1. The images at 100 x zoom suggest a less dense deposit when using ink 7.2.4, due to the larger area of uncovered substrate. The outlines of previously adhered material are also observed on the substrate for the sample of ink 7.2.4 in Figure 7.2.7.2. Higher magnification shows the plates of material to also exhibit a smooth surface. The edge of the plate in Figure 7.2.7.2.c and d appears cleaner and more well-defined than the edge of the plate in Figure 7.2.7.1.d. There is also the presence of a small particle with a diameter ca. 2 µm that can be seen on the bottom left corner of Figure 7.2.7.2.c.

EDXS showed a presence of 48.91 % Ti and 7.40 % Nb by weight for the annealed sample of ink 7.2.3, with 19.94 % Ti and 2.49 % Nb by weight for the annealed sample of ink 7.2.4, confirming the presence of Nb within the films (See Table A.7.2.7.1). This gives a ratio of 0.15

Nb:Ti for ink 7.2.3 and 0.12 Nb:Ti for ink 7.2.4. The difference in ratio is likely due to human error within the ink formulation process. The discontinuous nature of the printed samples indicates the lack of a potential pathway required for a current to flow through the deposited material. In addition to the absence of a measurable thin film sheet resistance and poor optical transmittance, this shows that the printed samples using ink 7.2.3 and 7.2.4 are not suitable for use as potential TCOs. An alternative strategy is likely required for achieving inkjet printed thin films of niobium doped TiO_2 that have potential applications as TCO or electronics materials. One such strategy could be the incorporation of a niobium dopant into anatase nanoparticles and subsequent formulation into a nanoparticle or hybrid alkoxide / nanoparticle ink.

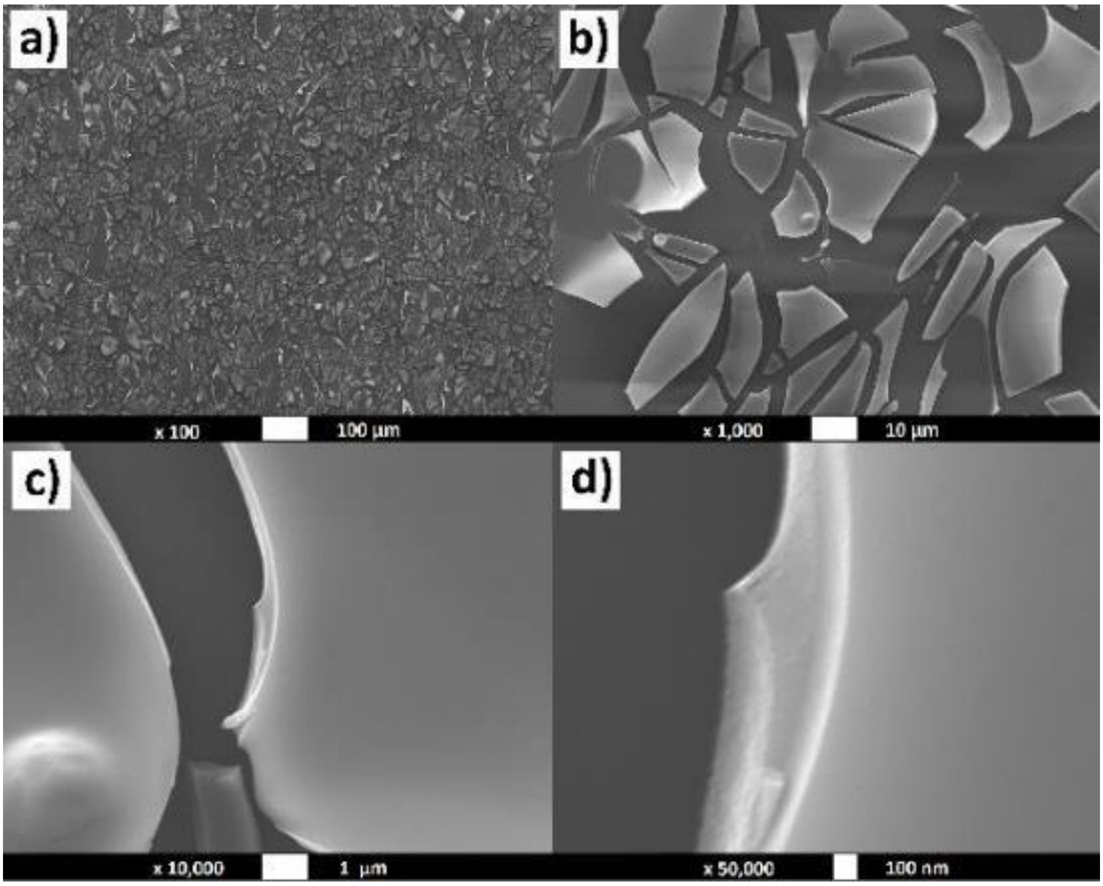

Figure 7.2.7.2 SEM of inkjet printed 5 pass ink 7.2.4 on a glass substrate without thermal treatment

7.3 Niobium Doped Inks Discussion & Conclusion

Introduction of a niobium alkoxide dopant to titanium alkoxide ink solutions was investigated, with the aim of inkjet printing niobium doped TiO_2 transparent and conductive thin films for potential use in TCOs and electronics. Initial inks used the supplied EpiValence solution as a basis, with iterative ink formulations resulting in ink 7.2.3, consisting of the EpiValence solution with the addition of DME and ^iPrOH. It was found that use of just the ^iPPE carrier gave unsatisfactory prints, likely resulting from the high boiling point of ^iPPE.

Optical microscopy of the printed samples using ink 7.2.3 suggested that satisfactory prints were obtained after adding DME and ^iPrOH to the original EpiValence solution. An additional ink was also formulated, using ink 4.3.2 as a basis and adding an equivalent loading of $Nb(OEt)_5$ to form ink 7.2.4. Ink 7.2.4 also yielded satisfactory prints by optical microscopy. Ink 7.2.3 was shown to be more stable than ink 7.2.4 over a 28 day maturation period, likely due to the presence of the additional ^iPPE stabilising agent. Unfortunately, phase analysis could not be performed due to the small sample thickness of the printed samples and poor adhesion of the drop-tested inks to the glass substrates.

Profilometry measurements did not provide useful data as to the thickness of the films, caused primarily by uneven baselines and soft, badly adhered samples. The profilometry again exhibited large and sudden increases to sample height, resulting in an overall spiky appearance of the profiles. SEM analysis showed the prints of both ink 7.2.3 and 7.2.4 to consist of irregularly shaped and sized plates of material, which could explain the spiky appearance of the profilometry data. This spiky profile phenomenon was exhibited by all other samples analysed throughout this thesis, suggesting that it is likely caused by the instrument.

Optical transmittance revealed the niobium doped films displayed a lower transmittance than un-doped samples, clearly indicating the unsuitable application of these inks as potential TCOs. Furthermore, due to the SEM analysis indicating the lack of a continuous pathway for a current to flow and sheet resistance measurements displaying an error result, the possibility for an appreciable conductivity in the deposited materials is also unlikely. Overall, the incorporation of niobium into the TiO_2 films was achieved through the addition of a niobium alkoxide to the ink formulations. The properties of the films that resulted from these inks were unsuitable for use in TCO or electronics applications, having a poor optical transmittance and displaying no appreciable electrical conductivity. Further work would be needed to explore other avenues for obtaining conductive niobium doped TiO_2 printed films.

7.4 References

1. N. Straue, M. Rauscher, M. Dressler and A. Roosen, *Journal of the American Ceramic Society*, 2012, **95**, 684-689.
2. J. Du, X.-l. Chen, C.-c. Liu, J. Ni, G.-f. Hou, Y. Zhao and X.-d. Zhang, *Applied Physics A*, 2014, **117**, 815-822.
3. H. Kim, C. M. Gilmore, A. Piqué, J. S. Horwitz, H. Mattoussi, H. Murata, Z. H. Kafafi and D. B. Chrisey, *Journal of Applied Physics*, 1999, **86**, 6451-6461.
4. E. Fortunato, D. Ginley, H. Hosono and D. C. Paine, *MRS Bulletin*, 2007, **32**, 242-247.
5. N. Rahimi, R. A. Pax and E. M. Gray, *Progress in Solid State Chemistry*, 2016, **44**, 86-105.
6. M. A. de Araújo, M. F. Gromboni, F. Marken, S. C. Parker, L. M. Peter, J. Turner, H. C. Aspinall, K. Black and L. H. Mascaro, *Applied Catalysis B: Environmental*, 2018, **237**, 339-352.
7. C. Sudakar, P. Kharel, R. Suryanarayanan, J. S. Thakur, V. M. Naik, R. Naik and G. Lawes, *JOURNAL OF MAGNETISM AND MAGNETIC MATERIALS*, 2008, **320**, L31-L36.
8. A. Cirera, J. Arbiol, g. dezanneau, J. R. Morante, J. R. Morante, F. Peiro and C. Calveras, *Journal of applied physics*, 2002, **92**, 853-861.
9. A. M. Ruiz, G. Dezanneau, J. Arbiol, A. Cornet and J. R. Morante, *Chemistry of Materials*, 2004, **16**, 862-871.
10. Y. Furubayashi, T. Hitosugi, Y. Yamamoto, K. Inaba, G. Kinoda, Y. Hirose, T. Shimada and T. Hasegawa, *Applied Physics Letters*, 2005, **86**, 1-3.
11. G. Q. Wang, W. Lan, G. J. Han, Y. Wang, Q. Su and X. Q. Liu, *Journal of Alloys and Compounds*, 2011, **509**, 4150-4153.
12. J. Yue, C. Suchomski, P. Voepel, R. Ellinghaus, M. Rohnke, T. Leichtweiss, M. T. Elm and B. M. Smarsly, *Journal of Materials Chemistry A*, 2017, **5**, 1978-1988.
13. M. C. Wu, T. H. Lin, J. S. Chih, K. C. Hsiao and P. Y. Wu, *Japanese Journal of Applied Physics*, 2017, **56**, 04CP07.
14. A. J. Gardecka, PhD Thesis, University College London (University of London), 2016.
15. C.-T. Wang, H.-S. Lin and W.-P. Wang, *Materials Science in Semiconductor Processing*, 2019, **99**, 85-91.
16. Y. Liu, J. M. Szeifert, J. M. Feckl, B. Mandlmeier, D. Fattakhova-Rohlfing, T. Bein, J. Rathousky and O. Hayden, *ACS Nano*, 2010, **4**, 5373-5381.

17. B. Fleming and S. Rushworth, *Journal of Sol-Gel Science and Technology*, 2017, **82**, 308-314.

Chapter 8

Conclusions

In this thesis, the inkjet printing of TiO_2 has been demonstrated using a variety of different ink formulations and approaches. Each ink formulation was developed, analysed, and optimised with the intention of depositing a functional thin film of TiO_2. After deposition, the printed films were analysed to investigate their suitability towards any potential applications. The aims of this project were to: further develop and optimise a solution-based ink using a TTIP precursor, develop an ink formulation with a preference towards obtaining the anatase polymorph at low temperature, synthesise titanium oxo-clusters and formulate them into RMC inks, and explore the use of a niobium dopant with the intention of producing films with sufficient transparency and conductivity for use as TCOs.

The use of TTIP as a titanium precursor for a solution-based ink was achieved by using a DME stabilising agent and ^iPrOH carrier solvent. The ink was compatible with the inkjet technology and the ink formulation was optimised. The printed amorphous TiO_2 deposit was shown to begin converting to anatase at 450°C. This shows the first aim had been achieved, but further modification would be required to increase preference towards formation of anatase at low temperature.

Through the addition of anatase nanoparticles to the ink formulation, a hybrid alkoxide / nanoparticle ink was formulated. It was shown that anatase formation occurred at a reduced temperature of 200°C, satisfying the second project aim. The nanoparticles were shown to behave as a seed or template for crystallisation of the amorphous TTIP-sourced TiO_2. To the best of our knowledge, this is the first example of a hybrid alkoxide / nanoparticle ink for use in inkjet systems. The hybrid ink was also printed onto a PET flexible plastic substrate and shown to exhibit the same seeding effect.

Four titanium oxo-clusters were synthesised: $[Ti_{12}O_{16}(O^iPr)_{16}]$, $[Ti_{28}O_{40}(O^tBu)_{20}(OAc)_{12}]$, $[Ti_{16}O_{16}(OEt)_{32}]$, and $[Ti_{11}O_{13}(O^iPr)_{18}]$. The first three clusters were synthesised by reported methods, whereas the last cluster was synthesised using a novel in-house method. An RMC ink was formulated using the $[Ti_{11}O_{13}(O^iPr)_{18}]$ cluster and printed with, achieving the third project aim. A 450°C anneal resulted in a mixture of rutile and anatase peaks, as shown by

Raman spectroscopy. 450°C is a relatively low temperature for the formation of rutile TiO_2, indicating a potential use for this ink.

Two solution-based inks were formulated and optimised for printing niobium doped TiO_2 films. Both inks proved difficult to analyse, with no successful conductivity measurements and displaying poor optical transmittance. Although the films were unsuitable for use as TCOs, the printed samples indicated the incorporation of niobium into the film and demonstrated that a solution-based ink formulation could be used for printing doped TiO_2.

In conclusion, all of the aims of this project were met to varying degrees of success. This preliminary research could be expanded upon with future work. Development, analysis, and optimisation of the ink formulations presented within this thesis could be expanded upon to target other MO systems. Although TiO_2 was used as the demonstrator in this work, the strategies utilise chemistries shared by other metal systems, particularly those with a background in sol-gel chemistry. Of particular interest is the selective functionalisation of RMC inks, which could lead to many potential applications due to the high level of tuneability.

Appendix

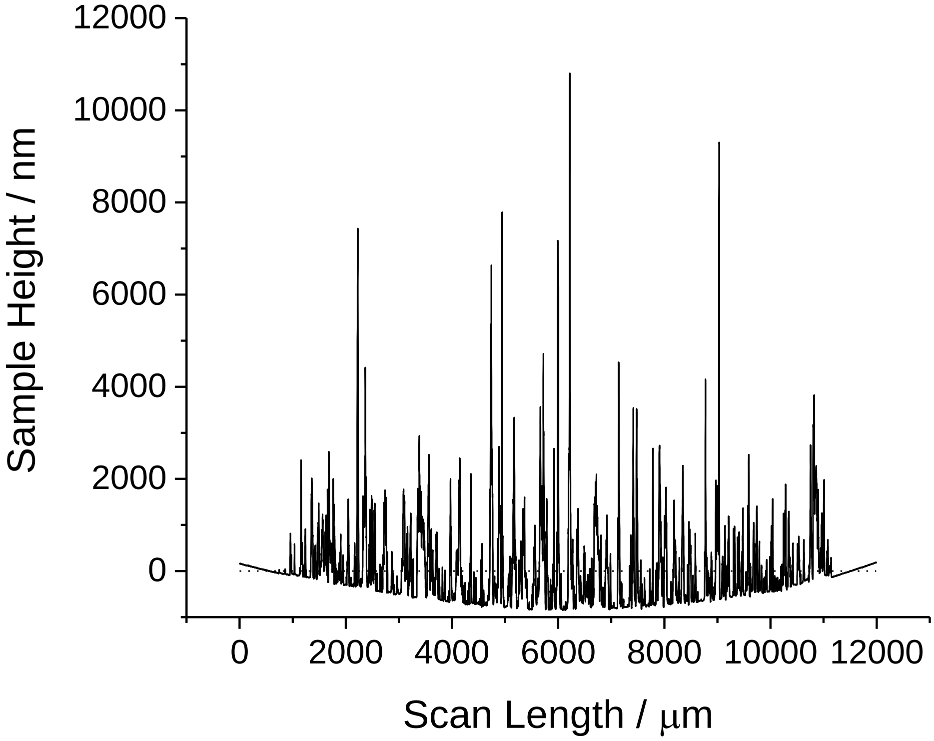

Figure A.4.4.2.2 Right profile of 5 pass 1 cm^2 print using ink 4.3.2 on a glass substrate without annealing (average height of 40 nm)

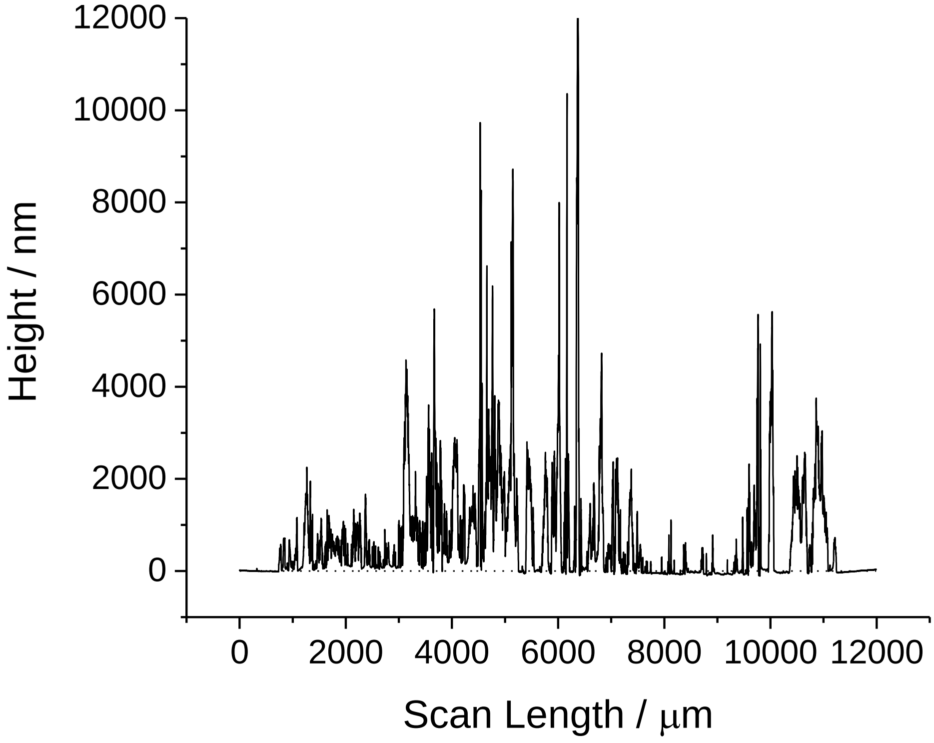

Figure A.4.4.2.3 Bottom profile of 5 pass 1 cm^2 print using ink 4.3.2 on a glass substrate without annealing (average height of 776 nm)

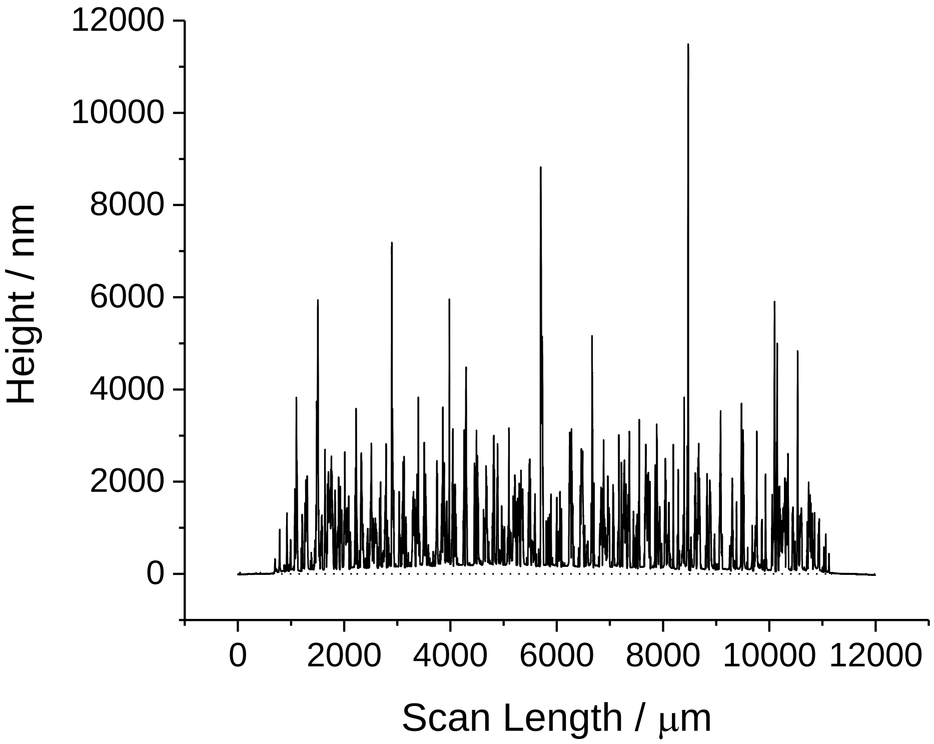

Figure A.4.4.2.4 Right profile of 5 pass 1 cm^2 print using ink 4.3.2 on a glass substrate after annealing at 450°C for 40 minutes (average height of 697 nm)

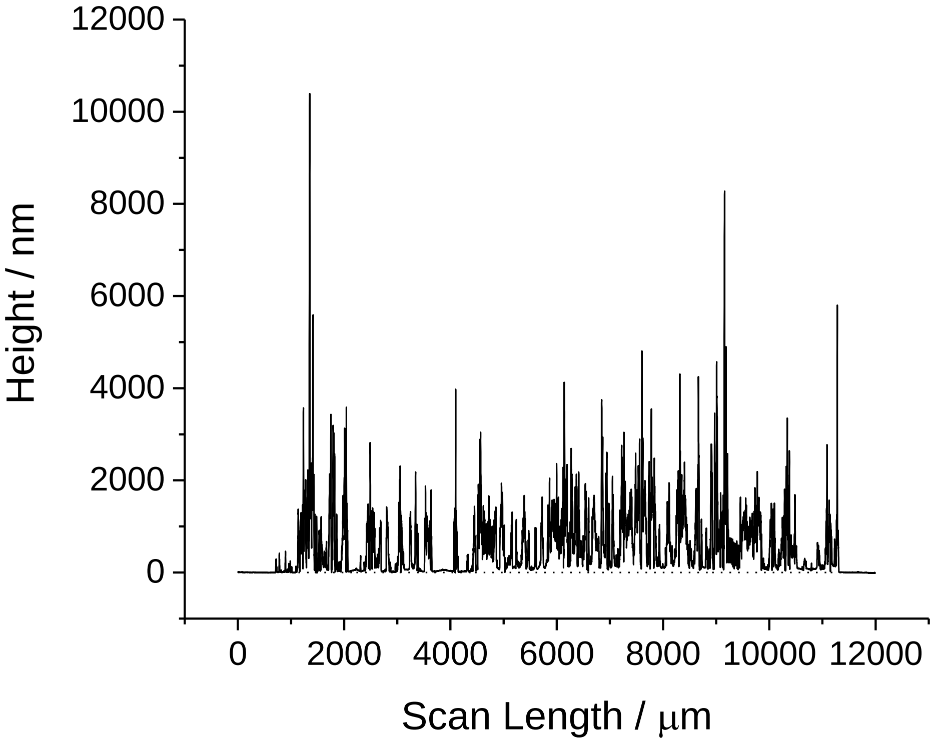

Figure A.4.4.2.5 Bottom profile of 5 pass 1 cm^2 print using ink 4.3.2 on a glass substrate after annealing at 450°C for 40 minutes (average height of 619 nm)

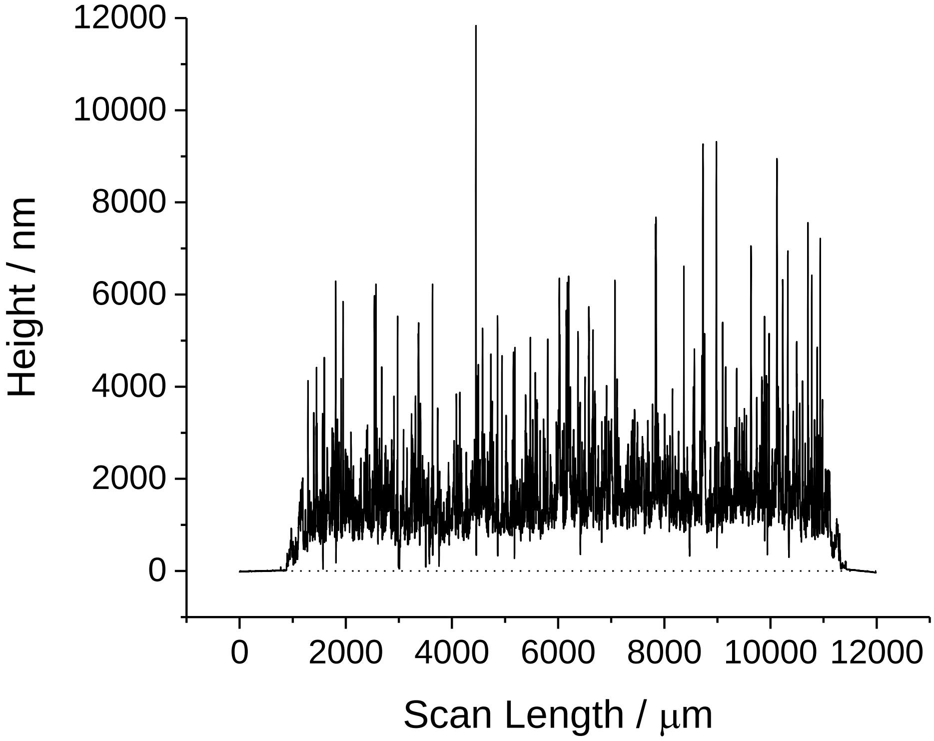

Figure A.5.3.5.1 Right profile of 5 pass 1 cm^2 print using ink 5.3.2 on a glass substrate without annealing (average height of 1640 nm)

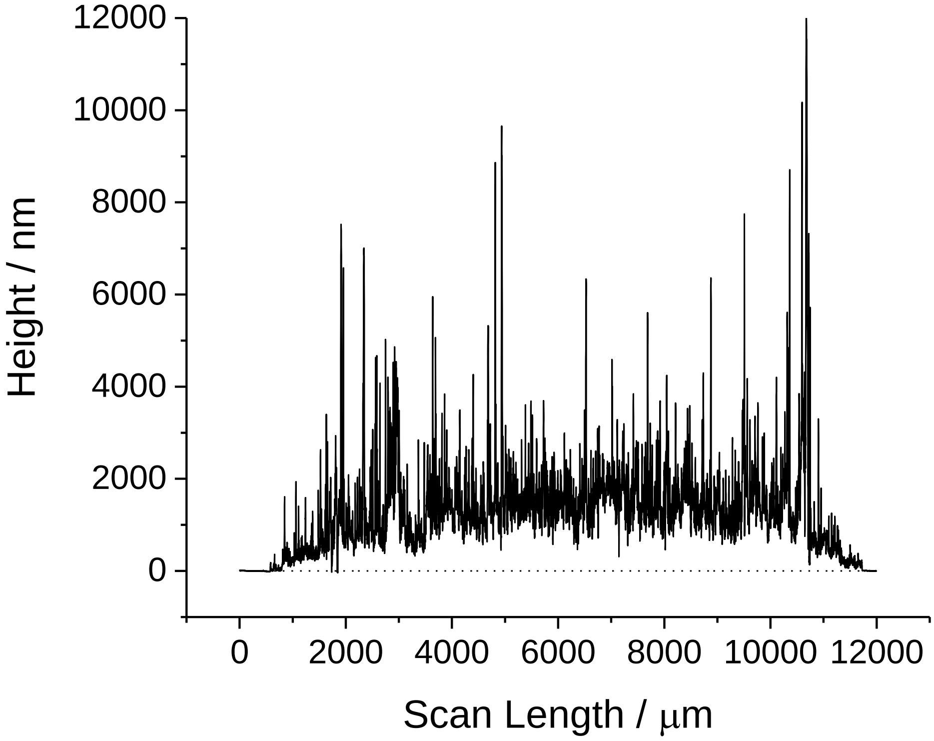

Figure A.5.3.5.2 Bottom profile of 5 pass 1 cm^2 print using ink 5.3.2 on a glass substrate without annealing (average height of 1379 nm)

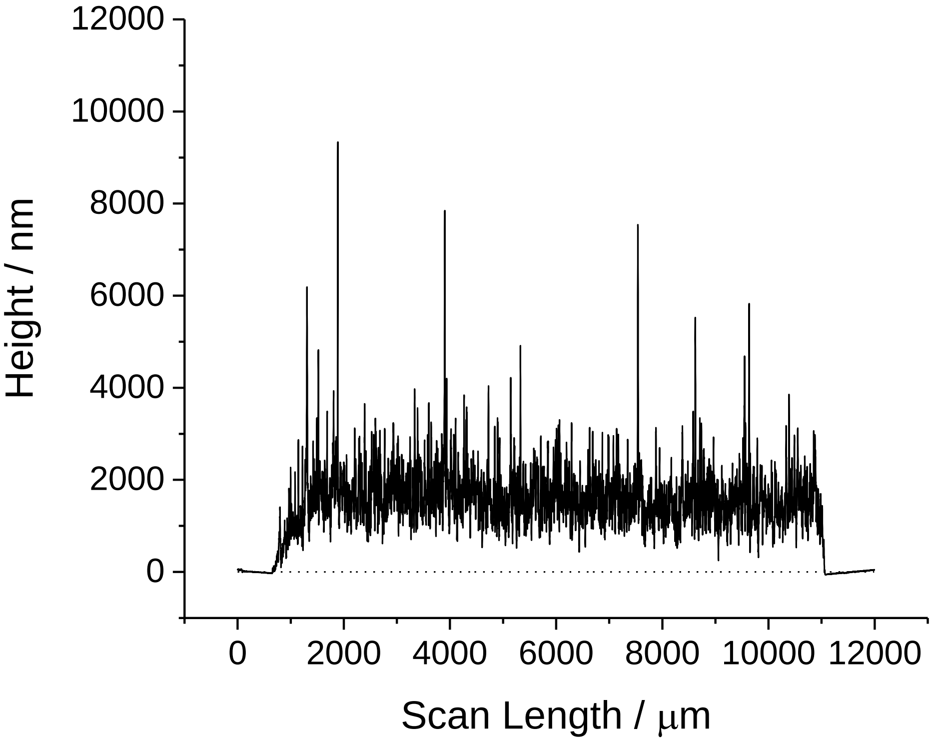

Figure A.5.3.5.3 Right profile of 5 pass 1 cm^2 print using ink 5.3.2 on a glass substrate after annealing at 200°C for 160 minutes (average height of 1602 nm)

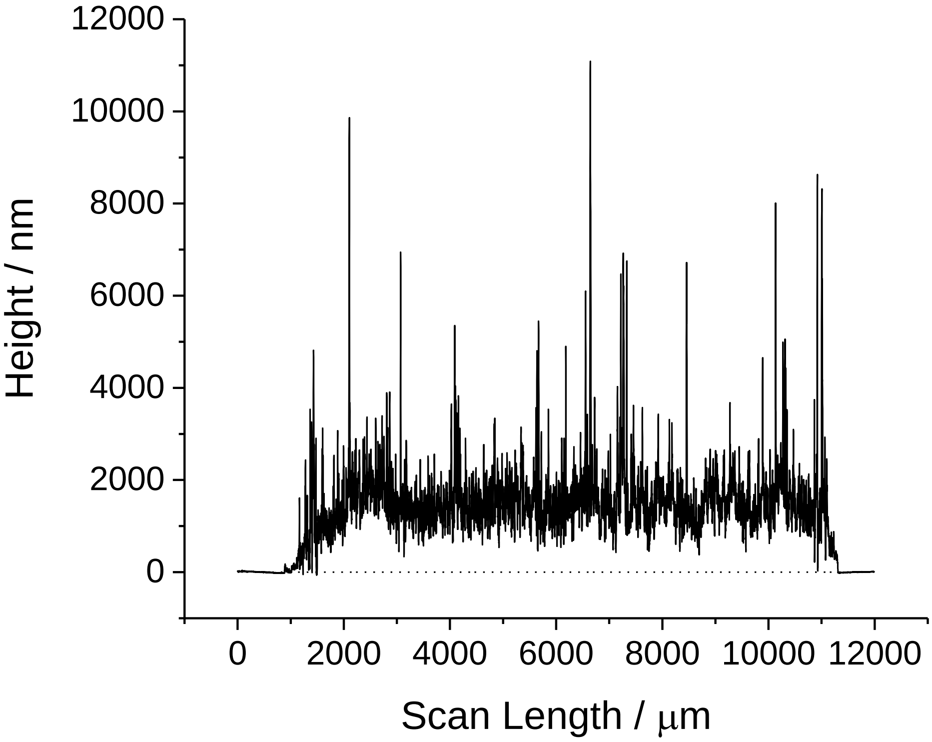

Figure A.5.3.5.4 Bottom profile of 5 pass 1 cm^2 print using ink 5.3.2 on a glass substrate after annealing at 200°C for 160 minutes (average height of 1508 nm)

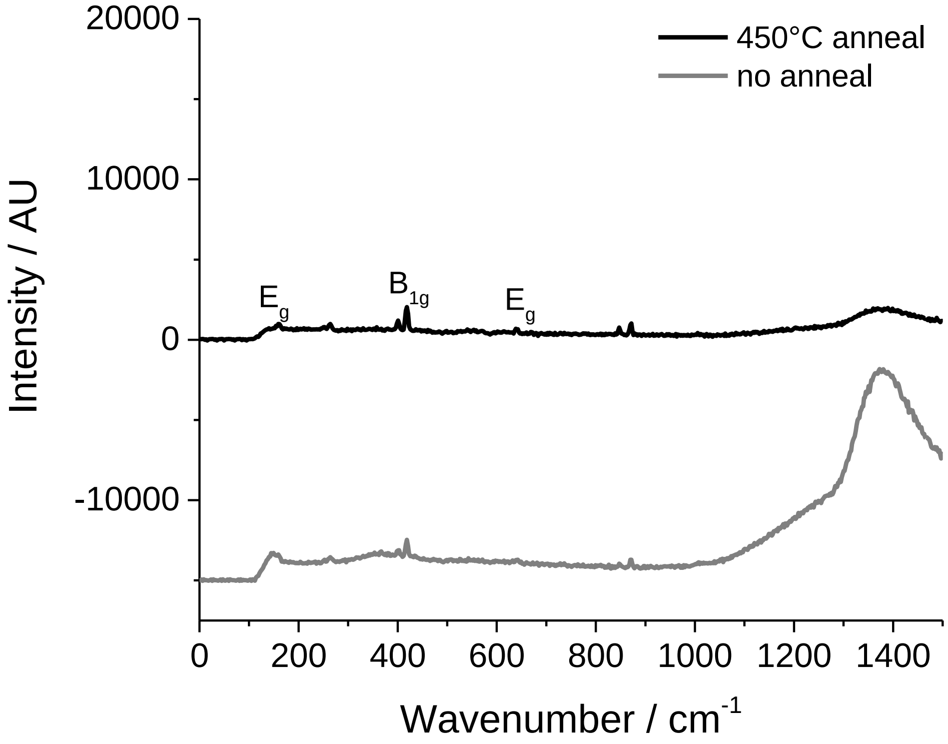

Figure A.7.2.5.1 Raman spectra of drop-tested samples using ink 7.3.4 on a glass substrate before and after annealing at 450°C for 40 minutes

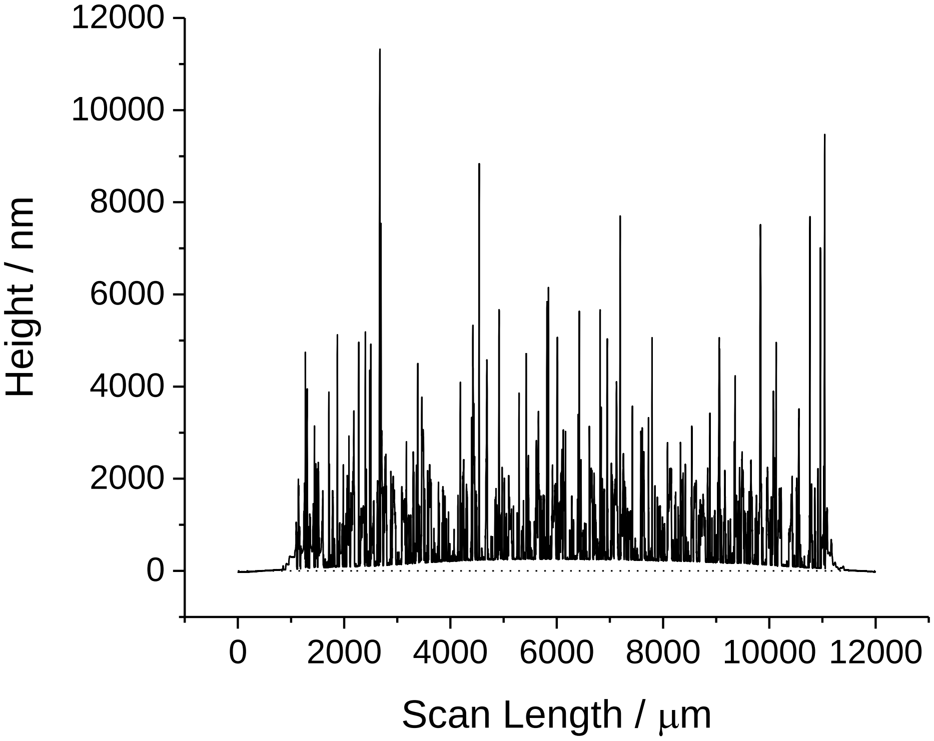

Figure A.7.2.6.1 Right profile of 5 pass 1 cm^2 print using ink 7.2.3 on a glass substrate without annealing (average height of 766 nm)

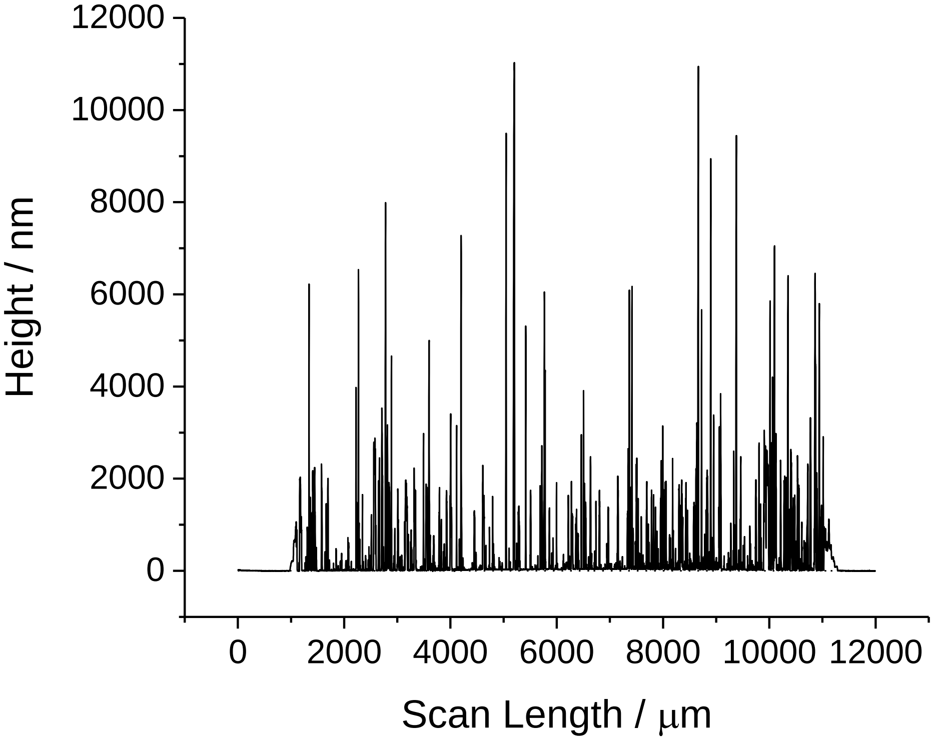

Figure A.7.2.6.2 Bottom profile of 5 pass 1 cm^2 print using ink 7.2.3 on a glass substrate without annealing (average height of 428 nm)

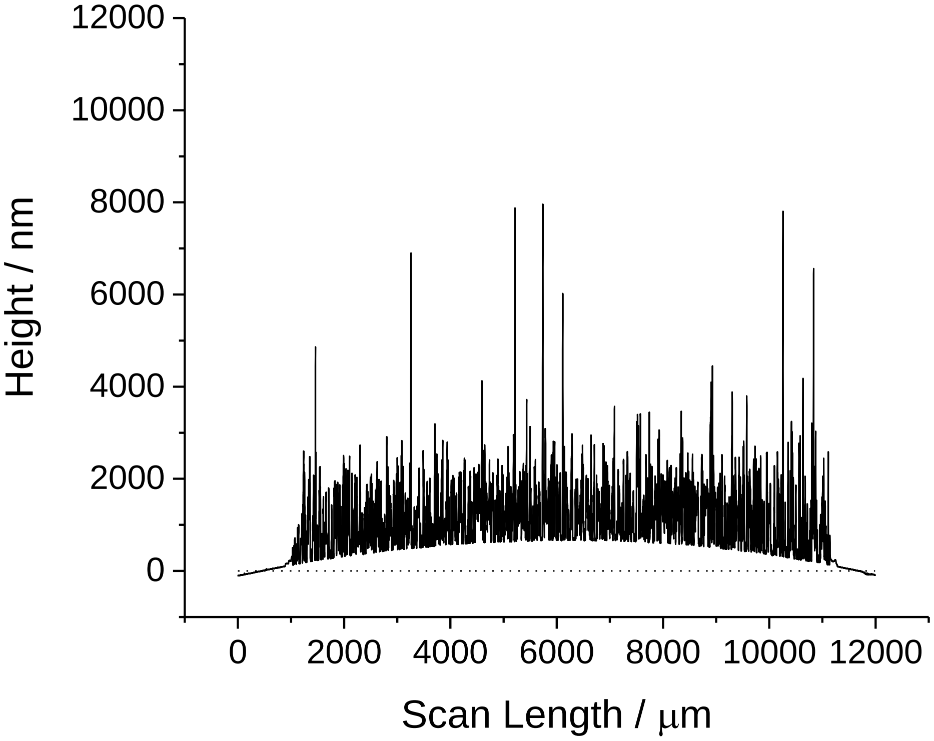

Figure A.7.2.6.3 Right profile of 5 pass 1 cm^2 print using ink 7.2.3 on a glass substrate after annealing at 450°C for 40 minutes (average height of 1147 nm)

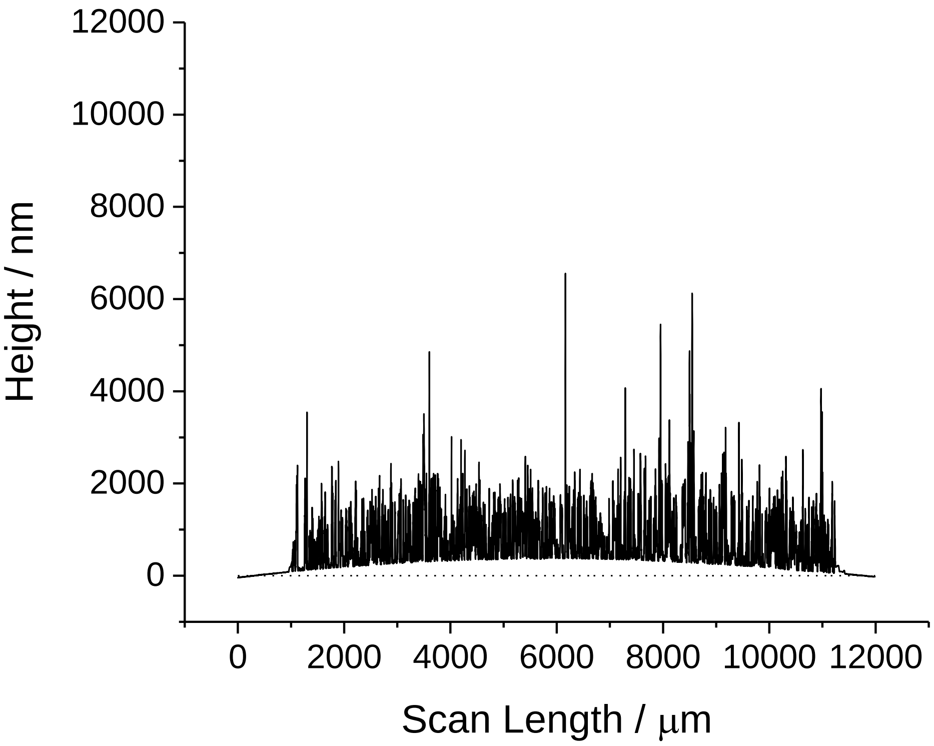

Figure A.7.2.6.4 Bottom profile of 5 pass 1 cm^2 print using ink 7.2.3 on a glass substrate after annealing at 450°C for 40 minutes (average height of 812 nm)

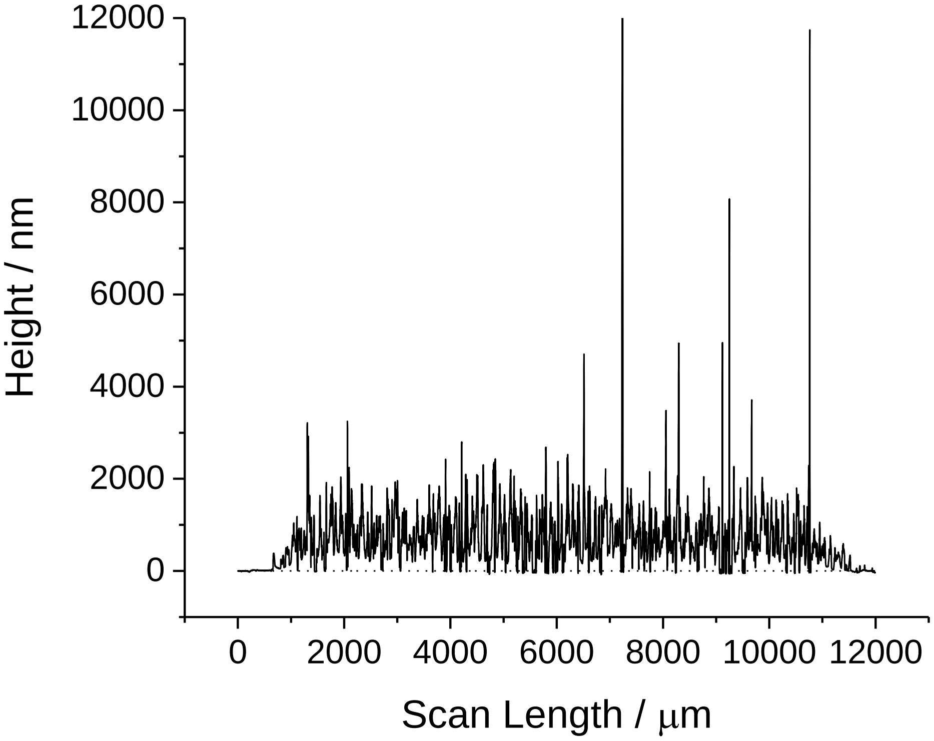

Figure A.7.2.6.5 Right profile of 5 pass 1 cm^2 print using ink 7.2.4 on a glass substrate without annealing (average height of 741 nm)

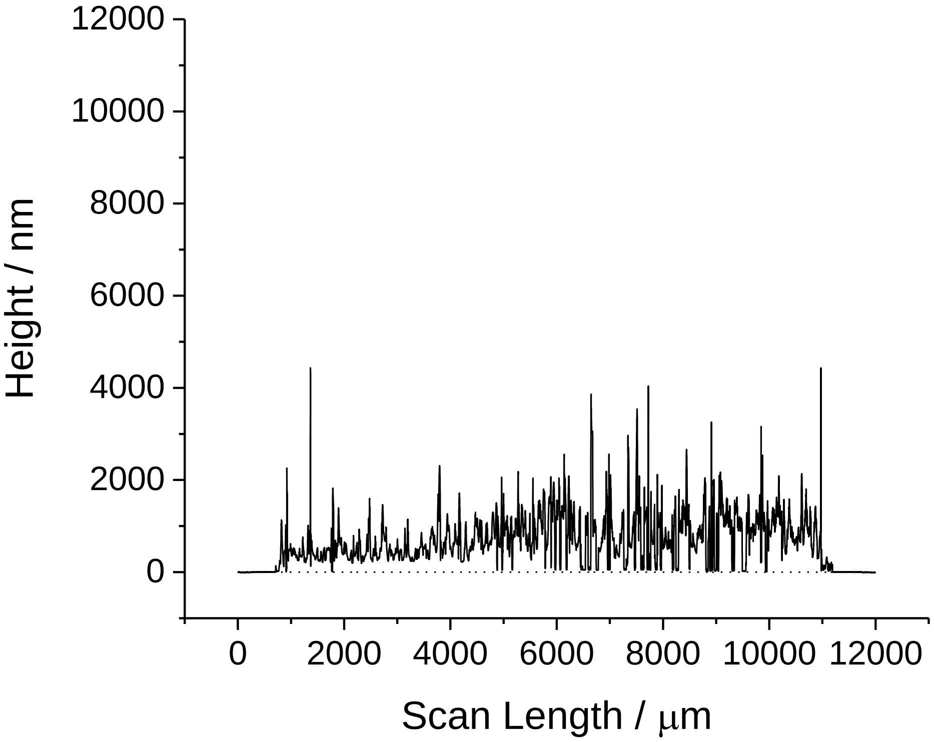

Figure A.7.2.6.6 Bottom profile of 5 pass 1 cm² print using ink 7.2.4 on a glass substrate without annealing (average height of 742 nm)

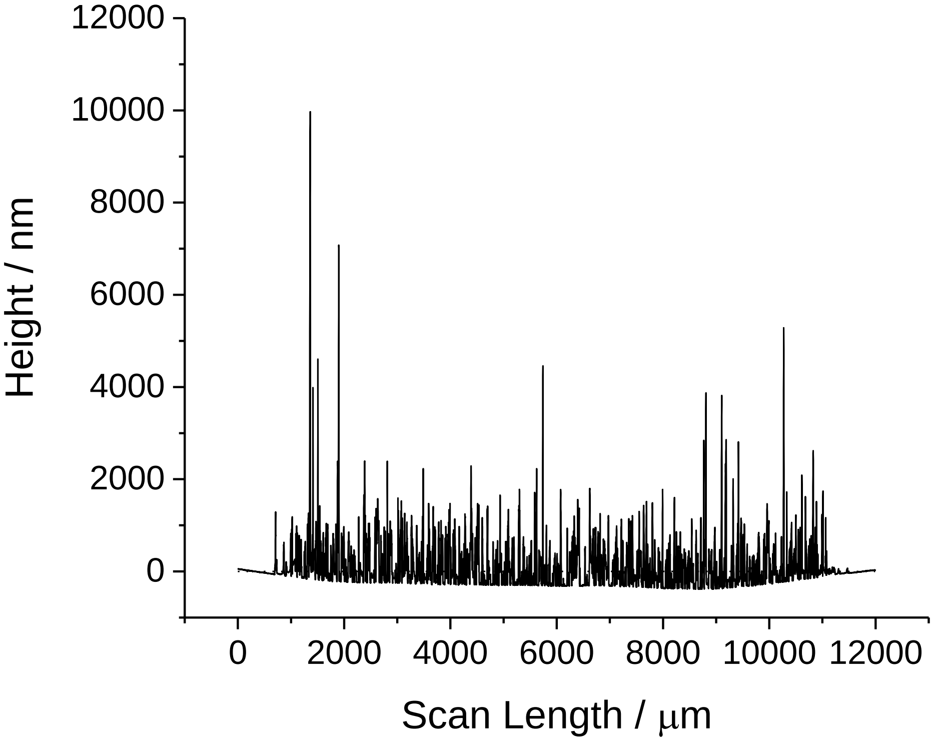

Figure A.7.2.6.7 Right profile of 5 pass 1 cm² print using ink 7.2.4 on a glass substrate after annealing at 450°C for 40 minutes (average height of 136 nm)

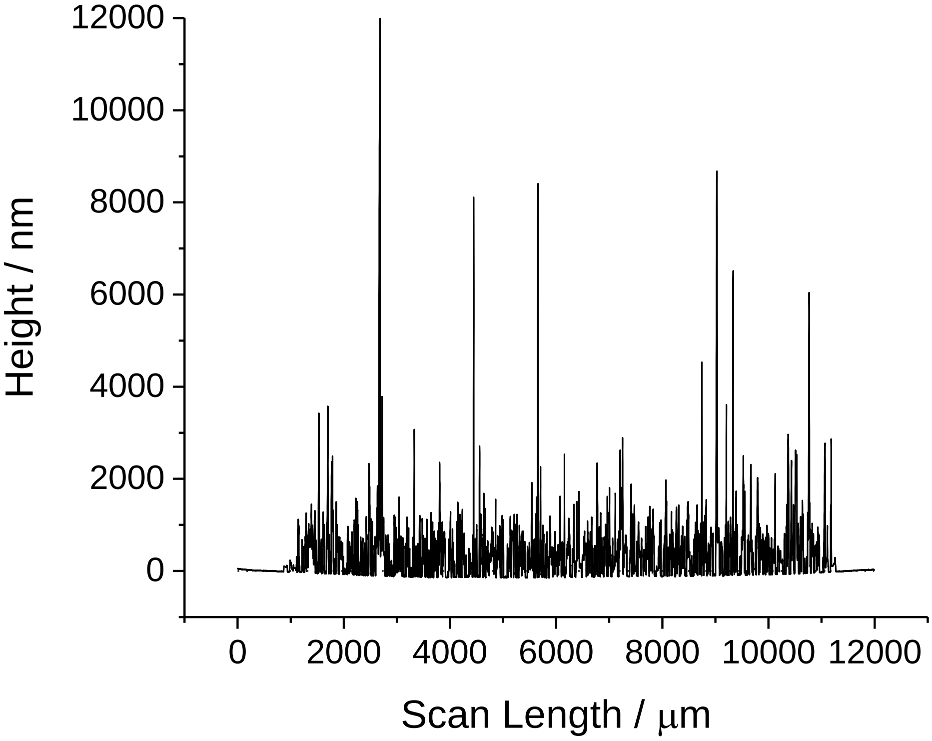

Figure A.7.2.6.8 Bottom profile of 5 pass 1 cm^2 print using ink 7.2.4 on a glass substrate after annealing at 450°C for 40 minutes (average height of 434 nm)

Table A.7.2.7.1 EDXS data for printed 5 pass 1 cm^2 samples of inks 7.2.3 and 7.2.4 on glass substrates

Element	Weight %, Ink 7.2.3	Weight %, Ink 7.2.4
C	0.00	0.00
O	39.54	40.13
Na	0.62	5.22
Mg	0.00	1.72
Si	1.65	23.84
K	0.00	0.69
Ca	0.00	3.27
Ti	48.91	19.94
Cr	1.87	2.70
Nb	7.40	2.49